

2mit

SQT



72-10

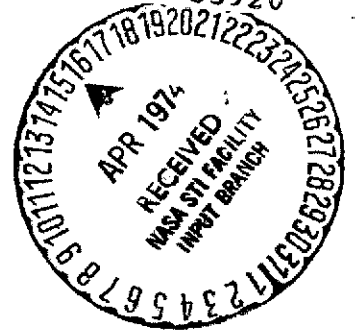
# THE INNER ZONE ELECTRON MODEL AE-5

NOVEMBER 1972

(NASA-TM-X-69987) THE INNER ZONE  
ELECTRON MODEL AE-5 (NASA) 200 P HC  
\$13.00 190 CACL 03B

74-20502

Unclas  
G3/30 33920



NATIONAL SPACE SCIENCE DATA CENTER

NATIONAL AERONAUTICS AND SPACE ADMINISTRATION • GODDARD SPACE FLIGHT CENTER, GREENBELT, MD.

The Inner Zone Electron Model AE-5

By

Michael J. Teague  
The KMS Technology Center

and

James I. Vette  
National Space Science Data Center

November 1972

National Space Science Data Center  
National Aeronautics and Space Administration  
Goddard Space Flight Center  
Greenbelt, Maryland 20771

## CONTENTS

	<u>Page</u>
Notation .....	vii
1. Introduction .....	1
2. The Analytical Unidirectional Flux .....	3
3. Data Analysis .....	11
4. High-Energy Electrons .....	21
5. The Omnidirectional Flux Model AE-5 .....	29
A. The Inner Zone Model .....	29
B. The Interface Region $L \sim 2.6$ .....	32
6. Temporal Variations in the Inner Radiation Belt .....	35
A. Variations with Solar Cycle .....	35
B. The Effects of Starfish Electrons .....	42
7. Model Presentation and Data Products .....	59
Appendix A - Use of Carpet Plots .....	63
Acknowledgments .....	65
References .....	67

## LIST OF ILLUSTRATIONS

<u>Table</u>		<u>Page</u>
1	Quiet Day Model Parameters .....	69
2	Sample MODEL Output .....	70
3	Satellite Calibration Constants .....	71
4	Pitch Angle Coverage .....	72
5	Quiet Day Periods .....	72
6	Solar Cycle Flux Ratios .....	73
7	Coefficients of Pitch Angle Dependence of Starfish Electrons .....	74
8	Starfish Decay Times .....	75
9	High-Energy Background Flux Estimates .....	76
10	Significance of Starfish Flux Component .....	77
11	Starfish Flux Cutoff Times .....	78

LIST OF ILLUSTRATIONS (continued)

<u>Table</u>		<u>Page</u>
12	Comparison of Integral Flux Decay Times .....	79
13	Comparison of Integral Flux Cutoff Times .....	80
14	Cutoff Times from 1963-38C Data .....	81
15	Omnidirectional Flux Confidence Codes .....	82
16	Integral Flux Solar Cycle Parameter Confidence Codes .....	83
<u>Figure</u>		<u>Page</u>
1	Radial Profile of the Reference Electron Content Parameter .....	85
2	Hardness Parameter $X_R$ .....	86
3	Pitch Angle Parameters $m$ and $n$ .....	87
4	Atmospheric Cutoffs $B_C$ .....	88
5-7	Quiet Day Perpendicular Integral Flux Distributions .....	89
8-9	Model Parameters $(J_I)_R$ and $X_R$ .....	90
10	Data Coverage .....	91
11-12	1963-38C Calibration Curves .....	92-93
13	Explorer 26 Calibration Curves .....	94
14-57	Data and Model Plots .....	95-108
58-59	Pfizer's Pitch Angle Distributions .....	109-110
60-61	Quiet Day High-Energy Equatorial Perpendicular Flux .....	111-112
62-63	High-Energy Quiet Day Integral Spectra .....	113-114
64	Storm Model .....	115
65	Storm Flux Ratio $R_S$ .....	116
66	Probability of Storm Flux Contribution .....	117
67	Average Storm High-Energy Spectra $L \geq 1.7$ ....	118
68-70	Modifications to Quiet Day Model .....	119-121
71	High-Energy Differential Spectra $L \leq 1.6$ .....	122
72-73	Extrapolated High-Energy Spectra .....	123-124
74-77	High-Energy Mirror Point Distributions .....	125
78-79	Inner Belt Radial Profiles .....	126-127
80-81	Radial Profiles in Interface Region $L \sim 2.6$ ..	128-129
82	Interpolated Spectrum $L = 2.6$ .....	130
83	Interpolated $B$ Dependence $L = 2.6$ .....	131
84	Solar Cycle Ratios for $L = 2.4$ .....	132
85	$L$ Dependence of Solar Cycle Ratios .....	133
86-88	OGO-Based Solar Cycle Ratios .....	134-136

LIST OF ILLUSTRATIONS (continued)

<u>Figure</u>		<u>Page</u>
89	Comparison of 1963-38C and OGO Solar Cycle Parameters .....	137
90-93	Integral Flux Solar Cycle Ratios .....	138-141
94	Sunspot Number $R_z$ .....	142
95	Separation of Flux Components .....	143
96	Temporal Variation of Low-Energy OGO Data ....	144
97-114	Pitch Angle Dependence of the Residual Starfish Flux .....	145-150
115-118	Temporal Variation of Residual Starfish Flux .....	151-154
119-127	Pitch Angle Dependence of High-Energy Residual Starfish Flux .....	155-157
128-129	Temporal Variation of High-Energy Residual Starfish Flux .....	158-159
130	Estimated High-Energy Omnidirectional Background Flux .....	160
131-134	Flux Component Radial Profiles .....	161-164
135	Extrapolated Starfish Radial Profiles .....	165
136-137	Comparison of OGO 3 and 1963-38C Integral Residual Spectra .....	166-167
138	Comparison of OGO 3 and OV3-3 Integral Spectra .....	168
139-140	Comparison of OGO 3 and OV3-3 Flux .....	169-170
141	Comparison of OGO, Pegasus, and Explorer 26 Decay Times .....	171
142-148	AE-5 Omnidirectional Flux Carpet Plots .....	173-183
149-151	AE-5 B-L Flux Maps .....	185-187
152-154	AE-5 R- $\lambda$ Flux Maps .....	188-190
155-160	AE-5 Three-Dimensional Omnidirectional Flux Plots .....	191-192
161	Carpet Plot Interpolation .....	193

## NOTATION

### Parameters

$a$	Spectral parameter (equation 6)
$B, B_c$	Magnetic field strength (equations 1, 9)
$E$	Energy (equation 1)
$E_{ij}$	Energy limit (equation 10)
$E_T$	Energy threshold (equation 12)
$f_1, f_2$	Pitch angle dependence functions (equations 6, 7)
$F$	Average storm flux (Figure 64)
$h_q$	Storm model parameters (Figure 64)
$j$	Unidirectional electron flux (equation 1)
$j_i$	Average differential flux in channel $i$ (equation 10)
$J$	Omnidirectional flux (equation 12)
$J_I$	Electron content parameter (equation 8)
$L$	McIlwain shell parameter (equation 1)
$m, n$	Pitch angle parameters (equations 6, 7)
$p$	Ratio of Starfish to total flux (equation 23)
$P$	Probability of storm flux (Figure 64)
$R_S$	Storm ratio (equation 11)
$R_T$	Solar cycle ratio (equation 15)
$s, t$	Storm parameters (Figure 64)
$t_c$	Starfish flux cutoff time (equation 21)
$T$	Universal time from solar minimum (equation 1)
$X$	Spectral hardness parameter (equation 4)
$\alpha$	Local pitch angle (equation 1)
$\alpha_0, \alpha_c$	Equatorial pitch angle (equations 2, 6)
$\theta$	Starfish pitch angle cutoff (equation 22)
$\tau$	Starfish decay time (equation 20)
$\phi$	Pitch angle cutoff (equation 6)

**PRECEDING PAGE BLANK NOT FILMED**

NOTATION (continued)

Suffixes

q	Quiet day
r	Reference condition
s	Storm
st	Starfish
T	Time
l	Mirror point

## 1. INTRODUCTION

This report is a description of the work performed in the development of the inner radiation zone electron model AE-5. It will be distributed to the users of this model together with a document providing a brief user-oriented description of the model and associated computer programs (Teague et al., 1972).

A complete description of the omnidirectional flux model is given for energy thresholds  $E_T$  in the range  $4.0 > E_T/(\text{MeV}) > 0.04$  and for L values in the range  $2.8 > L > 1.2$  for an epoch of October 1967. Confidence codes for certain regions of B-L space and certain energies are given based on data coverage and the assumptions made in the analysis. The electron model programs that can be supplied to a user are referred to. One of these, a program for accessing the model flux at arbitrary points in B-L space and arbitrary energies, includes the latest outer zone electron model and proton model. Efforts have been made to ensure that the two electron models are compatible at the interface of  $L = 2.6$ . In addition, a program for integrating the model flux along an arbitrary orbit can be supplied.

The model AE-5 is based on data from five satellites, OGO 1, OGO 3, 1963-38C, OV3-3, and Explorer 26, spanning the period December 1964 to December 1967. Because these data primarily provide unidirectional fluxes, a unidirectional flux form of AE-5 was first derived. This unidirectional form can be supplied to users in a variety of ways, as described in this document. The method used to derive AE-5 is dependent on both L and energy, owing to the varying effect of magnetic storms in the inner radiation zone. For most L values at energies below 700 keV, a sufficient average description of the inner zone flux can be obtained without regard to storm effects, and for this region an analytical description of the flux is presented. The derivation of this analytical

form is described in Sections 2 and 3. At high L values and high energies, however, the effect of storms on the average flux becomes significant and is included in AE-5. The derivation of the high-energy portion of the model is discussed in Sections 4 and 5. In the course of deriving the analytical quiet day (i.e., storm free) flux, two temporal variations were modeled. First, long-term increases in the inner radiation belt flux were observed that were considered to be correlated with increased solar activity over the period 1964 to 1967. A tabular form of this solar cycle effect is presented for energies  $E < 700$  keV. At higher energies similar temporal variations are observed, but these generally become insignificant in the context of an average flux because of the increased significance of magnetic storms. Solar cycle effects are discussed in Section 6A. The second temporal variation modeled was that caused by the decay of residual electrons from the Starfish nuclear explosion of July 1962. A model of these residual electrons is presented that describes the decay time as a function of energy and L value. In addition, cutoff times are presented that represent the times at which the flux has essentially decayed to the quiet day background. For the AE-5 model with epoch October 1967, Starfish electrons remain significant only at low L values and intermediate energies ( $E = 1$  MeV, approximately). Starfish electrons are discussed in Section 6B.

## 2. THE ANALYTICAL UNIDIRECTIONAL FLUX

The differential unidirectional electron flux in the inner radiation belt is a function of five variables: the local magnetic field strength  $B$ , the local pitch angle  $\alpha$ , the local  $L$  value, the particle energy  $E$ , and the universal time  $T$ . That is,

$$j = j(\alpha, B, E, L, T) \quad (1)$$

The first adiabatic invariant relates the local pitch angle and field strength to the equatorial pitch angle  $\alpha_0$  and the equatorial field strength  $B_0$ . The equatorial field strength is a function of  $L$  and the magnetic moment of the earth only. Equation 1 then becomes

$$j = j(\alpha_0, E, L, T) \quad (2)$$

which is referred to as the equatorial pitch angle distribution. An alternate form of equation 1 is the perpendicular flux. The local pitch angle and field strength can be reduced to the mirror point field strength  $B_{\perp}$  by using the first adiabatic invariant, and equation 1 becomes

$$j = j(B_{\perp}, E, L, T) \quad (3)$$

A complete description of the unidirectional flux at given  $E$ ,  $L$ , and  $T$  is then given by the equatorial pitch angle distribution for  $90^\circ \geq \alpha_0 \geq \alpha_c$  or by the perpendicular flux distribution for  $B_c \geq B_{\perp} \geq B_0$ , where  $\alpha_c$  and  $B_c$  are, respectively, the equatorial pitch angle and the field strength corresponding to the atmospheric cutoff.

Both equatorial pitch angle distribution and perpendicular flux data sets are used in the development of the present model (Section 3). The analytical model is given in terms of a spectrum, an equatorial pitch angle dependence, and sets of coefficients describing the temporal changes occurring over the time period September 1964 to December 1967. It is considered that the total electron flux in the inner belt at any given time is composed of four components: (1) a quiet day (that is, periods remote from the effects of magnetic storms) background flux at solar minimum, (2) a quiet day component that is dependent on solar cycle, (3) storm time flux, and (4) residual flux from the 1962 Starfish nuclear explosion. Since the diffusion equation is linear and since the particles already at a given L value will not affect the particles diffusing to that L value to a first approximation, these components can be separated and studied as separate processes. The components are not necessarily attributed to different physical phenomena but are merely modeled separately. It is evident, for example, that the flux increase with solar cycle is physically associated with the storm time component. The last two components, (3) and (4), are discussed in detail in later sections (Sections 6A and 6B), because the present analytical model is primarily an attempt to describe the first two components. Evidently the four components of the flux are not easily separated, and any possible separation is heavily dependent on the L value, the particle energy, and the universal time. For instance, in late 1964 for  $L \leq 2$ , the dominant flux component is the residual Starfish flux, and no description of the other components can be obtained directly. In late 1967, however, the residual Starfish flux for  $E < 1$  MeV has decayed to an insignificant level for most L values, and observations of the remaining three components can be made. The present analytical model describes the inner belt quiet day flux for energies  $E \leq 690$  keV at an arbitrarily chosen epoch of October 1967. No attempt is made to separate the first two flux components because no data are available at solar minimum, although an elementary description of the solar cycle

effect is given for certain L values in Section 6A. At energies  $E > 690$  keV, the data available were limited and an analytical quiet day model is not presented. Detailed discussion of high-energy electrons is presented in Section 4.

The assumed spectral form is that previously discussed by Teague and Vette (1971), and the unidirectional flux at some reference time  $T_R$ , reference equatorial pitch angle  $\alpha_R$ , and L value is

$$j_R = a_R(L, \alpha_R, T_R) E \exp [-E/X_R(L, \alpha_R, T_R)] \quad (4)$$

where  $a_R$  and  $X_R$  are the reference parameters. Teague and Vette (1971) showed that this spectral form provided a better description of the quiet day flux than a power law, an  $E^2$  times exponential form, or the more normally assumed simple exponential law. The reference time  $T_R$  is taken as October 1967, and the reference pitch angle  $\alpha_R$  is taken as  $90^\circ$ . It is also assumed that equation 4 can be generalized to give

$$j = a_R f_1(L, T) E \exp [-E/X_R f_2(L, T)] \quad (5)$$

where the pitch angle dependences of the parameters are given by the expressions

$$\begin{aligned} a(\alpha_0, L, T) = a_R f_1 &= a_R \left[ \frac{\sin^m(\alpha_0 - \alpha_c)}{\sin^m(\phi - \alpha_c)} \right] \text{ for } \phi > \alpha_0 \geq \alpha_c \\ &= a_R \text{ for } 90^\circ \geq \alpha_0 \geq \phi \end{aligned} \quad (6)$$

and

$$\begin{aligned} X(\alpha_0, L, T) = X_R f_2 &= X_R \left[ \sin^n \alpha_0 / \sin^n \phi \right] \text{ for } \phi > \alpha_0 \geq \alpha_c \\ &= X_R \text{ for } 90^\circ \geq \alpha_0 \geq \phi \end{aligned} \quad (7)$$

In equations 6 and 7,  $m$  and  $n$  are  $L$ -dependent pitch angle parameters and  $\phi$  is an  $L$ -dependent limit for the pitch angle variation. The five model parameters  $a_r$ ,  $X_r$ ,  $m$ ,  $n$ , and  $\phi$  are given in Table 1 for .05 intervals in  $L$  for  $L \leq 2$  and at .1  $L$  intervals at higher  $L$  values. A sixth variable  $(J_I)_r$  is also given in this table, where

$$(J_I)_r = \int_0^{\infty} a_r E \exp(-E/X_r) dE = a_r X_r^2 \quad (8)$$

This parameter is included because the variable  $a_r$  has little physical significance, whereas  $(J_I)_r$  approximates to the total unidirectional electron flux at the reference condition for energies above thermal energy. This parameter will be referred to as the electron content parameter; however, it is not a measure of electron density or total number of electrons. The hardness parameter  $X_r$  is a measure of how fast the spectrum falls with increasing energy; that is, the larger  $X_r$ , the harder the spectrum. The variation of  $(J_I)_r$  and  $X_r$  with  $L$  is also shown in Figures 1 and 2, and it can be seen that the peak hardness parameter occurs at  $L = 1.8$  and the peak electron content occurs at  $L = 1.9$ . In addition, Table 1 and Figure 3 show that the pitch angle dependences become progressively more steep with decreasing  $L$ , particularly at low  $L$  values where large changes in the parameter  $m$  can be seen. Note that no particular significance can be attributed to the larger changes of  $m$  as opposed to  $n$  at low  $L$  values. In general, both parameters are required for adequate modeling of the data, but the marked steepening of the pitch angle distribution at low  $L$  values could have been modeled by a large change in the parameter  $n$  rather than  $m$ , as shown in Figure 3. The parameter  $\phi$  in Table 1 appears irregular in its variation with  $L$ . However, the parameter  $\phi/\alpha_c$  is monotonic with  $L$  and indicates that the flux changes with pitch angle occur over a decreasing pitch angle range as the lower  $L$  values are approached.

The atmospheric cutoff field values  $B_c$  assumed for the present model are shown in Table 1 and Figure 4. For  $L \geq 1.7$ ,  $B_c$  is assumed to be linear with  $L$  and is given by the relation

$$B_c = .16 + .06L \quad (9)$$

The atmospheric cutoff based on the Jensen and Cain 1960 magnetic field model with a minimum altitude of 100 km is shown in Figure 4; equation 9 is a reasonable approximation to this cutoff. As will be seen from later sections, for  $L \geq 1.7$  no data were available in the region of the atmospheric cutoff, and the influence of equation 9 on the fit between the model and the data is minimal. For  $L < 1.7$ , however, good data were available in the region of the atmospheric cutoff, and the  $B_c$  values given in Table 1 are essentially determined by the data. Figure 4 shows that the  $B_c$  values for  $L < 1.7$  are below the values given by the linear approximation equation 9.

The model parameters and equations presented in this section and the temporal parameters discussed in later sections are included in the APL (A Programming Language) routine AMODEL on the Goddard Space Flight Center IBM 360/95. A sample of the output from the program is shown in Table 2. The model equatorial pitch angle distribution is shown for three energy intervals and for one energy threshold at an epoch of October 1967. The energy intervals, pitch angle range, and epoch are input data.

In addition to the APL programs mentioned above, a FORTRAN program UNI, which is capable of generating arbitrary flux from the analytical model, is available. Further discussion of these programs is given in Section 7, and more detailed information can be obtained from the publication by Teague (1972). While the analytical model fits the available data well (Section 3), some care must be taken in determining fluxes at energy thresholds or in energy ranges different from

those used to evaluate the model parameters. In particular, for a given energy threshold or energy range, significant differences in the fluxes predicted in the cutoff region result from different assumptions concerning the energy range used for the pitch angle dependence. It was determined that the best results were obtained by using the energy limits for the pitch angle distribution corresponding to the measurement that was closest to the desired energy interval. For example, if the unidirectional flux distribution in the interval 150 to 250 keV were required, program UNI would use the energy range 133 to 292 keV corresponding to data from the OGO spectrometer (Section 3) for evaluation of the pitch angle dependence. This adjustment is performed automatically by program UNI.

Three-dimensional SD-4060 plots of the analytical quiet day model flux as a function of B and L are given in Figures 5 through 7 for energy thresholds

$$E_T = 40, 100, \text{ and } 250 \text{ keV}$$

for an epoch of October 1967. It should be noted that, while the analytical model is applicable for electrons with energies  $E < 690$  keV, the ability of this model to represent fluxes of particles above a given threshold,  $E_T$ , becomes suspect for  $E_T > 500$  keV for  $L < 1.6$  approximately, and for  $L \leq 1.4$  the technique described in this section for determining  $J_I$  and  $X$  becomes more complex because of the significant hardening of the spectrum for  $E_T > 690$  keV. This high-energy spectrum is discussed in detail in a later section.

Similar plots are presented in Figures 8 and 9 for the parameters  $J_I$  and  $X$ . These diagrams are intended as a pictorial representation of the inner belt. The steepening of the pitch angle distribution at low L values can be clearly seen. It is also evident that the peak

integral electron flux above thermal energies in the inner belt occurs at  $L \sim 1.8$  with a sharp falloff at low  $L$  values and a relatively slower falloff at higher  $L$  values. It is apparent that the model electron content parameter  $J_I$  has the same characteristics as the model flux in contrast to the hardness parameter  $X$ , which exhibits a greater falloff at higher  $L$  than at lower  $L$ .

### 3. DATA ANALYSIS

For the work described in this document, data from five satellites were used: OGO 1, OGO 3, 1963-38C, OV3-3, and Explorer 26. The prime data sets for the quiet day flux described in the previous section were obtained from the first three of these satellites. At a late date, however, data from the OV3-3 satellite became available and were incorporated into the flux model with a minimum of data analysis. All of the satellite data were used to derive the residual Starfish electron model described in Section 6B.

Data from the University of Minnesota electron spectrometers (Principal Investigator - Prof. John Winckler) carried on board the OGO 1 and 3 satellites were used (NSSDC data sets 64-054A-21A and 66-049A-22A). Measurements from these satellites extended over the period September 1964 to December 1967 (Figure 10). A complete description of the spectrometers and the derivation of the calibration constants and energy ranges of the five channels have been given elsewhere (Teague, 1970). In this document comparison is made between the present OGO calibration constants and those originally presented by Pfitzer (1968). The relevant calibration constants are summarized in Table 3. The 1963-38C satellite was launched into an 1100-km circular orbit on September 28, 1963, and provided data for the present model through 1967 (Figure 10). Data from the Applied Physics Laboratory integral electron spectrometer (Principal Investigators - Drs. C. O. Bostrom and D. J. Williams) were used (Beall, 1969). Total particle unidirectional flux measurements were made, corresponding to nominal electron thresholds of .28, 1.2, 2.4, and 3.6 MeV. Useful data for the present requirement were obtained only from the lowest energy channel because the remaining channels had fallen to the proton background for the time interval under consideration. However, the present Starfish model is compared with results based on data including those from the higher energy channels.

PRECEDING PAGE BLANK NOT FILMED

Calibration information for the two lower energy channels was obtained by integration of the efficiency curves using program EPSBART (Teague, 1972). The results are shown in Figures 11 and 12. In each case the parameter  $\bar{\epsilon} = 1/c \times \text{geometric factor}$  is averaged over a range of spectral hardness appropriate to the observed spectra.  $E_0$ ,  $X_1$ , and  $X_2$  are the hardness parameters for an exponential spectrum, an energy times exponential spectrum, and an energy squared times exponential spectrum, respectively. For the higher energy channel the exponential spectrum is appropriate, whereas for the lower energy channel the energy times exponential spectrum is chosen (Teague, 1970). The present calibration values are also shown in Table 3 and are compared with the values given by previous authors. Data over the time period mid-1966 to late 1967 were used in the present study. Explorer 26 data from the University of California at San Diego detectors (Principal Investigator - Prof. C. E. McIlwain) were used for the time interval January to June 1965. Data from two integral detectors with thresholds at 500 keV and 5 MeV were available. These data proved to be of very limited use, however, because it was clear that the data were in disagreement with other data sets. Since the data appeared less inconsistent with other data sets in the outer electron zone study (Singley and Vette, 1972), it is likely that the proton contribution to the total flux was not accurately determined. The 5-MeV data were not used in the present analysis, and the 500-keV data were used only to estimate Starfish decay times over a limited L range (Section 6B). EPSBART runs were also made for this detector, and the results are shown in Figure 13 and Table 3. OV3-3 data from the Aerospace Corporation differential nine-channel electron spectrometer were used. These data were kindly supplied by the Principal Investigator, Dr. A. Vampola, at a late date in the evolution of the model and were incorporated in only an elementary way. The spectrometer provided unidirectional differential total particle fluxes in nine energy intervals corresponding (approximately) to electron energies in the range  $2310 \geq E/(\text{keV}) \geq 300$  (Table 3). Data from only the two lowest

energy intervals were used in determining the analytical quiet day model, corresponding to electron energies in the ranges  $375 \geq E/(\text{keV}) \geq 225$  and  $600 \geq E/(\text{keV}) \geq 350$ . Data from the seven higher channels were used as the sole basis for the high-energy model discussed in Section 4. No separate evaluation was made of the detector calibration constants.

As noted previously, the data sets used for the development of the analytical inner belt model were OGO 1, OGO 3, 1963-38C, and OV3-3. Table 3 indicates that the OGO spectrometer provided unidirectional electron flux measurements in five energy ranges. The OGO data sets were averaged into monthly intervals over the period September 1964 to December 1967 and into 0.1-L intervals over the range  $2.0 \geq L \geq 1.3$  and 0.2-L intervals over the range  $2.4 \geq L \geq 2.0$ . No OGO data were available over the period October 1965 to June 1966. By using the first adiabatic invariant, the data were transformed into the form of an equatorial pitch angle distribution. The pitch angle coverage obtained for the time interval and L value range of interest is summarized in Table 4. It is apparent that the coverage obtained at high L values at the model epoch is poor and also that no data were available at this time for  $L < 1.5$ . At earlier times, however, pitch angle coverage was considerably better, and, with the assumption that the shape of the equatorial pitch angle distribution is time independent, these earlier data can be reduced to a common epoch for the development of the model. However, it is first necessary to establish which periods in the data interval are significantly influenced by residual Starfish electrons and storm time electrons and which periods are free of these effects and are therefore quiet periods. These quiet periods were primarily established by investigation of the OGO data sets, but confirmation of these periods was obtained by analyzing the 1963-38C data and the OV3-3 data. This analysis was previously described by Teague and Vette (1971), and a summary table of the quiet periods obtained is presented in Table 5. The monthly averaged data sets from

these quiet periods were normalized to an epoch of October 1967 using an  $\alpha_0$ -independent factor. The average data sets so obtained formed the major basis for the analytical model. The monthly averaged OGO data sets indicated that the counts for energies greater than 690 keV registered nonzero values only for periods when Starfish and storm time effects were significant. It was therefore decided to develop a quiet day model valid for energies  $E \leq 690$  keV. Observations from the OV3-3 data indicated significant fluxes for  $E > 690$  keV, however, and it became apparent that the OGO satellite generally was not measuring these because of a combination of a high intensity threshold and the sampling of only low equatorial pitch angles.

The 1963-38C data were available in the form of total counts as a function of time for a specified narrow  $B_{\perp}$  interval (.02 to .01 gauss) at .05 intervals in L for  $1.2 \leq L \leq 1.6$  and .1 intervals for  $1.6 < L \leq 2.0$ . In addition, perpendicular flux distributions were available at certain epochs over the period 1966 to 1967. The approximate equatorial pitch angle range covered by these distributions is indicated in Table 4. The proton background was removed from the total flux measurements using the 1963-38C measurements given by Beall (1969). In general, flux distributions were not available for quiet periods, and it was assumed that the shape of the storm time distributions was identical to that on a quiet day. Average perpendicular flux distributions were obtained by normalizing to epoch October 1967 using count rates as a function of time for a fixed  $B_{\perp}$  interval.

As noted previously, the OV3-3 data did not become available until much of the modeling activity had been performed. Dr. Vampola provided microfilm plots of equatorial perpendicular flux as a function of time for the period late 1966 through 1967 for each of the nine channels. Complete data analysis had been performed by Dr. Vampola. The unidirectional flux measurements after removal of the proton

background had been reduced to equatorial perpendicular fluxes by use of pitch angle distributions based on the OV3-3 data. For  $L > 2$ , however, Dr. Vampola had made the assumption of linear pitch angle dependence owing to poor data coverage. The assumed pitch angle dependences were not available to NSSDC at the time of the modeling activity. Only equatorial perpendicular flux values for the two lower energy channels (Table 3) were used for the analytical quiet day model.

Plots of the OV3-3 data used in developing the present quiet day model are given in Figures 14 and 15, and CalComp plots of the OGO and 1963-38C data are presented in Figures 16 through 57. The averaged count rate distributions given by the 1963-38C data are shown with the equatorial pitch angle distributions from the OGO data for the quiet periods previously discussed. The OGO data sets are not shown normalized to a common epoch in order to illustrate temporal flux changes. These changes are the subject of following sections. The ordinate scale on Figures 16 through 57 is arbitrary count rate. Pfitzer (1968) performed normalization of the absolute count rates measured by OGO 1 and OGO 3 in order to obtain a common data base. Furthermore, the 1963-38C data shown in these figures do not provide absolute count rates because they are normalized to a common epoch.

The OV3-3 data are shown as a function of  $L$  in Figures 14 and 15 for the mid-1966 and early 1967 periods, respectively. To reduce the model to the correct epoch, the flux ratios determined from the OGO 3  $690 \geq E/(\text{keV}) \geq 292$  data were used. In general, more data were available for the earlier epoch shown in Figure 14, and more emphasis is given to these data in determining the model parameters. The broken line in Figure 14 represents the estimated background in August 1966, and the full line indicates this background with the Starfish residual flux added (Section 6B). In Figure 15 the broken line represents the model for epoch August 1966, and the full line represents the model

for epoch April 1967. A small Starfish residual not shown remains at low L values for epoch April 1967. However, the data at these L values remain slightly above the model. It can be seen that the agreement between model and data in Figure 15 is poorer than in Figure 14, with the data usually below the model. As noted, the model parameters were determined giving greater emphasis to the August 1966 epoch because of the more limited data available at the April 1967 epoch. However, the comparison shown in Figure 15 does cast some doubt on the accuracy of the solar cycle parameters obtained with the OGO data for high L values at these energies (Sections 6A and 7).

In general, the data from the OGO 3, 1963-38C, and OV3-3 satellites provide reasonable pitch angle coverage, as can be seen from the tables. However, in a number of regions data are poor, and the analytical model is no better than extrapolation from higher pitch angles or other L values. For example, at high L value ( $L > 2$  approximately), poor pitch angle coverage at the model epoch is obtained from the OGO data, as shown in Figures 48 through 57. This deficit is in part offset by the better coverage at earlier quiet periods and by the equatorial perpendicular measurements from the OV3-3 data. That is, the shape of the pitch angle dependence is well determined, but the absolute fluxes at the model epoch may be suspect. Further, at low L values ( $L < 1.4$  approximately) the OGO data are no longer useful, and thus limited spectral information is available. Fortunately, at these L values excellent pitch angle coverage is afforded by the 1963-38C data, although the background proton flux becomes significant in comparison to the electron flux, and the data standard deviation increases accordingly. Again there is the problem of reducing the OV3-3 and the 1963-38C data to a common epoch, which results in some uncertainty in the absolute value of the electron content parameter  $(J_I)_T$ . At intermediate L values where the coverage of the independent variables is best, some conflict arises between the 1963-38C data and the OGO data in the region of the atmospheric cutoff, thus resulting in some uncertainty in the pitch angle parameters  $m$  and  $n$ .

A case in point is  $L = 1.6$ , Figures 32 through 35. It is apparent from the comparison of the OGO data and the model plots that the model plots indicate a more rapid fall at low equatorial pitch angles than the OGO data would indicate. In Figure 35, however, the discrepancy between the 1963-38C data and the model is seen to be the reverse; i.e., the model is slightly higher than the data would indicate in the region of the atmospheric cutoff. The conflict between the two data sets occurs at  $L$  values in the range  $1.9 \geq L \geq 1.6$ , and the 1963-38C data are generally considered to be more reliable. The model is primarily a fit to these data for low  $L$  values. It was noted in the previous section that at low  $L$  values the atmospheric cutoff is essentially determined by the 1963-38C data and that  $B_c$  in this region deviates from the linear assumption for higher  $L$  values. Very significant model flux changes occur in the cutoff region as small changes in  $B_c$  are made, owing to the  $(\alpha_0 - \alpha_c)$  term in equation 6. Since this region is ill defined at high  $L$  values, it is probable that the model flux is associated with a considerable error for low pitch angles at these  $L$  values. An error of a factor of 3 or 4 is not unlikely.

The equation for the differential spectrum, equation 4, was chosen on the basis of the work performed by Teague and Vette (1971). A number of functional forms describing the pitch angle dependence of the spectral parameters were tested. Equations 6 and 7 were chosen because they best describe the flux change with pitch angle. Other functions can be used that better describe the pitch angle dependence at low or high  $L$ , but these equations represent the best compromise for the total range. In addition, the inclusion of the  $\alpha_c$  parameter in equation 6 ensured that the model flux became zero at  $\alpha_0 = \alpha_c$ . The model parameters were fitted to the data by hand iteration using the APL program AMODEL (Teague, 1972) previously discussed. Also, a separate APL program, FLUXOV (Teague, 1972), giving the equatorial perpendicular flux was written for the OV3-3 data. An integrated form

of the differential spectrum, equation 4, was used for fitting to the measured fluxes in a given energy interval. That is, the average differential flux,  $j_i$ , in the energy interval  $E_{i2}$  to  $E_{i1}$  is

$$j_i = \frac{(J_I)_r}{E_{i2} - E_{i1}} \left\{ \left( 1 + \frac{E_{i1}}{X_r} \right) \exp \left( - \frac{E_{i1}}{X_r} \right) - \left( 1 + \frac{E_{i2}}{X_r} \right) \exp \left( - \frac{E_{i2}}{X_r} \right) \right\} \quad (10)$$

Fits were initially performed in the areas where the data coverage was good, i.e., intermediate L values. The results for these L values were used to establish trends for estimating the model parameters in L regions where the data coverage was poor. At low L values for which no OGO data were available, the least squares APL library program NONLIN (Wilson, 1971) was used for fits to the 1963-38C data. The OV3-3 data were used exclusively for determining the cutoff  $\phi$  for the pitch angle functions. In addition, the data set provided valuable confirmation of the model parameters determined from the OGO data. A complete description of the APL programs mentioned here can be found in the document "Inner Zone Computer Programs" (Teague, 1972).

Figures 14 through 57 show that in general the agreement between the model and the data is good, and it is considered that the model flux is within the standard deviation of the data. It is further considered that the model flux provides as good an estimate of the data at high energy ( $E \approx 690$  keV) as at low energy; that is, the spectral function is not a simply linearly weighted fit to the data. In Figure 15 agreement between the model and the low-energy OV3-3 data is not particularly good. However, the data have a large standard deviation, and the model is reduced to an epoch of August 1966 by using B-independent factors based on OGO 3 data that are associated with a significant error. This point is discussed further in a following section.

Pfizer (1968) performed polynomial least squares fits to the OGO data sets to model the pitch angle dependence. It is interesting to compare these polynomial fits with the present model. Pfizer's fits were performed to both OGO 1 and OGO 3 data sets, and a B-independent factor was used to normalize the different epochs. The comparison with the AE-5 model for October 1967 is made by normalizing at the equator, and the results are shown in Figures 58 and 59. It should be noted that differences between the two pitch angle distributions at low  $\alpha_0$  may be artificial owing to the normalizing process. The slopes can be compared, however, and it is apparent that the present pitch angle dependence gives a greater slope for most cases. This result is partly due to the inclusion of the 1963-38C data in the present model, as noted previously.

#### 4. HIGH-ENERGY ELECTRONS

The preceding sections have discussed the development of a quiet day analytical model appropriate for electrons with  $E < 690$  keV. As noted in Section 3, a limited amount of data from OV3-3 were available for electrons in the energy range  $2.31 \geq E/(\text{MeV}) \geq 0.3$ . It is apparent from Table 3 that the OGO spectrometer sampled the flux for  $E > 690$  keV in the two higher channels. However, for those periods not influenced by Starfish electrons (Section 6B), these channels generally registered no flux because of a combination of high intensity threshold and low equatorial pitch angle sampling. In this section, the development of the OV3-3 data into a high-energy model is discussed. It should be emphasized that this portion of AE-5 is based on only a single data set that provides no information concerning the pitch angle distribution. This portion is therefore somewhat provisional, and development of a more comprehensive model for high energies has already begun using additional data from other experiments that have become available.

In addition to the lack of data, a fundamental problem of electron modeling arises for the high-energy electrons in the inner belt. The inclusion of the effects of magnetic storms in an electron model is necessary for those regions of B-L-E space where these effects significantly influence the average environment. Three variables must be considered in determining the influence of magnetic storms: (1) the frequency, (2) the flux change in relation to the undisturbed (quiet day) background, and (3) the duration. Assessment of the importance of magnetic storms can be performed in practice with consideration of the first two variables alone because these exhibit much greater variation with E and L than does the third variable.

**PRECEDING PAGE BLANK NOT FILMED**

The implicit assumption of the quiet day analytical model presented in Section 2 is that storm effects do not significantly affect the average environment for  $E < 690$  keV and  $2.4 > L > 1.2$ . It will be shown in this section that the frequency and magnitude of the flux change caused by magnetic storms are such that this is a true statement with the exception of the higher L values at certain energies. As L increases through the slot region and into the outer belt, both the frequency and relative flux change due to storms increase rapidly, until at  $L \sim 3.0$  it is impossible to isolate quiet day periods from disturbed periods. Thus the only modeling approach available in the outer belt is to average the electron fluxes, including the storm effects, and to treat the significant excursions of the fluxes from this average statistically. This is a valid technique, provided that the averaging period is sufficiently large to represent a random sample of the storm effects, because a model user will be applying the environment to a period other than the averaging period. In general, the frequency of effective magnetic storms is sufficiently high in the outer belt for a random sample to be obtained with a relatively short averaging period. The latest outer belt model AE-4 averaged over the period mid-1966 to late 1967 for this purpose. In principle, variations of storm effects with solar cycle can be included in both the average value and in the standard deviation, although in practice for AE-4 it has been possible to derive only average flux conditions approximating to solar maximum and solar minimum owing to the data coverage (Singley and Vette, 1972).

As opposed to the outer belt, the frequency of effective magnetic storms in the inner belt is too low for a statistical approach. Over the period June 1966 to December 1967, for example, excursions of the flux above the quiet day level were observed for approximately 20% of the period. The problem of what approach to adopt arises when the frequency of effective magnetic storms is low and the relative flux change is high. It will be shown that this situation arises for high-energy electrons in the inner belt. In these circumstances the flux

varies considerably from quiet to storm condition and in such a way that the changes from one condition to the other are unpredictable and cannot easily be modeled. An average storm model requires an impractically long averaging period to obtain an effectively random sample. In addition, before the average environment becomes meaningful to the user, he must fly his satellite in that environment for a similarly long period. The most important variable becomes whether the satellite is flying in the quiet or the storm environment. The most meaningful approach may be to provide the user with (1) a quiet day environment and (2) the ability to obtain a storm environment corresponding to a storm of an arbitrary magnitude. That is, a storm model correlated with some magnetic index or parameter would be desirable. This approach is presently being investigated, but, because of the lack of data available for the present model, the effects of storms are included in a crude averaging fashion, as discussed below. However, it should be appreciated that the present high-energy model at best provides only an approximation to the environment.

The energy intervals covered by the OV3-3 spectrometer are shown in Table 3. As noted previously, no calibration information has yet been provided, but the data were supplied in the form of equatorial perpendicular flux. To assess the importance of magnetic storms, quiet day flux levels were determined at a variety of epochs together with the average storm time flux based on the period June 1966 to December 1967. It was considered that the ratio of these two fluxes was indicative of the importance of magnetic storms.

The quiet day high-energy equatorial flux is shown in Figures 60 and 61 for two epochs August 1966 and October 1967 for selected L values. Some data from April 1967 are included in epoch October 1967. The data are plotted at the midpoint of each energy range. Two distinct temporal variations can be observed at different L values. In Figure 60 it is clear that the August 1966 data are lower than the

1967 data, as was observed at lower energies in the OGO and 1963-38C data. Above 1.49 MeV this temporal variation is not observed. The standard deviation of the data in this region becomes large, however. The August 1966 data for  $L = 2.0$  and  $2.2$  are not shown but exhibit a similar temporal variation. In Figure 61, the data at  $L = 1.8$  show a similar increase with time but, at  $L \leq 1.6$  approximately, a reduction in flux with increasing time is observed. This apparent decay is interpreted as depletion of residual Starfish electrons. These temporal variations are discussed further in following sections.

Integral spectra were derived from the differential fluxes, and the quiet day integral fluxes are shown for an epoch of October 1967 on Figures 62 and 63 for  $L \geq 1.7$  and  $L \leq 1.7$ , respectively. The data coverage at the epoch of October 1967 is poor, and a large portion of the data shown on Figures 62 and 63 are based on the early quiet epoch of April 1967. Where data are available at both epochs, any temporal variations are obscured by standard deviation in the data. Estimates were made of the flux above the energy range measured by the detectors. At low  $L$  values for which the spectra were hard, the contribution of this part of the spectrum to the integral flux above 2.31 MeV was significant in relation to the error of the data, which is large at the high-energy end of the spectrum. For  $L \geq 1.8$  approximately, fluxes at energies above those measured by OV3-3 did not contribute significantly to the integral spectra up to thresholds of 2.31 MeV. Figures 62 and 63 show that the spectrum becomes harder at low  $L$  values and that the flux exhibits a maximum at  $L = 1.3-1.4$ . That is, the radial profile at the high energies is markedly different from that at the lower energies discussed in previous sections that exhibit maxima at  $L = 1.8-1.9$ .

To assess the importance of magnetic storms, average flux values were derived for the period June 1966 to December 1967, including three storm periods corresponding to the magnetic events beginning in late August 1966, early January 1967, and late May 1967. The average fluxes  $\bar{F}$  were derived using the simplified model given in Figure 64. It was not possible in each case to measure all the variables shown in this figure, and many estimates were made from the available data, particularly concerning the storm decay times. From these results the ratio

$$R_S = \frac{\text{Average Flux June 1966 to Dec. 1967}}{\text{Quiet Day Flux Oct. 1967}} \quad (11)$$

was derived. The ratio  $R_S$  is shown as a function of energy for a variety of L values in Figure 65 and is based on differential fluxes. This ratio is plotted at the midpoint of each OV3-3 channel. It is clear conceptually that  $R_S$  is only a qualitative index, and considerable error may be associated with actual  $R_S$  values presented in Figure 65. It can be seen that the peak storm effect is observed in the energy range  $1100 > E/\text{keV} > 850$  for  $2.8 \geq L \geq 1.8$ , with sharp falloff with both increasing and decreasing E. Furthermore, the storm effect increases markedly as L increases. Below  $L = 1.8$ ,  $R_S$  was essentially unity. Of course, that does not imply that storm effects cannot be observed at these L values, but rather that their significance in the context of providing an average model is small and within the standard deviation of the quiet day model.

From Figure 65 it may be concluded that the quiet day model presented in Section 2 for  $690 \geq E/\text{keV} \geq 36$  provides a good estimate of the environment for  $L \leq 1.9$  and that the quiet day model of electrons with  $E > 690$  keV presented in this section provides good flux estimates for  $L \leq 1.8$ . For L values above these ranges, the occurrence of a magnetic storm is likely to increase the average flux by a significant

amount. It is interesting to consider the probability that the observed flux in the inner belt will be above the quiet day level or above the average flux. The probability distribution is determined largely by the idealized storm model used (Figure 64), and the probabilities are heavily dependent on the storm decay times. Figure 66 shows the probability that the flux is above the quiet day background (epoch October 1967) and above the average flux  $\bar{F}$  as a function of energy for  $L = 1.9$  and  $L = 2.8$  for the period June 1966 to December 1967. Clearly, the probability that the flux will be above the quiet day background  $P(h_q)$  is quite significant. The probability that the flux will be above the average,  $P(\bar{F})$ , is significantly lower, having a typical value for the  $L$  range  $2.8 > L > 1.8$  of approximately 14% for most energies. Note that no clear differences become apparent in  $P$  for different  $L$  values. Significant increases in the probability occur at low energies ( $L = 2.8$ , Figure 66) arising from increases in the storm decay times, but generally these are relatively unimportant in the inner belt because they coincide with small values of  $R_s$  (Figure 65).

As a crude estimate of storm effects, the average storm time flux  $\bar{F}$  is presented as the high-energy model. As noted above, if the period June 1966 to December 1967 can be regarded as typical, the probability of the flux being above this level is approximately 14%. However, it should be appreciated that this probability reduces only slowly with increasing flux level owing to the spiked nature of the storms. Figure 67 shows the averaged equatorial perpendicular integral spectrum for  $L \geq 1.7$  and can be compared with the quiet day fluxes presented in Figure 62. At  $L = 1.7$  the spectrum remains unaltered, but at higher  $L$  values the inclusion of storm effects results in a flattening of the radial profile to the extent that little change in flux occurs between  $L = 2.2$  and  $L = 2.4$ , with the flux at  $L = 2.4$  becoming

greater than that at  $L = 2.2$  for  $1.8 > E/(\text{MeV}) > 0.7$ . For  $L \leq 1.7$  the model spectra are unaffected by magnetic storm effects, and the spectra presented in Figure 63 are compatible with those shown in Figure 67.

## 5. THE OMNIDIRECTIONAL FLUX MODEL AE-5

In this section the development of the complete model in the form of omnidirectional flux and based on the information presented in Sections 2 and 4 is discussed. This model, designated AE-5, is valid for the epoch October 1967, for  $1.2 \leq L \leq 2.8$ , and for  $4.0 \geq E/(\text{MeV}) \geq .04$ . Efforts are made to ensure that the inner zone model AE-5 is compatible with the latest outer zone model AE-4 (Singley and Vette, 1972) at the interface slot region  $L \sim 2.6$ .

### A. The Inner Zone Model

The basic constituents of this model have been discussed in Section 2 (the analytical model for  $E < 690$  keV) and in Section 4 (the high-energy electron model. The form of the model is omnidirectional integral flux provided as a function of B, L and energy threshold  $E_T$ . The effects of magnetic storms and the high-energy electrons were discussed previously. It is clear from Figure 65, however, that storm effects are important at lower energies for  $L \geq 1.9$ , and thus some modification to the quiet day analytical model is necessary. In addition, the ability of the analytical model to estimate integral flux becomes suspect because the portion of the spectrum above 690 keV is estimated by fits to data for  $E < 690$  keV. Figure 68 shows the quiet day and the average storm time models for  $L \geq 1.9$  and  $900 \geq E/(\text{keV}) \geq 200$ . In this figure the analytical model is used to give the quiet day integral flux for  $E_T < 500$  keV, approximately. Above this energy the quiet day spectra are matched with those given by the high-energy OV3-3 data. In general, only minor modifications have been made, that is, within the standard deviation of the analytical model and the OV3-3 data. The full lines in Figure 68 represent the final equatorial

PRECEDING PAGE BLANK NOT FILMED

perpendicular integral flux model, and the modifications to the integral flux for  $E < 500$  keV to include the average storm effects can be assessed by comparison with the quiet day flux lines. In general, the analytic model can be used for determining integral fluxes up to energies  $E_T$  in the range 300 to 400 keV dependent on the L value.

At  $L < 1.9$  storm effects become insignificant. However, the quiet day analytic model requires significant modification because of the high-energy portion of the spectrum, which becomes increasingly hard at low L values. The integral flux spectra are indicated in Figure 69 for  $L = 1.8$  and  $1.7$ . In each case the analytic model is used for integral flux up to  $E_T = 500$  keV. It can be seen that no modification is made at  $L = 1.7$  for either storm effects or high-energy electrons, and only minor storm effects are evident at  $L = 1.8$ . It is interesting to note the crossover of the spectra at 560 keV that also occurs at the lower L values shown in Figure 70. In this figure it can be seen that considerable correction is required to the integral flux for  $E_T < 500$  keV owing to the hardening of the spectra at high energy. For example, at  $L = 1.3$  the integral flux at 500 keV is increased by an order of magnitude because of this effect. Despite these large corrections, there is no conflict between the differential spectrum given by the analytic quiet day model at 500 keV and the OV3-3 data. This is illustrated in Figure 71 for  $L = 1.3$  through  $1.5$ . In Figure 71 it is apparent that the effects of the high-energy electrons for  $L \leq 1.4$  are such that the method used for determining the quiet day model (Sections 2 and 3) is not applicable for these L values. This is because the average differential flux measurements of the OGO satellite are not compatible with the integral flux measurements of the 1963-38C satellite. Further, for  $L < 1.3$ , estimates of the quiet day parameters  $J_I$  and  $X$  cannot be obtained from the 1963-38C data. To account for the

effects of high-energy electrons, an iterative procedure is adopted, and Figures 20, 21, and 25 indicate the predictions of the quiet day model based on  $J_I$  and X and the final model, including the effects of the high-energy electrons.

To make the present AE-5 model compatible with the outer zone model AE-4 (Singley and Vette, 1972), the high-energy data are extrapolated to provide flux estimates for particles with energies up to  $E_T = 5$  MeV. The extrapolations performed are shown in Figures 72 and 73 for  $L \geq 1.6$  and  $L \leq 1.6$ , respectively. The extrapolation is performed until the flux has fallen to  $10^{-1}$  electrons/cm<sup>2</sup>-sec-ster (Section 6). The outer zone electron model AE-4 provides insignificant fluxes at all L values for  $E_T > 4.85$  approximately. The present extrapolation is performed with a similar criterion. Evidently the extrapolation procedure performed above leads to a considerable error for  $E_T > 3$  MeV, and the error at 4 MeV may be as much as an order of magnitude.

The analytic quiet day model provides the pitch angle dependence for electrons with  $E < 690$  keV. It is assumed that the storm contribution added to this model at high L values does not change this pitch angle distribution. Examination of the storm time pitch angle distribution from the OGO data supports this assumption. As noted in Section 3, no pitch angle information is available for  $E > 690$  keV. It is assumed that the observed pitch angle dependence for the energy range  $690 \geq E/(\text{keV}) \geq 292$  can be extended to higher energies. This assumption is supported by the fact that the observed pitch angle dependence in the outer zone is energy independent. This assumption is likely to result in some error, however, since the pitch angle distribution in

the inner radiation zone shows variation with energy for  $E < 690$  keV. Three-dimensional SD-4060 plots of the high-energy model flux as a function of  $B$  and  $L$  are given in Figures 74 through 77 for energy thresholds

$$E_T = 0.5, 1.0, 2.0, \text{ and } 4.0 \text{ MeV}$$

Using the equatorial perpendicular flux values presented in this section and the analytic model pitch angle distributions, omnidirectional integral fluxes  $J$  were obtained performing the integration

$$J(B, L, E_T) = \int_B^{B_C} \frac{j_{\perp}(B_{\perp}, L, E_T)}{B_{\perp}^{3/2} (B_{\perp} - B)^{1/2}} dB_{\perp} \quad (12)$$

where  $j_{\perp}$  is the perpendicular flux corresponding to  $B_{\perp}$ . The resulting inner belt radial profiles are presented in Figures 78 and 79 for selected energies. It is clear that the peak flux moves to lower  $L$  values as the energy increases. The hardening of the high-energy spectrum at low  $L$  value results in a doubly peaked profile at  $E_T = 500$  keV. This profile would not be expected from simple diffusion mechanisms, and it is considered that there is a significant Starfish contribution to the flux at these energies at low  $L$  values for an epoch of October 1967. This subject is discussed further in Section 6B.

#### B. The Interface Region $L \sim 2.6$

The above inner belt model is valid for  $1.2 \leq L \leq 2.4$ . Model AE-5 is extended to include  $L = 2.6$  earth radii by comparison with the outer zone model AE-4 (Singley and Vette, 1972). No data are considered at this  $L$  value, and the model is determined solely by interpolation

between  $L = 2.4$  and  $L = 2.8$  or  $3.0$ . The radial profile in the interface region is shown in Figures 80 and 81 for  $E \leq 1$  MeV and  $E \geq 2$  MeV, respectively. Figure 80 shows that the two models provide similar flux levels on either side of the interface region and that the trends given by the radial profiles are compatible. The minimum flux at any energy is observed to move to lower  $L$  values with increasing energy. Figure 81 shows that there are considerable differences between the flux levels on either side of the interface region at the higher energies. That is, the outer belt spectrum is significantly harder than the inner belt spectrum. However, we note that there is considerable error associated with the inner belt spectrum above 3 MeV because of the extrapolation process discussed in Section 5A. The trends given by the radial profiles of the two models are apparently contradictory for  $E_T \geq 3$  MeV. The outer zone model at  $L = 2.8$  at these energies is based entirely on Explorer 26 data and, as noted in Section 3, these data are anomalous at  $L$  values where the proton background becomes significant. In the final model shown in Figure 81, the outer zone model is modified at  $L = 2.8$  for  $E_T > 3$  MeV to make it compatible with the inner zone model. The interpolated spectrum at  $L = 2.6$  is shown in Figure 82 and the  $B$  dependence is shown in Figure 83. In Figure 83 the fluxes are normalized to unity at the equator.

## 6. TEMPORAL VARIATIONS IN THE INNER RADIATION BELT

Isolation of the periods remote from the influence of magnetic storms has been discussed in previous sections for energies  $E < 700$  keV approximately. Data from these periods exhibit temporal behavior attributable to decay of Starfish electrons and solar cycle effect. Separation of these two effects is not a simple process because a large portion of the data is significantly influenced by both, which results in an iterative procedure that also affects the model parameters described in the previous sections. In some cases, however, data that are predominantly affected by one or other of the variations can be isolated as in late 1964, when Starfish decay dominated for  $L \leq 2.0$ , and as in mid-1966 and later, when solar cycle variation dominated for low energies. The two temporal variations are discussed separately in the following sections with considerable cross-referencing between sections.

### A. Variations with Solar Cycle

The analysis in this section is concerned primarily with electrons of  $E < 690$  keV. It will be seen that similar variations can be detected at higher energies, but in many cases in the context of an electron model these variations are small in comparison to the effects of magnetic storms.

It is assumed that the solar cycle effect is not B dependent. Then, the ratio of the unidirectional flux at the epoch of October 1967 to that at time T months measured from solar minimum (assumed to be September 1964) is defined as  $R_T(E,L)$ . It is apparent in some instances,

PRECEDING PAGE BLANK NOT FILLED

however, that the solar cycle effect is B dependent, with the flux at the lower pitch angles exhibiting less variation than at higher pitch angles (e.g., Figures 42 and 46). In general, however, insufficient data are available for modeling this variation, and B independence is assumed.

It can be seen that at  $L = 2.4$  (Figures 55 through 57) Starfish electrons with  $E \leq 690$  keV have decayed to insignificant levels by early 1965, and consequently both the OGO 1 and OGO 3 data sets can be used for investigation of the solar cycle variations. Figure 84 shows the model ratio  $R_T$  for this L value. From Figures 55 through 57 it can be seen that the data are poor for  $L = 2.4$  and  $T = 37$  (October 1967), and the model for this time is considerably influenced by lower L values and by earlier data for which the pitch angle coverage is markedly better. It should be emphasized that there is very significant error associated with determining the ratios  $R_T$  that is caused primarily by standard deviation in the data and secondarily by unmodeled B dependence, and thus care must be taken in attributing significance to the shape of the curves presented in Figure 84 and to those subsequently presented for the variable  $R_T$ . In extreme cases this error may be 50% for energies  $690 \geq E/(\text{keV}) \geq 292$  and larger for lower energies where data are poor and  $R_T$  is smaller. From Figure 84, however, it can be concluded that the solar cycle effect increases markedly with energy up to 690 keV, and later it is shown that the L-dependent characteristics can be observed. In addition, in Figure 84 the broken lines indicate the ratio  $R_T$  for linear variations of flux with time at  $L = 2.4$  based on the first data point in each case at  $T = 27$ . At earlier times it is clear that for the two highest energy ranges the observed ratios  $R_T$  are significantly lower than the linear values, thus indicating a reduction of the solar cycle effect towards solar minimum, as would be expected. The reverse trend is observed for the lowest energy, and although it

is repeated at lower L values, it may simply result from error in the ratio  $R_T$  at  $T = 22$ . However, it is evident that the solar cycle effect is approximately linear for  $22 \leq T \leq 37$  independent of energy.

Similar qualitative observations can be made for  $L = 2.0$  and  $2.2$  because Starfish electrons cease to be significant by mid-1966. Further, at these L values the pitch angle coverage is more comprehensive and more accurate values of  $R_T$  can be determined. For  $L < 2.0$ , however, the flux at  $T = 22$  becomes influenced by Starfish electrons in the energy range  $690 \geq E/(\text{keV}) \geq 292$ . For the energy interval  $292 \geq E/(\text{keV}) \geq 133$ , Starfish electrons cease to be significant by mid-1965 (Section 6B) and all the OGO 3 data can be used for assessing the solar cycle variation. For the lowest energy range, Starfish electrons have decayed to insignificance by late 1964, and both the OGO 1 and OGO 3 data sets can be used for solar cycle effect. For the high-energy data containing a significant Starfish contribution, estimates of this contribution can be made using the analysis presented in Section 6B. As noted, these estimates are also a factor in determining the quiet day model parameters discussed in previous sections. The resulting quiet day flux distributions are shown in Figures 14 through 57, labeled "T = 22 EST BACK" together with the total model flux and the data at  $T = 22$ . This estimated background can be used to determine an approximate  $R_T$  value for  $T = 22$ . In addition, for the highest energy channel estimates of  $R_T$  at  $T = 31$  and  $27$  can be made using quiet day data from these epochs. As noted previously, for  $L = 2.4$  the flux varies approximately linearly with time for  $22 \leq T \leq 27$  for all energies. The L dependence of the ratio  $R_T$  is shown in Figure 85 for various epochs for the three channels of OGO data and at  $T = 22$  for the  $E > 255$  keV 1963-38C data. In general,  $R_T$  increases with L and reaches a peak at  $L = 2.0$  approximately, with a sharper falloff at lower L than at higher. The peak at  $L = 1.7$  in the  $133 \geq E/(\text{keV}) \geq 36$  is not considered significant owing to the standard

deviation in the data. A summary of the ratios  $R_T$  determined from the OGO 3 and 1963-38C data is shown in Table 6 for  $T = 22$  months. In addition, carpet plots of  $R_T(T,L)$  are given for energy ranges corresponding to the OGO satellite in Figures 86 through 88. (Note that a brief description of carpet plots is given in Appendix A.) Some smoothing of the data presented in Figures 86 through 88 and Table 6 has been performed, particularly at low energies and low  $L$  values. It is considered that the resulting changes are small in relation to the standard deviation of  $R_T$ . In determining the carpet plots for  $R_T$ , the Starfish model described in the next section has been used to estimate the contribution from Starfish electrons to the total flux at various values of  $T$ . As noted above and shown in Figures 14 through 57, this includes  $L < 1.9$  and  $T \leq 22$  for  $690 \geq E/(\text{keV}) \geq 292$  electrons. In addition, the same process is performed for  $292 \geq E/(\text{keV}) \geq 133$  electrons at  $T = 6$ . Where the Starfish contribution to the total flux is large, the possible error in the ratio  $R_T$  becomes very large, and the early epochs with low  $L$  value shown in Figures 87 and 88 must be regarded as provisional. However, it is interesting that a certain consistency exists in the values of  $R_T$  at early epochs. For electrons  $690 \geq E/(\text{keV}) \geq 292$  approximately, 85% of the total increase in flux between  $T = 6$  and 37 occurs over the period  $T = 22$  to 37. This approximate figure of 85% is independent of  $L$ . A corresponding effect is observed for lower energies with 75% for  $292 \geq E/(\text{keV}) \geq 133$  and 27% for  $133 \geq E/(\text{keV}) \geq 36$ .

To provide solar cycle parameters compatible with the model presented in previous sections, it is necessary to derive values of  $R_T$  as functions of a given energy threshold  $E_T$ . These values can be based only on those presented in Figures 86 through 88 and determined

from the OGO data. The integral flux at an arbitrary epoch T can be expressed in terms of the OGO energy ranges as

$$j(T, E_T) = \sum_{i=1}^k j_i(E_{i1}, E_{i2}, T) + j(>690, T) \quad (13)$$

where  $E_{i1} = E_T$ ,  $E_{k2} = 690$  keV, and  $E_{i2}$  is the upper energy limit of the channel measuring electrons with energy  $E = E_T$ . From Figures 60 and 61 it is clear that particles with  $E > 690$  and  $L > 1.6$  exhibit a solar cycle effect that decreases with increasing energy and also that Starfish decay is evident at lower L values. It is also clear from the discussion of magnetic storms, however, that this solar cycle effect is unimportant in relation to these storm effects, and for the present model it has not been possible to model the variation of these effects with solar cycle. The effect of the Starfish decay process at low L values is also unknown, and it is therefore assumed that  $j(>690)$  is not dependent on time. In general, however, this term has a relatively small effect on the value of  $R_T$  for integral energy fluxes. In addition to storm particles with  $E > 690$  keV, it has been shown that significant storm contributions exist at lower energies for high L values. It is assumed that these contributions are also time independent and that equation 13 can be written as

$$j(T, E_T) = \left[ \sum_{i=1}^k j_i(T, E_{i1}, E_{i2}) \right]_q + \left[ \sum_{i=1}^k j_i(E_{i1}, E_{i2}) \right]_s + j(>690) \quad (14)$$

In general, a solar cycle ratio  $R_T(E_T)$  for a given energy threshold can be given by the expression

$$j(T, E_T) = \frac{j(37, E_T)}{R_T(T, E_T)} = \left[ \sum^k \frac{j_i(E_{i1}, E_{i2}, 37)}{(R_T)_i} \right]_q + \left[ \sum^k j_i(E_{i1}, E_{i2}) \right]_s + (j(>690)) \quad (15)$$

where  $J(37, E_T)$  is given by equation 13 with  $T = 37$ , and  $(R_T)_i$  is the solar cycle ratio for Channel  $i$  presented in Figures 86 through 88. There are obvious errors involved with equation 15, particularly for regions of  $E, L$  space where significant modification to the quiet day spectra is made by high-energy or storm time particles that are assumed independent of time. Equation 15 can be used to relate to the OGO and 1963-38C solar cycle parameters presented in Table 6. In practice simpler forms of equation 15 can be given for certain  $L$  value regions. At  $L$  values where the storm contribution is insignificant below 690 keV,  $R_T(E_T)$  becomes

$$R_T(T, E_T) = j(37, E_T) / \left\{ \left[ \sum^k \frac{j_i(37, E_{i1}, E_{i2})}{(R_T)_i} \right] + j(>690) \right\} \quad (16)$$

and at  $L$  values for which storm effects become most significant as

$$R_T(T, E_T) = j(37, E_T) / \left\{ \left[ \sum^k \frac{j_i(37, E_{i1}, E_{i2})}{(R_T)_i} \right] + \left[ j(E_T) \right]_s \right\} \quad (17)$$

The comparison between 1963-38C and the predictions of equation 15 is shown in Figure 89. The agreement is well within the standard deviation of 1963-38C data, which is typically 25%. The term  $[j(E_T)]_s$  in equation 17 was not a factor in the present calculation, although  $j(>690)$  in equation 16 became significant for all L values. Equations 16 and 17 were used to derive carpet plots of  $R_T(E_T, T)$  for  $E_T = 40, 100, 250, \text{ and } 500 \text{ keV}$ . These plots are presented in Figures 90 to 93. Note that the carpet plot technique could not be employed for  $E_T = 500 \text{ keV}$  because of the shape of  $R_T(T)$  at the various L values. For  $E_T > 250 \text{ keV}$ , the storm term is unimportant, but the high-energy term  $j(>690)$  is significant, particularly at low L values. At 500 keV both terms became very significant, especially at low and high L values, and Figure 93 must be regarded as very provisional because of unmodeled temporal variations of these terms. In general the effect of these terms becomes most important at low values of T, and thus the early epochs are less reliable than the later epochs.

This section has been concerned with determining solar cycle ratios for  $T < 37$  months. A more important and less well-defined problem, in the context of the usage that the present electron model will receive, is extrapolation for  $T > 37$  months. Of course, there is no guarantee that solar cycle ratios determined for one particular solar cycle are applicable to another. Also, owing to asymmetries in the solar cycle about solar maximum, error is likely to be introduced by the assumption that ratios based on data between solar minimum and maximum (as with the present values) can be applied to a time period between the maximum and the subsequent minimum. However, the errors due to these sources are small in comparison with the considerable error associated with the present values of  $R_T$ . These values of  $R_T$  extend over the period  $37 > T > 22$ ; that is, they do not cover the complete period solar minimum to solar maximum. Figure 94 shows the time-averaged sunspot number  $R_z$  as a function of time for the present solar cycle. It is evident

that the present epoch of  $T = 37$  coincides approximately with the maximum  $R_z$  observed for this cycle. Further, the earliest value of  $R_T$  at  $T = 6$  coincides approximately with a minimum in  $R_z$ . Therefore, coverage of the period  $37 > T > 22$  incorporates the majority of the flux increase due to solar cycle for the present cycle. From Figure 94 it is clear that  $R_z$  remains essentially constant over the period 1968 to mid-1970. If the inner belt solar cycle effect is well-correlated with sunspot number, it may be assumed that the flux remains constant at the October 1967 value until, for example, June 1970, i.e.,  $T = 69$  months. For values of  $T > 69$ , presumably the flux will decrease, and to a first approximation it may be assumed that this decrease can be estimated using the values of  $R_T$  presented in this section.

As a consequence of assuming that the solar cycle parameter  $R_T$  is independent of  $B$ , values of  $R_T$  presented in this section may be used with both omnidirectional and unidirectional fluxes.

#### B. The Effects of Starfish Electrons

At some general point in time later than July 1962, the time of Starfish injection, the total inner belt electron flux  $j$  on a quiet day is

$$j = j_q + j_{st} \quad (18)$$

where the suffixes  $q$  and  $st$  denote, respectively, the natural quiet day background component and the residual Starfish component. If the decay of the Starfish component is assumed to be exponential with characteristic time  $\tau$ , and the time dependence of the quiet day flux is written as

$$j_q = j_{oq} f(t) \quad (19)$$

and then the change of the total population with time is

$$\frac{dj}{dt} = j_{oq} \left( \frac{df}{dt} + \frac{f}{\tau} \right) - \frac{j}{\tau} \quad (20)$$

i.e., the difference of the source and loss terms. For epochs such that  $j \gg j_{oq}$ , equation 20 reverts to the normal exponential decay expression. In the general case, however, the term  $j_{oq}$  must be considered to avoid determining values of  $\tau$  too large or too small for positive and negative  $df/dt$ , respectively. Note that  $\tau$  in equation 20 represents the observed net depletion rate of residual Starfish electrons as opposed to the lifetime of these particles; it is well known that cross L and pitch angle diffusion does occur. The variable  $\tau$  is referred to as the decay time.

As noted in Section 6A, the major problem in determining the temporal variations is the separation of the two components, i.e., the residual Starfish flux and the solar cycle dependent quiet day flux. These components are determined in an iterative manner. Using data as near to the Starfish injection epoch as possible (in the present case September 1964), an initial decay time is determined assuming  $j \gg j_{oq}$  in equation 20, and the flux is decayed using this value of  $\tau$  until the observed flux is significantly larger than the decayed flux. The difference of these fluxes approximates to the quiet day background at this epoch. In practice, the epoch for this comparison is determined by the availability of data. With this quiet day background flux value and other similar values from later epochs for which it is clear that the Starfish residual has become insignificant, an extrapolated quiet day flux estimate can be made for the epochs on which the initial decay time is based. A corrected decay time can then be determined and the process repeated. The iteration procedure is lengthy and many iterations are not warranted, since significant error is introduced by extrapolating for the background flux. Further, for cases where the Starfish residual is small compared with the quiet day flux for all the data epochs, only a very approximate value of  $\tau$  can be determined.

A second iteration procedure is adopted for determining the decay times for the residual Starfish fluxes. In general, decay times will be quoted for equatorial fluxes on the assumption that  $\tau$  is B independent. It is known that this is an approximation for low L value (Stassinopoulos and Verzariu, 1971), although in general decay times are not determined for L values at which this introduces appreciable error. The pitch angle dependence of the residual Starfish is removed in the following manner. An approximate determination of the pitch angle dependence is made using the month of data with the greatest pitch angle range at any given L value. Data from all epochs are normalized to the equator assuming that the pitch angle distribution of the residual electrons is not time dependent, and initial values of  $\tau$  are determined. With these values of  $\tau$ , the time dependence is removed and, assuming that  $\tau$  is B independent, an average pitch angle distribution is obtained for all epochs. After normalizing to the equator, an improved  $\tau$  value is obtained. As with the previous iteration procedure, the accuracy of the technique and the data standard deviation do not warrant iterating more than once. In the following paragraphs only the final iterated values of  $\tau$  are presented.

The procedure described above is adopted for analysis of the OGO 1 and 3 data only. No decay times are presented here for the 1963-38C data, but the OGO-based values are compared with the decay time model of Stassinopoulos and Verzariu (1971) based on the 1963-38C data. A typical situation that results from separation of the two flux components is shown in Figure 95 for  $L = 1.5$  and  $1.9$  and for  $292 \leq E/(\text{keV}) \leq 690$ . The two flux components and the total flux are indicated together with residual Starfish flux data from OGO 1. At the lower L value, the dominant component at the early epochs is clearly the Starfish residual and, even at epoch 6/66, 51% of the total flux is Starfish residual. At the higher L value, the quiet day background component is discernible in late 1964 and early 1965, and at epoch 4/65 this component contributes

approximately 20% of the total flux. As a result, the final value of  $\tau$  is significantly different from the initial value obtained assuming that  $j \gg j_{0q}$  in equation 20. An approximate expression can be given for the ratio of the initial decay time  $\tau_i$  and the final value  $\tau_f$  accounting for the background component as

$$\frac{\tau_f}{\tau_i} = 1 - \frac{\tau_f}{\Delta t} \log_e \left( 1 + \frac{j_q}{j_{st}} \right) \quad (21)$$

where  $\Delta t$  is the time period over which  $\tau_f$  and  $\tau_i$  are determined and  $j_q$  and  $j_{st}$  are evaluated at the end of the period  $\Delta t$ . For the case of  $L = 2.2$ , equation 21 gives that  $\tau_f = 0.81 \tau_i$ . Postulating that the quiet day background  $j_q$  at time  $t$  may be in error by a factor of 2, the final decay  $\tau_f$  has an error from this source of  $\pm 20\%$ . Although  $\tau_f$  will be a better estimate of the decay time than  $\tau_i$ , other error considerations such as data standard deviation dictate that the iteration procedure is not worthwhile for  $j_q/j_{st} > 0.5$  approximately.

The determination of the OGO-based decay times is discussed separately for  $E < 690$  keV and  $E > 690$  keV, since in the first case the OGO data itself can be used for estimating the quiet day flux, whereas in the second case the OV3-3 equatorial perpendicular flux measurements must be used. The iteration procedures described in the early paragraphs of this section are used for  $E < 690$  keV only. Three variables will be presented: the decay times, the residual flux for epoch September 1964, and the residual flux pitch angle dependence.

Analysis of the low-energy data from OGO 1 indicated no residual Starfish fluxes except at low  $L$  values in late 1964 for  $36 \leq E/(\text{keV}) \leq 133$ . This is indicated in Figure 96. The broken lines on this plot are intended to indicate trends only. For the purposes of this diagram, the OGO data have been normalized to the equator using the quiet day

model pitch angle distribution and have been averaged. For  $L > 1.3$ , the general trend is for the equatorial perpendicular flux to increase with time. For  $L < 1.3$ , however, fluxes at the late 1964 epoch are above those at the later epochs by approximately a factor of 2, thus indicating the possible presence of a Starfish residual in 1964. The quality and time span of the OGO data at this  $L$  value are not such that a decay time can be determined, and it is merely noted that the Starfish contribution to the total flux has become insignificant by mid-1966 at the latest. For all other  $L$  values, all epochs covered by the OGO data can be used for estimating the solar cycle variation as noted in Section 6A.

The iterated residual flux pitch angle dependences of the Starfish-dominated fluxes are presented in Figures 97 through 105 for  $292 \geq E/(\text{keV}) \geq 133$  and Figures 106 through 114 for  $690 \geq E/(\text{keV}) \geq 292$ . In each case the OGO I data have been approximately normalized to October 1964. Simple polynomial fits to the data were made using the expressions

$$\log_{10} (j_{st}) = a_0 + a_1(\theta - \alpha_0) + a_2(\theta - \alpha_0)^2 + a_3(\theta - \alpha_0)^3$$

$$\text{for } \alpha_0 < \theta$$

and

(22)

$$\log_{10} (j_{st}) = a_0 \text{ for } \alpha_0 \geq \theta$$

where  $\theta$  is an  $L$ -dependent cutoff for the pitch angle function analogous to the variable  $\phi$  used in the quiet day model (Section 2). The  $L$ -dependent constants  $a_0$ ,  $a_1$ ,  $a_2$ ,  $a_3$ , and  $\theta$  are presented in Table 7. By comparison with Figures 14 through 57, it can be seen that the spread of the Starfish data is comparable to that of the quiet day data. The polynomial fits represent least squares fits weighted with the logarithm of the data and the standard deviation of the individual points. On each

of Figures 97 through 114, the Starfish flux pitch angle distributions are compared with the quiet day pitch angle distributions given by equations 6 and 7 of Section 2. In each case the quiet day distribution is normalized at  $\alpha_0 = \Theta$ . At low L values, the Starfish distributions appear flatter than the quiet day distributions. At high L values, a similar effect is observed, particularly if the pitch angle dependences are normalized at  $\alpha_0 = 90^\circ$ , although at these L values there is some doubt about the value of  $\phi$ , and any differences in pitch angle dependence may be artificial. At intermediate L values, the two pitch angle dependences appear very similar in terms of both the cutoff angle and the variation of flux with  $\alpha_0$ . Such differences as exist are observed at low  $\alpha_0$ , and these may be artificial because the quiet day pitch angle dependence is primarily influenced by the 1963-38C data in this region, and it was noted in Section 3 that these data indicated a faster rate of falloff in the cutoff region than did the OGO data.

The temporal variation of the OGO data corrected for background and normalized to the equator using these pitch angle dependences is presented in Figures 115 to 118. Approximate decay times are given for these data assuming an exponential decay process. The residual fluxes are extrapolated to an epoch of June 1966 for later comparison with the quiet day flux at the same epoch. No decay times are given for  $L = 1.3$ , primarily because the data coverage is poor. In addition, however, Stassinopoulos and Verzariu (1971) have shown that  $\tau$  is B dependent in this region, and thus normalizing to the equator produces erroneous results. At low L values it is apparent that the data coverage is poor, and thus the accuracy of the decay times is suspect. Further reference is made to the accuracy of  $\tau$  later in this section. In Figure 118 the effects of the magnetic storm of February 7, 1965 (maximum  $|Dst| = 59\gamma$ ), are evident for  $L \geq 2.0$ . In addition, the equatorial perpendicular fluxes obtained from the OGO data are shown following the magnetic storm of April 18, 1965 (maximum  $|Dst| = 185\gamma$ ). Consistent with the discussions of magnetic storms presented in Section 4, no effects of the earlier storm

are observed for  $L < 2.0$ . No data were available for the later storm for  $L < 2.0$ . The injection of storm electrons at high  $L$  values evidently casts severe doubt on interpreting the observed flux levels at these energies in October 1964 and later as purely Starfish residual fluxes, and thus the flux is not extrapolated to June 1966 using the observed decay times. The variation of  $\tau$  from the data before and after the February 1965 storm is well within the standard deviation of  $\tau$ , and since storm time electrons and Starfish electrons decay in approximately the same manner, the observed  $\tau$  values are interpreted as Starfish decay times. A summary of the OGO-based decay times is presented in Table 8 for  $690 \geq E/(\text{keV}) \geq 292$  and  $292 \geq E/(\text{keV}) \geq 133$ .

For the two highest energy ranges of the OGO spectrometer, little information is available concerning the quiet day background, and a different approach to determining the decay times is adopted. In Section 4 it was inferred from the radial profiles obtained from the high-energy OV3-3 data that a significant Starfish residual was present in late 1967 at  $L \leq 1.6$  approximately. A crude analysis of the high-energy OGO 1 data is presented here in order to make approximate estimates of this residual flux and thus of the background flux after this component has decayed away.

The pitch angle dependence of the Starfish electrons in the two energy ranges  $1970 \geq E/(\text{keV}) \geq 690$  and  $4740 \geq E/(\text{keV}) \geq 1970$  are shown, respectively, in Figures 119 through 123 and 124 through 127. These values were obtained by the same iterative method described above, except that the assumption was made that the quiet day background flux was small in comparison to the Starfish residual flux. Polynomial fits were obtained using equation 22, and the coefficients are presented in Table 7. In Section 4 it was assumed that the pitch angle dependence for electrons in the range  $690 \geq E/(\text{keV}) \geq 292$  was applicable to higher energies. This pitch angle dependence is compared with the high-energy

Starfish residual pitch angle dependence in Figures 119 through 127. As with the lower energies, the Starfish distribution appears flatter at  $L = 1.3$  and  $1.4$ , but good agreement is observed at intermediate  $L$  values. This lends credence to the assumption of pitch angle distribution energy independence for  $E > 292$  keV. Using these pitch angle distributions, the OGO 1 data were normalized to the equator and are shown in Figures 128 and 129 for  $1970 \geq E/(\text{keV}) \geq 690$  and  $4740 \geq E/(\text{keV}) \geq 1970$ , respectively, plotted as undashed points. A limited amount of data was available at these energies from the OGO spectrometer over the period June through August 1966. It will be shown later that there is reasonable agreement between these data and the quiet day OV3-3 data from the same period. The averaged OGO and OV3-3 data at epoch August 1966 are shown in Figures 128 and 129, with the OV3-3 data for epoch April 1967. Note that some error is involved in estimating the flux at energies  $4740 \geq E/(\text{keV}) \geq 1970$  using the OV3-3 data because of the energy coverage of this satellite. In Figure 128 it is apparent that the Starfish component has become insignificant by August 1966 at  $L = 1.7$  because solar cycle effects are evident. A similar effect is observed at  $L = 1.6$  for  $4740 \geq E/(\text{keV}) \geq 1970$ . For higher  $L$  values, it will be shown that the OGO 1 data from the late 1964 period are in approximate agreement with the OV3-3 data from later epochs; that is, the Starfish component has become insignificant by approximately early 1965. On the assumption that the decay process is exponential, for  $L$  values having a significant Starfish component in April 1967 it is possible to make a crude estimate of the background flux and the decay time by removing flux increments from the total flux until the residual data lie in a straight line on a logarithmic plot. The results of this process are shown in Figures 128 and 129, where the residual flux data are indicated by dashed points. At all except the highest  $L$  value at each energy, the flux at epoch late 1964 is dominated by the Starfish component. At these highest  $L$  values, however, the background component is significant in late 1964, and the process becomes less

accurate because no information concerning the variation of the background flux with solar cycle is available. It is appreciated that this process is highly inaccurate, and the resulting background flux values must be regarded as speculative. A summary of these background fluxes is presented in Table 9, and the decay times are shown in Table 8. Note that no information is presented for  $L = 1.3$  because of the data coverage at this  $L$  value. In Section 4 it was shown that the magnetic storm effects did not affect the low  $L$  values to a significant extent, and these background flux values can be used for estimating the omnidirectional flux for epochs for which the Starfish component has decayed to insignificance. These estimates are presented in Figure 130, and it can be seen that the double peak in the 500-keV radial profile is no longer present and that the peak flux at higher energies has moved to an  $L$  value of approximately 1.6. These estimated radial profiles are very approximate and are not incorporated into the model AE-5.

It is interesting to compare the radial profiles of the Starfish and quiet day components at various epochs. These radial profiles are shown for epochs September 1964, June 1966, and October 1967 in Figures 131 through 134 for the four higher energy ranges covered by the OGO spectrometer. In Figure 131 for  $292 \geq E(\text{keV}) \geq 133$  it is shown that the Starfish component has become small in comparison to the quiet day background by June 1966. For  $690 \geq E(\text{keV}) \geq 292$ , however, the two components are comparable in June 1966 for  $L \leq 1.6$ , and at  $L = 1.9$  the Starfish component still contributes 20% of the total flux. By October 1967, however, the Starfish component is clearly insignificant. A summary table giving the percentage contribution of the Starfish component to the total flux at the equator is presented in Table 10 for the three epochs September 1964, June 1966, and October 1967. Owing to the differences in the quiet day and Starfish flux pitch angle distributions, the Starfish component generally contributes a higher percentage of the total flux than is indicated in Table 10 for the actual pitch angles used for determining the residual Starfish flux. The residual

flux radial profiles in Figures 131 and 132 exhibit peaks in the L range 1.5-1.7 depending on energy and epoch. These radial profiles are apparently not what would be expected from the artificial injection of a large electron population at a low L value and subsequent radial diffusion, but rather they are what would be expected from an external source and inward radial diffusion. The explanation lies in the variation of the decay time with L value. It can be seen that  $\tau$  exhibits a maximum in the region of  $L = 1.6-1.8$  for the lower two energy ranges, thus resulting in a slower depletion rate at these L values. Extrapolation of these radial profiles back to epochs nearer the Starfish injection in July 1962 results in profiles decreasing essentially monotonically from low L values, as shown in Figure 135 presented for epoch September 1963.

It is possible to obtain confirmation of the OGO residual flux levels by using the 1963-38C data and the OV3-3 data. Figures 136 and 137 compare the residual Starfish flux integral spectra given by the OGO and 1963-38C satellites for epochs January 1965 and June 1966. The comparisons are made at B values appropriate to the 1963-38C measurements. For the data presented in Figure 136, OGO measurements taken approximately at the mirror B value were used, and thus no extrapolation using the polynomial fits was required. For the later epoch, however, some extrapolation was required. Intensity thresholds are shown for the OGO data corresponding to 1 cps. It is clear that the agreement between the two data sets is good. The model lines on Figures 136 and 137 represent the integral flux predictions of the polynomial fits to the OGO data (Table 7) and the decay times  $\tau$  (Table 8). Some modifications have been made to the values of  $a_0$  in Table 7 to obtain the best fit to the two data sets shown in Figures 136 and 137. The values of  $a_0$  in Table 7 represent the equatorial perpendicular flux with units of electrons/cm<sup>2</sup>-ster-keV and do not correspond to the arbitrary flux curves presented in Figures 97 through 114 and 119 through 127. Note

that the coefficients of the polynomials given in Table 7 should not be used with the decay times for decaying the flux in the energy range  $292 \leq E/(\text{keV}) \leq 690$  for  $L \geq 2.0$  owing to the effects of magnetic storms. In Figure 138, the OGO 3 and OV3-3 data are compared for epoch August 1966. Total integral flux is compared for those L values for which a Starfish residual remains in August 1966. It can be seen that the two data sets agree reasonably well. The averaged total flux shown in Figures 129 and 130 for epoch August 1966 was determined from the lines presented in Figure 138, and it is clear that no substantial error results from this averaging process. For  $L > 1.6$  the Starfish flux component had generally become insignificant by late 1965, as noted previously. The quiet day OV3-3 and OGO data are compared for these L values in Figures 139 and 140 for a variety of epochs. The OGO data presented in these figures have been normalized to the equator using polynomial fits to the pitch angle distribution as with the lower L values. These distributions are not shown here; however, the coefficients of the polynomial are presented in Table 7. In Figure 139 it can be seen that a Starfish residual remains in late 1964 at  $L = 1.8$  for  $1970 \geq E/(\text{keV}) \geq 690$ . In addition, the effects of the storm of February 7, 1965, are evident in the OGO 1 data, and no attempt is made to calculate a decay time for  $L = 1.8$ . At  $L = 1.9$  and  $2.0$ , there is essentially no Starfish component at these energies later than December 1964. Note that the agreement between the OGO 3 and OV3-3 data in mid-1966 is not as good as at the higher L values. The OGO data for this epoch are based on a few measurements taken at pitch angles providing low count rates of order unity, and thus the OV3-3 measurements must be preferred. At the highest energy range of the OGO spectrometer shown in Figure 140, OGO data are available only for  $L = 1.7$  in late 1964 and early 1965. It can be seen that a small Starfish residual is present in early 1965, but this effect has apparently become insignificant by late 1965.

From the above analysis, the times at which the Starfish component has become insignificant in relation to the remaining components can be derived. Some discussion of the word 'insignificant' is required in the present context. A cutoff time  $t_c$  can be given by the expression

$$t_c = \tau \log_e \left[ \frac{(1-p) j_{st}(t=0)}{p j_q(t_c)} \right] \quad (23)$$

where  $p$  is the ratio of the residual Starfish to total flux at time  $t = t_c$ . Since  $j_q$  is time dependent for  $E < 690$  keV and for  $T > 6$ , equation 23 must be solved by iteration. Equation 23 presupposes that the only significant component is the quiet day background. It has been demonstrated that magnetic storm effects are apparent for high  $L$  values and intermediate energies, and equation 23 is not applicable in this context since it is not possible to separate the Starfish and storm components. The accuracy of the foregoing analysis is such that solution of equation 23 is not warranted for  $p < 0.25$  approximately. Equation 23 is solved for  $p = 0.5$  ( $j_{st} = j_q$ ) and  $p = 0.25$  ( $j_{st} = j_q/3$ ) for those  $L$  values for which storm effects are not a factor. The resulting cutoff times are presented in Table 11. The time  $t_c$  is quoted as year and month and also as months,  $T_{st}$ , from Starfish injection in July 1962. No cutoff times are given for  $133 \geq E/(\text{keV}) \geq 36$ . It is clear from Figure 96 that for  $L > 1.3$  for these energies, no significant Starfish residual remained later than September 1964 ( $T_{st} = 26$ ). For  $L = 1.3$ , an approximate cutoff date of June 1965 ( $T_{st} = 35$ ) may be given. It is clear from Table 11 that the cutoff times  $t_c$  show considerable variation with energy and  $L$  value at high energies. The longest lived electrons occur in the range  $1970 \geq E/(\text{keV}) \geq 690$  at low  $L$  values, with the higher energy electrons decaying away only slightly earlier. It should be noted that the background flux for these regions has been determined in a very crude manner, and errors of 6 months may be associated with  $t_c$ . For other  $L$  values and energies,  $t_c$  may be associated with an error of 3 months. By extrapolation from low  $L$  values for the

two higher energy channels, it is likely that residual electrons at these energies at  $L = 1.3$  persist for longer periods. A crude estimate of  $t_c$  at  $L = 1.3$  can be made by extrapolating on the background fluxes given in Figures 133 and 134, using the averaged OV3-3 and OGO 3 data for epoch mid-1966, and by taking the decay times of Stassinopoulos and Verzariu (1971). Cutoff times for  $690 \leq E/(\text{keV}) \leq 1970$  of August 1968 and September 1969 are obtained for  $p = 0.5$  and  $0.25$ , respectively. The corresponding dates for  $1970 \leq E/(\text{keV}) \leq 4740$  are April 1968 and March 1969.

Little quantitative information has been given so far for the accuracy of the parameters determined in this section. Perhaps the most important variable from a practical viewpoint is the cutoff time  $t_c$ . The accuracy of this variable depends on the value of  $t_c$  and the accuracy of (a) the decay times  $\tau$ , (b) the Starfish flux model for epoch September 1964, and (c) the solar cycle dependence of the quiet day model. While the accuracy of each of these three variables is not entirely independent, estimates of their effect on  $t_c$  can be made. Taking as an example the case  $L = 1.5$  and  $690 \geq E/(\text{keV}) \geq 292$  shown in Figure 95, if the Starfish model is associated with a 25% error, i.e.,  $j_{st} = 6.92 \times 10^3 \pm 1.73 \times 10^3$  in September 1964, this  $t_c$  has an error of  $\pm 1$  month for  $p = 0.5$  and  $\pm 2$  for  $p = 0.25$ . A 25% error in the decay time is more significant in its effect on  $t_c$ . If  $\tau = 230 \pm 57$  days, the error associated with  $t_c$  is  $\pm 2$  months for  $p = 0.5$  and  $\pm 4$  months for  $p = 0.25$ . A 25% error in the quiet day flux has approximately the same effect as a corresponding error in the Starfish flux. The agreement between the OGO 1 data and the 1963-38C data has been demonstrated (Figure 136) for values of  $B$  off the equator, and the pitch angle distribution is generally well defined by the OGO data for all  $\alpha_0$  except at high  $L$ , where a 25% error in the equatorial perpendicular flux is possible. However, from the above example it is clear that error on the decay time is the major parameter as far as the accuracy of  $t_c$  is concerned. It is considered that the error contributions from (b) and (c) above are relatively unimportant, except perhaps

at low L values and high energies, where the background flux estimate is associated with an error that may be as high as a factor of 2, thus resulting in a 6-month error in  $t_c$ . Error in the Starfish decay time  $\tau$  is a function of (1) the data time sample, (2) the standard deviation of the data, and (3) the significance of the quiet day background. Note that  $\tau$  is not dependent on normalizing to the equator, since it is independent of B for the L values covered here (Stassinopoulos and Verzariu, 1971). As an example, if a 6-month sample of data is available and the residual flux at either end of that period is in error by  $\pm 10\%$ , the resulting error in  $\tau$  is  $\pm 20\%$  approximately. The decay times  $\tau$  were determined from the OGO data by weighting on the number of data points resulting in the monthly averaged residual flux and the standard deviation of the averaged figure. A representative standard deviation is 10% (except for the high energies where there is greater uncertainty in the background flux); however, the sampling period varies considerably, and thus the error on the decay time varies considerably. With reference to Figures 115 through 118 and 128 and 129, it can be seen that the sampling period varies from 4 months at low L and energy to 2 years at low L and high energy. Estimates were made of the accuracy of  $\tau$  and are presented in Table 8. Although presented as such in this table, the errors on  $\tau$  are generally not symmetrical, and  $\tau$  is likely to be in error on the larger as opposed to the smaller side. It is clear that the maximum error occurs at low L values and low energies primarily because of the poor time coverage in this region, and these decay times must be interpreted cautiously. From these decay time errors, estimates can be made of the accuracy of the cutoff times, including the effects of factors (b) and (c) described at the beginning of the paragraph. These error estimates are given in Table 11 for  $p = 0.5$  only. Because of the increased extrapolation time for  $p = 0.25$ , these cutoff times must be regarded as crude estimates only.

Verification of the OGO-based decay times can be obtained by comparison with those values based on other data sets and also by comparison with the decay time model of Stassinopoulos and Verzariu (1971). As noted previously, the decay time model is based on data from the 1963-38C satellite taken at  $E_T = 255$  keV, 1.34 MeV, and 2.4 MeV. The model is analytic, provides  $\tau(B, L, E_T)$ , and is valid in the energy range  $200 \leq E_T/(\text{keV}) \leq 3000$  approximately.  $\tau$  is found to be independent of  $B$  for  $L \geq 1.4$ , as noted previously. For comparison with this model, the OGO residual fluxes are summed to provide integral residual fluxes for  $E_T = 133, 292, 690,$  and  $1970$  keV. Integral flux decay times are determined from these residual fluxes and are presented in Table 12, together with errors and the corresponding values given by the Stassinopoulos and Verzariu model; the accuracy of the latter decay times is given as  $\pm 15$  days. Two decay times are given at  $L = 1.3$  for the Stassinopoulos and Verzariu model; the high value corresponds to  $B = B_0$ , and the lower value to  $B = .22$  gauss (atmospheric cutoff  $B_c = .232$  gauss approximately). No comparison is presented to  $E_T = 133$  because of the energy range of the Stassinopoulos and Verzariu model. For the higher two channels, the present values are generally less than the values given by the Stassinopoulos and Verzariu model, although the agreement is considered to be reasonable. For  $E_T = 292$  keV, however, there is substantial disagreement between the two sets of values for  $L \leq 1.8$ . Two legitimate reasons exist for differences between the two sets of decay times: (a) the effect of the background flux not included in the Stassinopoulos and Verzariu model, and (b) the variation of decay time with time. The present integral flux decay times are compared with those based on the 500-keV data from Explorer 26 (Section 3) and those given by Rosen and Sanders (1971) based on the Pegasus A and B satellites for 300 and 500 keV. It has been noted that the absolute flux levels from the Explorer 26 data are apparently anomalous, and decay times are determined from these data only for  $L$  values for which the quiet day background is clearly insignificant. The comparison between the OGO,

Pegasus, and Explorer 26 decay times is made in Figure 141. The Stassinopoulos and Verzariu model is shown as broken lines in this figure. The full lines are added merely to indicate trends, and the figures at the side of the points indicate the standard deviation of  $\tau$ . No clear pattern emerges from the comparison of the various data. At some energies the OGO decay times appear too low, at others too high. However, it is clear that all the data lie below the corresponding model curves by 70-140 days for  $E_T \leq 500$  keV. From the comparison of the OGO decay times, the Stassinopoulos and Verzariu model, and data from other sources, a conflicting picture arises. The model indicates that the OGO decay times are too low by approximately 140 days for  $L \leq 1.8$  and  $E_T = 292$ , whereas the other data indicate that the OGO decay times are approximately correct within the standard deviations of  $\tau$ . It is recommended that in general the most appropriate value of  $\tau$  might be the upper limit of the OGO-based values for  $L \leq 1.9$  and the Stassinopoulos and Verzariu figures for higher  $L$  values and those regions where no OGO values are quoted. As noted, there is essential agreement between those two for  $E_T \geq 690$  keV. Correspondingly, in Table 11 it is recommended that the upper limit of the cutoff times for channels 2 and 3 be used. For the higher energy channels,  $t_c$  in Table 11 is considered appropriate. The poor comparison between the various  $\tau$  values for  $E_T = 292$  keV does cast doubt on the accuracy of the solar cycle parameters for  $690 \geq E/\text{keV} \geq 292$  for  $L \leq 1.7$  approximately, since these values were determined by iteration on the residual Starfish flux component at epoch  $T = 22$ . Since the model decay times are greater than the OGO-based values, the Starfish component may be larger than that assumed at  $T = 22$ , and thus the solar cycle parameters presented in Figure 99 must be regarded as minimum values.

As a final stage in the analysis of the effects of the Starfish injection, integral flux cutoff times can be determined. These are presented in Table 13 for  $p = 0.5$ . For comparison, three sets of decay

times are used: (a) the OGO-based values, (b) the values recommended in the previous paragraph, and (c) the Stassinopoulos and Verzariu model values. Points (a) and (c) can be regarded as limits on the recommended values given by (b).

Earlier it was noted that equation 23 could not be used with the OGO data for estimating cutoff times for those L values and energies for which storm effects are significant, i.e., at high L values for  $690 \geq E/(\text{keV}) \geq 292$ . Integral flux cutoff times, however, can be determined for  $E > 255$  keV using the 1963-38C data at epochs early enough for the storm contribution to be small in comparison to the Starfish flux. Flux levels were obtained from the 1963-38C data for epoch late 1963 and used with the decay times given by the Stassinopoulos and Verzariu model to determine cutoff times for  $p = 0.5$ . These are shown in Table 14 for  $2.2 \geq L \geq 1.8$ . For the low L values of this range, cutoff times have been computed from the OGO data for  $E > 292$  keV using the previously described method, and these are compared to the 1963-38C based values for  $E > 255$  keV in Table 14. It should be noted that at the higher L values cutoff times have been determined using the quiet day background and, in relation to the background flux storm component, the Starfish component reaches this level of significance at earlier epochs than those given in Table 14.

## 7. MODEL PRESENTATION AND DATA PRODUCTS

In this section a description of the model forms available to a user is given. These model forms include graphical presentation and a variety of computer programs that can be supplied to a user. The user is reminded that AE-5 is presented for an epoch of October 1967 and that temporal variations may result in significant flux changes in certain regions of B-L-E space. These temporal variations include magnetic storm effects (Section 4), solar cycle effect (Section 6A), and residual Starfish electrons (Section 6B). The present report attempts to account for the last two effects. The results of these analyses, however, are not incorporated into computer programs and are presented primarily for guidance to the user. The temporal variations, however, generally are such that the flux decreases from that given by AE-5 at epoch October 1967, and the model as such provides an adequate tool for assessing the influence that trapped inner zone electrons have on orbital vehicles.

In previous documentation on trapped particle models, the major source of data has been in the form of omnidirectional integral flux tables. The present model, however, is presented in the form of two-dimensional carpet plots  $J = J(B, L)$  for given energy thresholds. A short description of the use of carpet plots is given in Appendix A. The omnidirectional flux is shown as a function of B and L in Figures 142 through 148 for  $E_T = 0.04, 0.1, 0.25, 0.5, 1.0, 2.0,$  and  $4.0$  MeV. In addition, the model is presented in the more familiar forms of B-L flux maps and R- $\lambda$  plots in Figures 149 through 154 for energy thresholds of 40 keV, 500 keV, and 1 MeV. These three energies typify the three types of radial profiles in the inner belt: the lowest energy having a peak at  $L = 1.9$  approximately, and the doubly peaked intermediate energy and the highest energy having a peak at  $L = 1.4$  owing to the Starfish residual. Three-dimensional plots of

the model flux are shown in Figures 155 through 160 for  $E_T = 40, 100, 500$  keV, 1, 2, and 4 MeV. These plots provide a complete pictorial view of the inner belt model AE-5. The model AE-5 is incorporated into an orbit integration program (ORP) with the outer zone model AE-4 (Singley and Vette, 1972) to estimate flux doses along arbitrary orbits. The integration is performed for  $0^\circ, 30^\circ, 60^\circ,$  and  $90^\circ$  inclination circular orbits at altitudes in the range 150 to 18,000 n.m. These integrations are not presented in the present document but were reported by Singley and Vette (1972) with plots of flux/day as a function of altitude for the four inclinations.

A wide variety of computer programs associated with AE-5 are available to the user. A modification of a matrix storage technique developed by Kluge and Lenhart (1971) for trapped radiation models is used in program MODEL. The program outputs omnidirectional integral flux for an arbitrary set of input B, L and  $E_T$  values and can provide differential flux for a user-specified energy range. The outer zone model AE-4 (Singley and Vette, 1972) and a smoothed version of the proton models AP-5, AP-6, and AP-7 (Kluge and Lenhart, 1971; King, 1967; Lavine and Vette, 1969; Lavine and Vette, 1970) are included in program MODEL. The program may be operated with all or any of these models included. Versions of MODEL can be supplied for operation on IBM 360 series, UNIVAC 1108, and CDC 6000 series computers. MODEL also can be supplied with plot routines suitable for use with a CalComp 570 plotter. The inner zone electron model provided by program MODEL has been smoothed for equatorial grid point integral and differential fluxes. This smoothing process resulted in a maximum 5% change in the model fluxes described in the previous sections.

The orbital integration program ORP is available to the user and is capable of performing integration of the model flux along an arbitrary inputted orbit. Program ORP is a replacement for TRECO (Lucero,

1968) previously supplied by the National Space Science Data Center and requires input in the form of B, L coordinates. Programs generating B, L coordinates from orbital elements can be supplied by NSSDC (Kluge, 1970; King, 1971). User documentation and program descriptions are supplied with MODEL and ORP (Teague et al., 1972). Model AE-5 can be supplied in unidirectional differential flux form for  $E < 690$  keV and in integral form for  $4.5 \geq E_T/\text{MeV} \geq 0.04$  by program UNI. The unidirectional integral flux model can also be provided in the matrix format used for the omnidirectional flux model. The program UMODEL outputs unidirectional fluxes for AE-5 only. An APL (A Programming Language) version of the unidirectional flux model AMODEL has been included in the Goddard Space Flight Center library on the IBM 360/95 and can be used with the APL program FLUXCO to determine omnidirectional fluxes. Complete user documentation for programs UNI, UMODEL, AMODEL, and FLUXCO can be supplied (Teague, 1972). Microfilmed omnidirectional flux carpet plots can be supplied for user-specified energy thresholds.

To enable the user to assess the reliability of the model AE-5, a system of confidence codes is presented. In developing these codes a number of criteria were used: number of data sets used, data coverage, and uncertainties introduced by temporal variations. A scale of 1 to 10 is used, where 10 corresponds to the highest reliability with an expected error of a factor of 2 or less and 1 corresponds to the least reliability with an expected error in excess of a factor of 10. In general, however, efforts have been made to provide pessimistic flux estimates where low confidence codes are given which state that it is more probable that the flux is lower than the quoted value than higher. Two sets of codes are given - one for the omnidirectional flux at an epoch of October 1967 (Table 15), and one for the integral flux solar cycle parameters (Table 16). In each case a brief explanation for the code and a section reference are given.

## APPENDIX A. USE OF CARPET PLOTS

Carpet plots have been used in this document for the graphical presentation of the solar cycle ratios (Figures 80-88 and 90-93, Section 6A) and the omnidirectional model flux (Figures 142 through 148, Section 7). The general term for these multidimensional plots is nomograph (Adams, 1964), but the phrase "carpet plot" is used here to denote the special application for the present document. In the present usage, an arbitrary dependent variable  $Y$  is presented as a function of two independent variables  $X_1$  and  $X_2$ . In theory, an arbitrary number of independent variables  $X_i$  may be covered with a practical limit of  $i$  equal to 4. For  $i > 2$ , however, the plots become cumbersome and difficult to use.

In general, the dependent variable is plotted as a continuous function of an independent variable at a variety of specified values of the other; i.e.,

$$Y = f(X_1, X_2 = \text{const}) \quad (\text{A.1})$$

and

$$Y = f(X_2, X_1 = \text{const}) \quad (\text{A.2})$$

Conventionally, the dependent variable is plotted as abscissa and the independent variables as ordinates. The origin of each ordinate scale is sliding, although the scales themselves remain constant. These scales are indicated by bars on each plot presented in this report. The displacement of the origin for successive curves of the family given by equation A.1, for example, is determined by the scale of the variable  $X_2$  and the value of  $X_2$  on those successive curves.

**PRECEDING PAGE BLANK NOT FILMED**

Carpet plots are directly amenable to interpolation. In Figure 161, if the value of  $Y$  is required at some point  $X_2 = a_3$  and  $X_1 = b_3$ , the four points  $(b_1, a_3)$ ,  $(b_2, a_3)$ ,  $(b_3, a_1)$ , and  $(b_3, a_2)$  can be easily located along the four lines of constant  $X_1$  and  $X_2$  given in the carpet plots using the scale factors for the independent variables. Other points lying on the curves  $X_2 = a_3$  and  $X_1 = b_3$  can be determined in a similar fashion for other given curves in the two families. The required curves  $X_2 = a_3$  and  $X_1 = b_3$  can then be determined to a degree of accuracy better than that given by simple linear interpolation, and the required value of  $Y$  at the point  $(b_3, a_3)$  can be obtained from the abscissa scale.

In general, the dependent variable for a grid point,  $(b_1, a_1)$  in Figure 161 for instance, can be retrieved from a carpet plot with an accuracy of 1-2%. Where interpolation is performed in the manner described above, it is estimated that this accuracy will be 2-3%. While the omnidirectional flux data have been presented tabularly in previous model documentation with greater resolution than can be obtained from carpet plots, error associated with determining the independent variable  $Y$  from the carpet plots is considered insignificant in comparison to the inherent error associated with obtaining the model (Section 7).

#### ACKNOWLEDGMENTS

Our thanks are due to Professor Winckler and Dr. Pfitzer for providing data from the OGO 1 and OGO 3 satellites, to Dr. Bostrom for the 1963-38C data, to Dr. Vampola for the OV3-3 data, and to Professor McIlwain for the Explorer 26 data. In addition, we express our appreciation to Dr. Vampola and Dr. Pfitzer, who provided valuable assistance in incorporating their data into AE-5 and who reviewed this document and recommended several improvements.

## REFERENCES

1. Adams, D.P., Nomography, Archon Books, Hamden, Connecticut, 1964.
2. Beall, D.S., "Graphs of Selected Data from Satellites 1963-38C," Applied Physics Laboratory, TG 1050-1 through TG 1050-5, 1969.
3. King, J.H., Models of the Trapped Radiation Environment, Volume IV: Low-Energy Protons, NASA SP-3024, 1967.
4. King, J.H., Editor, "Handbook of Correlative Data," NSSDC 71-05, February 1971.
5. Kluge, G., "Computer Program SHELL for the Calculation of B and L from Models of the Geomagnetic Field," ESOC Internal Note No. 67, October 1970.
6. Kluge, G., and K. G. Lenhart, "A Unified Computing Procedure for Trapped Radiation Models," ESOC Internal Note, No. 78, 1971.
7. Lavine, J.P., and J.I. Vette, Models of the Trapped Radiation Environment, Volume V: Inner Belt Protons, NASA SP-3024, 1969.
8. Lavine, J.P., and J.I. Vette, Models of the Trapped Radiation Environment, Volume VI: High-Energy Protons, NASA SP-3024, 1970.
9. Lucero, A.B., "TRECO, An Orbital Integration Computer Program for Trapped Radiation," Data Users' Note, NSSDC 68-02, 1968.
10. Pfitzer, K.A., "An Experimental Study of Electron Fluxes from 50 keV to 4 MeV in the Inner Radiation Belt," University of Minnesota, Technical Report CR-123, August 1968.
11. Rosen, A., and N.L. Sanders, "Loss and Replenishment of Electrons in the Inner Radiation Zone during 1965-1967," J. Geophys. Res., 76, 110-121, 1971.
12. Singley, G.W., and J.I. Vette, "The AE-4 Model of the Outer Radiation Zone Electron Environment," NSSDC 72-06, 1972.
13. Stassinopoulos, E.G., and P. Verzariu, "General Formula for Decay Lifetimes of Starfish Electrons," J. Geophys Res., 76,(4), 1841-1844, 1971.

PRECEDING PAGE BLANK NOT FILMED

14. Teague, M.J., "The Calibration Constants for the OGO 1/3 Electron Spectrometer," NSSDC 70-14, October 1970.
15. Teague, M.J., "Programs for Inner Belt Modeling" (to be published in 1972).
16. Teague, M.J., and J.I. Vette, "Variation of the Electron Spectrum in the Inner Radiation Belt, Sept. 64 to Present," NSSDC 71-11, April 1971.
17. Teague, M.J., J.L. Stein, and J.I. Vette, "The Use of the Inner Zone Electron Model AE-5 and Associated Computer Programs," NSSDC 72-11, 1972.
18. Wilson, G.M., "Guide for APL Libraries," NASA X-543-71-69, February 1971.

TABLE 1 QUIET DAY MODEL PARAMETERS.

REFERENCE PITCH ANGLE = 90 DEGS.

EPOCH = 10/67

L (RE)	JI REF	A REF	X REF (KEV)	M	N	PHI (DEGS)	BC (GAUSS)
1.30	1.20E07	1.71E03	83.7	2.80	0.670	67.1	0.232
1.35	1.70E07	2.39E03	84.3	2.20	0.660	61.4	0.234
1.40	2.23E07	3.08E03	85.1	1.70	0.650	57.5	0.238
1.45	2.81E07	3.81E03	85.7	1.20	0.640	59.0	0.241
1.50	3.41E07	4.56E03	86.5	0.93	0.630	65.0	0.245
1.55	3.99E07	5.21E03	87.5	0.92	0.620	66.0	0.249
1.60	4.49E07	5.74E03	88.4	0.91	0.610	67.0	0.253
1.65	4.79E07	6.08E03	88.8	0.90	0.600	66.5	0.257
1.70	5.10E07	6.42E03	89.1	0.89	0.590	66.0	0.262
1.75	5.46E07	6.81E03	89.5	0.88	0.580	68.0	0.265
1.80	5.77E07	7.16E03	89.8	0.87	0.570	70.0	0.268
1.85	6.00E07	7.57E03	89.0	0.86	0.545	76.0	0.271
1.90	6.11E07	7.93E03	87.8	0.85	0.520	86.0	0.274
1.95	5.84E07	7.80E03	86.5	0.83	0.500	90.0	0.277
2.00	5.38E07	7.50E03	84.7	0.80	0.480	90.0	0.280
2.10	4.69E07	7.15E03	81.0	0.79	0.470	90.0	0.286
2.20	4.15E07	7.00E03	77.0	0.78	0.460	90.0	0.292
2.30	3.61E07	6.50E03	74.5	0.77	0.450	90.0	0.298
2.40	3.11E07	6.00E03	72.0	0.76	0.440	90.0	0.304

JI REF HAS UNITS 1/(SQCM.SEC.STER)

A REF HAS UNITS 1/(SQCM.SEC.STER.KEV.KEV)

TABLE 2

## SAMPLE MODEL OUTPUT

MODEL UNIDIRECTIONAL FLUX L = 1.7

CUT PITCH ANGLE = 29.472, BCUT = 0.262 GAUSS. EQUATORIAL B = 0.063434 GAUSS.

CUT OFF FOR PITCH ANGLE FUNCTIONS = 66 DEGREES.

UNIVERSAL TIME = 37 MONTHS FROM SOLAR MINIMUM. EPOCH: 10/67

M = 0.89 N = 0.59

SOLAR CYCLE RATIOS = 1 (133-36 KEV) 1 (292-133 KEV) 1 (690-292 KEV) 1 (&gt;255 KEV)

ALPHA (DEGS)	B (GAUSS)	INTEGRAL FLUX IN ENERGY INTERVALS (KEV)				X (KEV)	JI 1/(SQCM.SEC.STER)
		36-133	292-133	690-292	255		
2.9572E1	2.6039E-1	7.0901E4	4.3443E4	7.0175E3	1.1457E4	6.1959E1	1.3727E5
3.0000E1	2.5368E-1	3.1504E5	1.9564E5	3.2289E4	5.2493E4	6.2438E1	6.1315E5
3.5000E1	1.9277E-1	2.8185E6	2.0053E6	4.1177E5	6.4182E5	6.7706E1	5.8198E6
4.0000E1	1.5350E-1	5.3974E6	4.2692E6	1.0411E6	1.5726E6	7.2413E1	1.1768E7
4.5000E1	1.2684E-1	8.0793E6	6.9512E6	1.9455E6	2.8701E6	7.6604E1	1.8502E7
5.0000E1	1.0808E-1	1.0809E7	9.9495E6	3.1135E6	4.5108E6	8.0309E1	2.5856E7
5.5000E1	9.4519E-2	1.3530E7	1.3150E7	4.5058E6	6.4381E6	8.3548E1	3.3620E7
6.0000E1	8.4566E-2	1.6186E7	1.6435E7	6.0609E6	8.5688E6	8.6336E1	4.1558E7
6.5000E1	7.7217E-2	1.8728E7	1.9692E7	7.7017E6	1.0801E7	8.8683E1	4.9424E7
6.6000E1	7.5999E-2	1.9219E7	2.0330E7	8.0326E6	1.1250E7	8.9100E1	5.0967E7
9.0000E1	6.3434E-2	1.9219E7	2.0330E7	8.0326E6	1.1250E7	8.9100E1	5.0967E7

FLUX UNITS: ELECTRONS/SQCM.SEC.STER

TABLE 3. SATELLITE CALIBRATION CONSTANTS

		Present Values		Original Experimenter Values	
Satellite	Channel	Energy Range (keV)	C	Energy Range (keV)	C
OGO 1/3 (1964-54A) (1966-49A)	1	36-133	3.691	50-120	7.9
	2	133-292	6.23	120-290	8.4
	3	292-690	6.1	290-690	7.2
	4	690-1970	6.66	690-1700	9.5
	5	1970-4740	7.794	1700-4000	15.4
Explorer 26 (1965-78A)	1	>520	$2.34 \times 10^4$	>500	$2.5 \times 10^4$
1963-38C	1	>254	487.7	>280	600
	2	>1340	896	>1200	1200
OV3-3	1	2147-2472	-	2147-2472	-
	2	1880-2200	-	1880-2200	-
	3	1615-1925	-	1615-1925	-
	4	1329-1651	-	1329-1651	-
	5	1075-1375	-	1075-1375	-
	6	814.5-1099.5	-	814.5-1099.5	-
	7	574.5-849.5	-	574.5-849.5	-
	8	350-600	-	350-600	-
	9	225-375	-	225-375	-

C = Flux/Count Rate (cps)

TABLE 4. PITCH ANGLE COVERAGE

Data	Time	L Range	$\alpha_0$ Range	$B_{\perp}$ Range	$B_0$	$B_c$	$\alpha_c$	
OGO 3	6/66-1/67	1.3	65-80	.17-.145	.1418	.232	51.4	
	6/66-4/67	1.4	50-85	.194-.115	.1136	.237	44	
	6/66-11/67	1.5	45-80	.185-.095	.0923	.245	37.9	
	6/66-11/67	1.6	35-75	.231-.082	.0761	.254	33.2	
	6/66-11/67	1.7	30-65	.254-.077	.0634	.262	29.5	
	6-7/66	1.8	35-65	.162-.065	.0534	.268	26.5	
	9-11/67	1.8	27-50	.259-.091	.0534	.268	26.5	
	6-7/66	1.9	32-60	.162-.061	.0454	.274	24	
	9-11/67	1.9	25-45	.254-.091	.0454	.274	24	
	6-7/66	2.0	30-60	.156-.052	.0389	.28	21.9	
	9-11/67	2.0	22-40	.277-.094	.0389	.28	21.9	
	6-7/66	2.2	30-70	.117-.033	.0293	.292	18.5	
	9-11/67	2.2	20-28	.25-.133	.0293	.292	18.5	
	6-7/66	2.4	20-70	.192-.025	.0225	.304	15.8	
	9-11/67	2.4	16-25	.296-.126	.0225	.304	15.8	
	1963-38C	late 67*	1.25	61-87	.21-.16	.1596	.231	56.5
		late 67	1.3	53-70	.22-.16	.1418	.232	51.4
late 67		1.35-1.4	45-63	.23-.16	.1267-.1136	.234-.237	47.4-44	
late 67		1.45	41-51	.24-.17	.1022	.241	40.5	
late 67		1.5-1.55	37-47	.23-.17	.0923-.0837	.245-.249	37.9-35.5	
late 67/late 66 <sup>+</sup>		1.6	35-42	.23-.17	.0761	.254	33.2	
late 67/late 66		1.7	31-36	.24-.18	.0634	.262	29.5	
late 67/late 66		1.8	27-32	.26-.19	.0534	.268	26.5	
late 67/late 66		1.9-2.0	22-29	.26-.2	.0454-.0389	.274-.28	24-21.9	

\*late 1967: Days 285-300 and Days 335-350

<sup>+</sup>late 1966: Days 315-330

TABLE 5. QUIET DAY PERIODS

June to August 1966
October 1966 to January 1967
April to May 1967
September to November 1967

TABLE 6 SOLAR CYCLE FLUX RATIOS

$$R_{22} = \text{FLUX } (T=37) / \text{FLUX } (T=22)$$

L	R(36-133)	R(133-292)	R(292-690)	R(>255)
1.40	1.02	1.47	3.30	0.00
1.45	1.07	1.61	3.85	0.00
1.50	1.12	1.75	4.40	0.00
1.55	1.15	1.83	4.88	0.00
1.60	1.18	1.92	5.37	2.58
1.65	1.20	1.99	5.57	2.86
1.70	1.21	2.05	5.77	3.15
1.75	1.22	2.10	5.91	3.28
1.80	1.22	2.15	6.05	3.42
1.85	1.21	2.17	6.35	3.50
1.90	1.21	2.20	6.40	3.58
1.95	1.20	2.22	6.40	3.62
2.00	1.20	2.25	6.40	3.66
2.10	1.20	2.17	6.20	0.00
2.20	1.20	2.10	6.00	0.00
2.30	1.20	2.05	5.88	0.00
2.40	1.20	2.00	5.70	0.00

R=0 DENOTES NO MEASUREMENT.

TABLE 7. COEFFICIENTS OF PITCH ANGLE DEPENDENCE OF STARFISH ELECTRONS

L	292-133 keV					690-292 keV					1970-690 keV					4740-1970 keV				
	$a_0$	$a_1 \times 10^3$	$a_2 \times 10^4$	$a_3 \times 10^5$	$\theta$	$a_0$	$a_1 \times 10^3$	$a_2 \times 10^4$	$a_3 \times 10^5$	$\theta$	$a_0$	$a_1 \times 10^3$	$a_2 \times 10^4$	$a_3 \times 10^5$	$\theta$	$a_0$	$a_1 \times 10^3$	$a_2 \times 10^4$	$a_3 \times 10^5$	$\theta$
1.3	4.613	-11.94	-1.406	-3.291	75	4.447	-21.67	-1.007	-4.950	74	3.75	-41.4	11.9	-11.8	72.5	3.057	-32.00	.7505	-5.181	72.5
1.4	4.895	-25.68	-1.136	-2.656	71	4.529	2.770	-22.14	0	67.5	3.819	-22.14	-2.603	-.5512	70	3.182	-24.37	-.7157	-3.214	72.5
1.5	4.959	.4001	-5.455	0	77.5	4.622	-20.38	5.598	-5.702	66	3.750	-14.46	-13.44	0	67	2.857	-14.33	-3.551	-.6104	74.5
1.6	4.989	-7.791	3.874	-2.032	74	4.549	-22.23	-2.539	-1.328	64.5	3.494	-9.510	-9.798	0	67	2.321	-15.69	-5.382	-.4008	67
1.7	5.004	-13.06	1.852	-1.063	75	4.412	-18.90	-5.672	-.6142	63.5	3.037	-5.956	-9.806	0	66					
1.8	4.951	-15.28	-3.408	-.3547	65	4.250	-22.19	-6.253	.1122	60.5	2.629	-16.67	-5.856	-.0271	65					
1.9	4.913	1.128	-8.49	0	70	4.033	-11.82	-2.910	-1.070	63.5	2.255	-16.59	-6.773	.4596	65					
2.0	4.839	-7.729	1.624	-.8415	79	3.792	-18.58	7.626	-1.882	75	1.998	-16.32	-5.651	-.4836	65					
2.2	4.586	-2.266	-2.219	-.4664	70	3.29	-4.455	-1.576	-.2088	80										

Coefficients provide flux in units of electrons/cm<sup>2</sup> sec ster keV at epoch September 1964.

TABLE 8. STARFISH DECAY TIMES

L	Energy Ranges (keV)			
	292-133	690-292	1970-690	4740-1970
1.4	163 ± 60	216 ± 70	380 ± 20	310 ± 20
1.5	200 ± 70	230 ± 70	375 ± 20	310 ± 20
1.6	233 ± 45	260 ± 50	312 ± 20	290 ± 20
1.7	265 ± 42	230 ± 42	310 ± 40	ND
1.8	267 ± 37	230 ± 37	ND	ND
1.9	250 ± 30	211 ± 30	ND	ND
2.0	219 ± 30	150 ± 25	ND	ND
2.2	98 ± 30	103 ± 25	ND	ND

Decay times are in days.

ND denotes no data.

*TABLE 9 HIGH ENERGY BACKGROUND FLUX ESTIMATES*

<i>L</i>	<i>ENERGY RANGE (KEV)</i>	
	<i>690-1970</i>	<i>1970-4740</i>
<i>1.4</i>	<i>179.8</i>	<i>27.2</i>
<i>1.5</i>	<i>249.7</i>	<i>35.8</i>
<i>1.6</i>	<i>299.7</i>	<i>41.3</i>

*EQUATORIAL PERPENDICULAR FLUX ELECTRONS/SQCM.SEC.STER.KEV*

TABLE 10 SIGNIFICANCE OF STARFISH FLUX COMPONENT

STARFISH COMPONENT AS PERCENTAGE OF TOTAL FLUX

L	SEPTEMBER 1964				JULY 1966				OCTOBER 1967			
	CH2	CH3	CH4	CH5	CH2	CH3	CH4	CH5	CH2	CH3	CH4	CH5
1.3	95	99	ND	ND	ND	ND	ND	ND	ND	ND	ND	ND
1.4	75	98	97	98	4	52	87	87	0	3	68	60
1.5	72	98	95	96	8	52	75	71	0	3	54	47
1.6	71	98	90	86	10	51	56	40	0	3	24	5
1.7	69	97	82	65	12	36	29	0	0	1	8	0
1.8	67	95	70	0	11	24	0	0	0	0	0	0
1.9	66	92	0	0	9	15	0	0	0	0	0	0
2.0	63	89	0	0	6	ND	0	0	0	0	0	0
2.2	59	81	0	0	0	ND	0	0	0	0	0	0

CHANNEL ENERGY RANGE (KEV)  
 2 133-292  
 3 292-690  
 4 690-1970  
 5 1970-4740

ND DENOTES NO DATA.

0 DENOTES LESS THAN 1 PERCENT

TABLE 11. STARFISH FLUX CUTOFF TIMES

L	p = 0.5				p = 0.25			
	Ch 2	Ch 3	Ch 4	Ch 5	Ch 2	Ch 3	Ch 4	Ch 5
1.4	2/65 (31) ±3	7/66 (48) ±6	3/68 (68) ±8	1/68 (66) ±7	8/65 (37)	11/66 (52)	7/69 (84)	12/68 (77)
1.5	3/65 (32) ±3	7/66 (48) ±6	9/67 (62) ±7	4/67 (57) ±6	9/65 (38)	11/66 (52)	10/68 (75)	3/68 (68)
1.6	3/65 (32) ±2	7/66 (48) ±4	9/66 (50) ±2	3/66 (44) ±2	10/65 (39)	11/66 (52)	8/67 (61)	2/67 (55)
1.7	4/65 (33) ±2	2/66 (43) ±3	2/66 (43) ±2	~10/65 (39) ±2	12/65 (41)	8/66 (49)	8/66 (49)	~4/66 (45)
1.8	3/65 (32) ±2	2/66 (43) ±3	ND	< 12/64 (< 29)	10/65 (39)	6/66 (47)	ND	< 12/64 (< 29)
1.9	1/65 (30) ±2	11/65 (40) ±3	ND	< 12/64 (< 29)	9/65 (38)	4/66 (45)	ND	< 12/64 (< 29)
2.0	1/65 (30) ±2	ND	ND	< 12/64 (< 29)	7/65 (36)	ND	ND	< 12/64 (< 29)
2.2	10/64 (27) ±2	ND	ND	< 12/64 (< 29)	2/65 (31)	ND	ND	< 12/64 (< 29)

$$p = j_{st}/j$$

ND denotes no data because of magnetic storm effects or no measurements.

Figures in parentheses represent months from Starfish injection.

Channel	Energy Range (keV)
2	133-292
3	292-690
4	690-1970
5	1970-4740

TABLE 12. COMPARISON OF INTEGRAL FLUX DECAY TIMES

L	Energy Threshold (keV)						
	133	292		690		1970	
	Present	Present	S and V*	Present	S and V*	Present	S and V*
1.3	ND	ND	382-333	ND	368-317	ND	325-265
1.4	230 ± 60	265 ± 70	415	348 ± 20	390	310 ± 20	340
1.5	245 ± 60	280 ± 70	445	350 ± 20	410	310 ± 20	320
1.6	256 ± 45	270 ± 45	445	305 ± 20	400	290 ± 20	270
1.7	240 ± 42	240 ± 42	420	310 ± 40	360	ND	180
1.8	250 ± 37	230 ± 37	360	ND	300	ND	80
1.9	240 ± 30	211 ± 30	290	ND	215	ND	20
2.0	200 ± 30	150 ± 25	200	ND	135	ND	ND
2.2	100 ± 30	103 ± 25	64	ND	15	ND	ND

Decay times are in days.

ND denotes no data.

\*Stassinopoulos and Verzariu.

TABLE 13. COMPARISON OF INTEGRAL FLUX CUTOFF TIMES

L	133		292			690			1970		
	a	b	a	b	c	a	b	c	a	b	c
1.4	10/63 (39)	1/66 (42)	7/66 (48)	11/66 (52)	2/67 (55)	4/68 (69)	5/68 (70)	9/68 (74)	2/68 (67)	4/68 (69)	4/68 (69)
1.5	9/65 (38)	11/65 (40)	6/66 (47)	9/66 (50)	12/66 (53)	8/67 (61)	10/67 (63)	2/68 (67)	3/67 (56)	4/67 (57)	4/67 (57)
1.6	7/65 (36)	8/65 (37)	5/66 (46)	7/66 (48)	10/66 (51)	8/66 (48)	9/66 (49)	2/67 (55)	6/66 (44)	4/66 (45)	4/66 (45)
1.7	6/65 (35)	8/65 (37)	1/66 (42)	3/66 (44)	7/66 (48)	9/65 (38)	10/65 (39)	11/65 (40)	ND	~10/65 (39)	ND
1.8	5/65 (34)	6/65 (35)	8/65 (37)	10/65 (39)	12/65 (41)	ND	ND	ND	ND	ND	ND
1.9	3/65 (32)	4/65 (33)	4/65 (33)	5/65 (34)	6/65 (35)	ND	ND	ND	ND	ND	ND
2	2/65 (31)	3/65 (32)	ND	ND	ND	ND	ND	ND	ND	ND	ND
2.2	10/64 (27)	10/64 (27)	ND	ND	ND	ND	ND	ND	ND	ND	ND

ND denotes no data.

a. OGO decay times.

b. Recommended decay times.

c. Stassinopoulos and Verzariu model decay times.

**TABLE 14 CUT OFF TIMES FROM 1963-38C DATA**

	1963-38C	OGO 1
<i>L</i>	<i>ET= 255 KEV</i>	<i>ET= 292 KEV</i>
1.8	3/66 (44)	12/65 (41)
1.9	9/65 (38)	6/65 (35)
2.0	3/65 (32)	ND
2.2	6/64 (23)	ND

ND DENOTES NO DATA.

FIGURES IN PARENTHESIS DENOTE MONTHS FROM STARFISH.

TABLE 15. OMNIDIRECTIONAL FLUX CONFIDENCE CODES

Code	B Range	L Range	$E_T$ Range	Section	Comment
1	$>B_0$	1.2-1.4	$>3$ MeV	4	Extrapolation on both B dependence and spectrum, no data
2	$\sim B_0$	1.2-1.4	$>3$ MeV	4	Extrapolation on spectrum, no data
4	$\geq B_0$	1.2-1.7	$>250$ keV	6B	Possible presence of Starfish electrons
5	$\geq B_0$	1.9-1.4	4-2 MeV	4	Magnetic storm effects, single data set, B extrapolation
6	$>B_0$	1.7-1.9	$>500$ keV	4	Single data set, B extrapolation
6	$\geq B_0$	$< 1.25$	all energies	5	L extrapolation
6	$\sim B_0$	$>1.5$	all energies	3	Poor data
7	$\geq B_0$	1.3	all energies	3	Poor OGO data
8	$\gg B_0$	$>2$	all energies	3	Poor pitch angle coverage
10	$\geq B_0$	1.4-1.9	$< 250$ keV	3	Agreement between three data sets

TABLE 16. INTEGRAL FLUX SOLAR CYCLE PARAMETER CONFIDENCE CODES

Code	L Range	$E_T$	T Range	Section	Comment
3	<1.8	250,500	>22	6B	Significant Starfish flux at T=22 resulting in iteration
4	>1.9	all	all	3	Poor OGO data at high L values
4	all	40	all	6A	Small $R_T$ values; data standard deviation becomes significant.
5	<1.4	250,500	all	6B	Hardening of spectrum; assumed constancy of $j(>690)$ term in equation 16
5	>1.8	500	all	6A	Storm effects term in equation 17 becomes significant
7	1.6-2.0	250,500	all	6A	Two data sets available (i.e., OGO and 1963-38C)

Note that these confidence codes are low because integral flux values of  $R_T$  are determined from the OGO data using an approximate expression, and B independence has been assumed. Further, if  $R_T$  is used to extrapolate beyond the epoch of October 1967, as described in Section 7, the above confidence codes will be reduced because of asymmetries in the solar cycle.

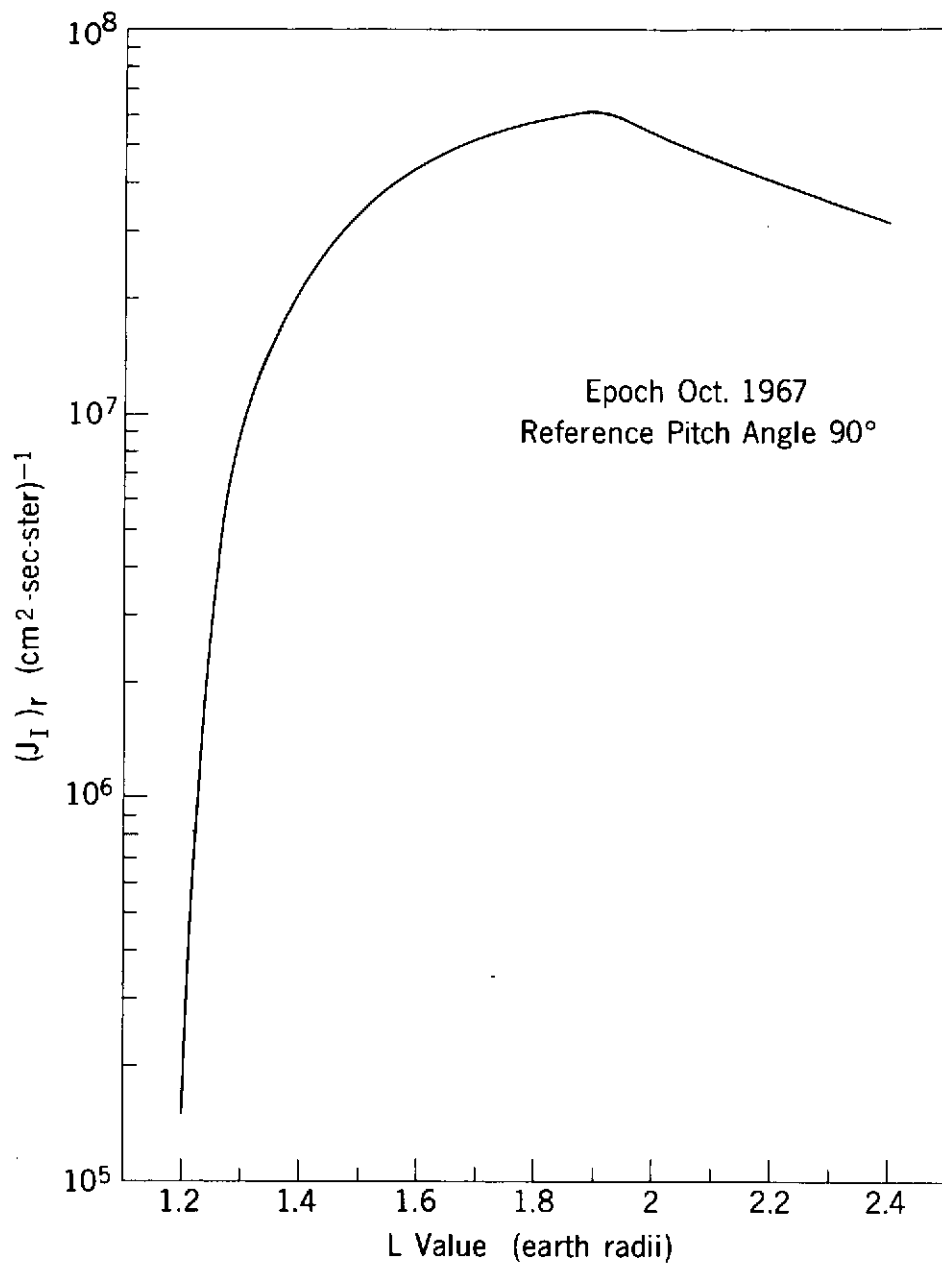


Figure 1. Radial Profile of the Reference Electron Content Parameter

$(J_I)_r$  approximates to the total unidirectional electron flux above thermal energies at the reference pitch angle  $\alpha_0 = 90^\circ$  (Section 2).

PRECEDING PAGE BLANK NOT FILMED  
8512 PAGE BLANK NOT FILMED

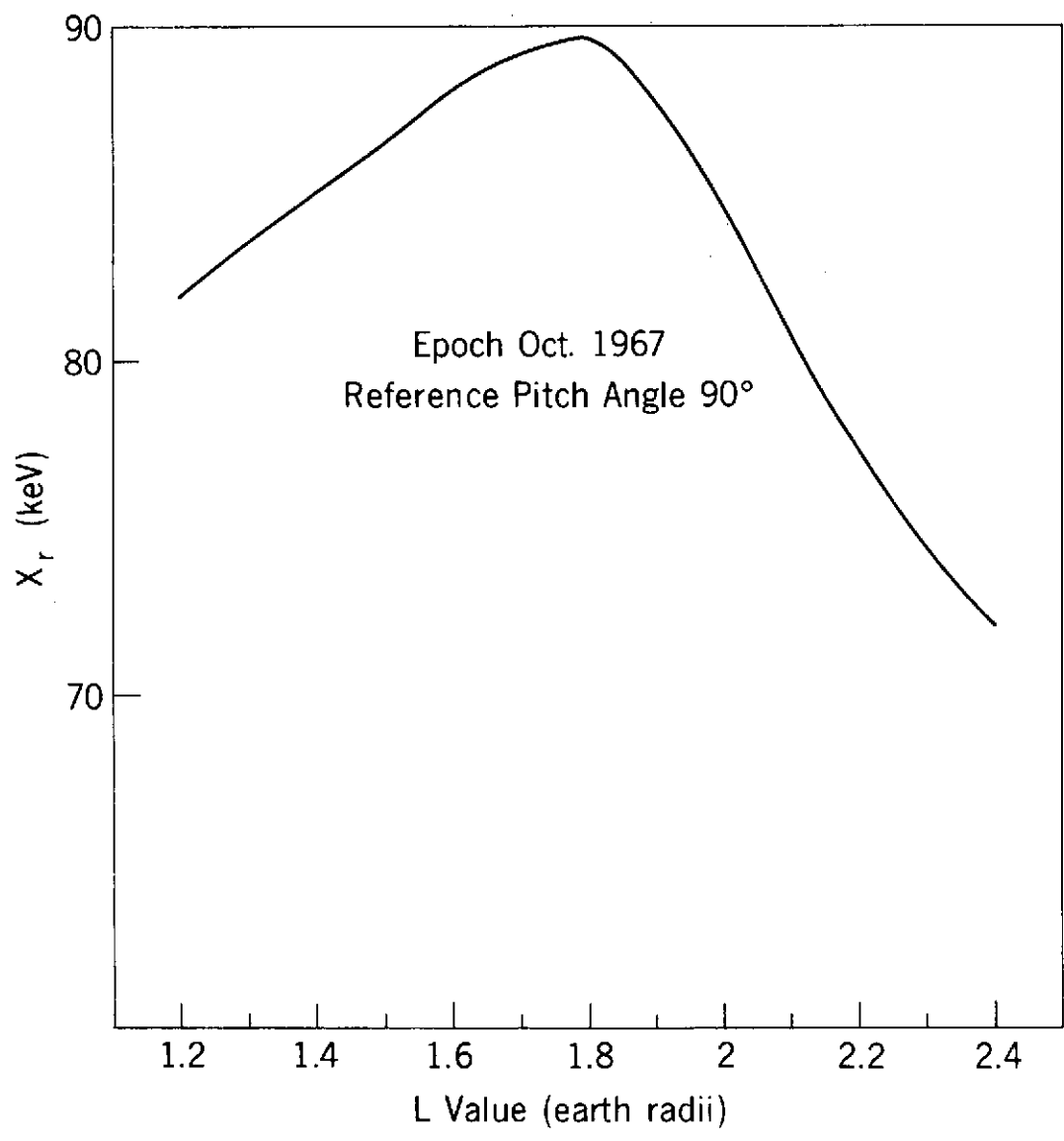


Figure 2. Hardness Parameter  $X_r$

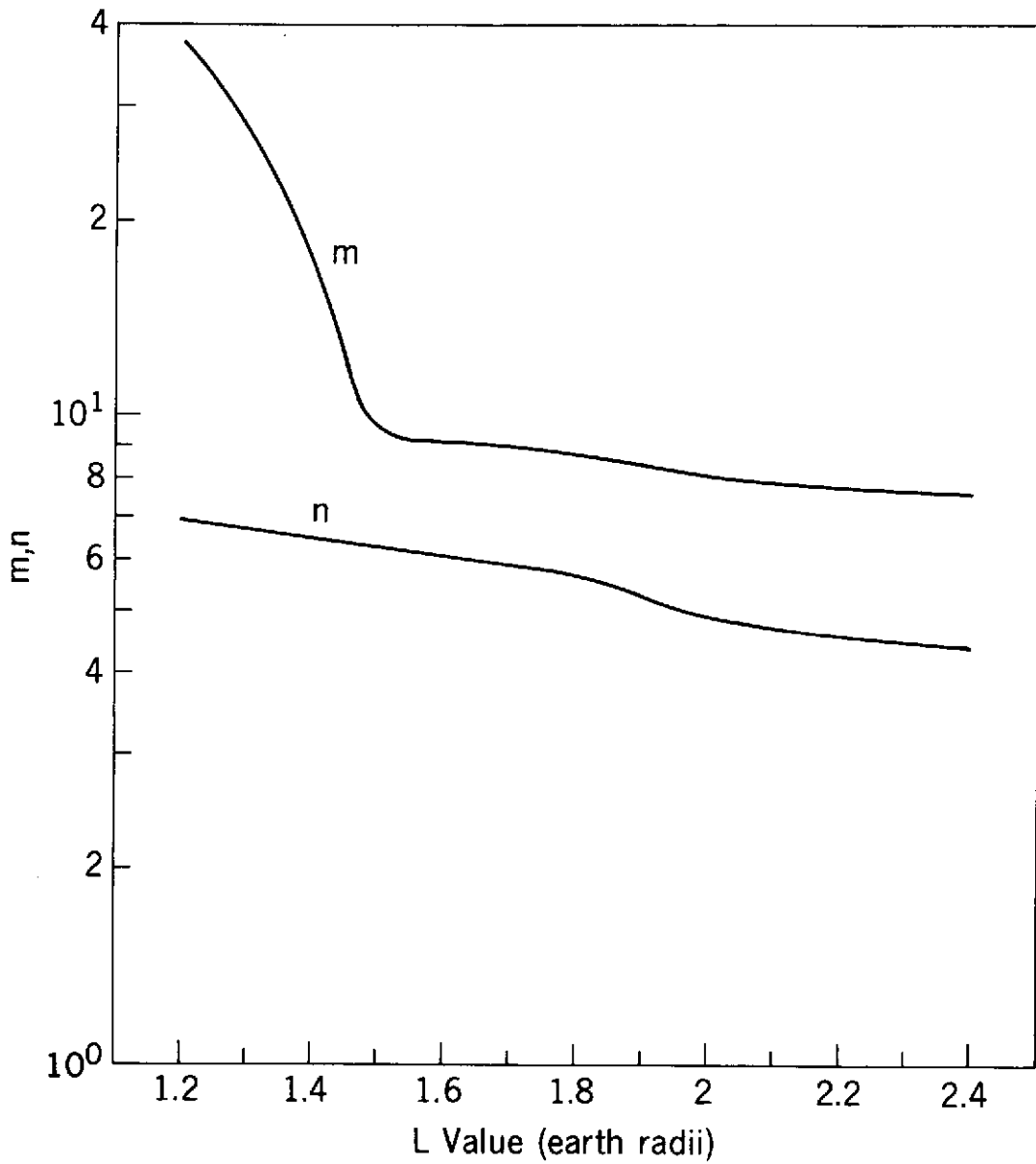


Figure 3. Pitch Angle Parameters m and n

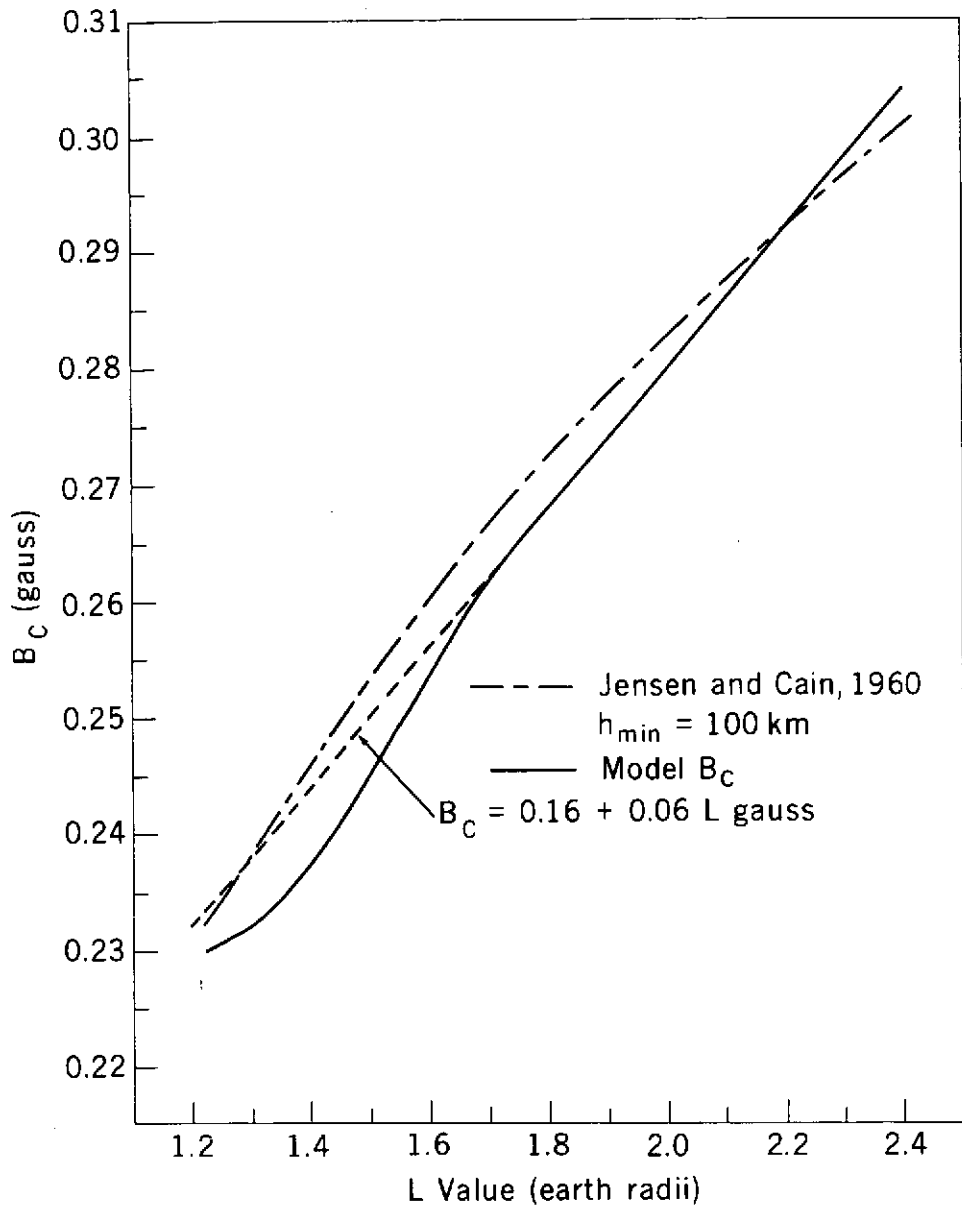


Figure 4. Atmospheric Cutoffs  $B_C$

FIGURE 5  
 QUIET DAY MODEL  
 PERPENDICULAR INTEGRAL FLUX  
 GREATER THAN 40 KEV  
 EPOCH OCTOBER 1967

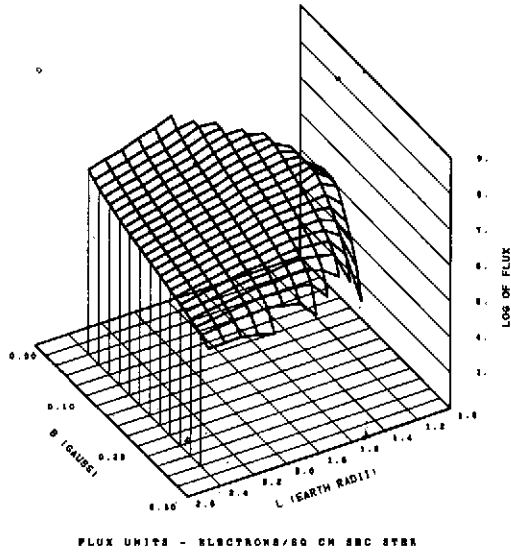


FIGURE 6  
 QUIET DAY MODEL  
 PERPENDICULAR INTEGRAL FLUX  
 GREATER THAN 100 KEV  
 EPOCH OCTOBER 1967

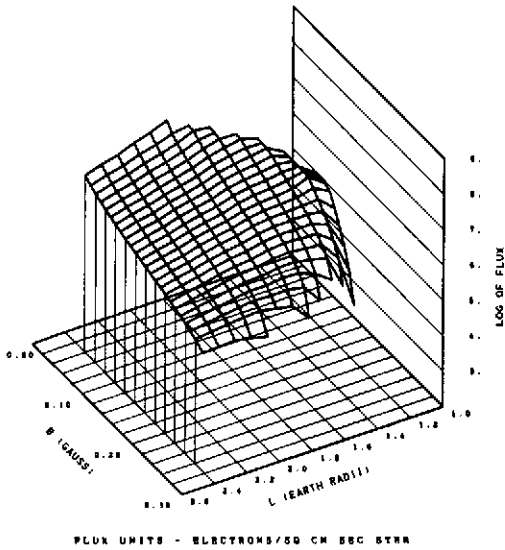
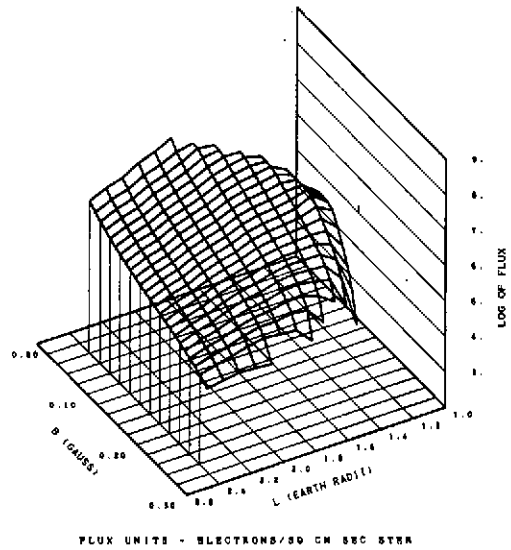
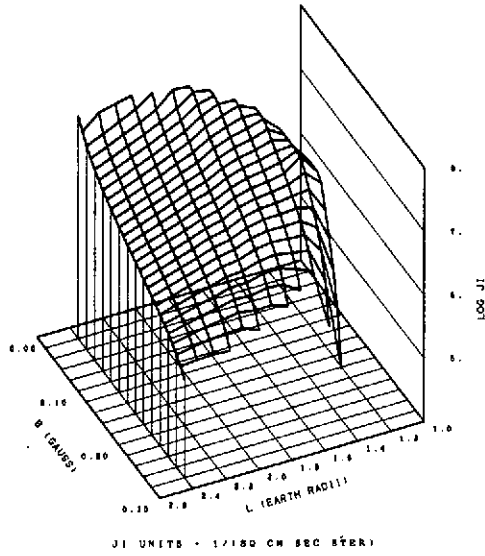


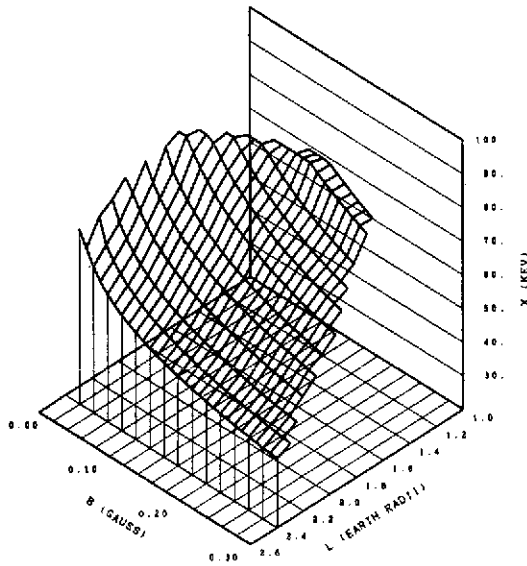
FIGURE 7  
 QUIET DAY MODEL  
 PERPENDICULAR INTEGRAL FLUX  
 GREATER THAN 250 KEV  
 EPOCH OCTOBER 1967



**FIGURE 8**  
**QUIET DAY MODEL**  
**ELECTRON CONTENT PARAMETER**  
**EPOCH OCTOBER 1967**



**FIGURE 9**  
**QUIET DAY MODEL**  
**HARDNESS PARAMETER**  
**EPOCH OCTOBER 1967**



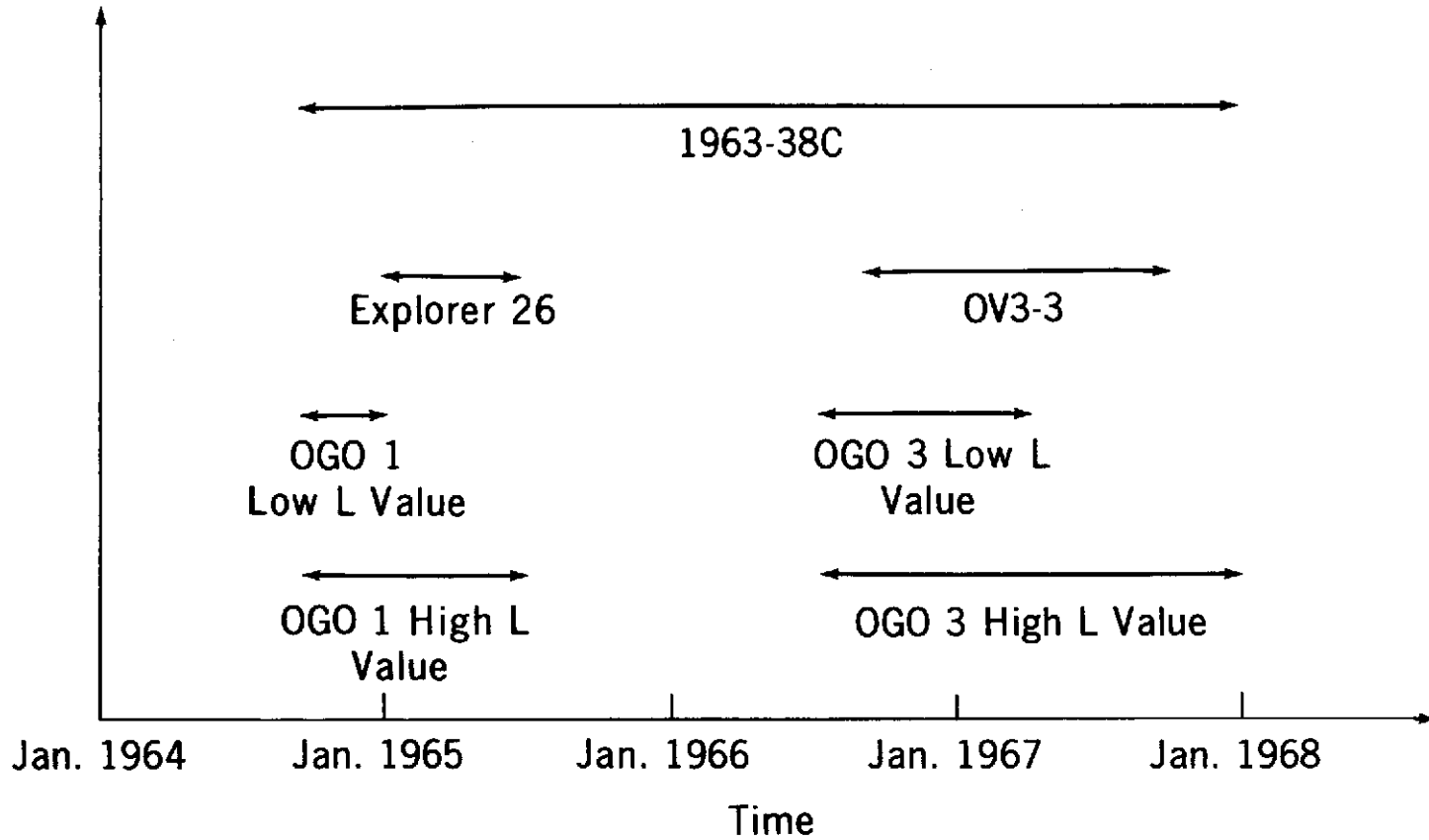


Figure 10. Data Coverage

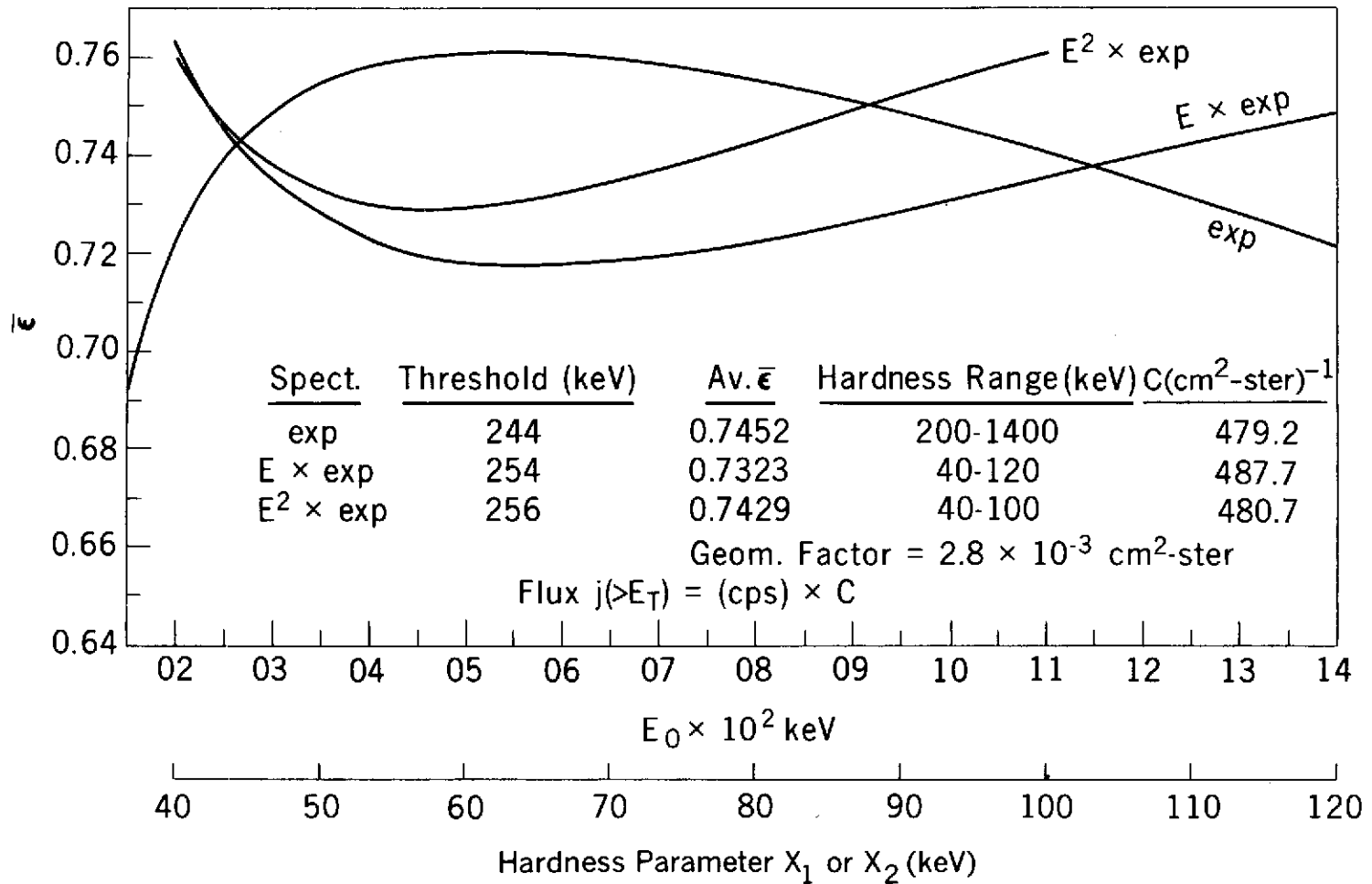


Figure 11. 1963-38C Calibration Curves

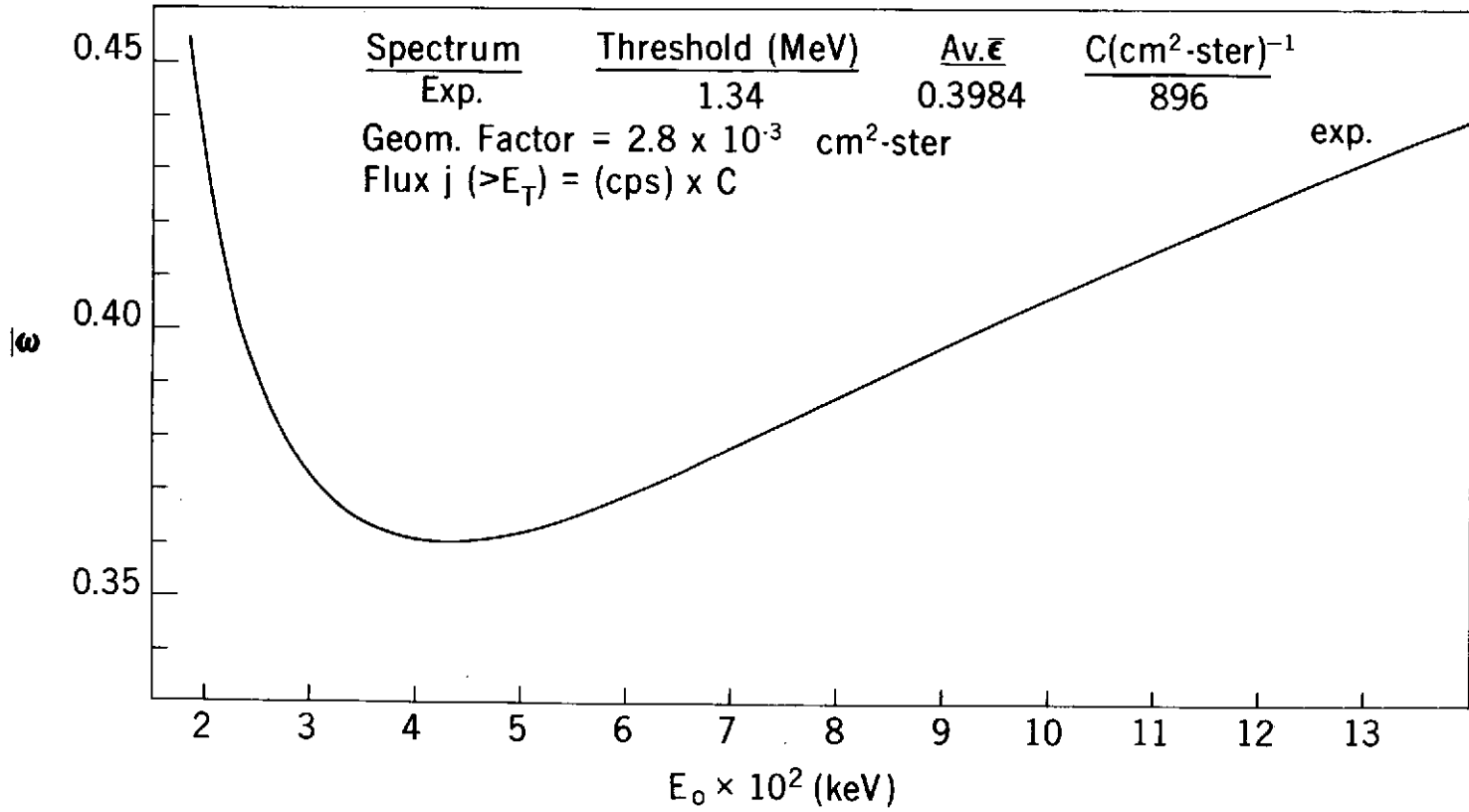


Figure 12. 1963-38C Calibration Curves

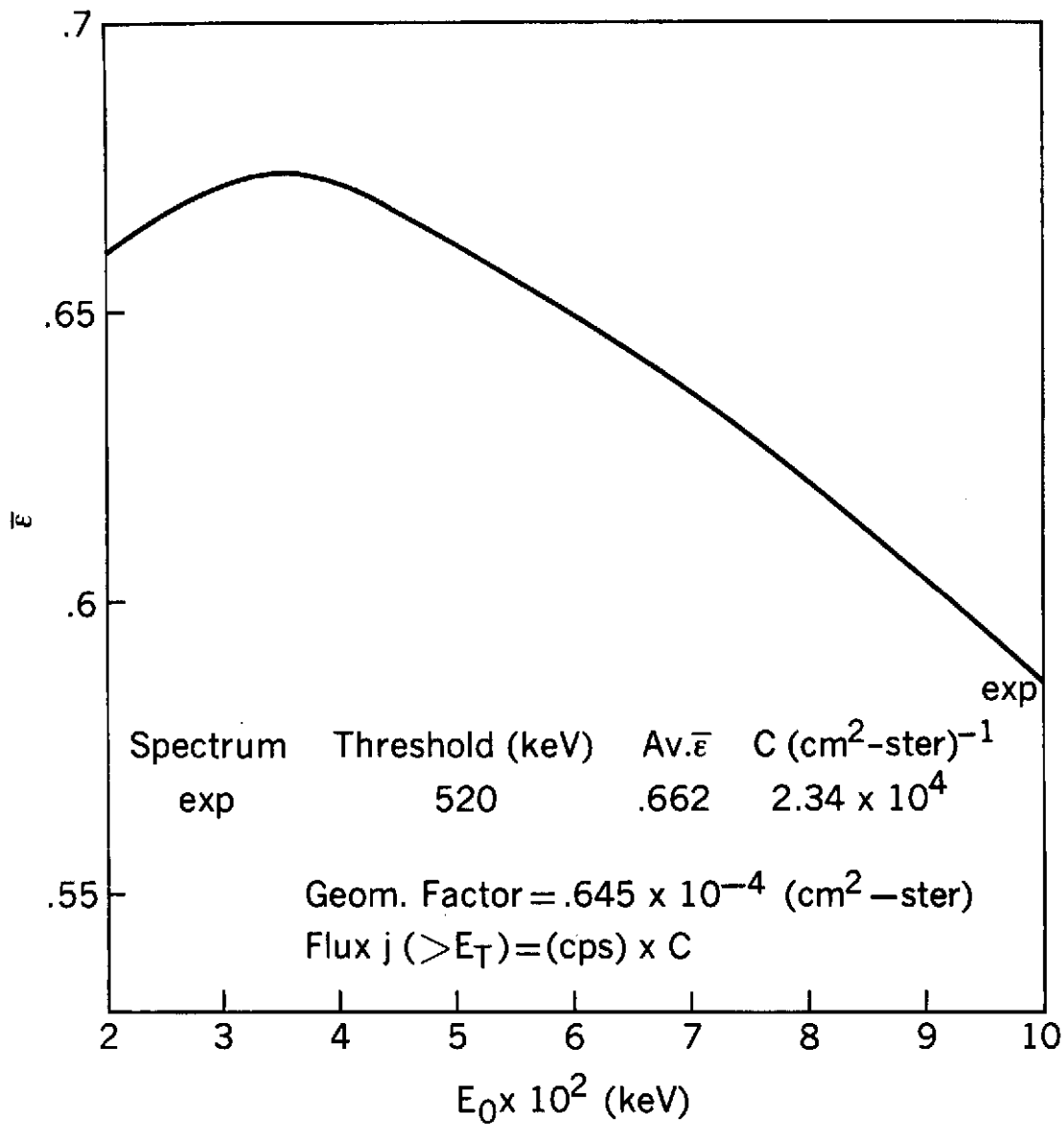


Figure 13. Explorer 26 Calibration Curves

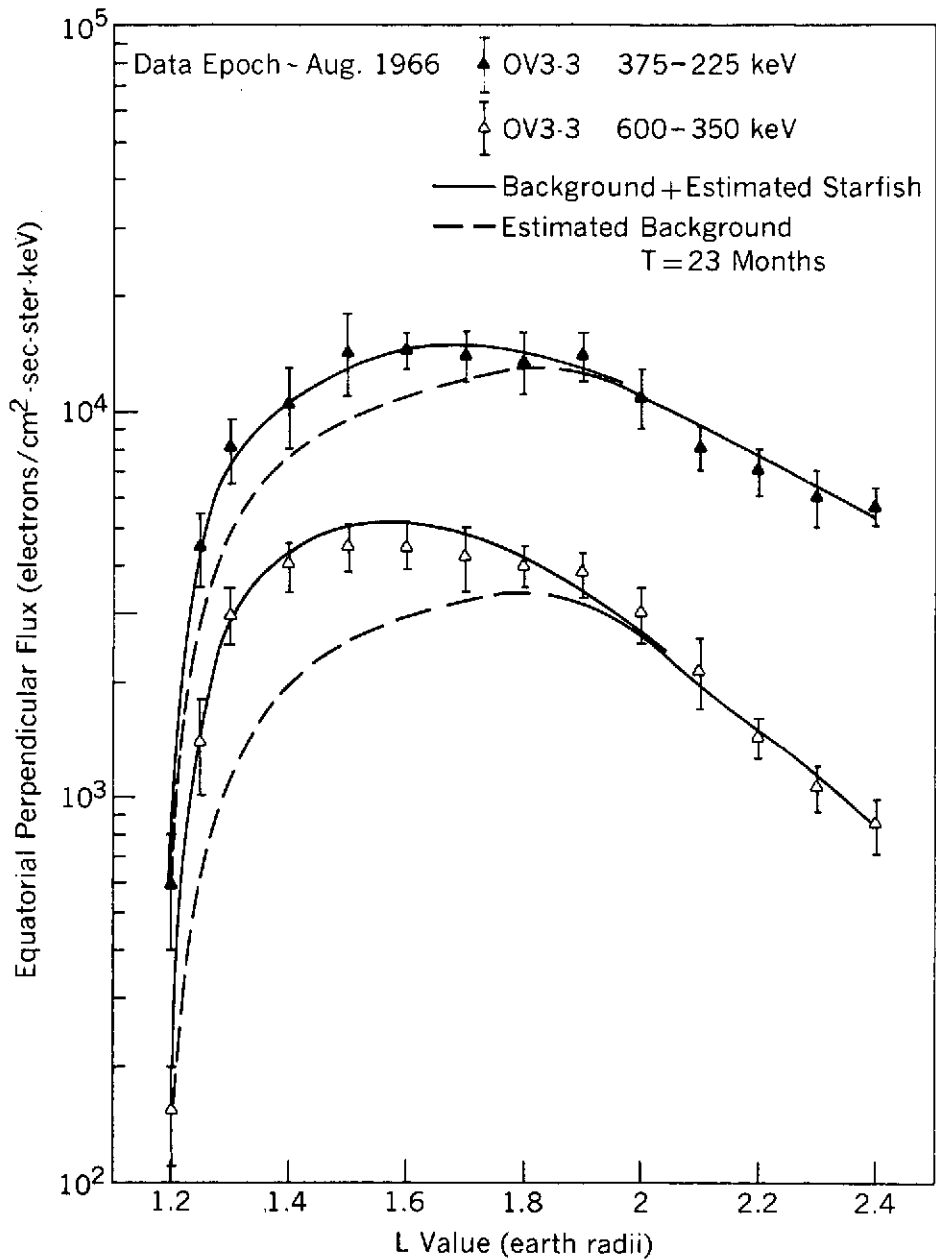


Figure 14. Data and Model Plots

The radial profile given by the OV3-3 data in August 1966 is compared with the analytical quiet day flux description given in Section 2 (broken line). A residual Starfish flux is observed for  $L \leq 1.8$  at this epoch, and the Starfish model (Section 6B) is used to estimate the total flux in August 1966 (solid line).

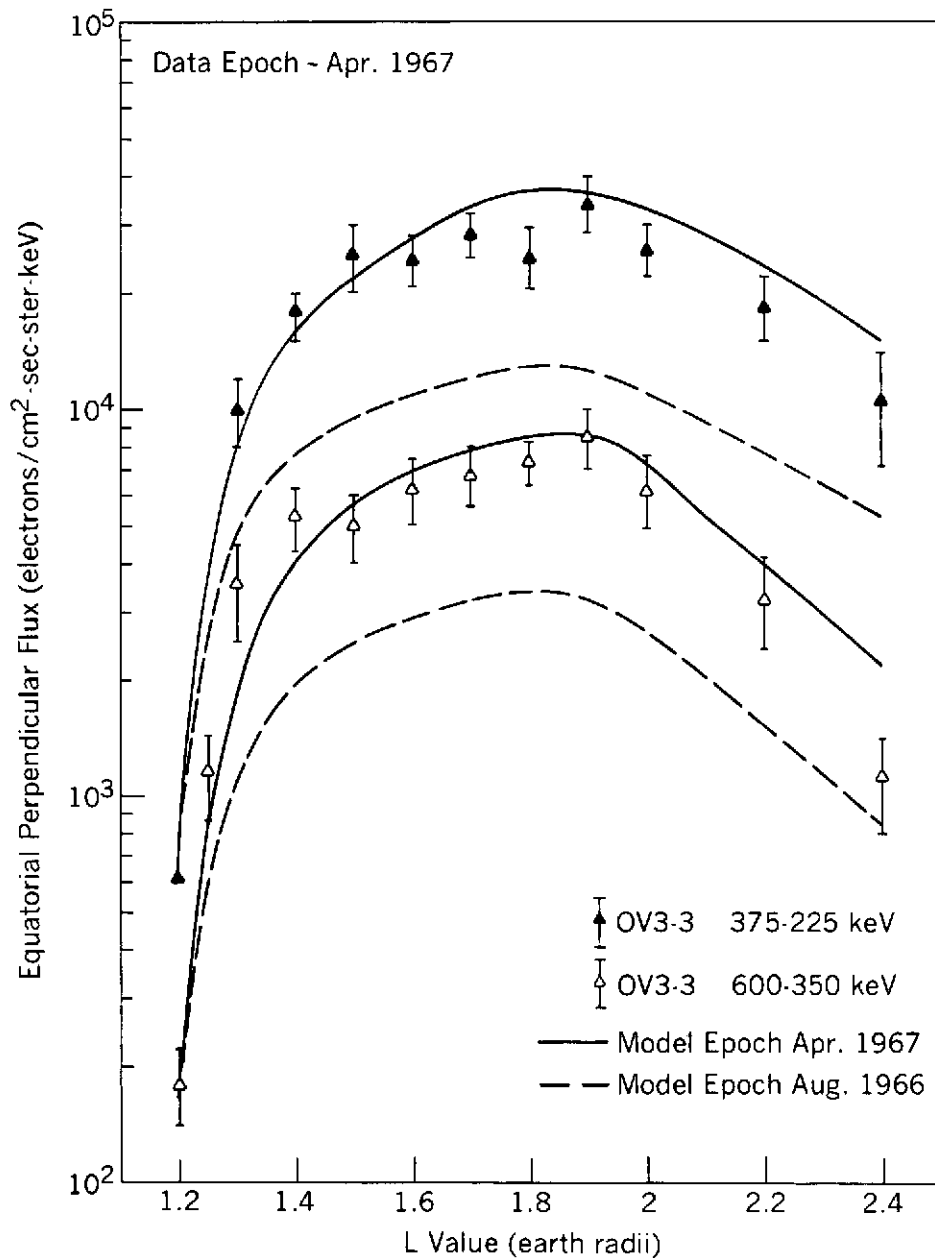


Figure 15. Data and Model Plots

The radial profile given by the OV3-3 data for epoch April 1967 approximately is compared with the analytical quiet day flux description given in Section 2 (the solid line). The broken line represents the quiet day flux for epoch August 1966.

Figures 16-57. These computer-generated plots compare the present inner zone electron model with the OGO 1, OGO 3, and 1963-38C data. The OGO data are presented at a variety of epochs to demonstrate solar cycle effects. Each model epoch is identified by a value of T measured in months from solar minimum taken as September 1964. T = 37 corresponds to the model epoch of October 1967. The ordinate scale on each plot is arbitrary counts/sec, and the conversion factors for flux are presented in Table 3. The OGO data are monthly averaged values from the time periods indicated in the legends. A consistent set of symbols is used:

- Δ September to November 1967 (T = 37 approx.)
- April to May 1967 (T = 31 approx.)
- \* December 1966 to January 1967 (T = 27 approx.)
- + June 1966 to July 1966 (T = 22 approx.)
- ⊗ September 1965 (T = 12 approx.)
- September 1964 to March 1965 (T = 6 approx.)

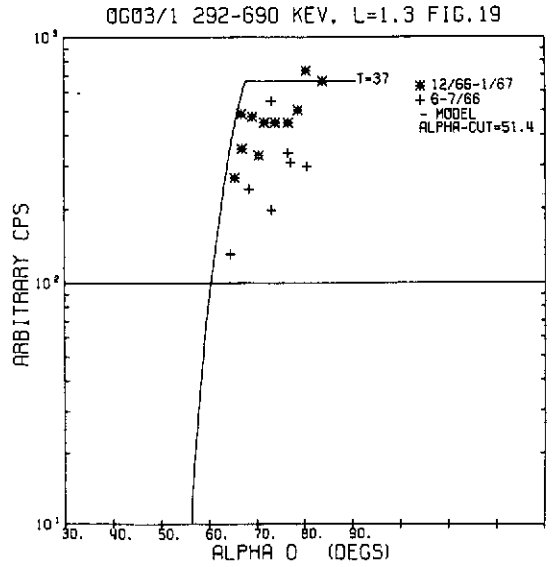
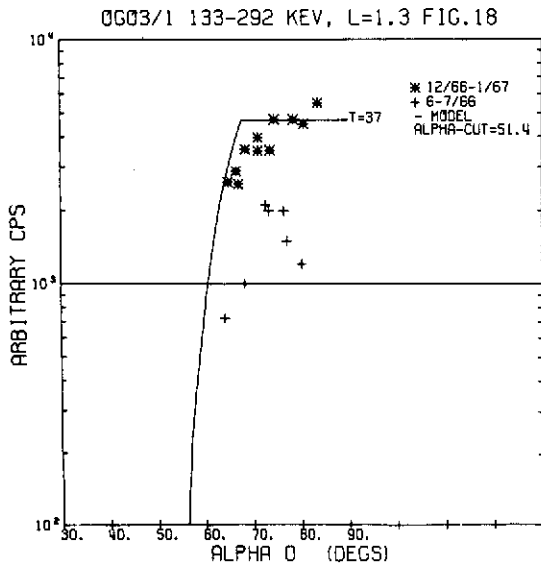
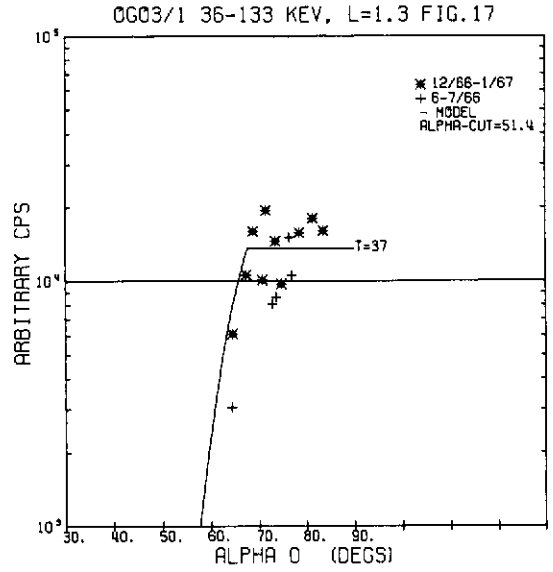
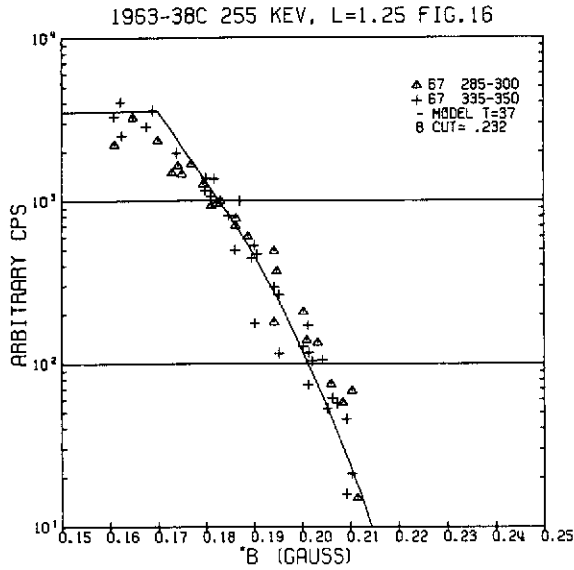
For the lower L values and for the 292- to 690-keV data, the estimated quiet day flux after removal of the Starfish residual flux is shown for T = 22 labeled as "T = 22 EST BACK." The determination of the solar effects and Starfish residual fluxes is discussed in Sections 6A and 6B, respectively. On each OGO plot the atmospheric cutoff equatorial pitch angle is given in degrees (Section 2).

Data from the 1963-38C satellite are normalized to an epoch of late 1967 (T = 37 approx.). The legend indicates the time period of the actual measurements as year and day range in that year. A consistent set of symbols is used:

- + 1967 Day 335-350
- Δ 1967 Day 285-300
- 1966 Day 315-330

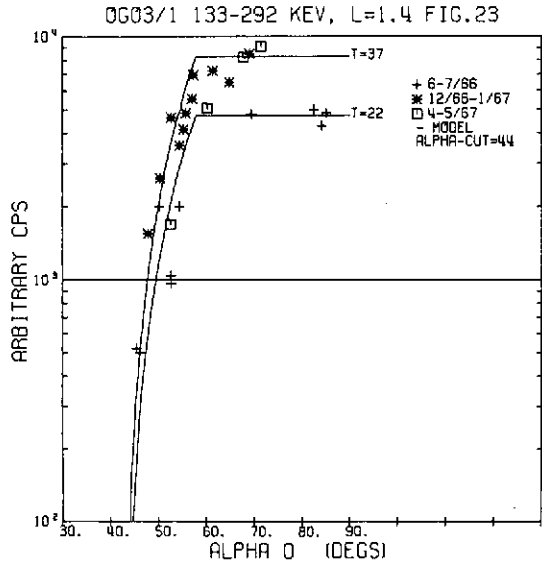
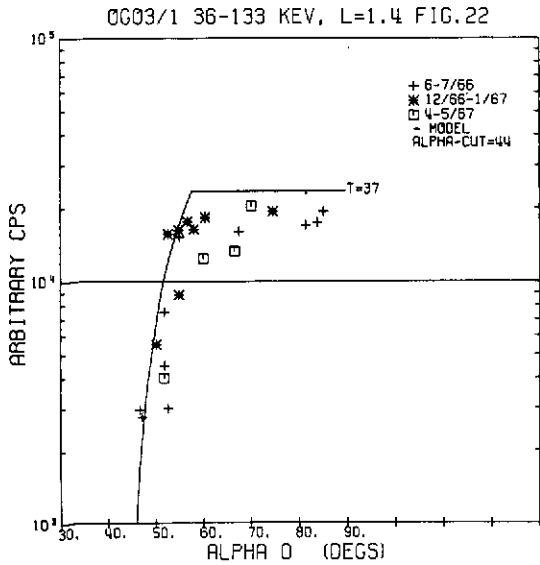
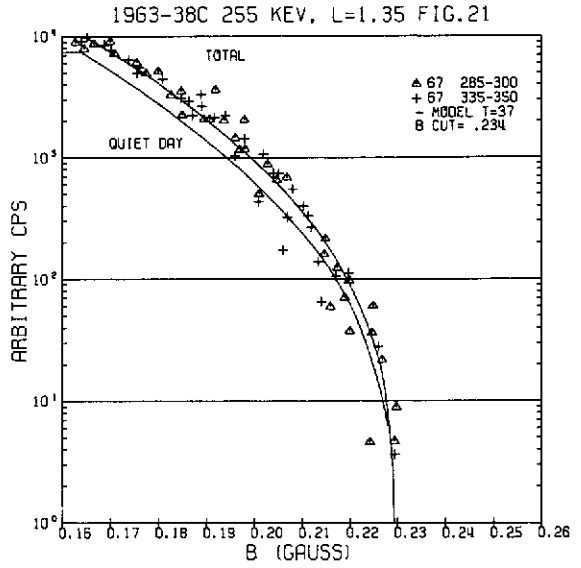
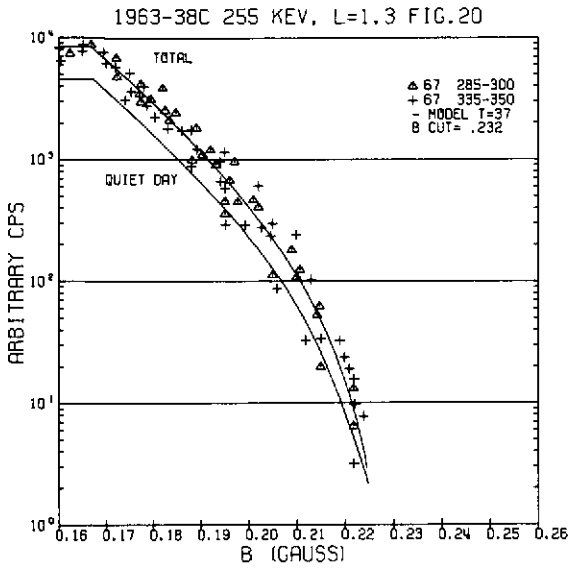
For  $1.3 \leq L/(\text{earth radii}) \leq 1.4$ , "TOTAL" and "QUIET DAY" model lines are shown for T = 37. The differences arise because of the hardening of the spectrum at low L values for  $E > 690$  keV (Section 5A). On each 1963-38C plot, the atmospheric cutoff B value is given in gauss.

ARBITRARY COUNT RATE, FIGURES 16 - 19

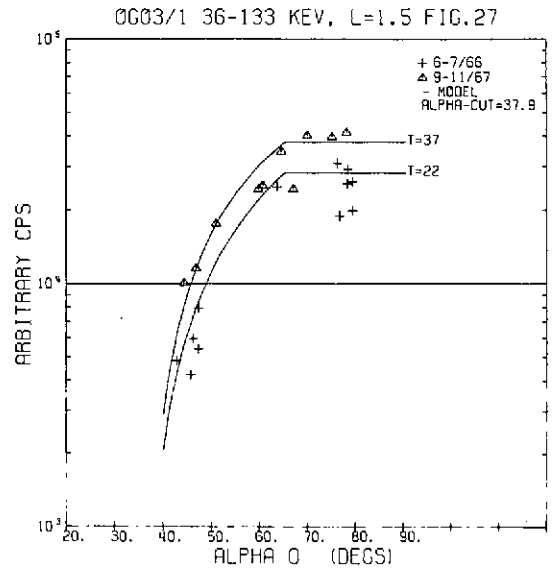
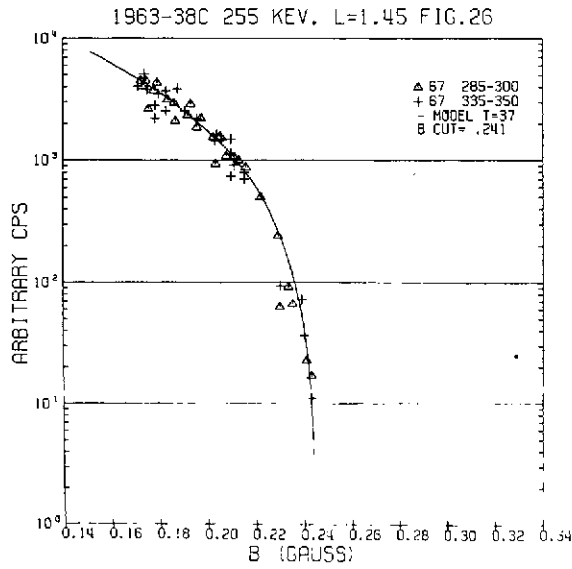
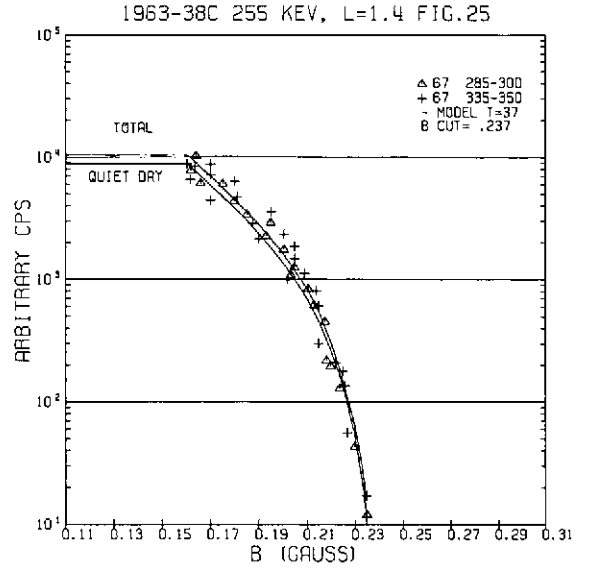
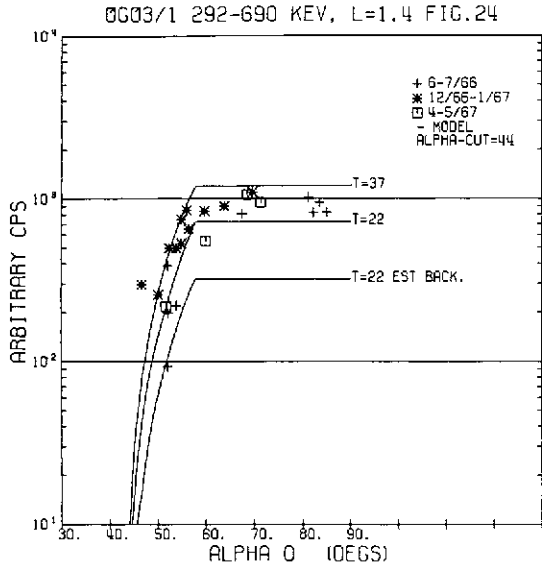


C-2

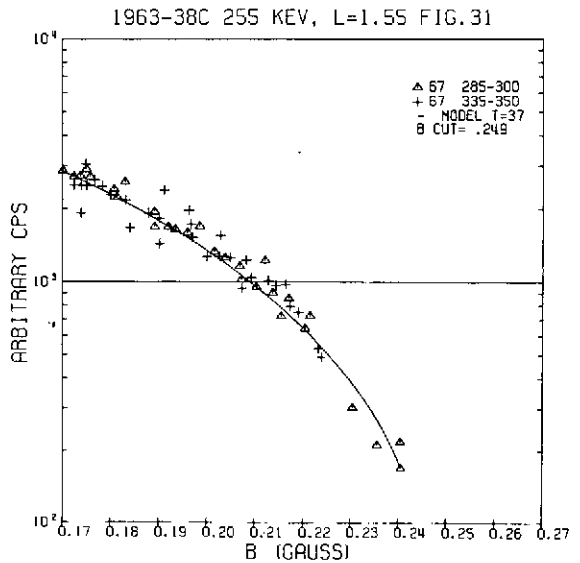
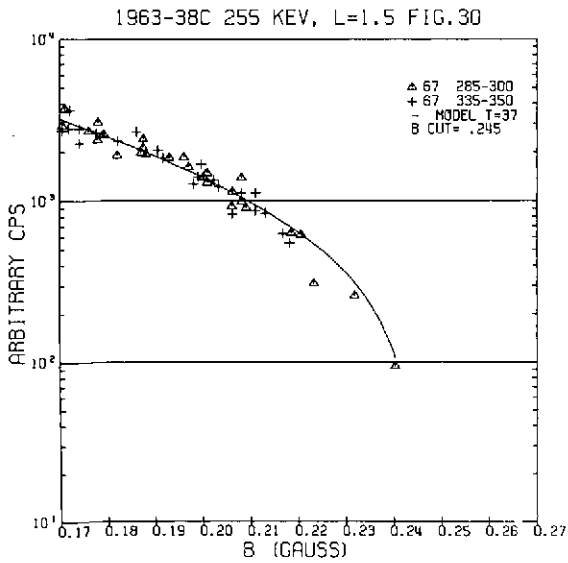
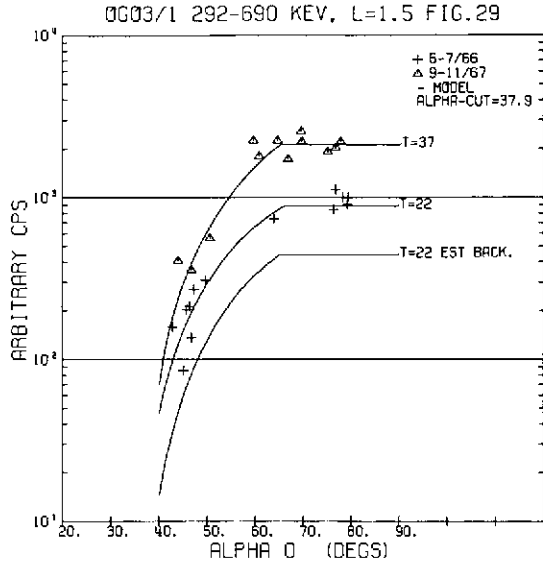
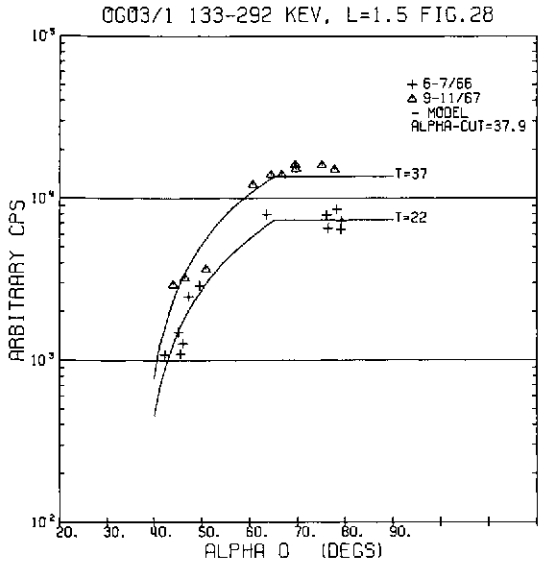
ARBITRARY COUNT RATE, FIGURES 20 - 23



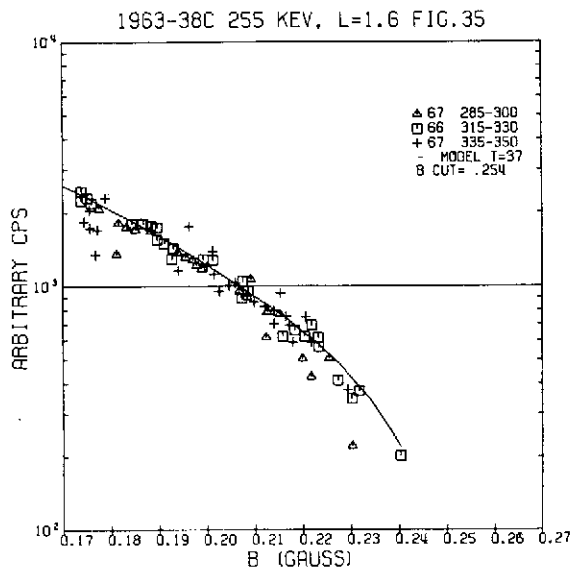
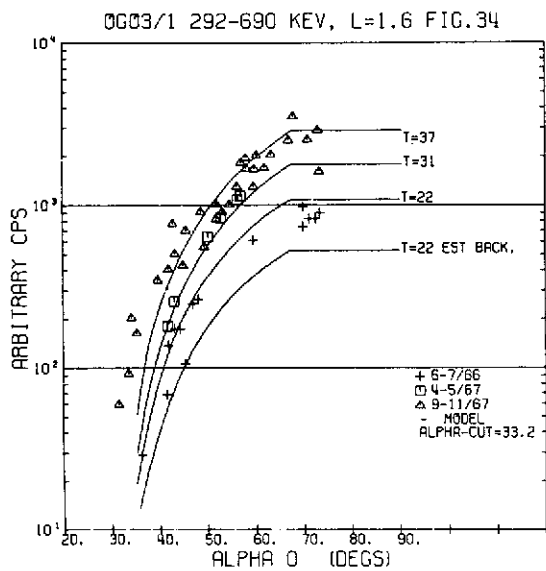
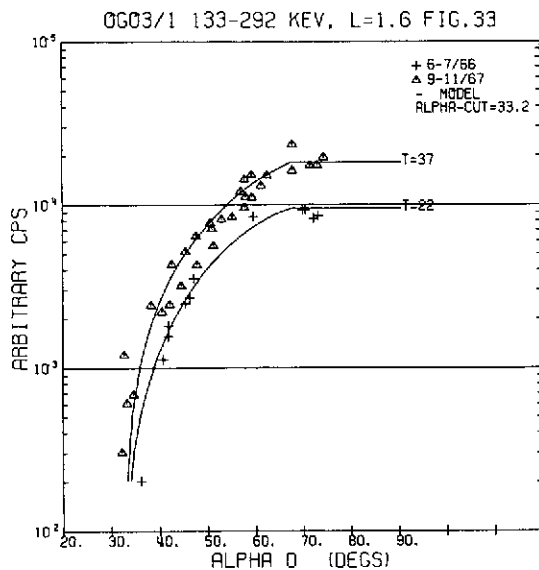
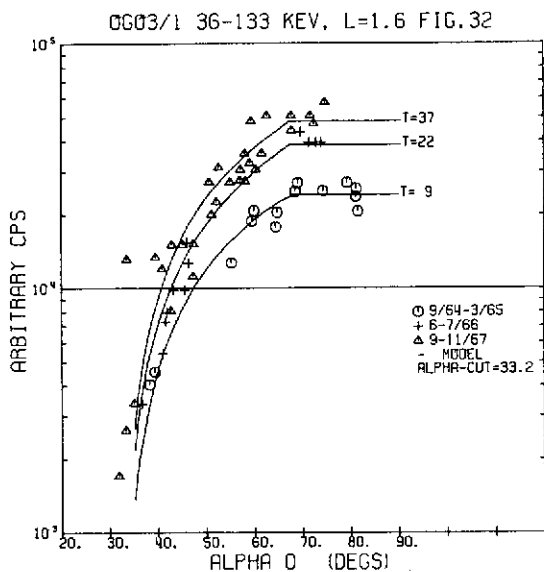
ARBITRARY COUNT RATE, FIGURES 24 - 27



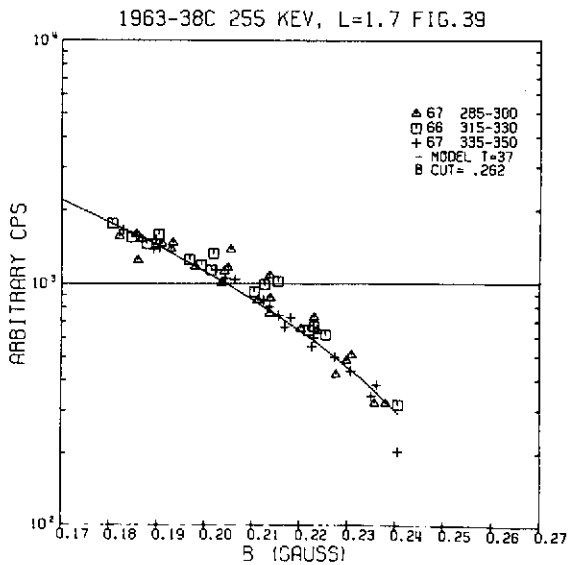
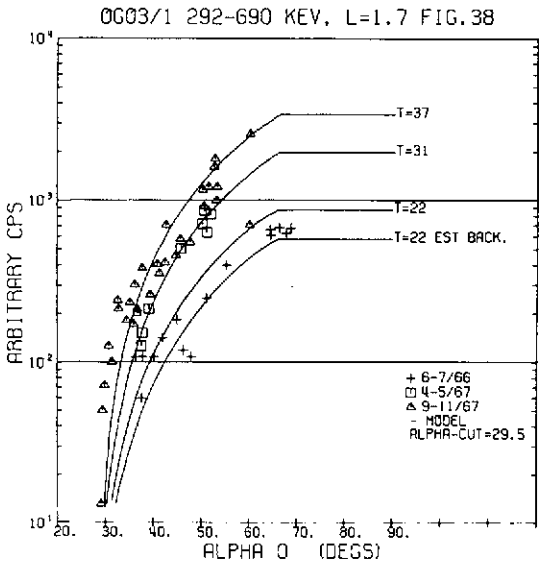
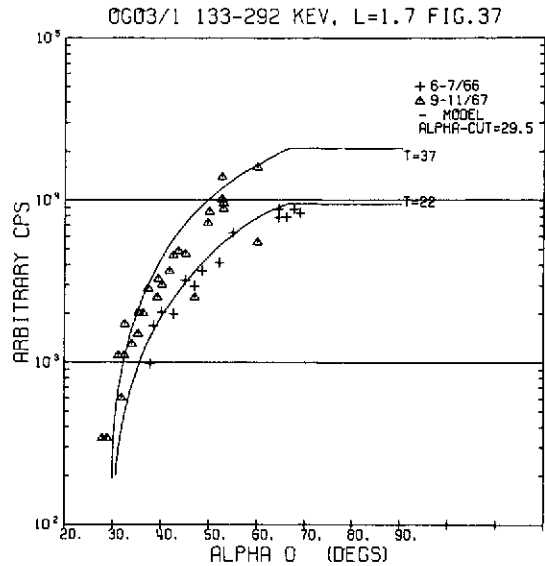
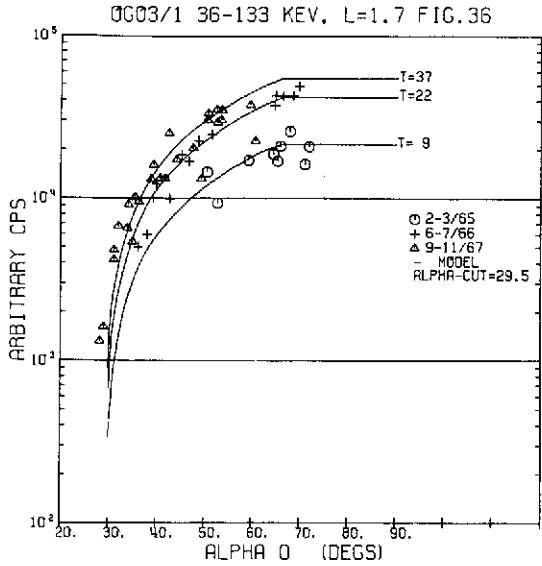
ARBITRARY COUNT RATE, FIGURES 28 - 31



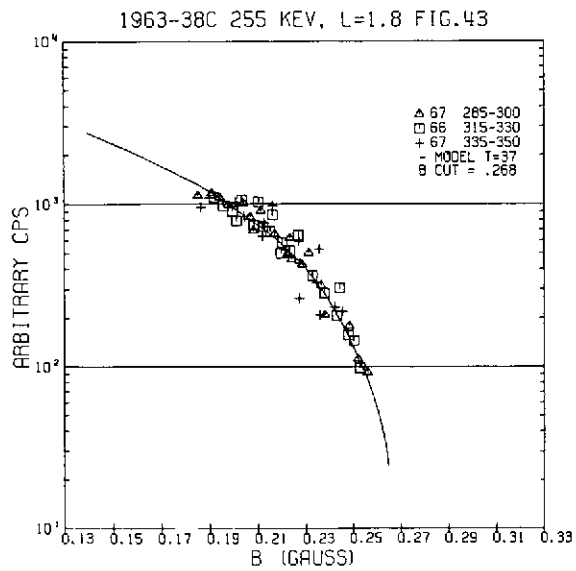
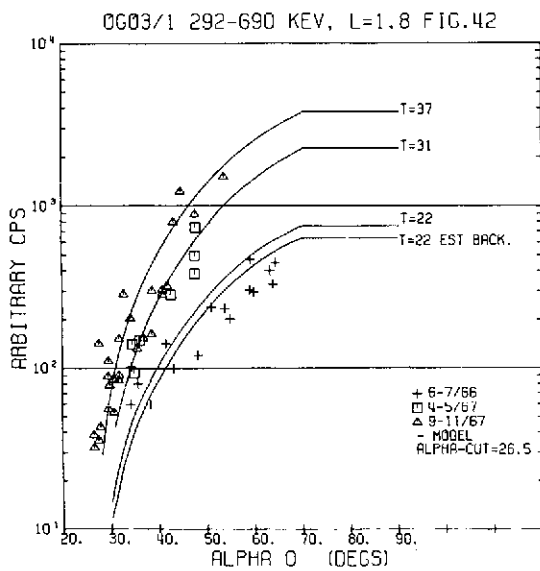
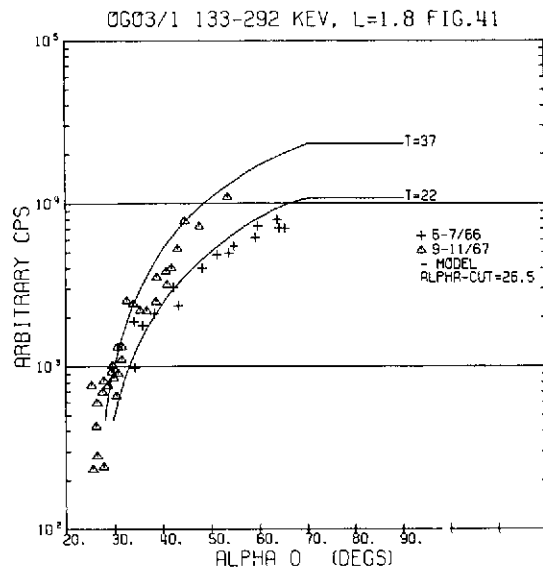
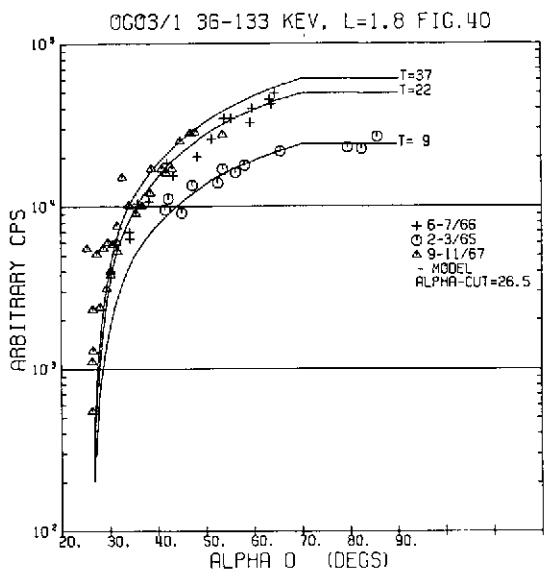
ARBITRARY COUNT RATE, FIGURES 32 - 35



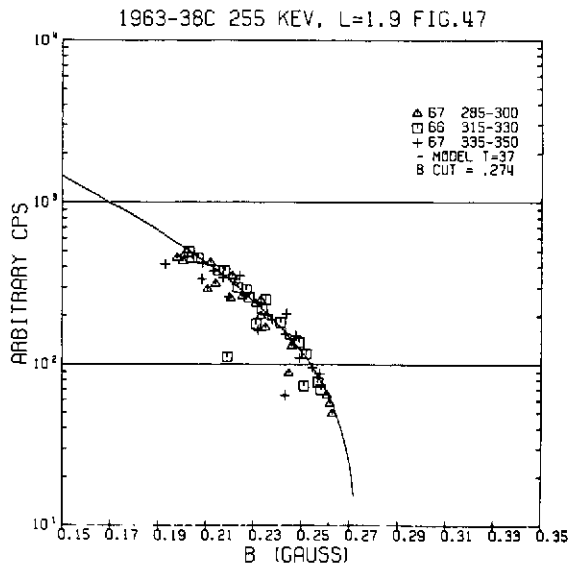
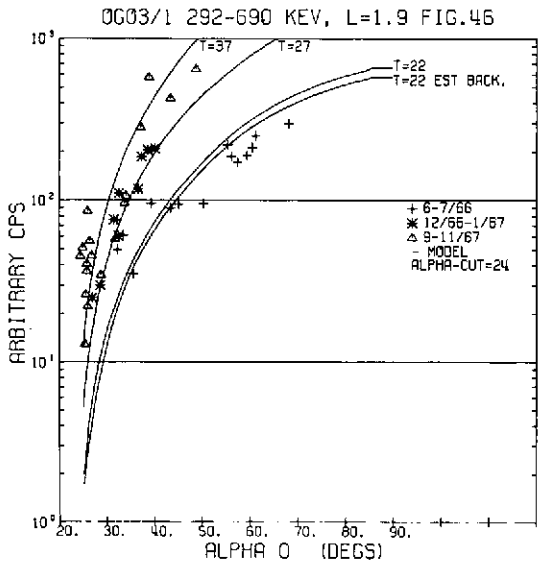
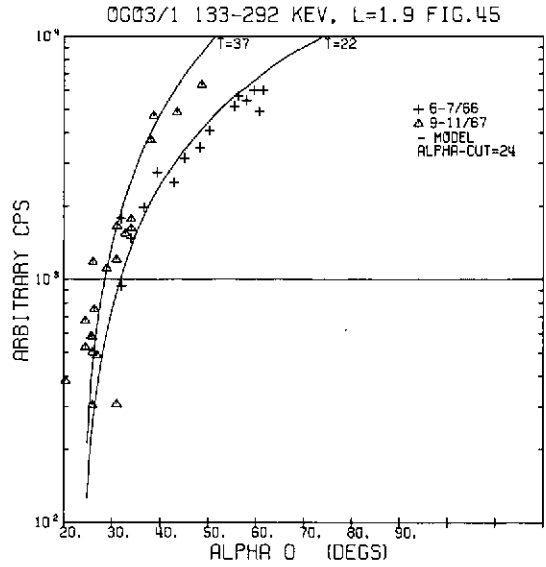
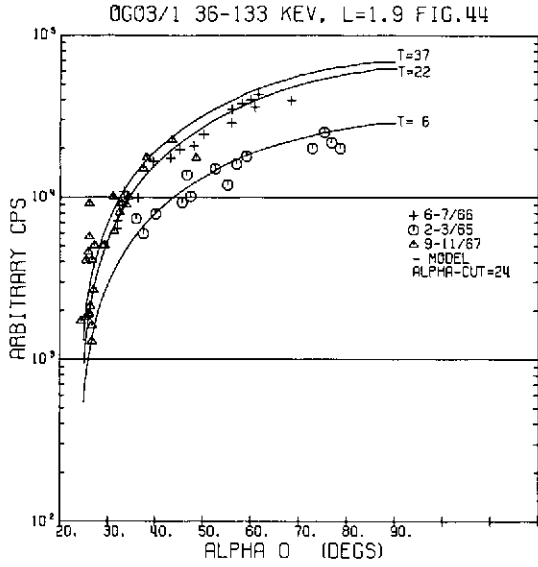
ARBITRARY COUNT RATE, FIGURES 36 - 39



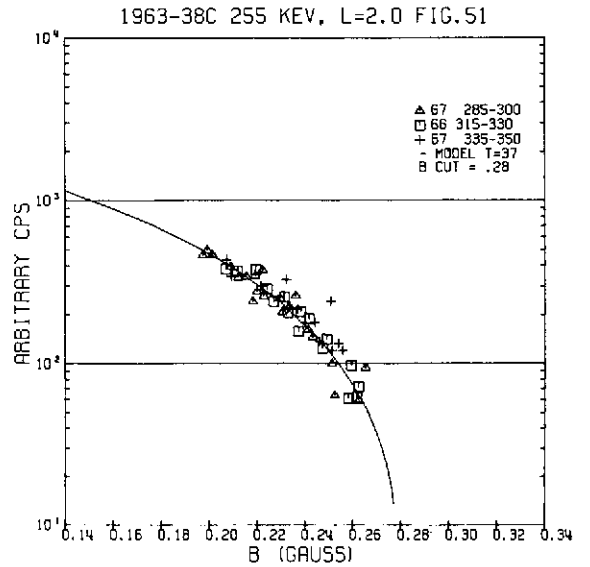
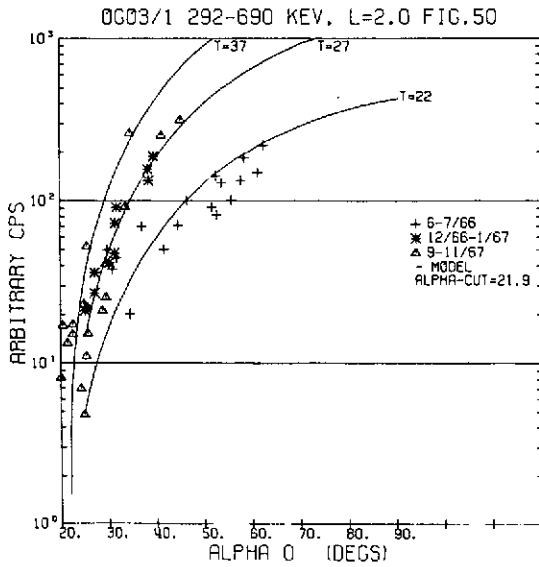
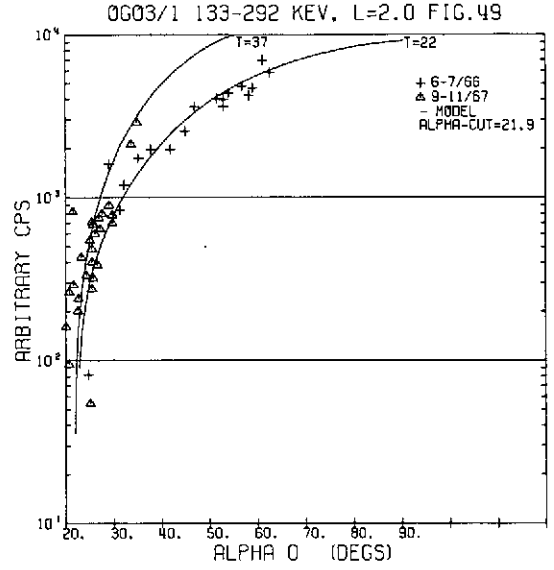
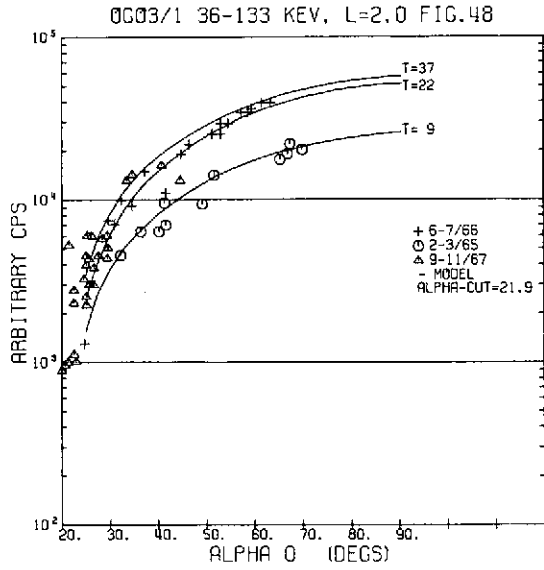
ARBITRARY COUNT RATE, FIGURES 40 - 43



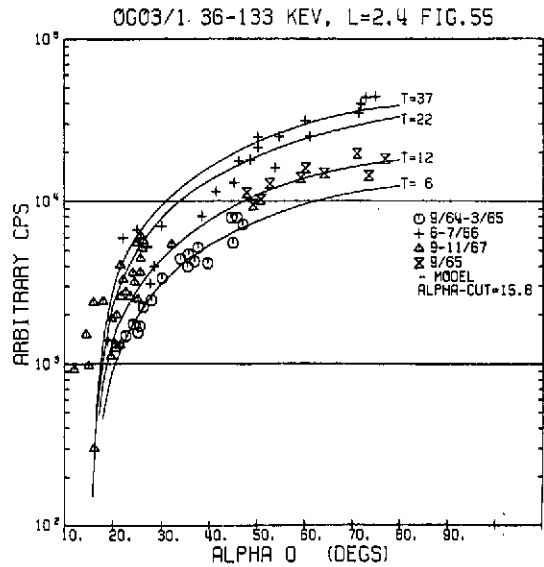
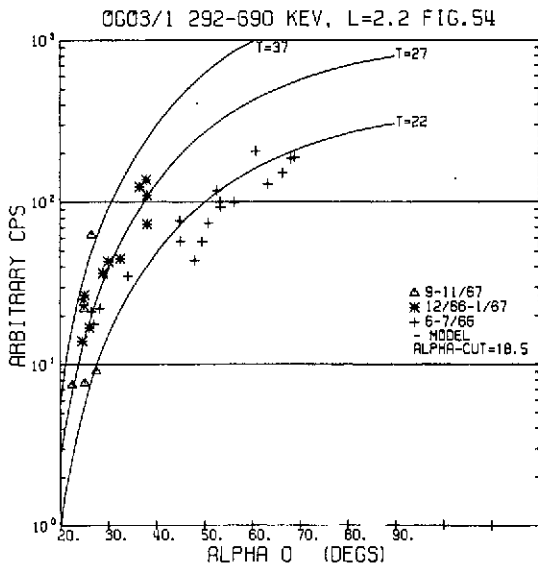
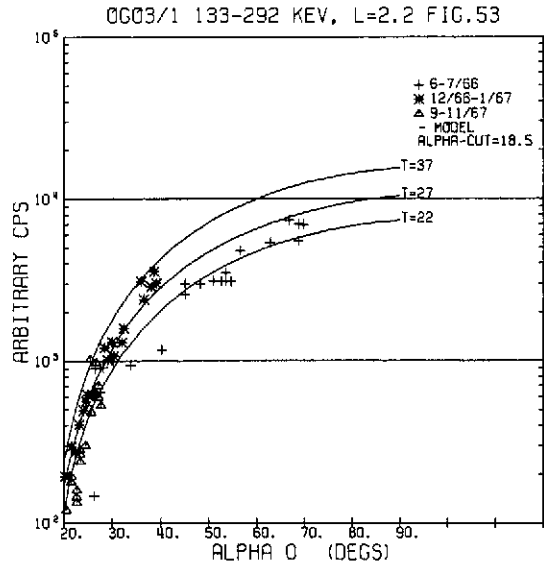
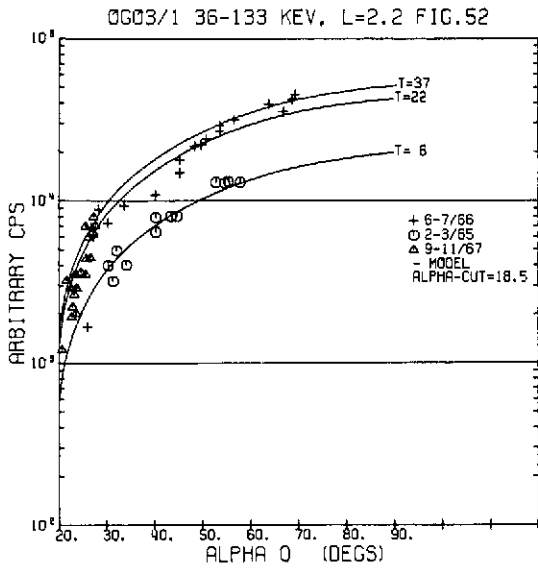
ARBITRARY COUNT RATE, FIGURES 44 - 47



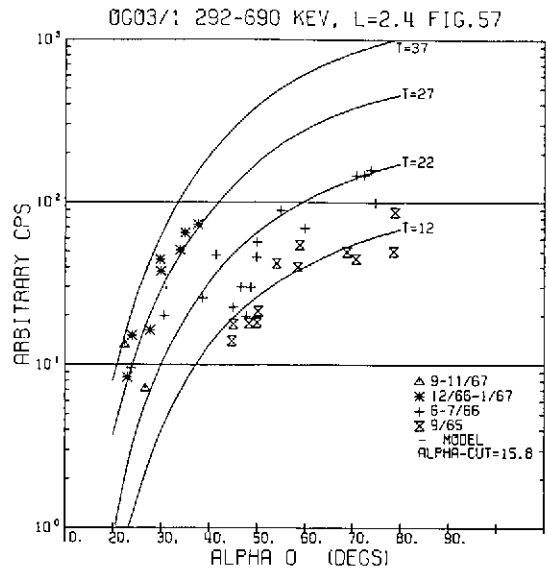
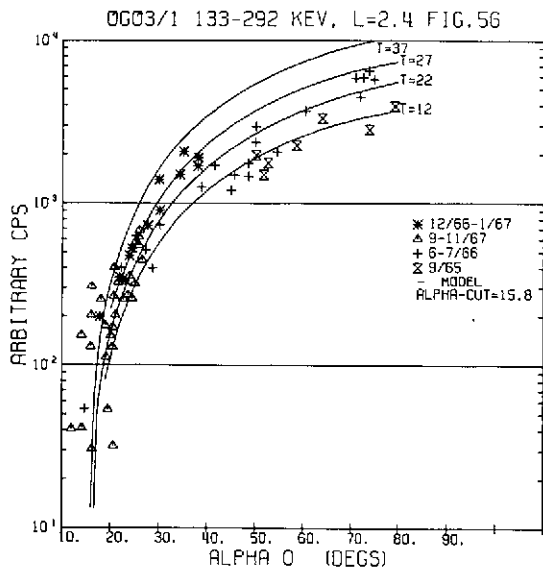
ARBITRARY COUNT RATE, FIGURES 48 - 51



ARBITRARY COUNT RATE, FIGURES 52 - 55



ARBITRARY COUNT RATE, FIGURES 56 - 57



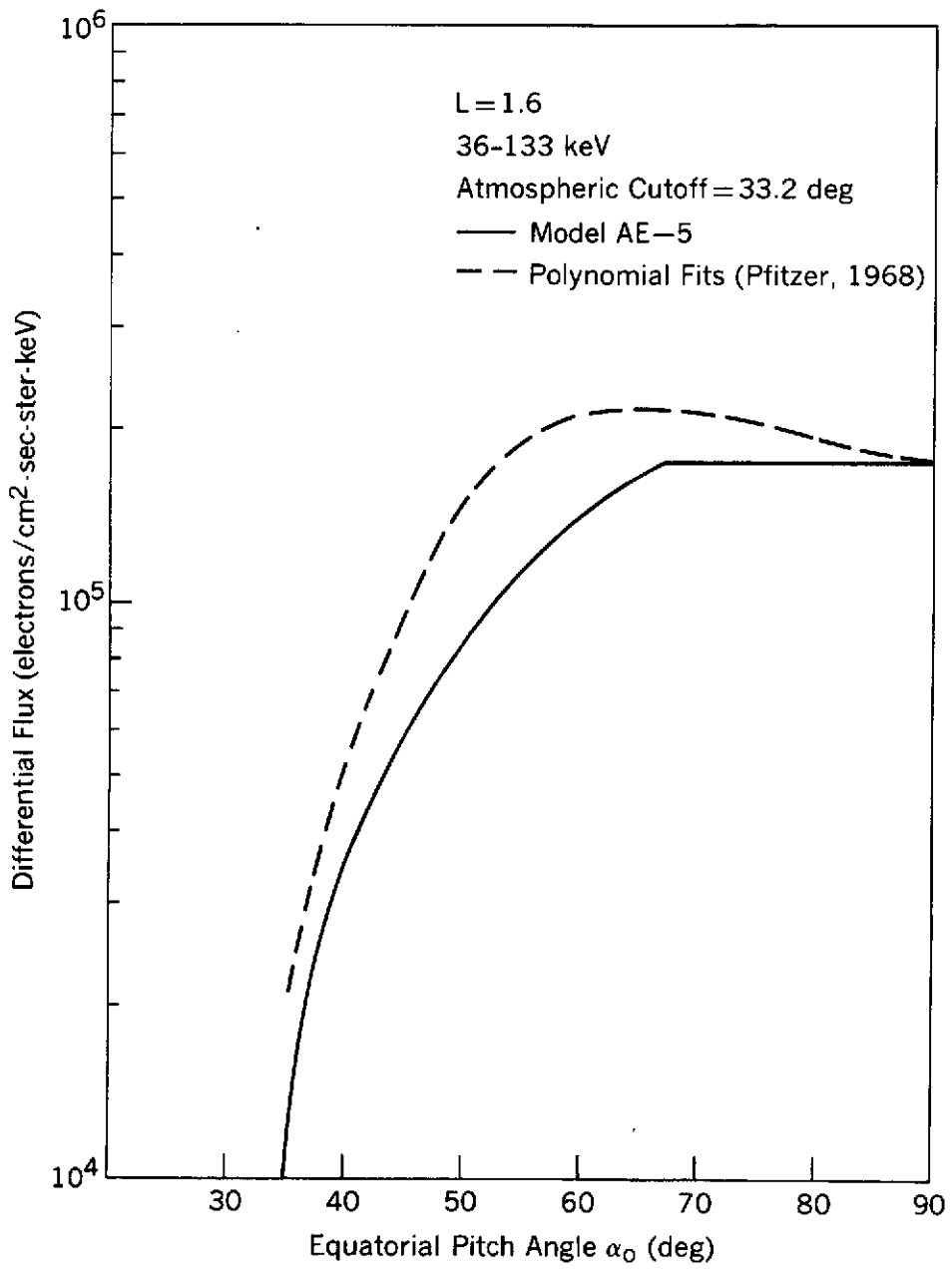


Figure 58. Pfitzer's Pitch Angle Distributions

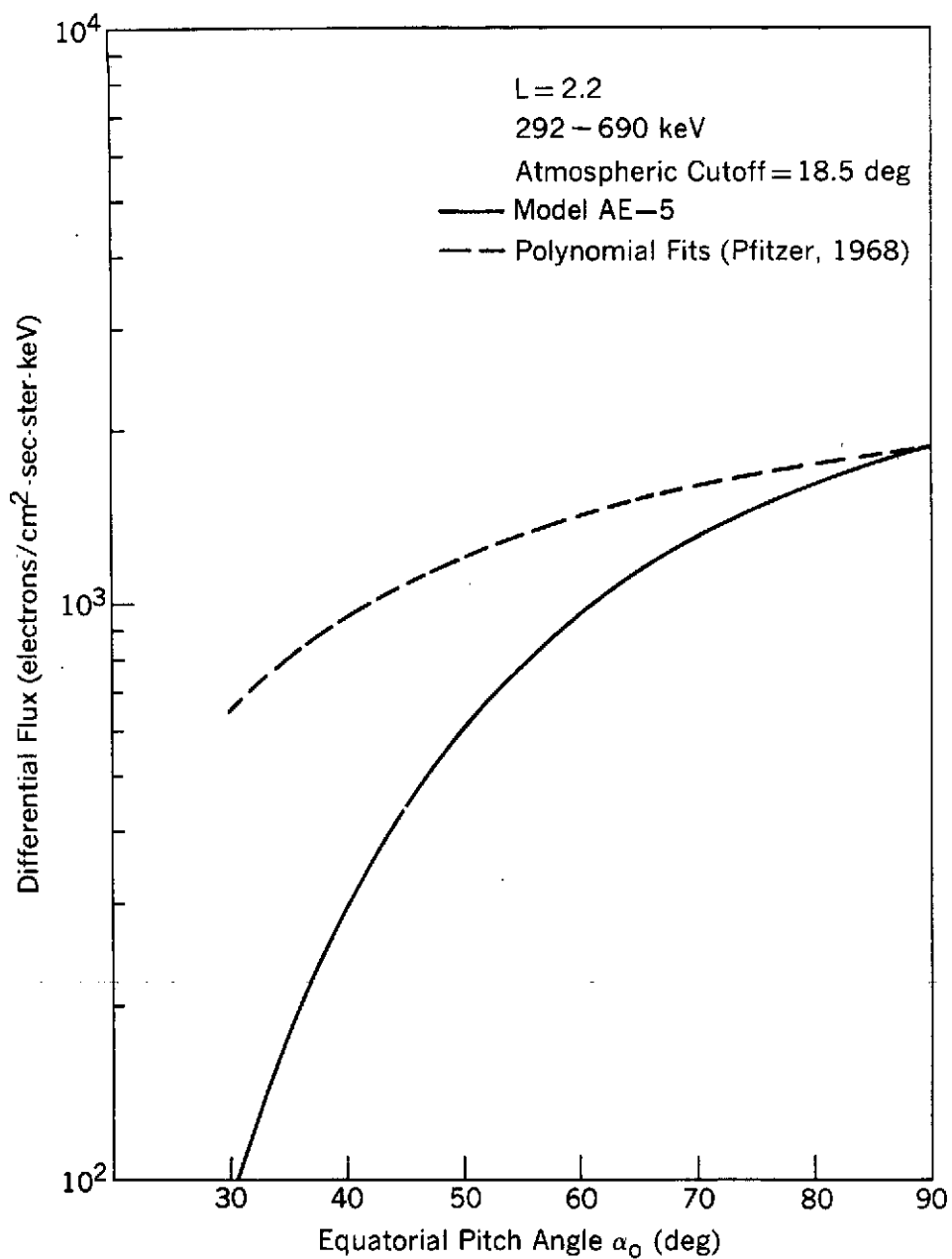


Figure 59. Pfitzer's Pitch Angle Distributions

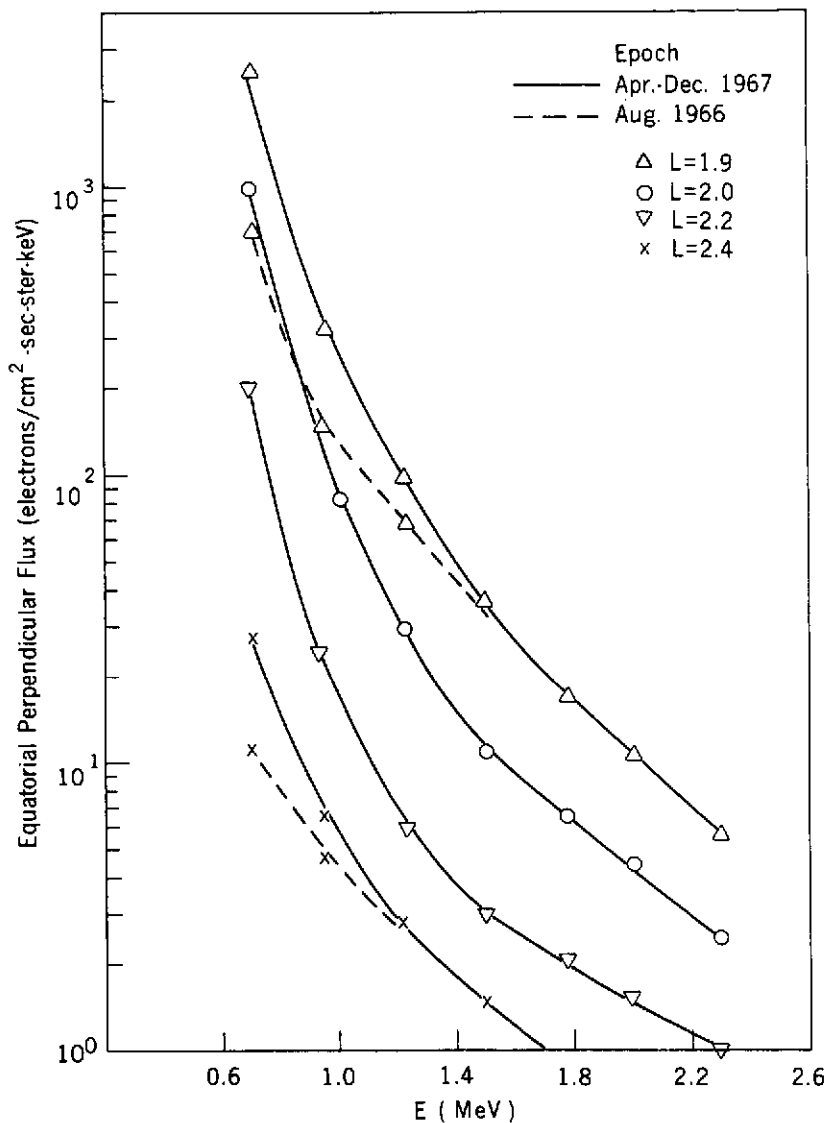


Figure 60. Quiet Day High-Energy Equatorial Perpendicular Flux

The OV3-3 quiet day differential spectra are shown for high L values. An increase in flux is observed at the lower energies from the earlier (broken line) to the later epoch (solid line) for L = 1.9 and 2.4. A similar effect (not shown) is observed at L = 2 and 2.2.

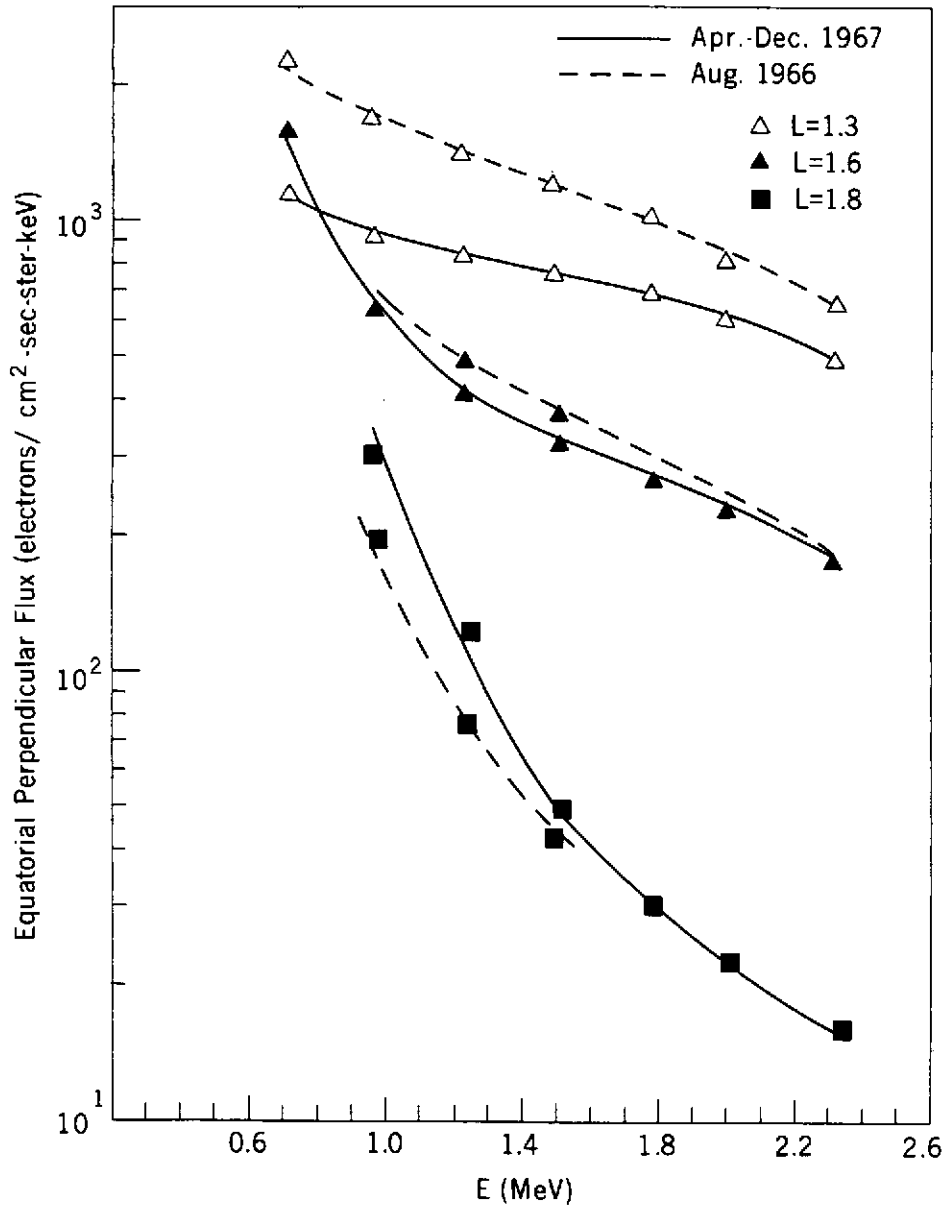


Figure 61. Quiet Day High-Energy Equatorial Perpendicular Flux

The OV3-3 quiet day differential spectra are shown for selected L values below 1.9 for two epochs. At L = 1.3 Starfish decay is observed, while at L = 1.8 an increase in the flux with time is observed, thus indicating solar cycle effect.

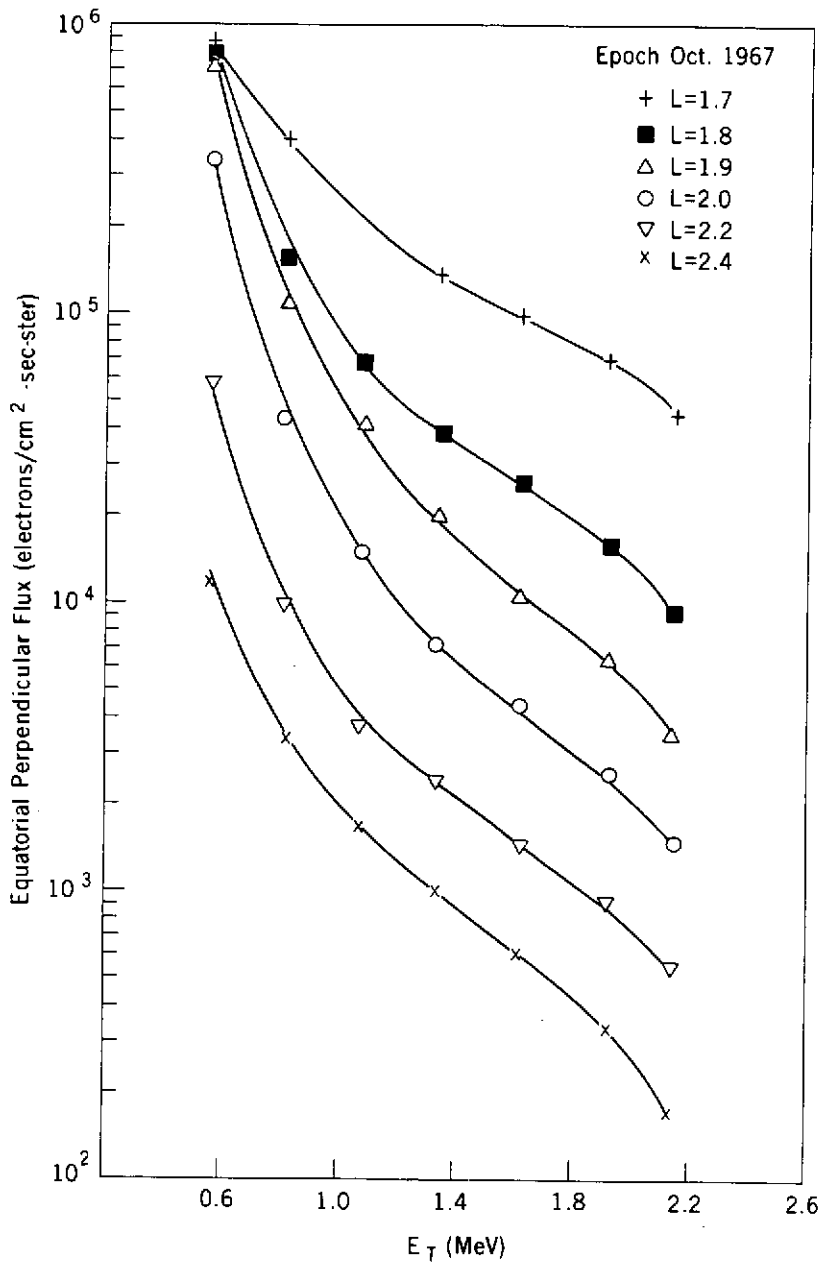


Figure 62. High-Energy Quiet Day Integral Spectra

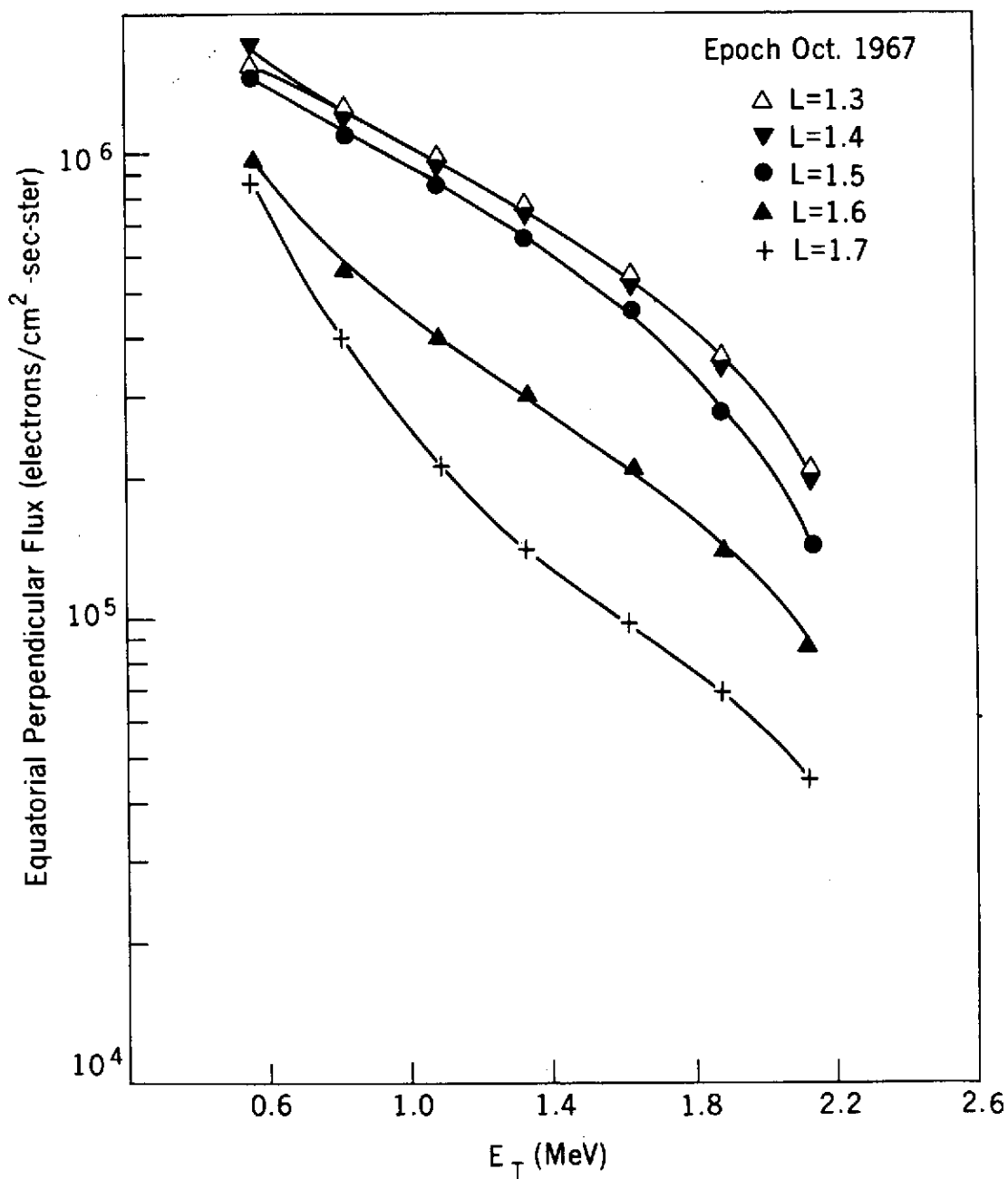
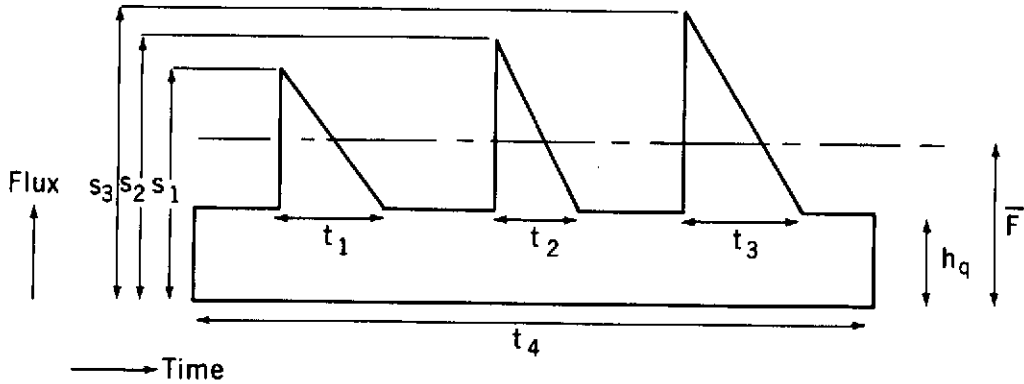


Figure 63. High-Energy Quiet Day Integral Spectra



Average Storm Flux,  $\bar{F}$  :

$$\bar{F} = h_q \left[ 1 - \frac{1}{2} \left( \frac{t_1 + t_2 + t_3}{t_4} \right) \right] + \frac{1}{2} (s_1 t_1 + s_2 t_2 + s_3 t_3) / t_4$$

Probability of flux being greater than  $s$ ,  $P(s)$ :

$$\begin{aligned}
 P(s) &= \left[ \left( \frac{s_1 - s}{s_1 - h_q} \right) \frac{t_1}{t_4} + \left( \frac{s_2 - s}{s_2 - h_q} \right) \frac{t_2}{t_4} + \left( \frac{s_3 - s}{s_3 - h_q} \right) \frac{t_3}{t_4} \right] \times 100\% \text{ for } s_1 \geq s \geq h_q \\
 &= \left[ \left( \frac{s_2 - s}{s_2 - h_q} \right) \frac{t_2}{t_4} + \left( \frac{s_3 - s}{s_3 - h_q} \right) \frac{t_3}{t_4} \right] \times 100\% \text{ for } s_2 \geq s > s_1 \\
 &= \left( \frac{s_3 - s}{s_3 - h_q} \right) \frac{t_3}{t_4} \times 100\% \text{ for } s_3 \geq s > s_2
 \end{aligned}$$

Figure 64. Storm Model

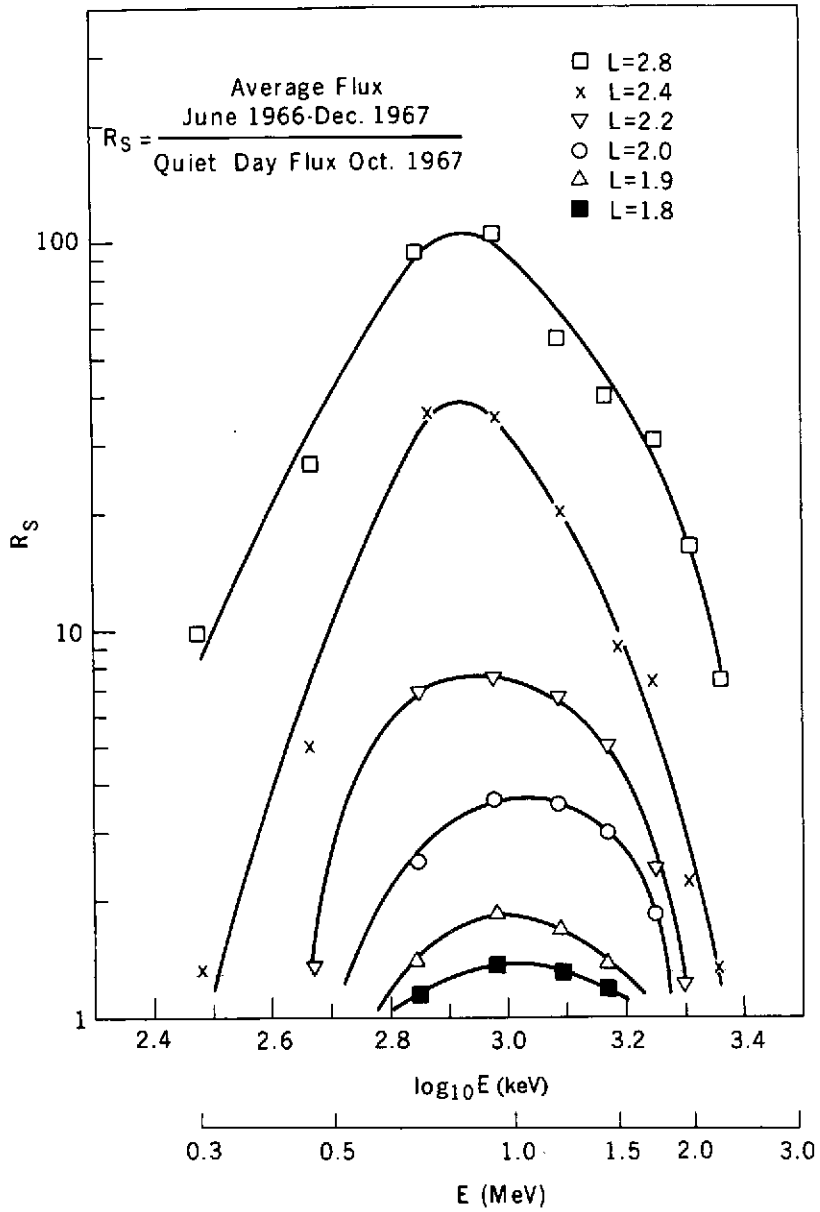


Figure 65. Storm Flux Ratio  $R_S$

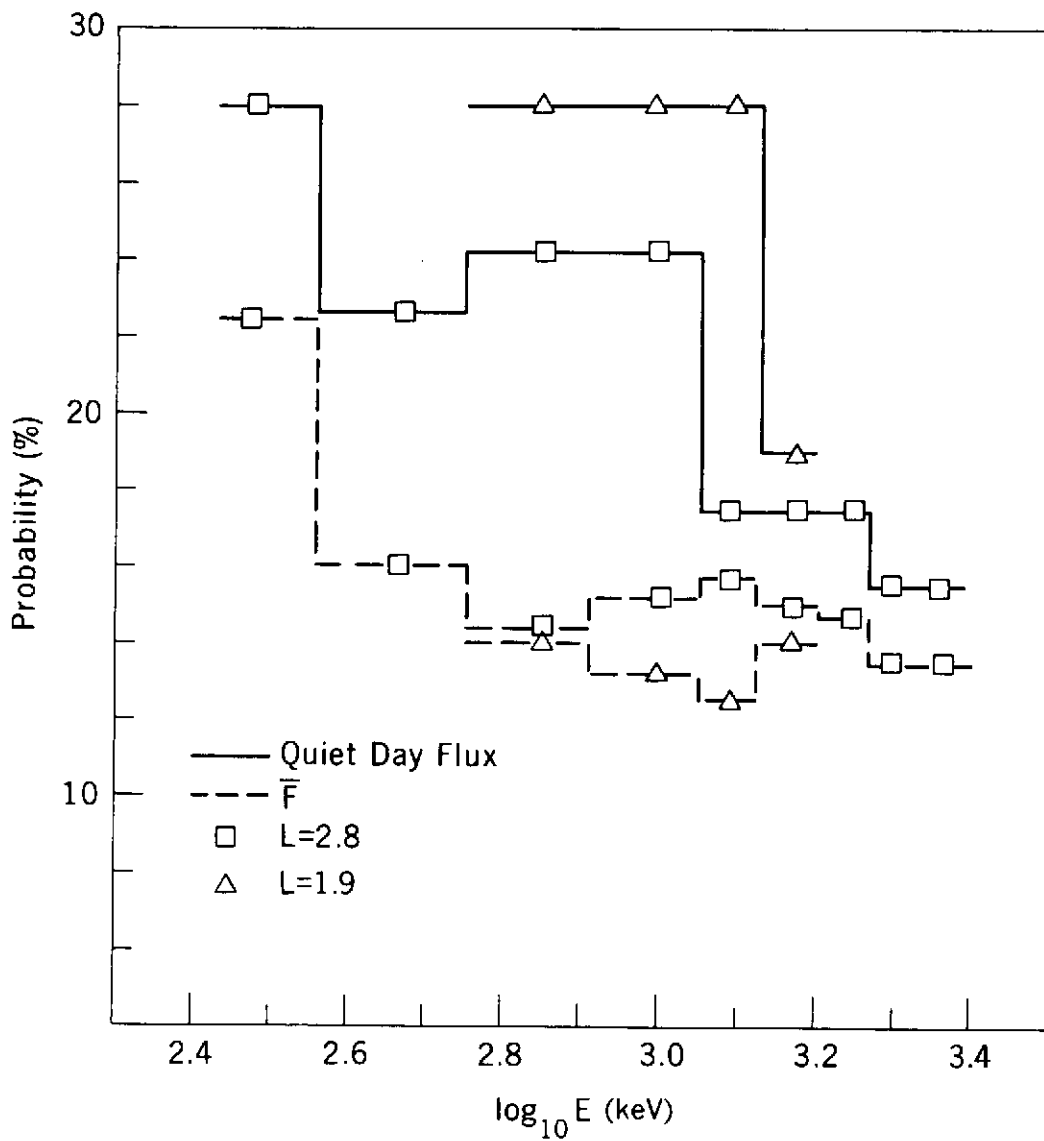


Figure 66. Probability of Storm Flux Contribution

The probability of the flux being greater than the quiet day value (solid line) or the averaged storm time value (broken line) is shown for  $L = 1.9$  and  $L = 2.8$ .

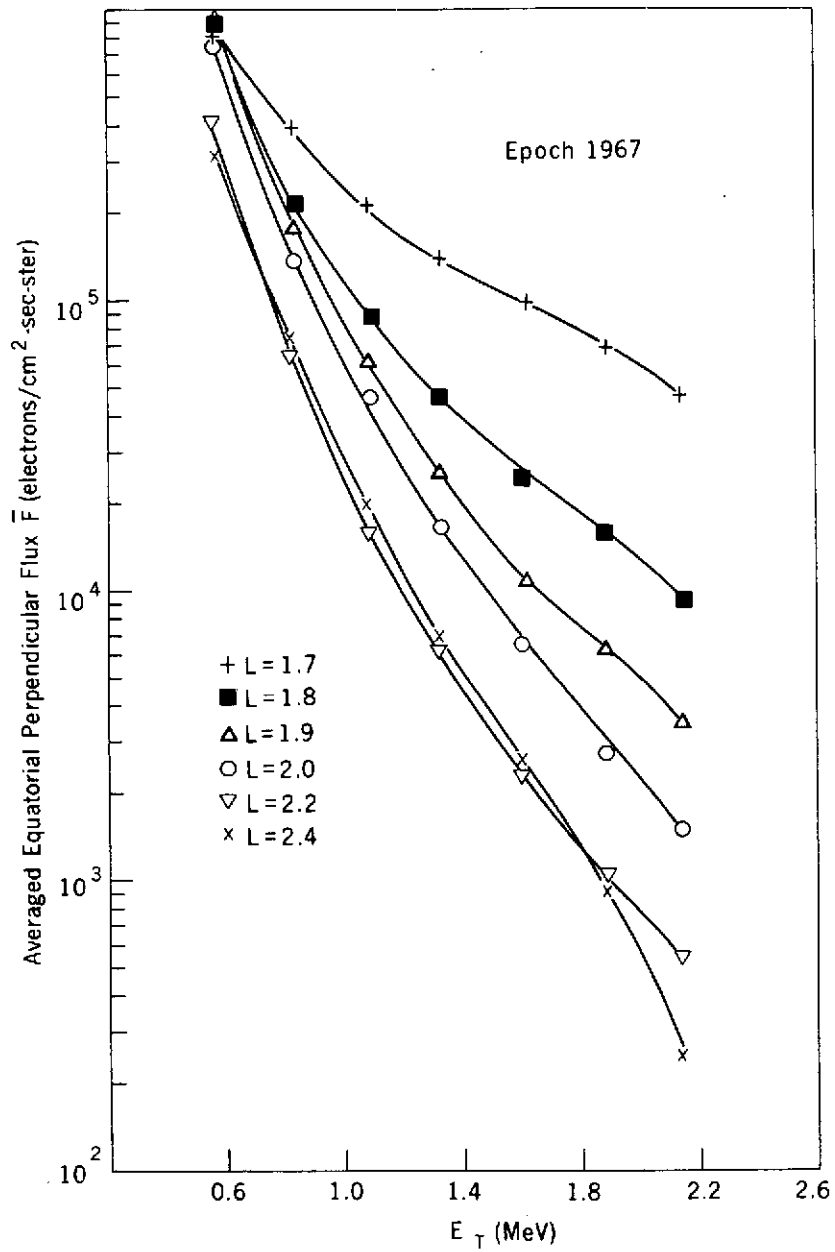


Figure 67. Average Storm High-Energy Spectra  $L \geq 1.7$

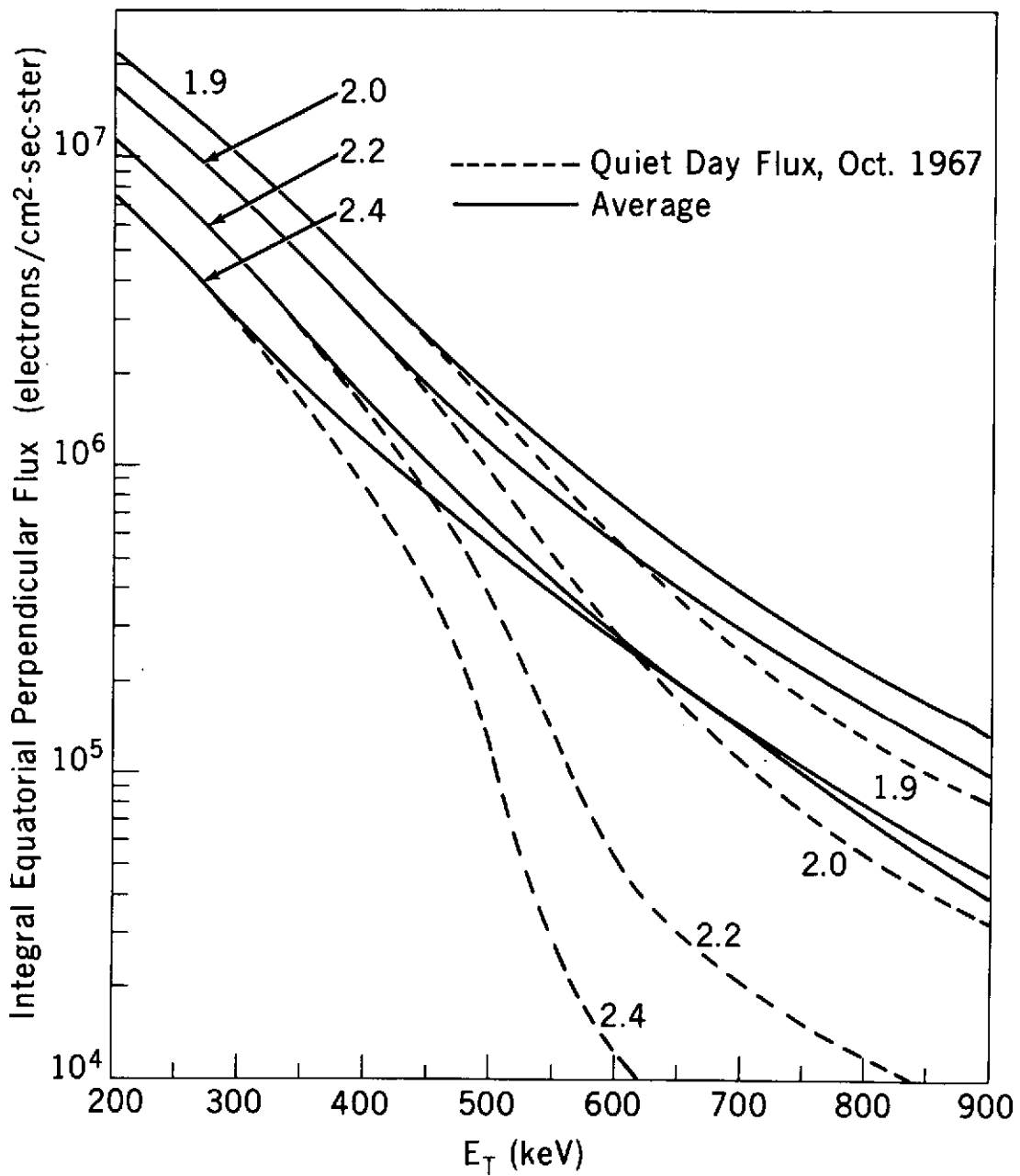


Figure 68. Modifications to Quiet Day Model

The high-energy integral flux spectra are shown for quiet times (broken line) and for the averaged storm time situation (solid lines) indicating the increased importance of storm effects at the higher L values.

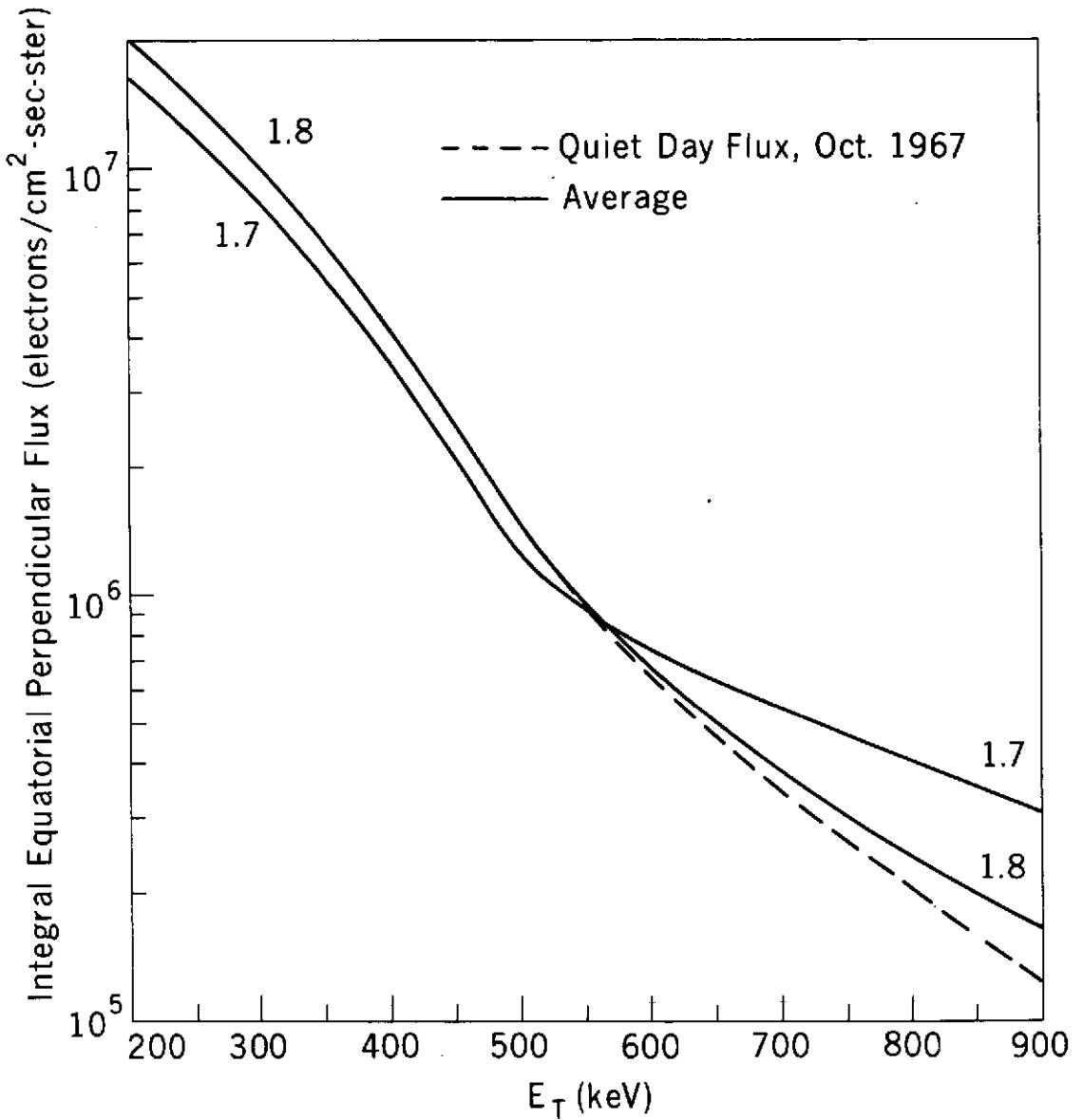


Figure 69. Modifications to Quiet Day Model

The high-energy integral flux spectra are shown for quiet times (broken line) and for the averaged storm situation (solid lines). At L = 1.7 magnetic storm effects do not significantly influence the average model and no modification is made to the quiet day flux.

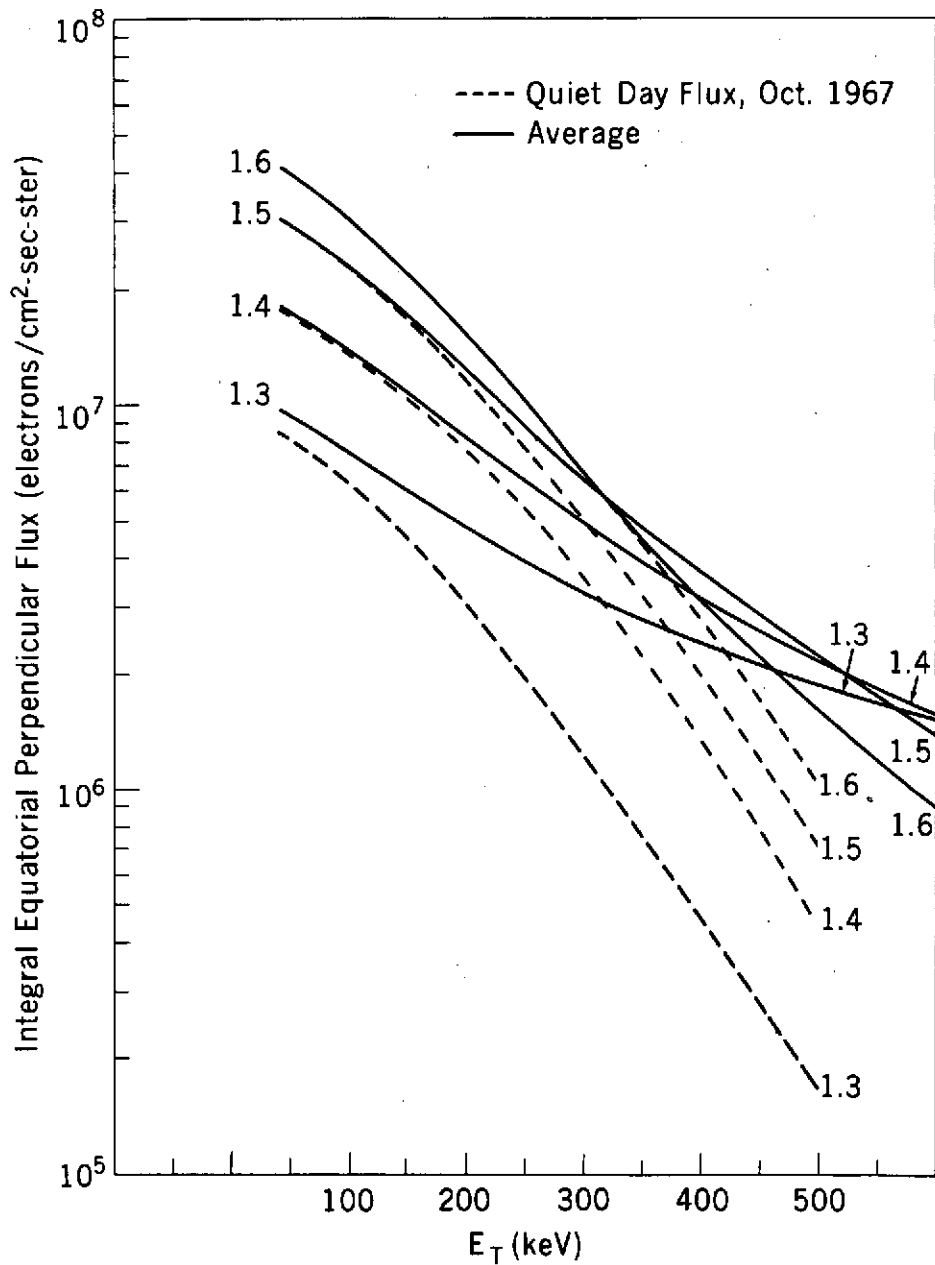


Figure 70. Modifications to Quiet Day Model

The low-energy integral flux spectra are shown for  $L \leq 1.6$ . The modifications to the low-energy quiet day flux based on the low-energy OGO data (broken line) are shown resulting from the hardening of the spectra at higher energies.

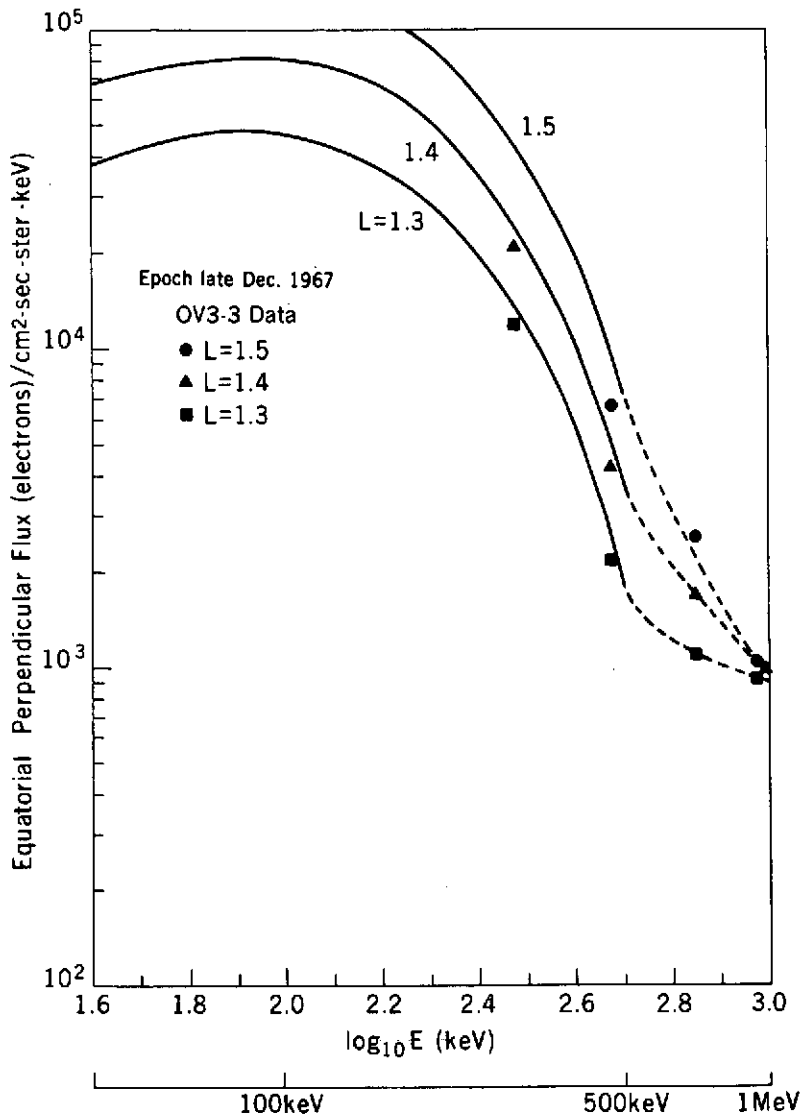


Figure 71. High-Energy Differential Spectra  $L \leq 1.6$

Differential spectra are shown for low energies and low L values. The solid lines indicate the analytical quiet day flux and the broken lines indicate that monotonic spectra are given by the OV3-3 data for higher energies.

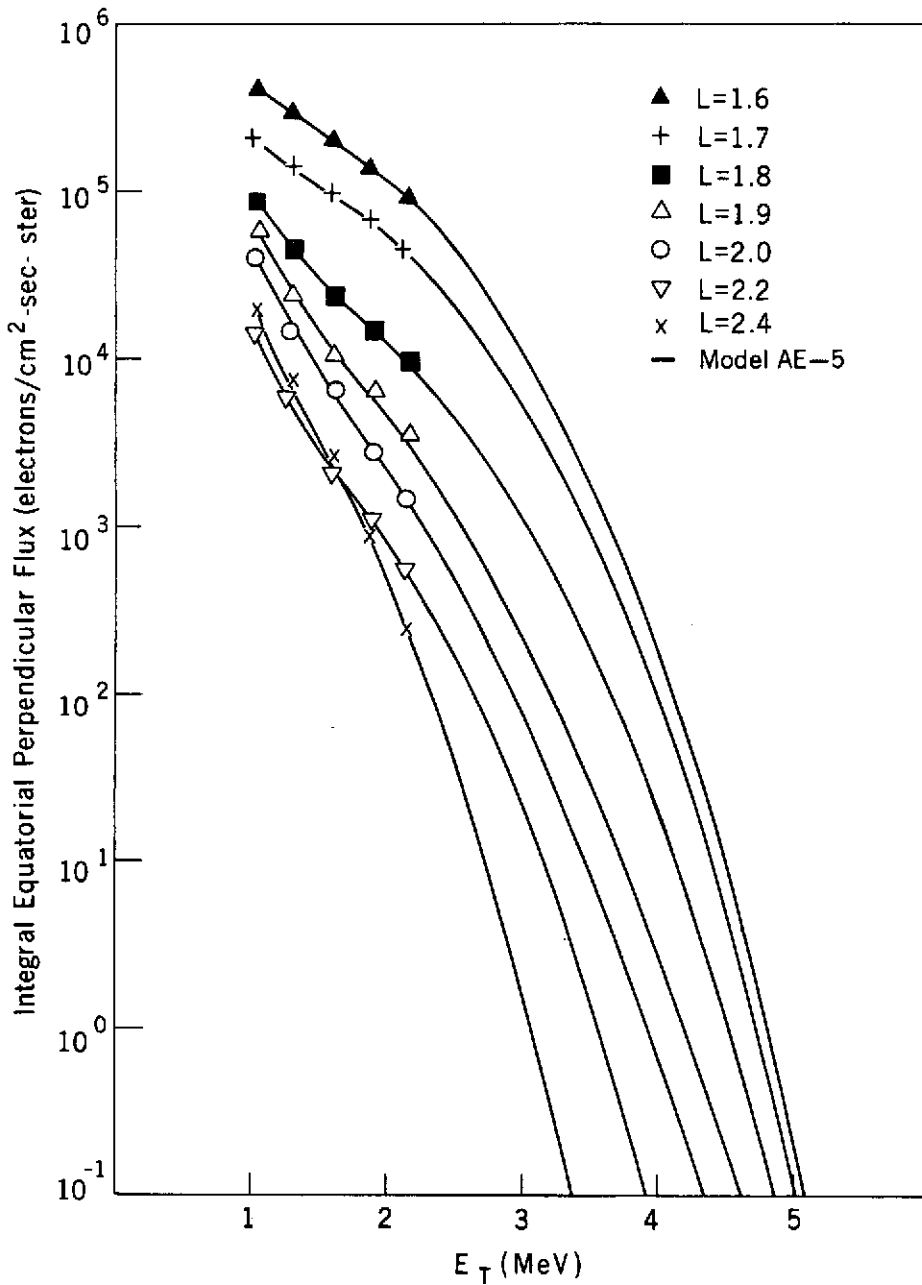


Figure 72. Extrapolated High-Energy Spectra  
Based on OV3-3 Data

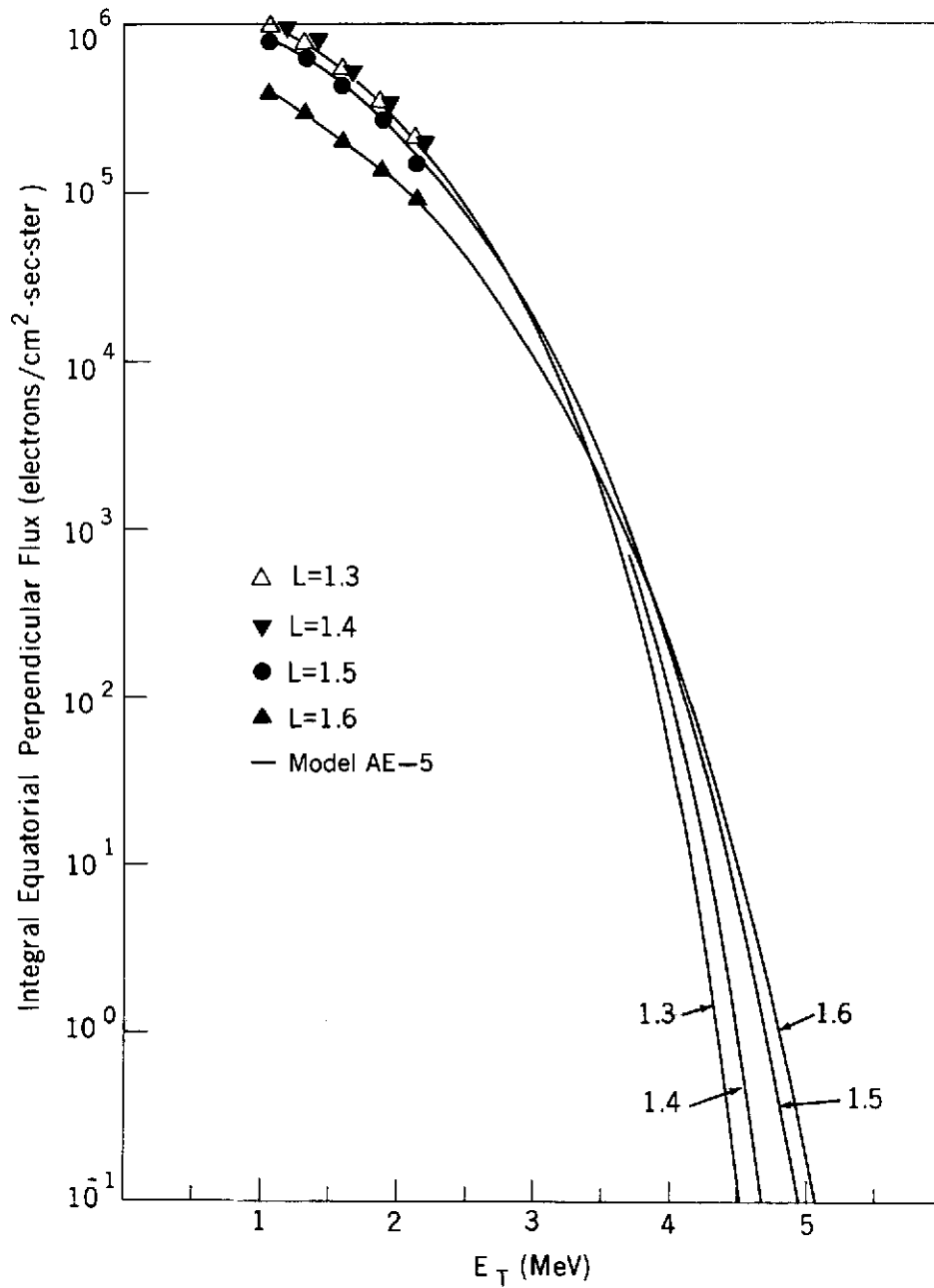
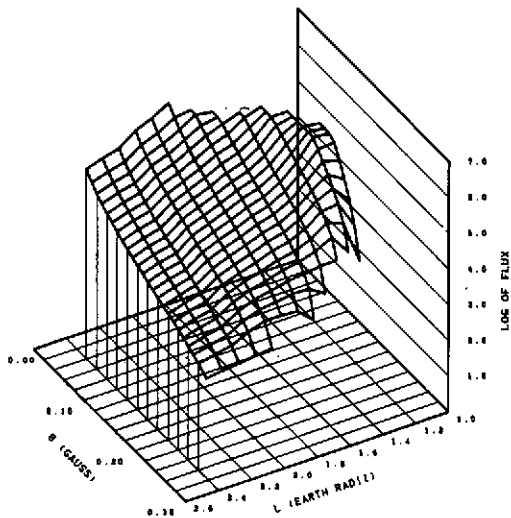


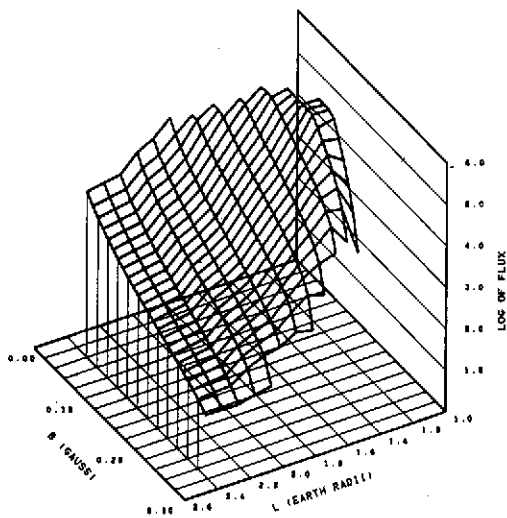
Figure 73. Extrapolated High-Energy Spectra Based on OV3-3 Data

**FIGURE 74**  
 PERPENDICULAR INTEGRAL FLUX  
 GREATER THAN 500 KEV  
 EPOCH OCTOBER 1967



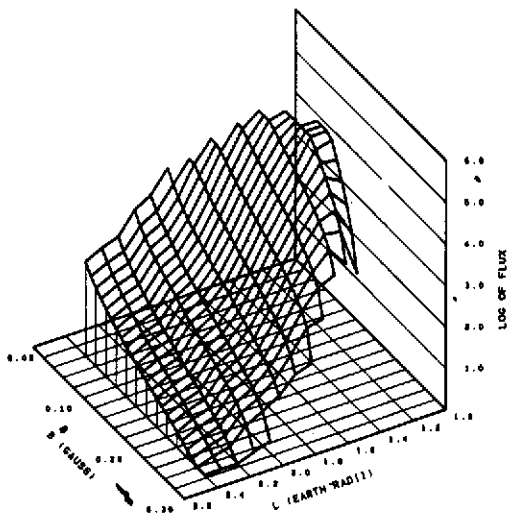
FLUX UNITS - ELECTRONS/50 CM SEC STRA

**FIGURE 75**  
 PERPENDICULAR INTEGRAL FLUX  
 GREATER THAN 1 MEV  
 EPOCH OCTOBER 1967



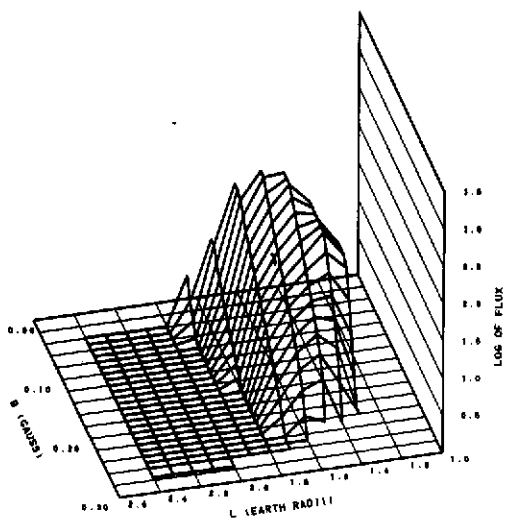
FLUX UNITS - ELECTRONS/50 CM SEC STRA

**FIGURE 76**  
 PERPENDICULAR INTEGRAL FLUX  
 GREATER THAN 2 MEV  
 EPOCH OCTOBER 1967



FLUX UNITS - ELECTRONS/50 CM SEC STRA

**FIGURE 77**  
 PERPENDICULAR INTEGRAL FLUX  
 GREATER THAN 4 MRV  
 EPOCH OCTOBER 1967



FLUX UNITS - ELECTRONS/50 CM SEC STRA

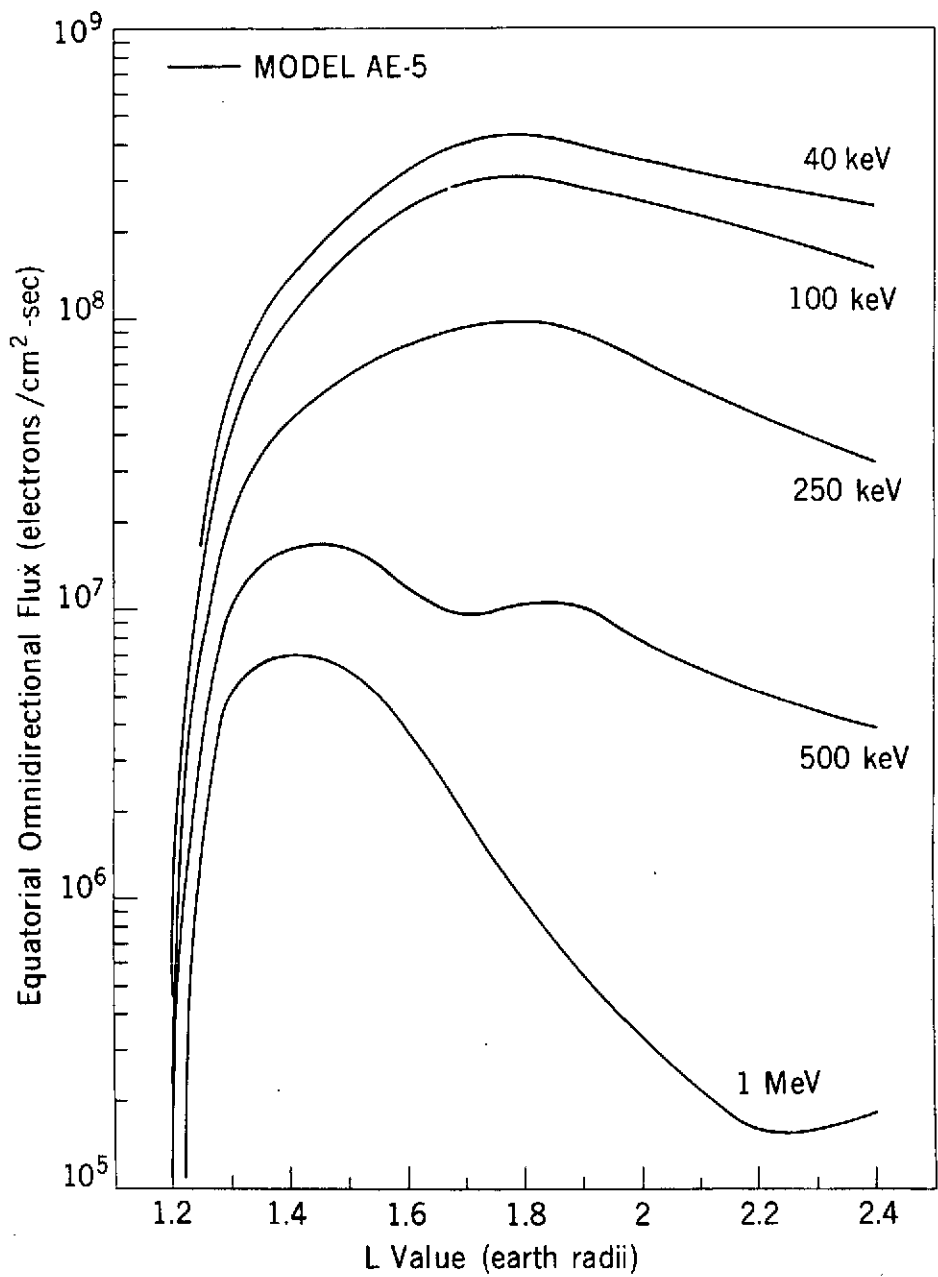


Figure 78. Inner Belt Radial Profiles

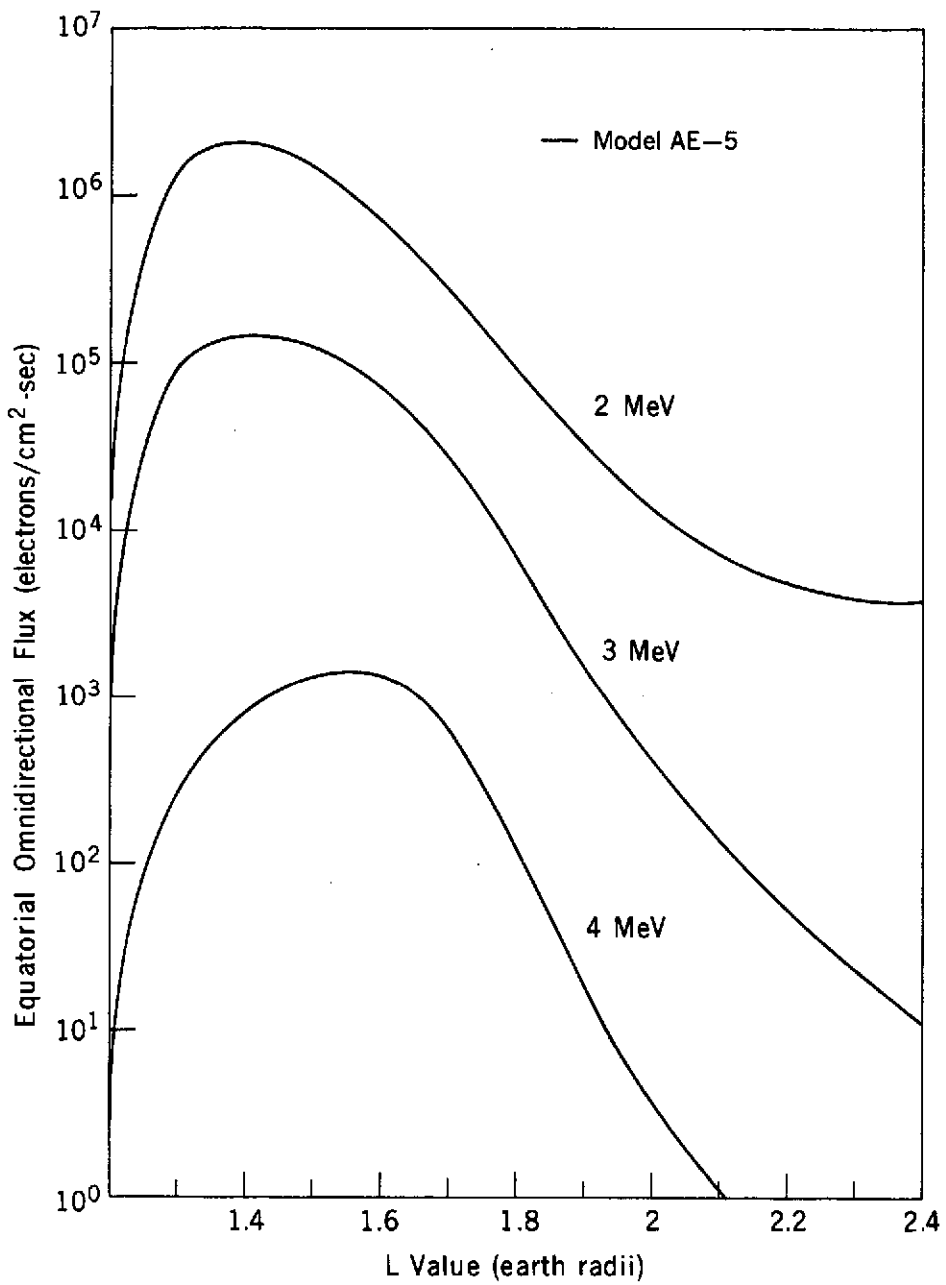


Figure 79. Inner Belt Radial Profiles

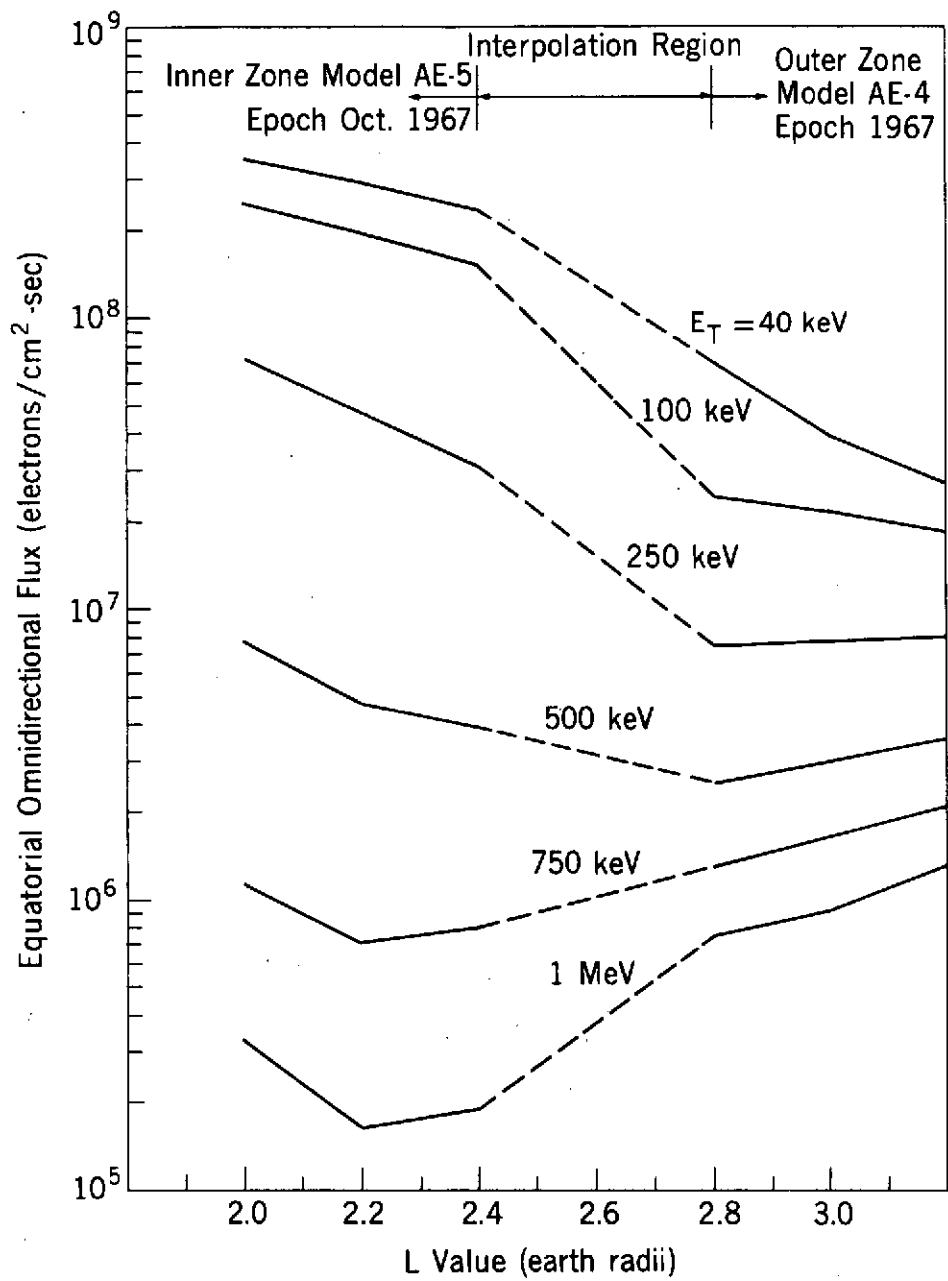


Figure 80. Radial Profiles in Interface Region L ~ 2.6

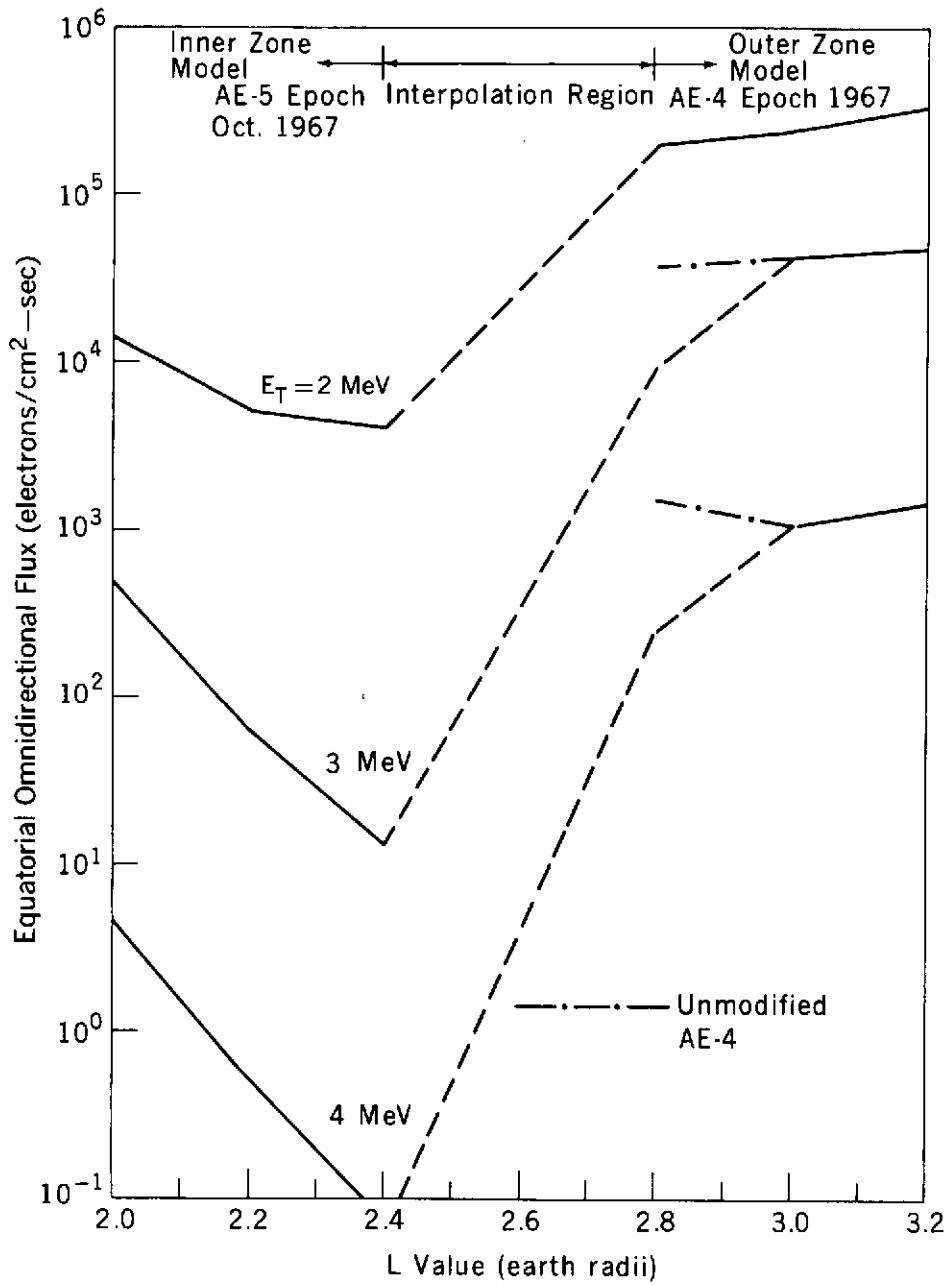


Figure 81. Radial Profiles in Interface Region  $L \sim 2.6$

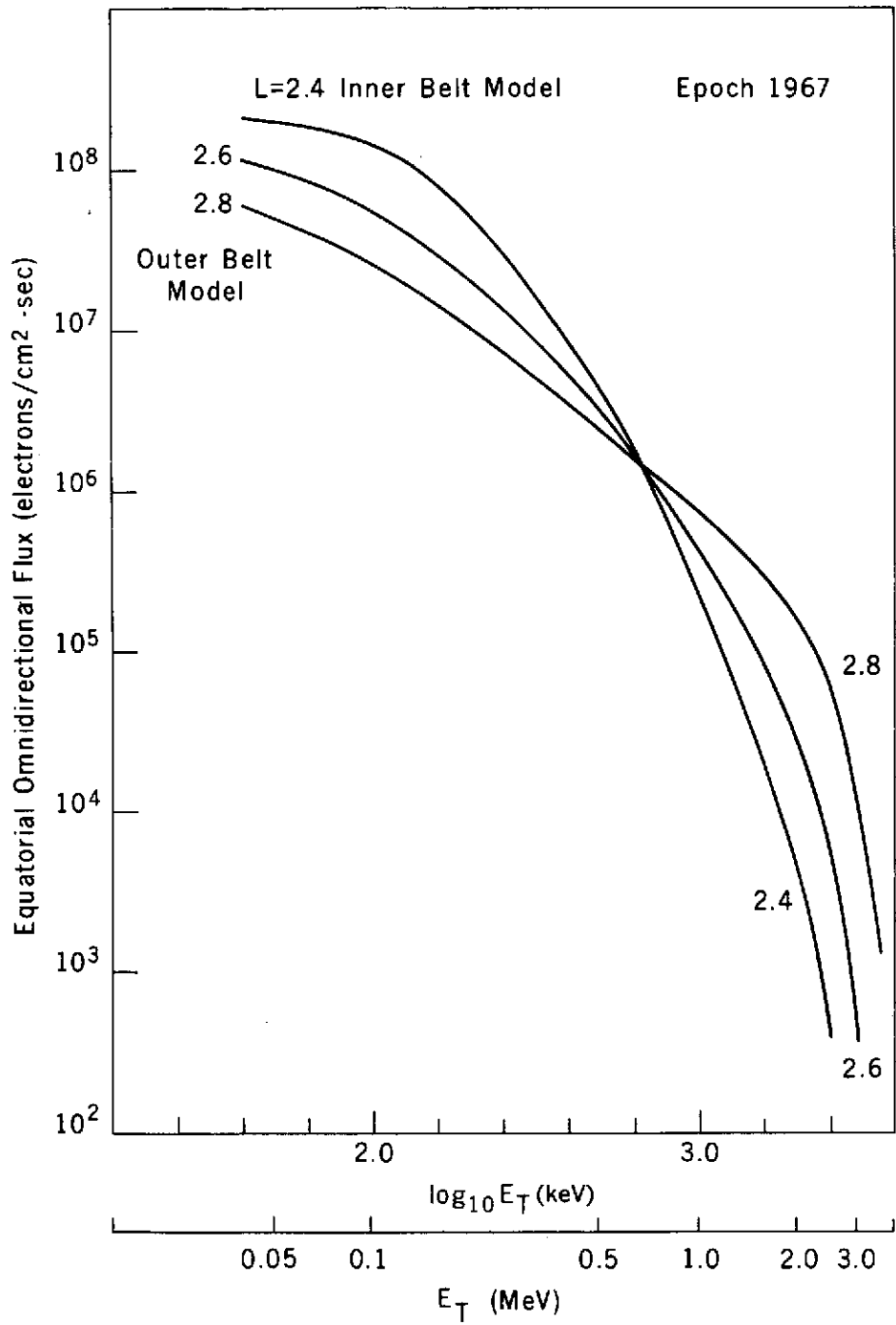


Figure 82. Interpolated Spectrum L = 2.6

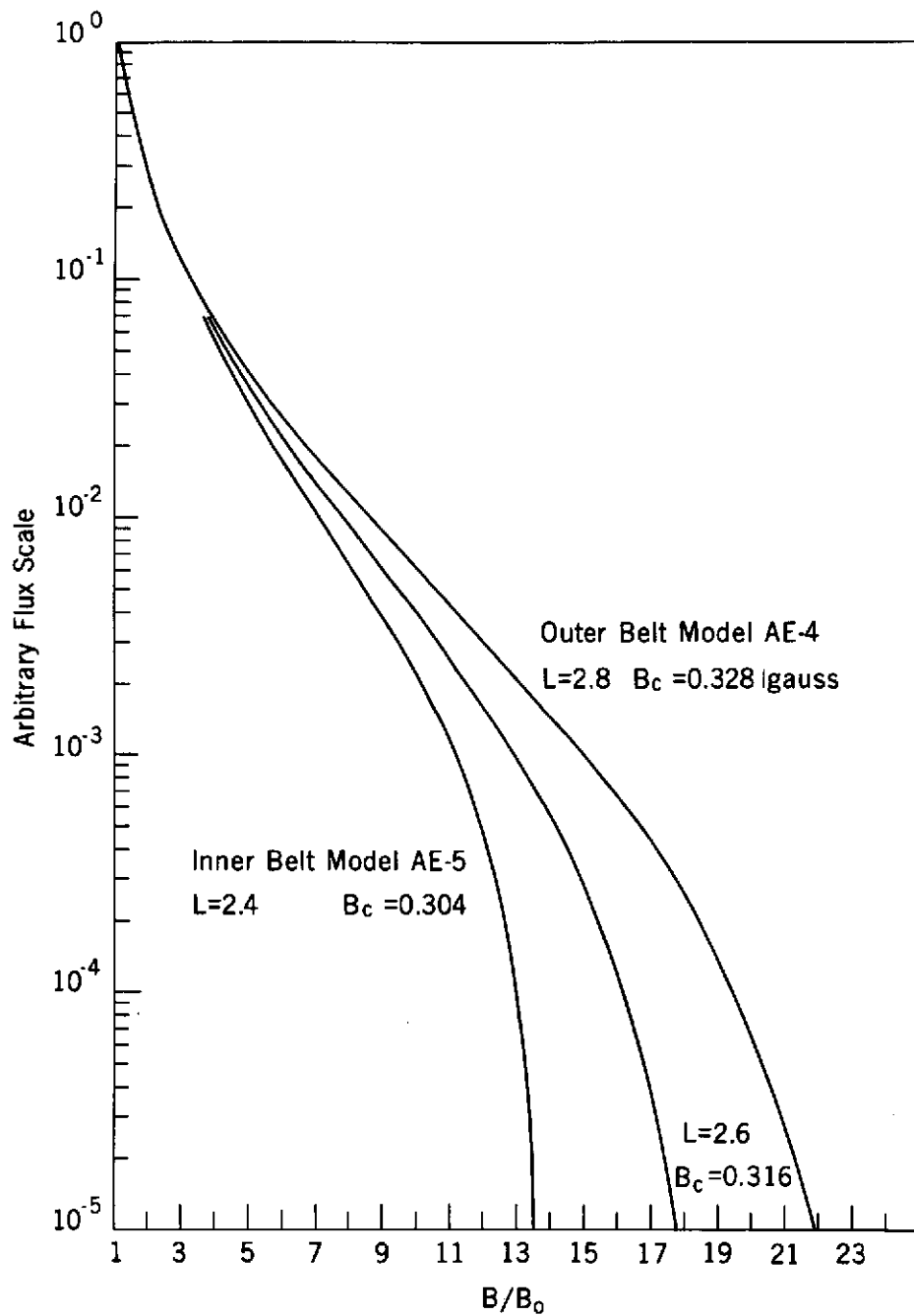


Figure 83. Interpolated B Dependence  $L = 2.6$

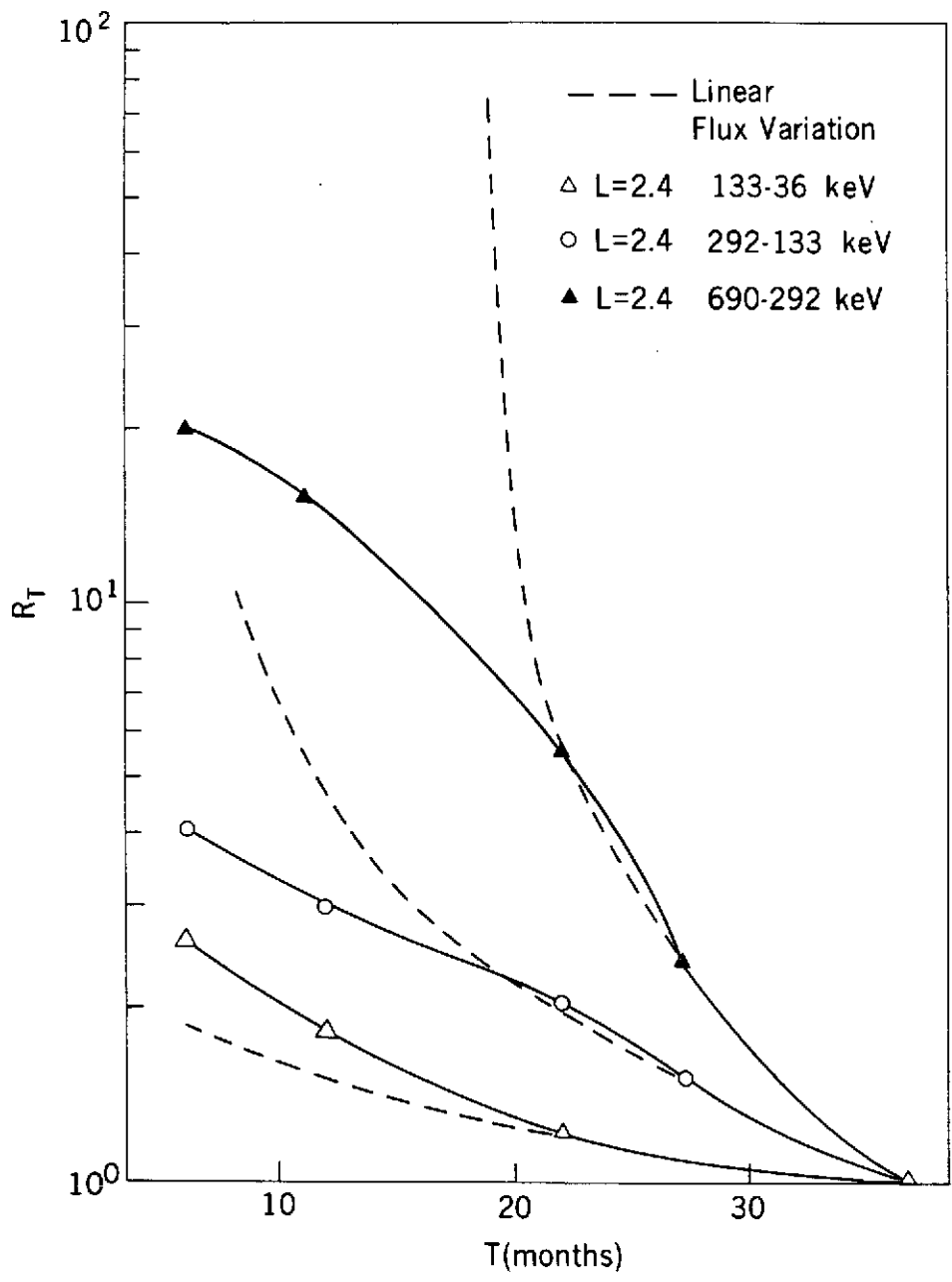


Figure 84. Solar Cycle Ratios for L = 2.4

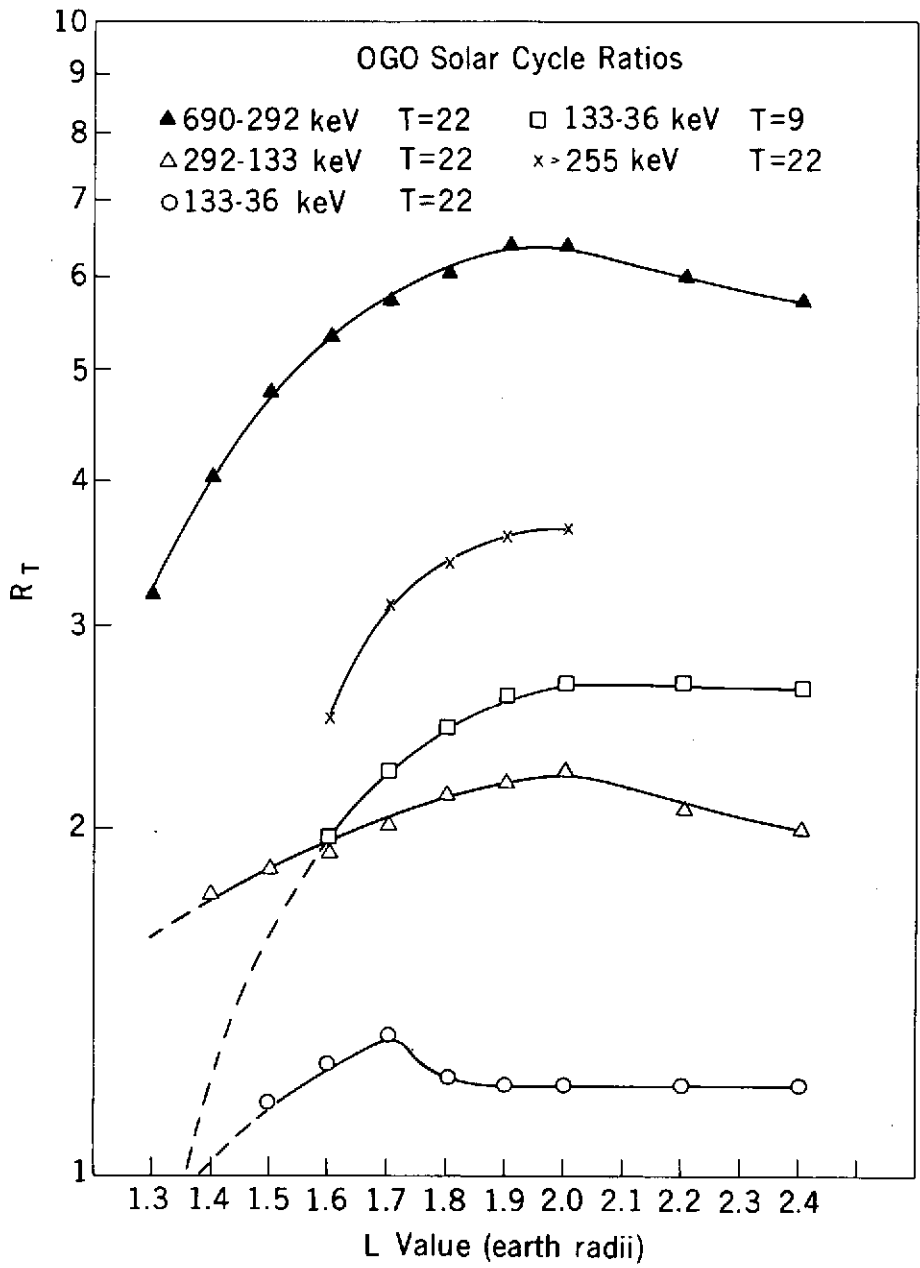


Figure 85. L Dependence of Solar Cycle Ratios

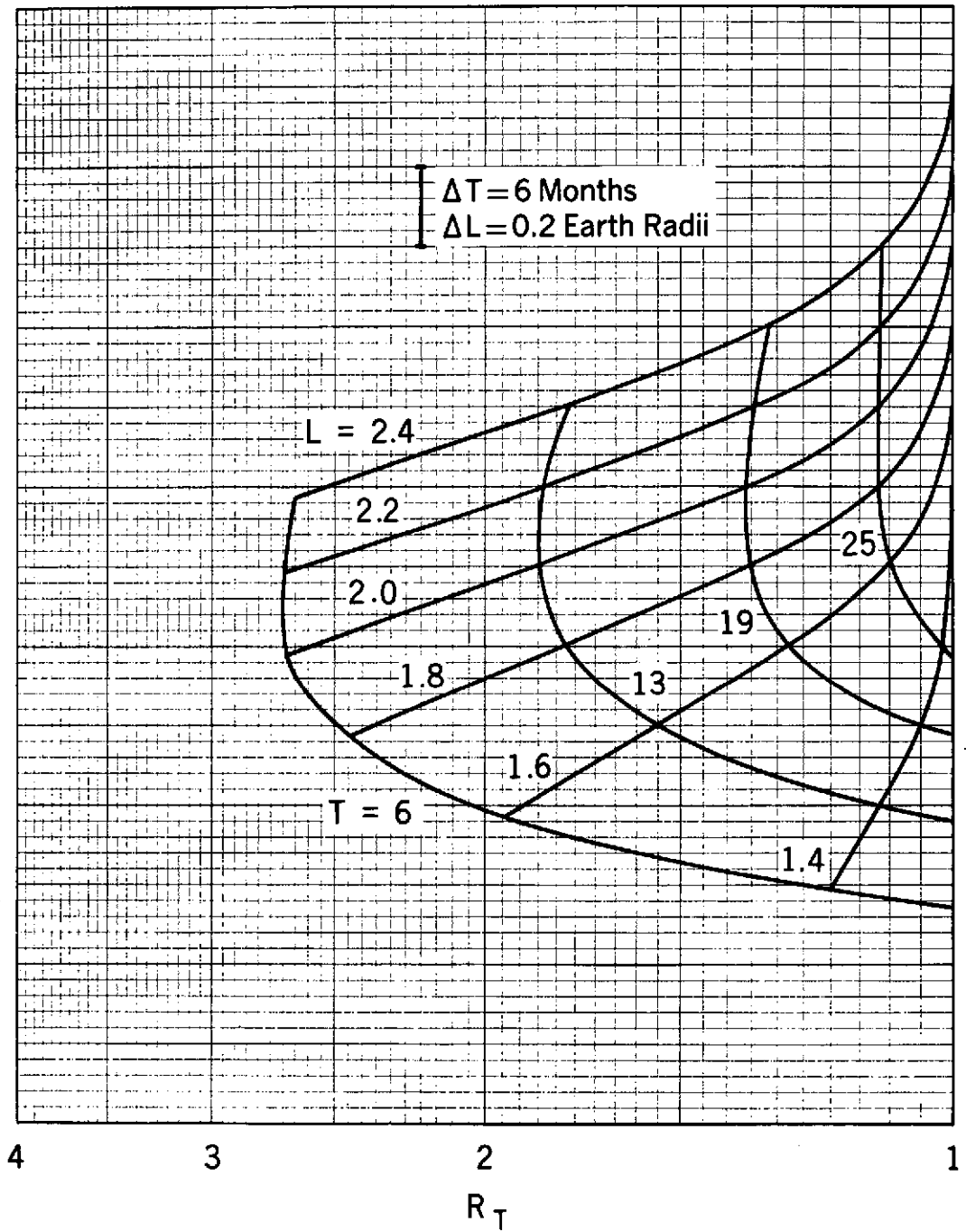


Figure 86. OGO-Based Solar Cycle Ratios  $R_T$ ,  $36 \leq E/(\text{keV}) \leq 133$

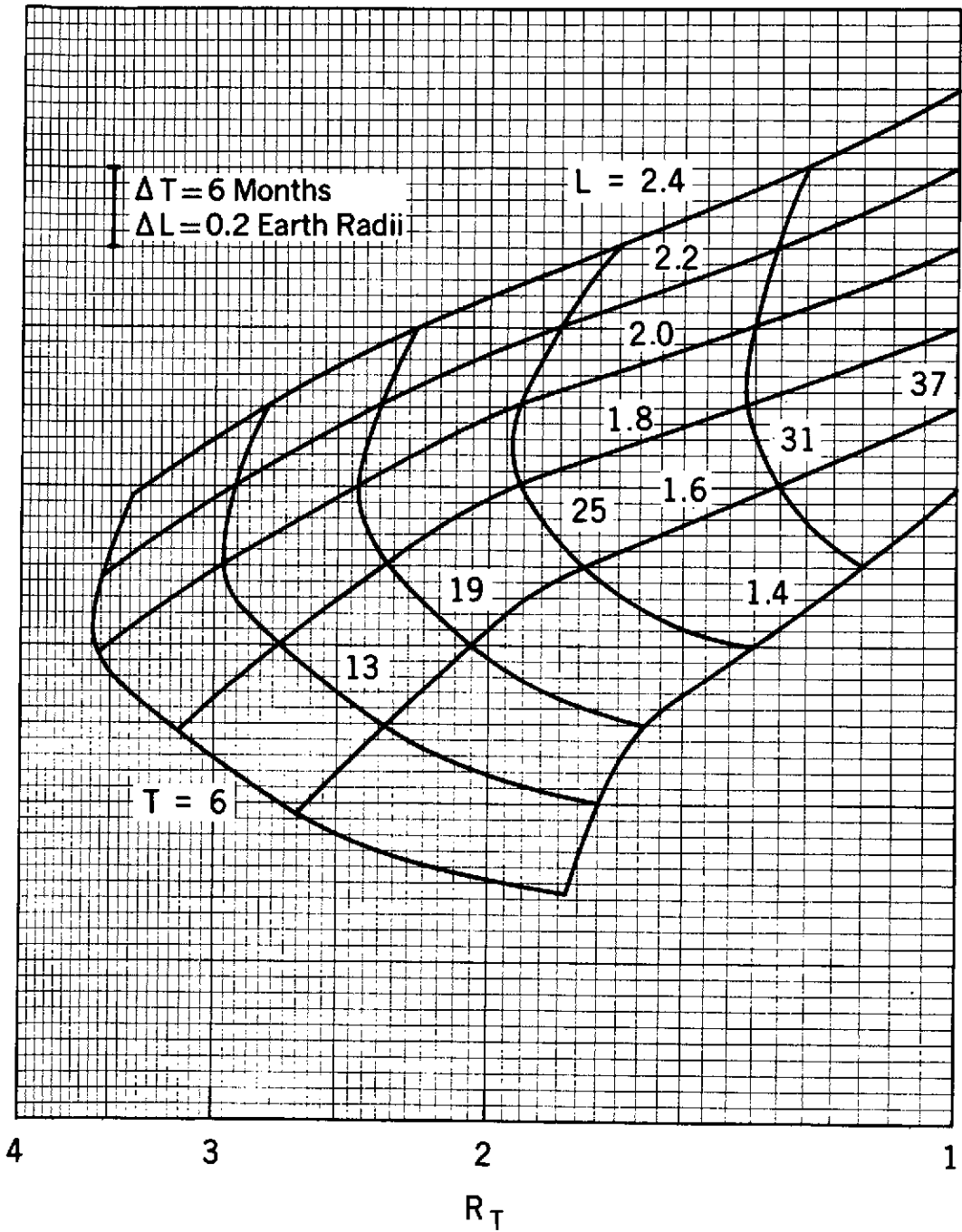


Figure 87. OGO-Based Solar Cycle Ratios  $R_T$ ,  $292 \geq E/(\text{keV}) \geq 133$

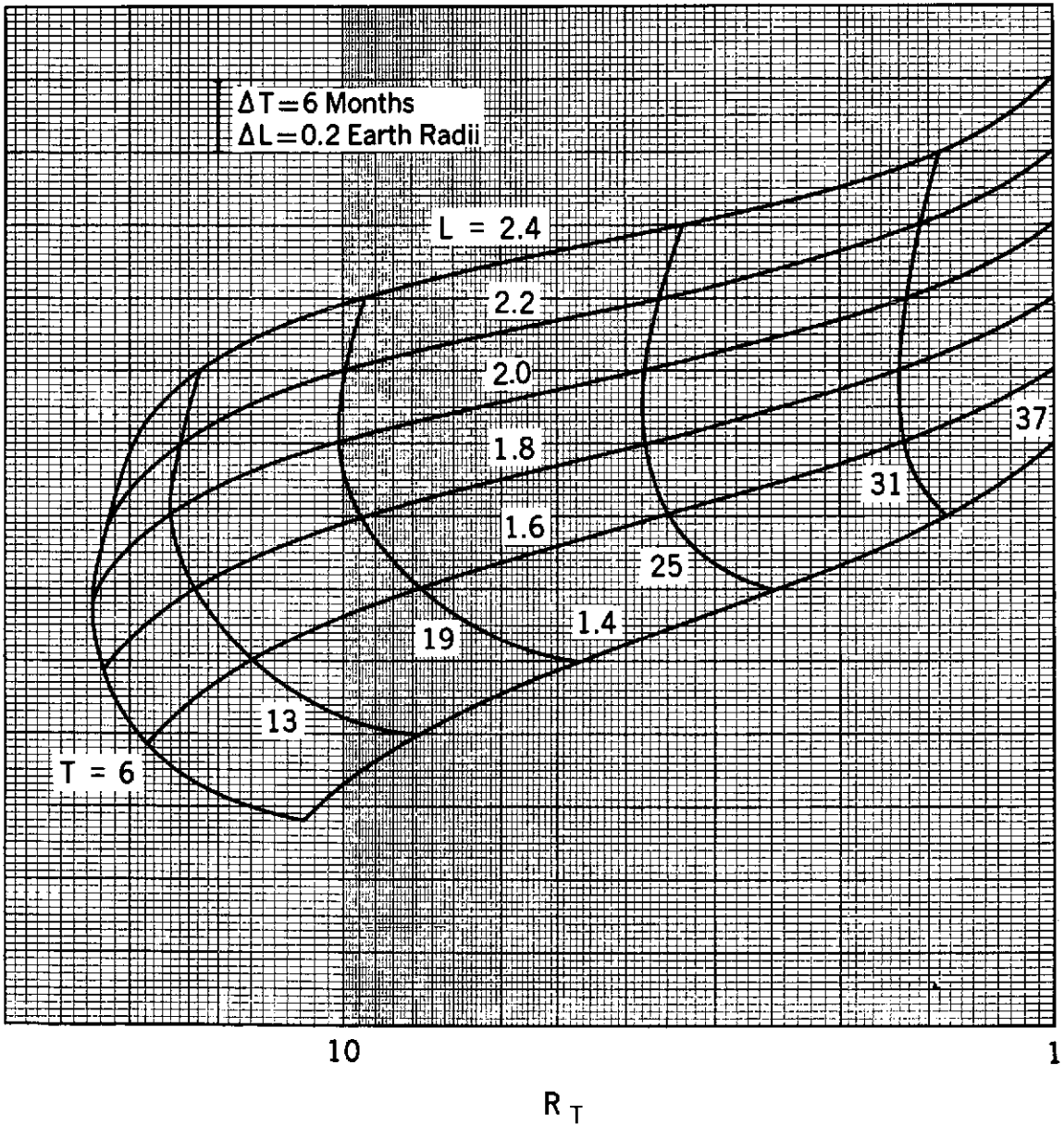


Figure 88. OG0-Based Solar Cycle Ratios  $R_T$ ,  $690 \geq E/(\text{keV}) \geq 292$

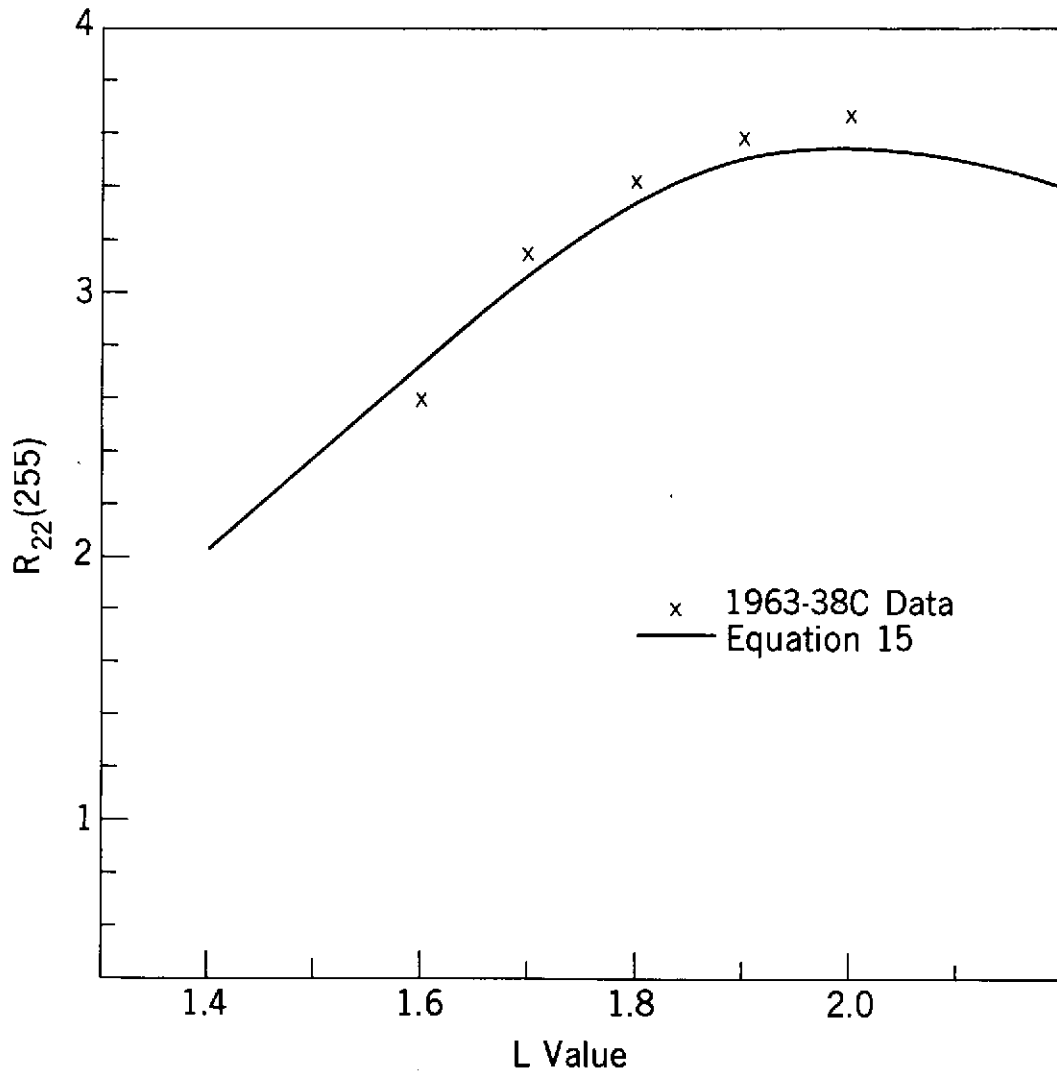


Figure 89. Comparison of 1963-38C and OGO Solar Cycle Parameters

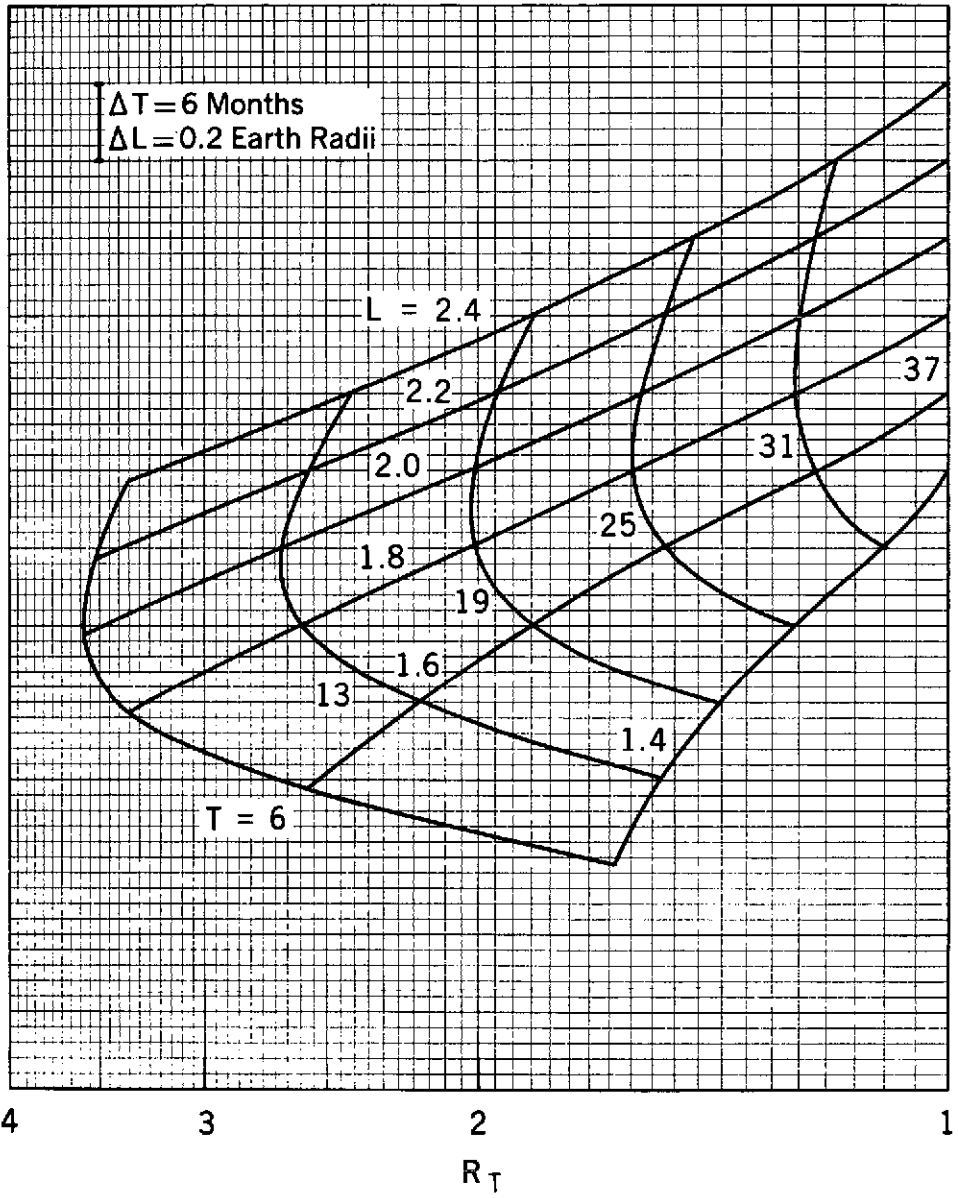


Figure 90. Integral Flux Solar Cycle Ratios  $R_T$ ,  $E > 40$  keV

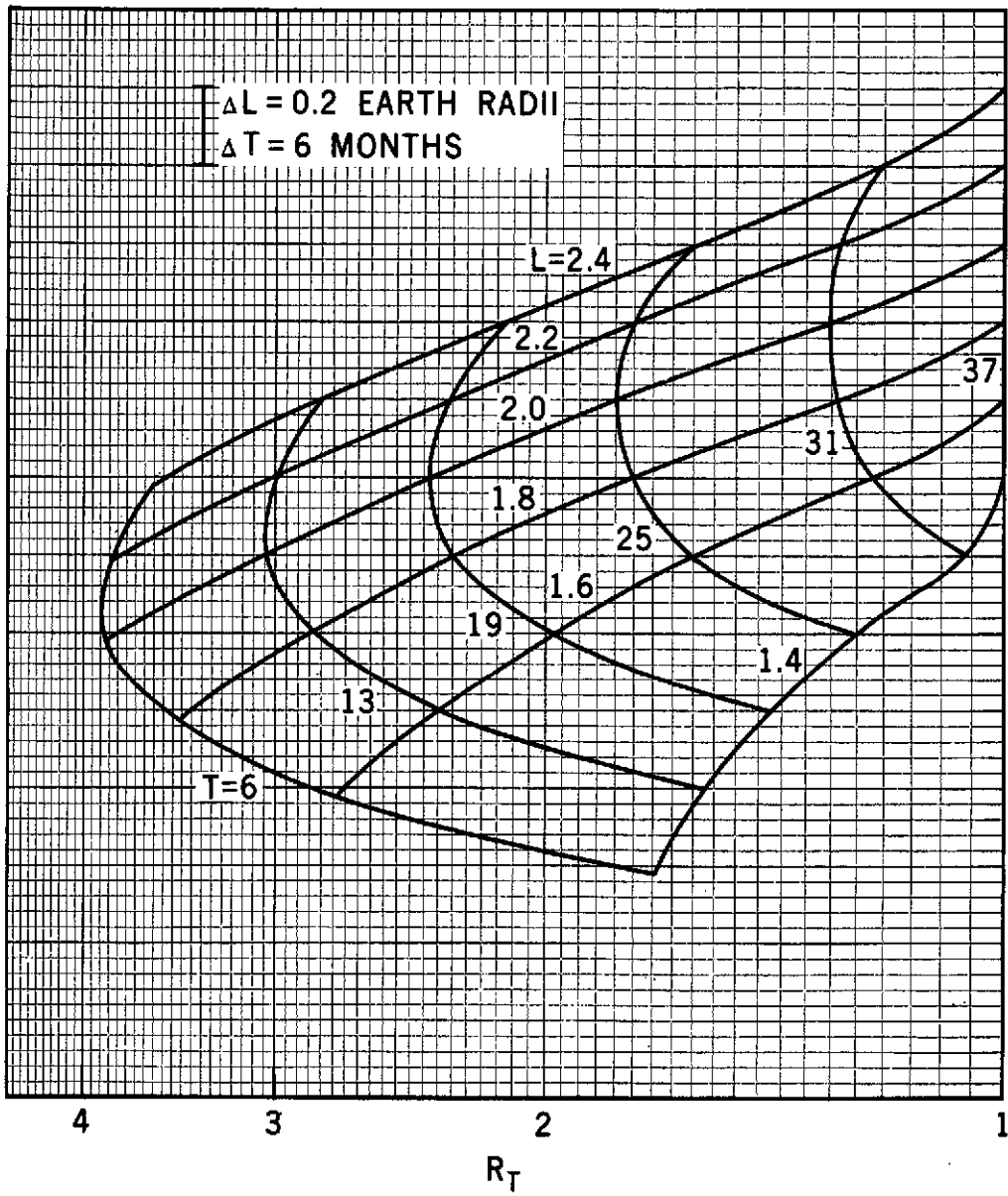


Figure 91. Integral Flux Solar Cycle Ratios  $R_T$ ,  $E > 100$  keV

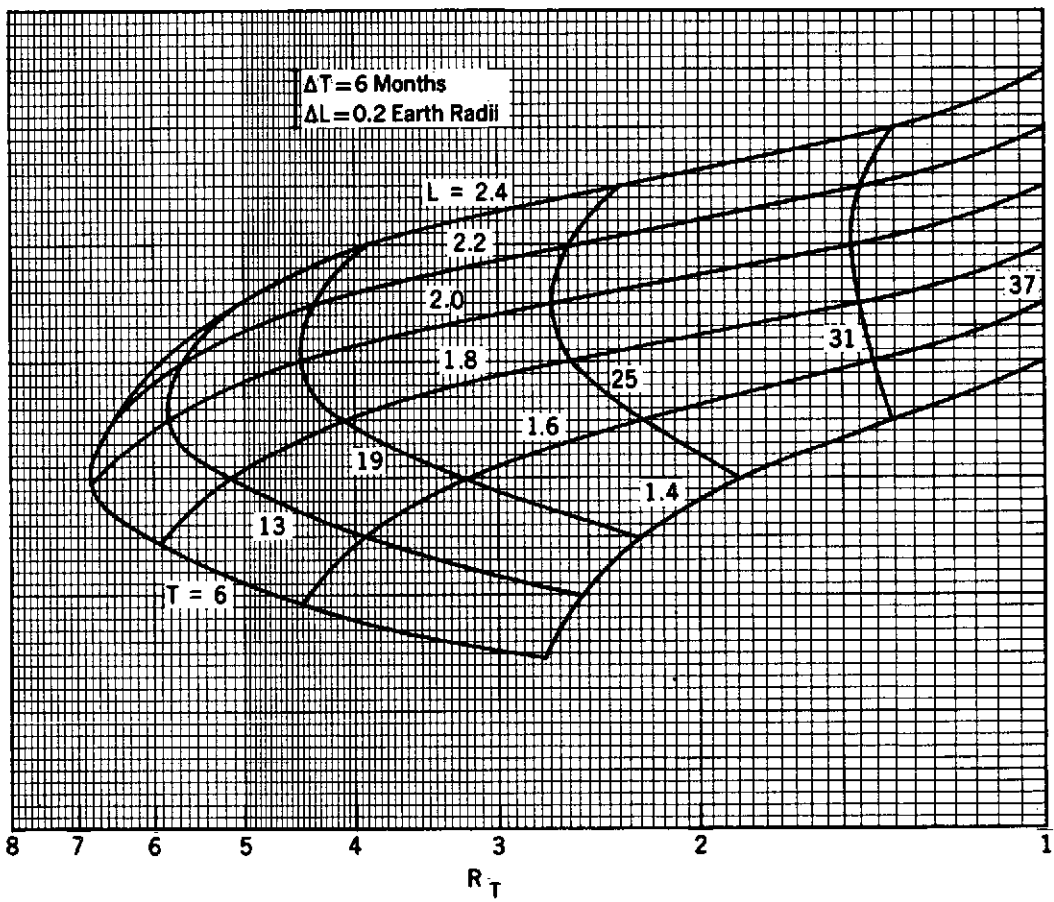


Figure 92. Integral Flux Solar Cycle Ratios  $R_T$ ,  $E > 250$  keV

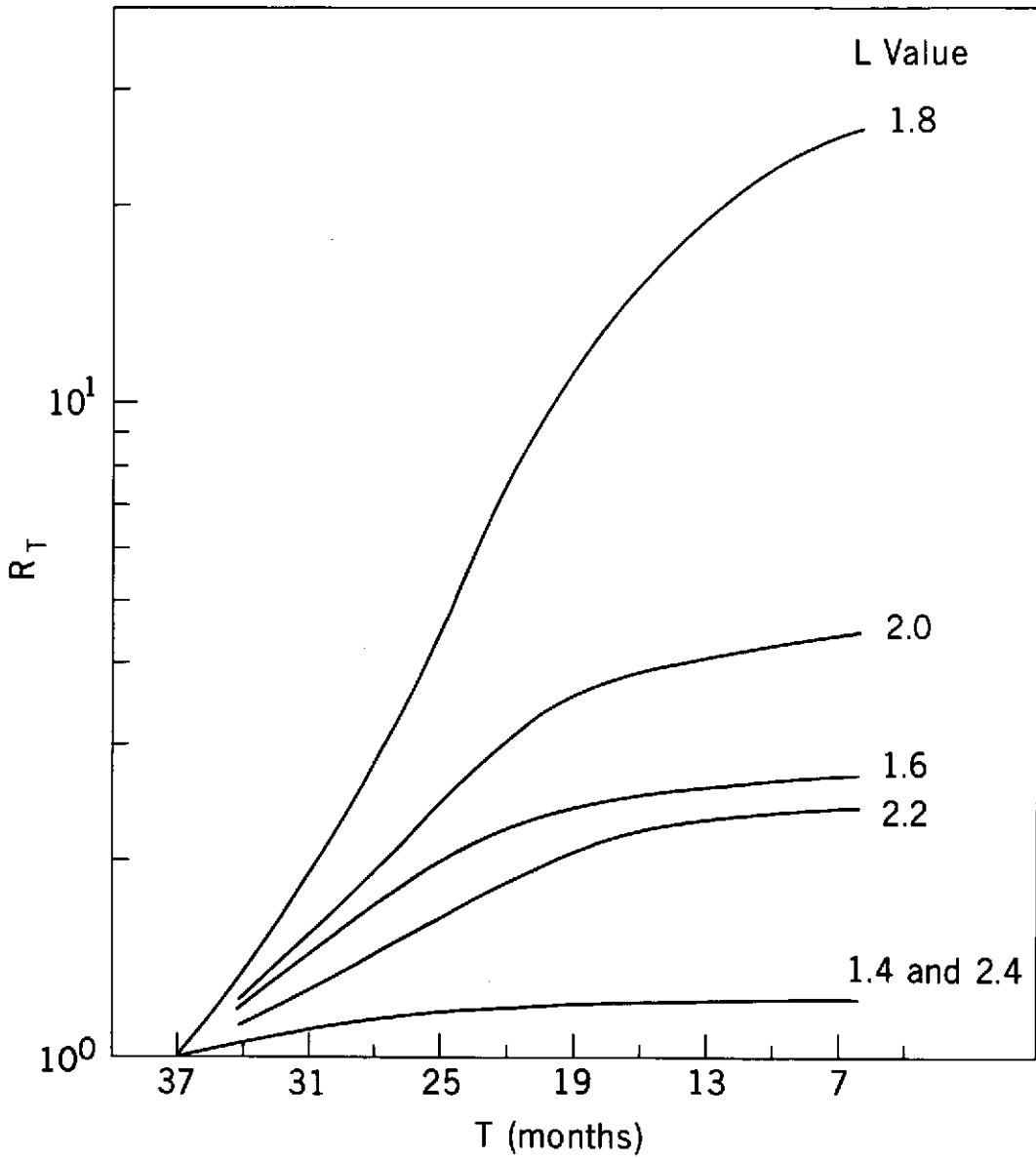


Figure 93. Integral Flux Solar Cycle Ratios  $R_T$ ,  $E > 500$  keV

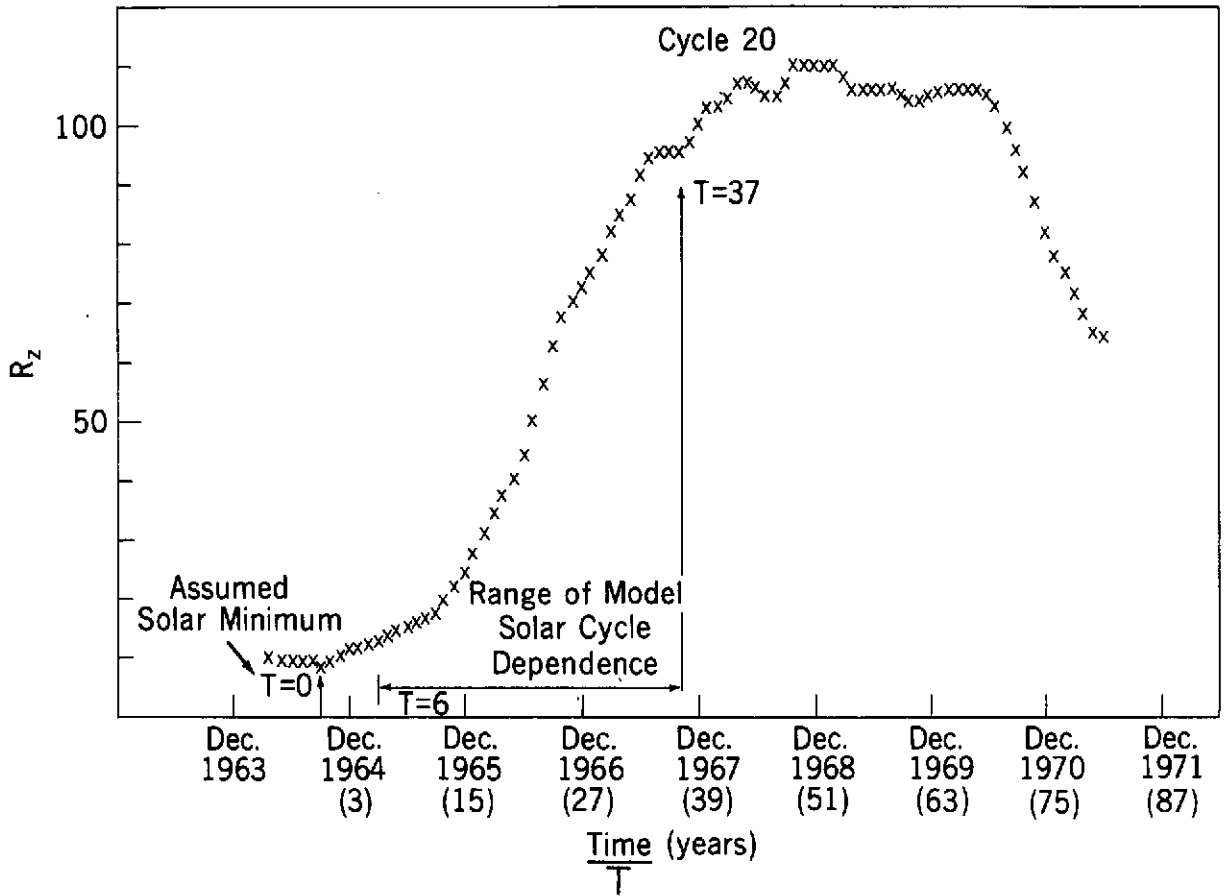


Figure 94. Sunspot Number  $R_z$

The smoothed Zurich sunspot number is shown as a function of time indicating that the solar cycle parameters have been obtained over a period covering most of the change from solar minimum to solar maximum. The numbers in parentheses on the abscissa scale are months from solar minimum.

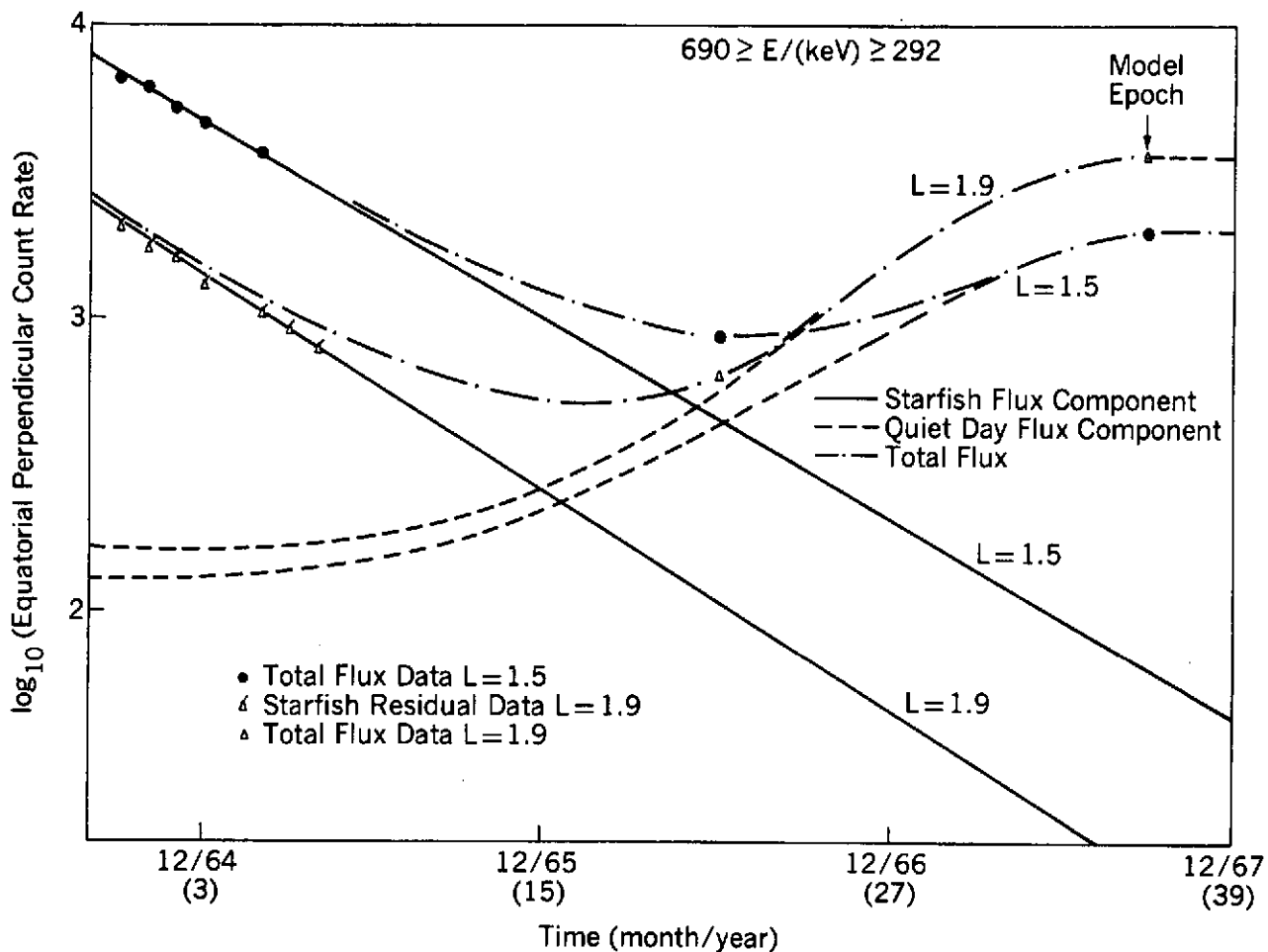


Figure 95. Separation of Flux Components

The relative importance of the Starfish and quiet day flux components is shown as a function of time for the interval  $690 \leq E/(\text{keV}) \leq 292$  and  $L = 1.5$  and  $1.9$ . Representative data only are shown for the June 1966 and October 1967 epochs. The numbers in parentheses on the abscissa scale are months from solar minimum.

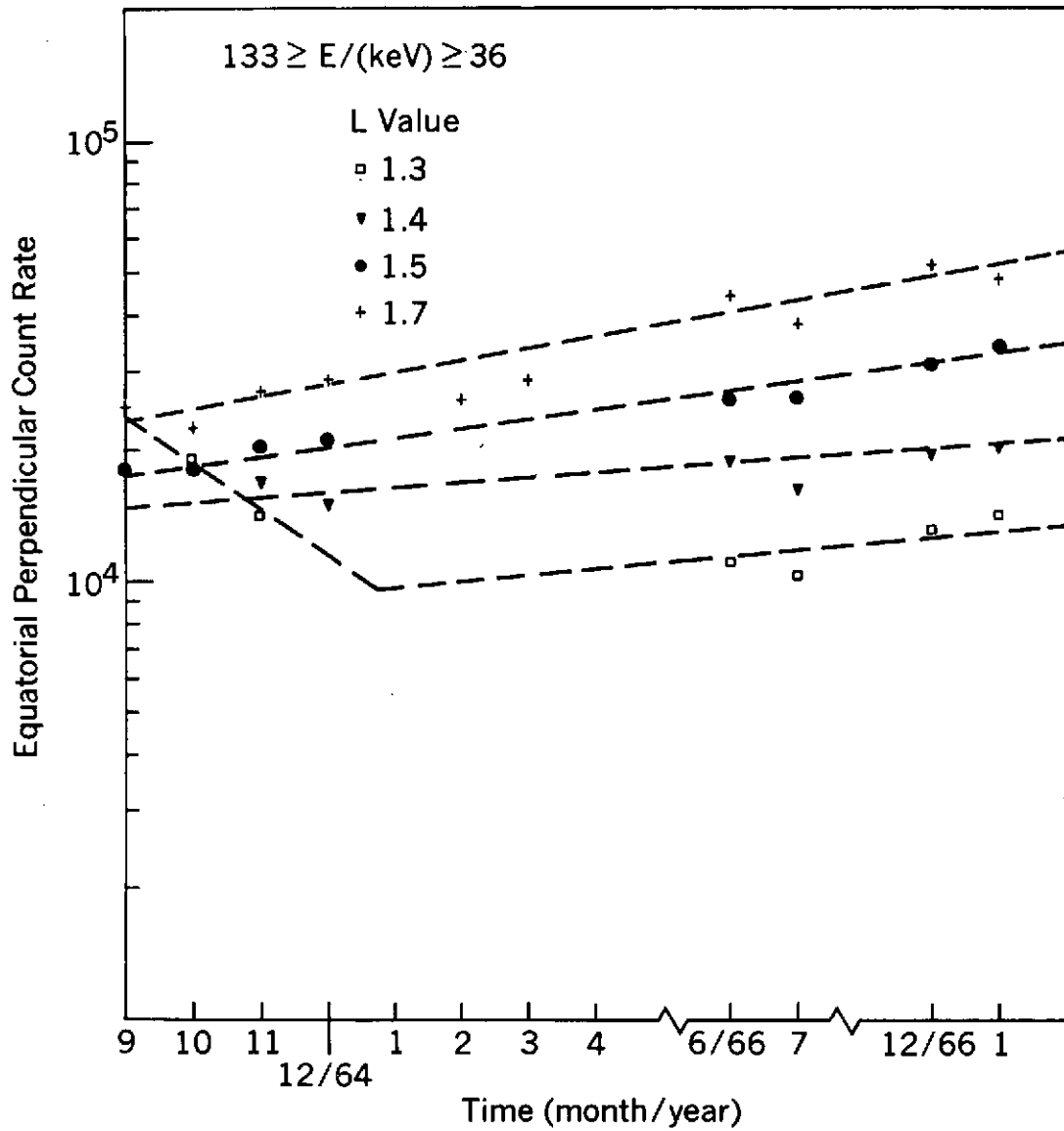
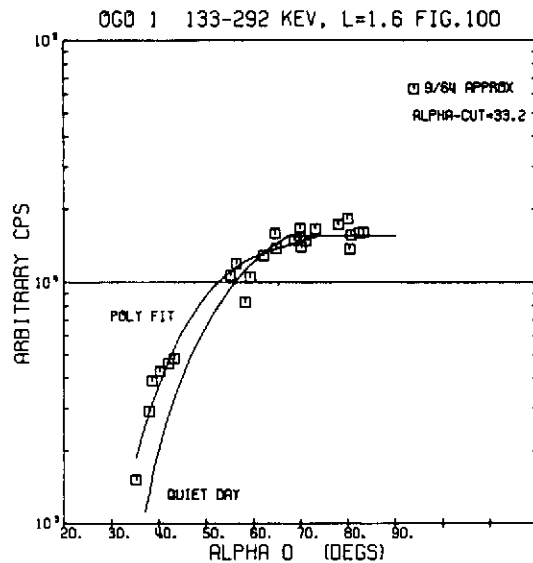
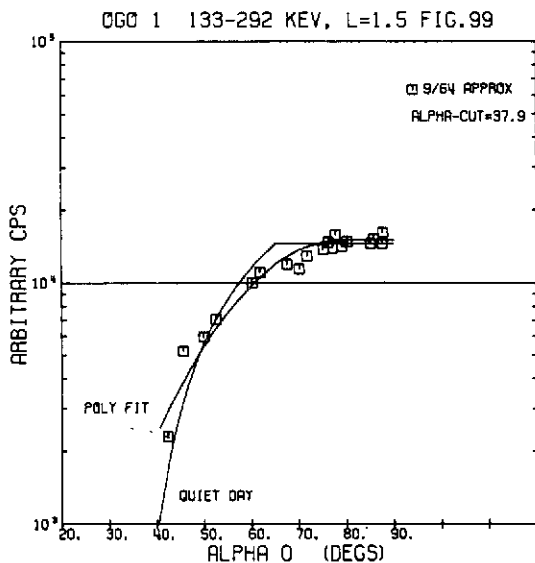
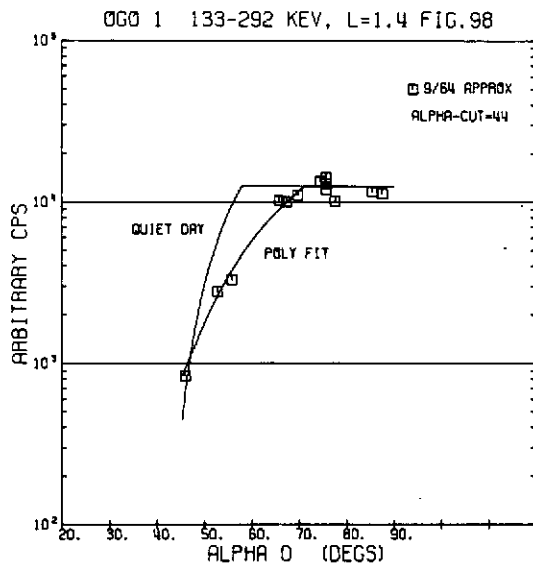
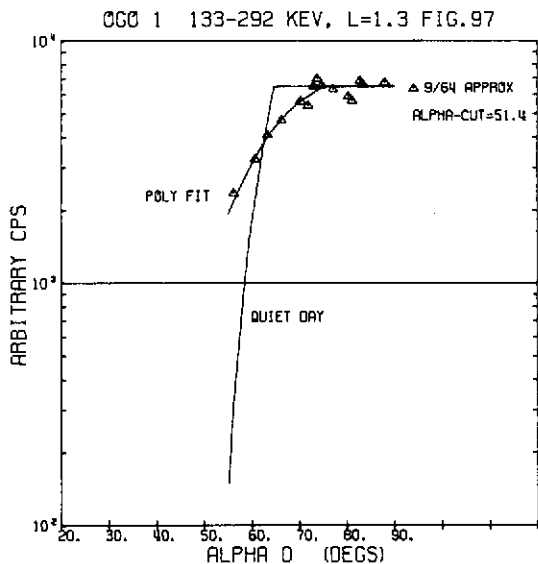


Figure 96. Temporal Variation of Low-Energy OGO Data

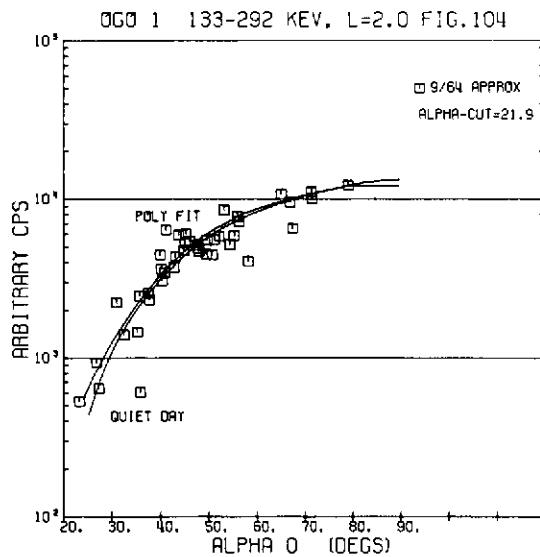
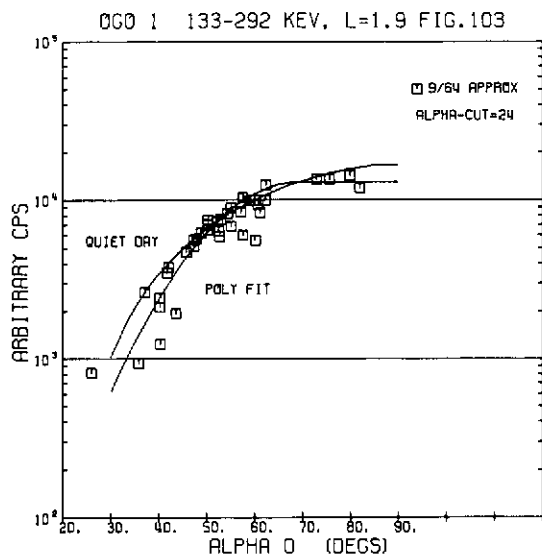
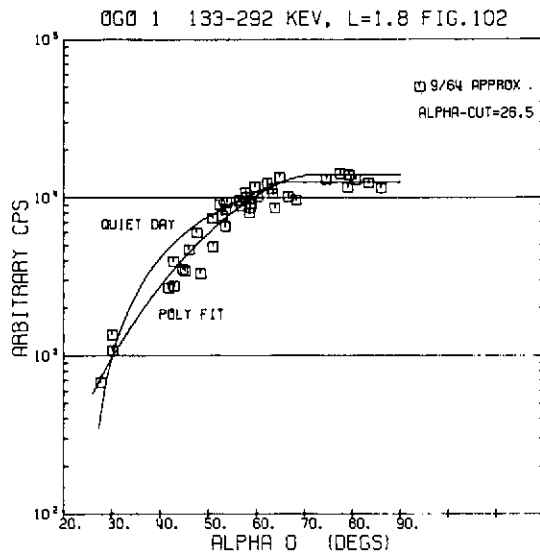
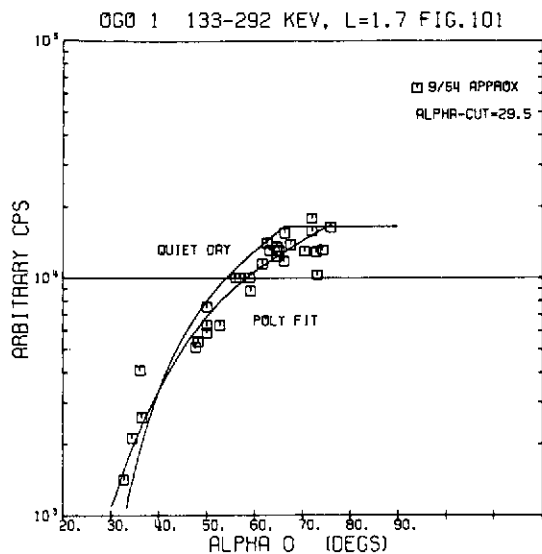
The variation of count rate with time is shown for the lowest energy of the OGO spectrometer. The broken lines indicate trends, and the possible presence of Starfish electrons at L = 1.3 is evident.

Figures 97-114 and 119-127. These computer-generated plots present comparisons between the residual Starfish electron flux data from the OGO 1 satellite and the Starfish model discussed in Section 6B. The ordinate scale is arbitrary residual Starfish counts/sec and may be converted to flux using the constants given in Table 3. On each plot comparison is made between the polynomial fit of the Starfish model (labeled POLY FIT) and the quiet day model normalized to the equatorial flux given by polynomial fit (labeled QUIET DAY). The OGO data and the model lines are normalized to an epoch of September 1964. On each plot the atmospheric cutoff equatorial pitch angle is given in degrees.

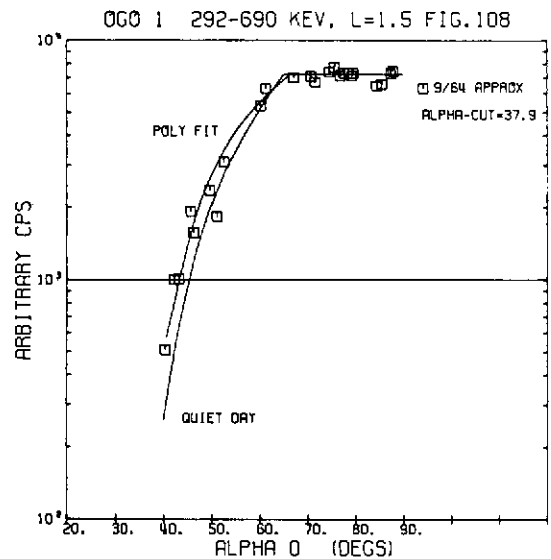
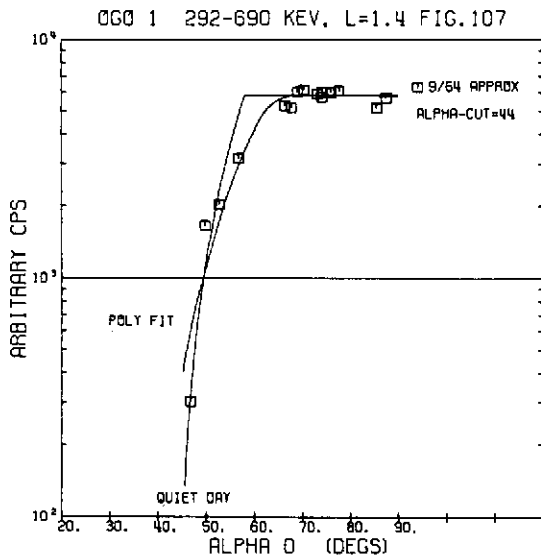
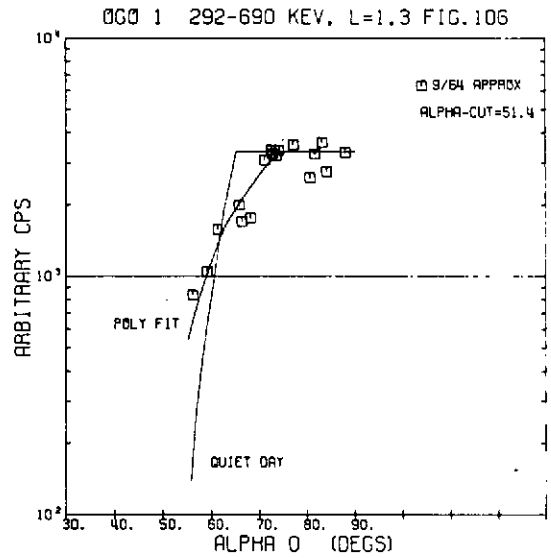
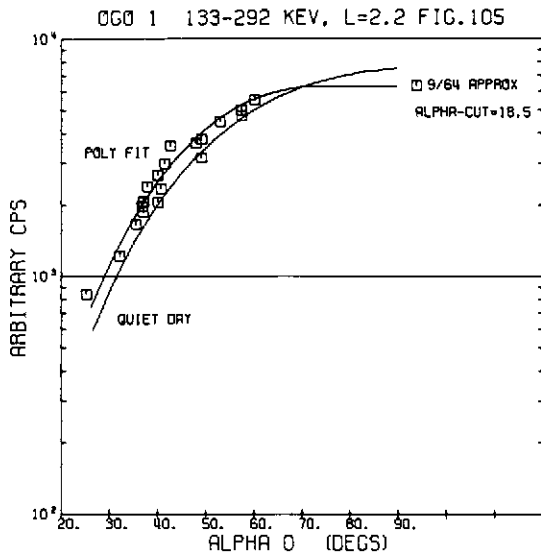
RESIDUAL STARFISH FLUX FIGURES 97 - 100



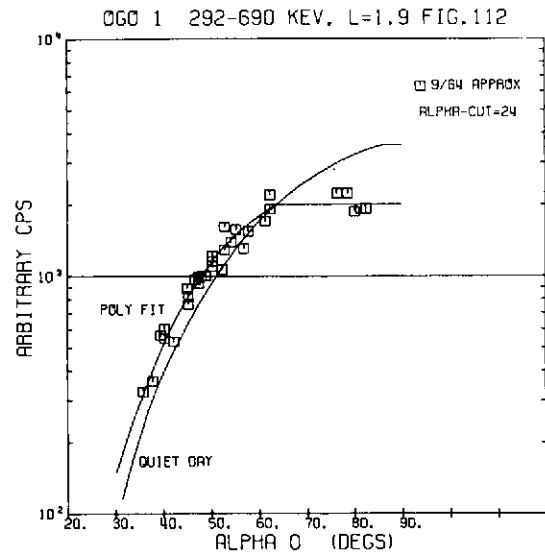
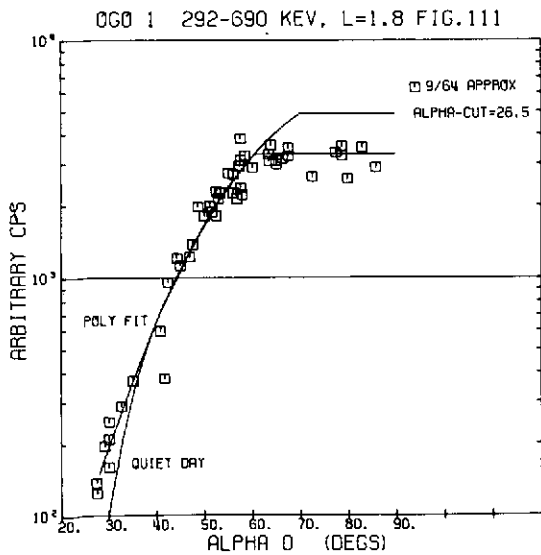
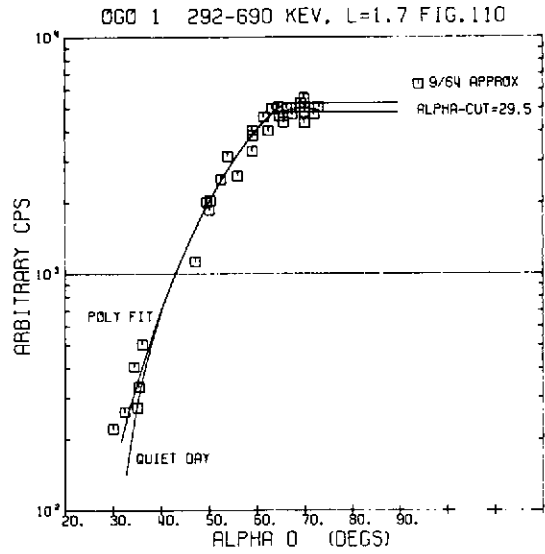
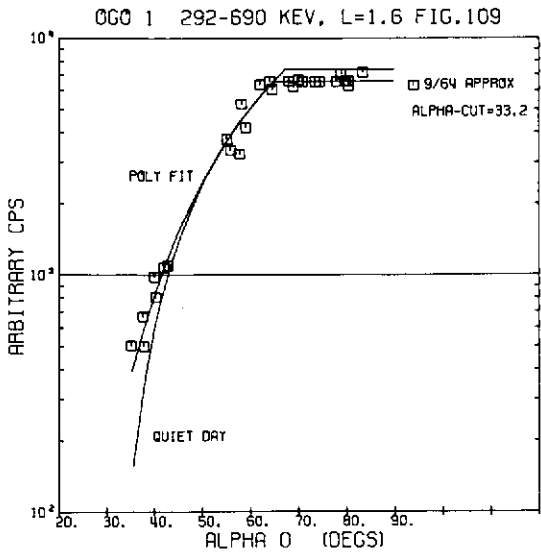
RESIDUAL STARFISH FLUX FIGURES 101 - 104



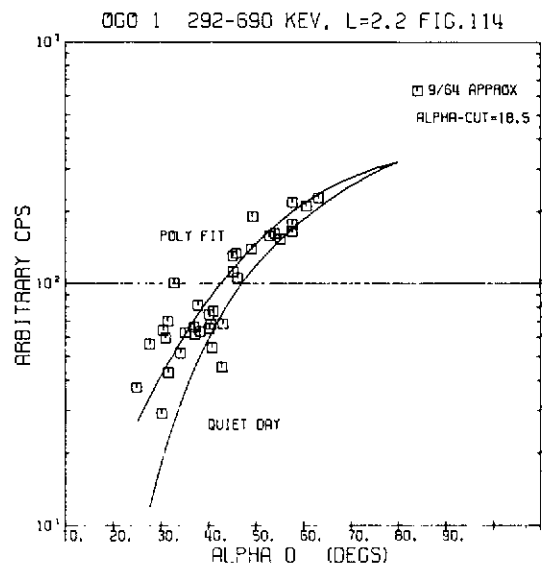
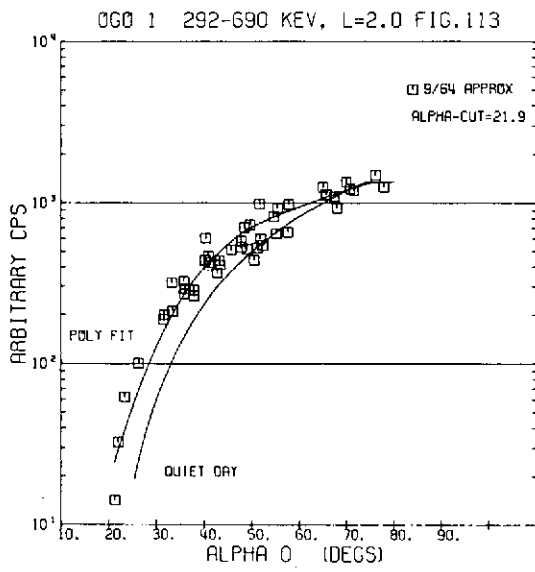
RESIDUAL STARFISH FLUX FIGURES 105 - 108



RESIDUAL STARFISH FLUX FIGURES 109 - 112



RESIDUAL STARFISH FLUX FIGURES 113 - 114



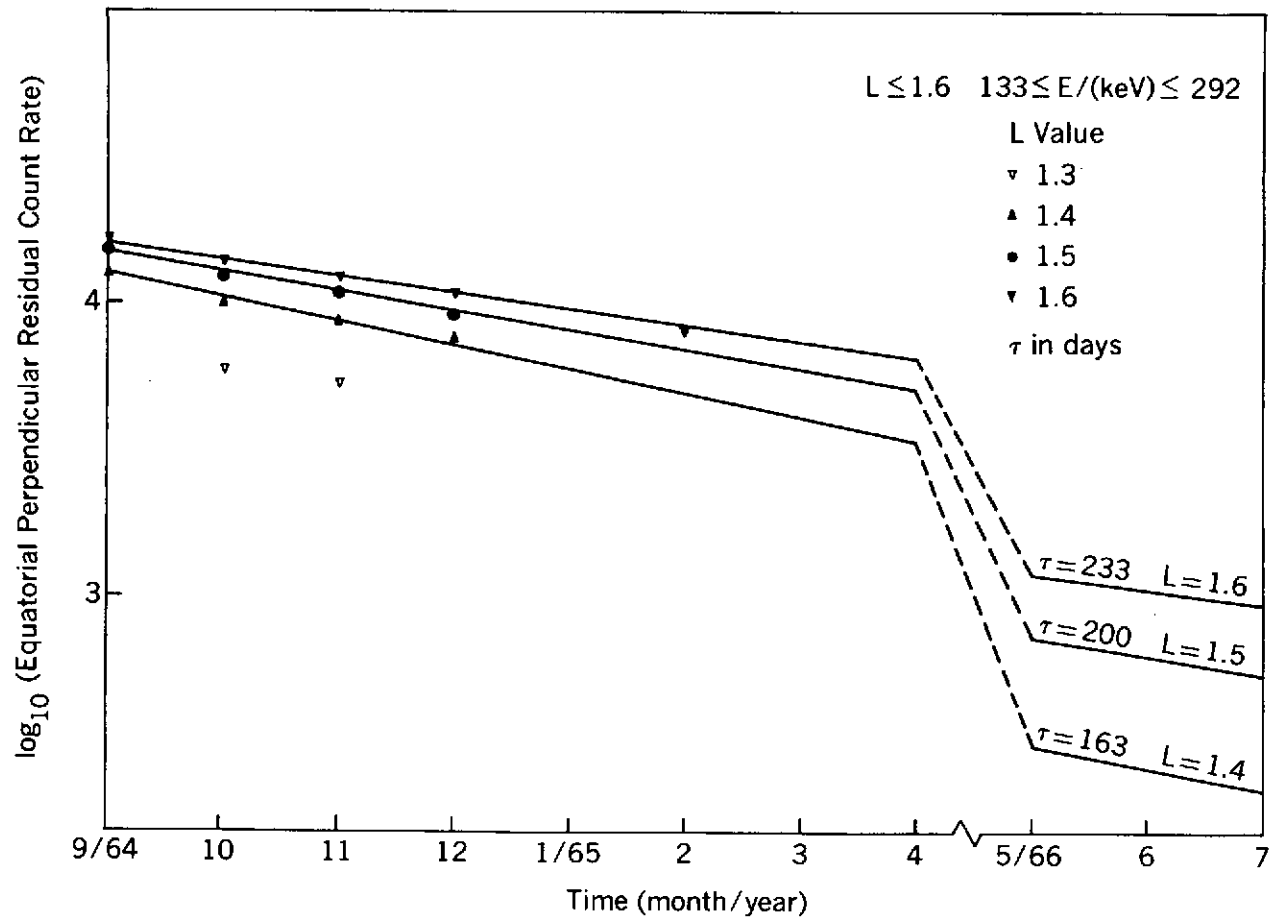


Figure 115. Temporal Variation of Residual Starfish Flux  
Based on OGO 1 Data

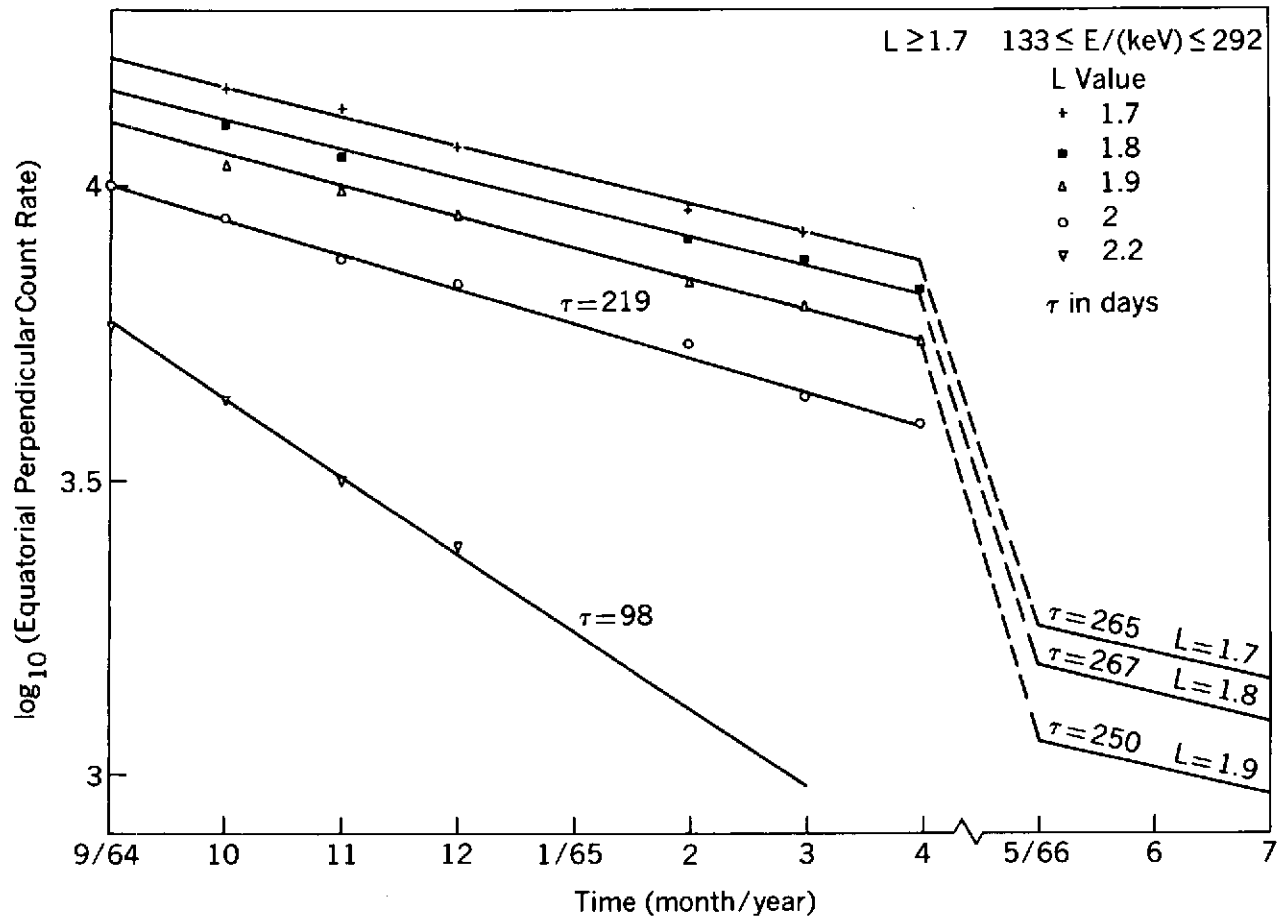


Figure 116. Temporal Variation of Residual Starfish Flux

Based on OGO 1 Data

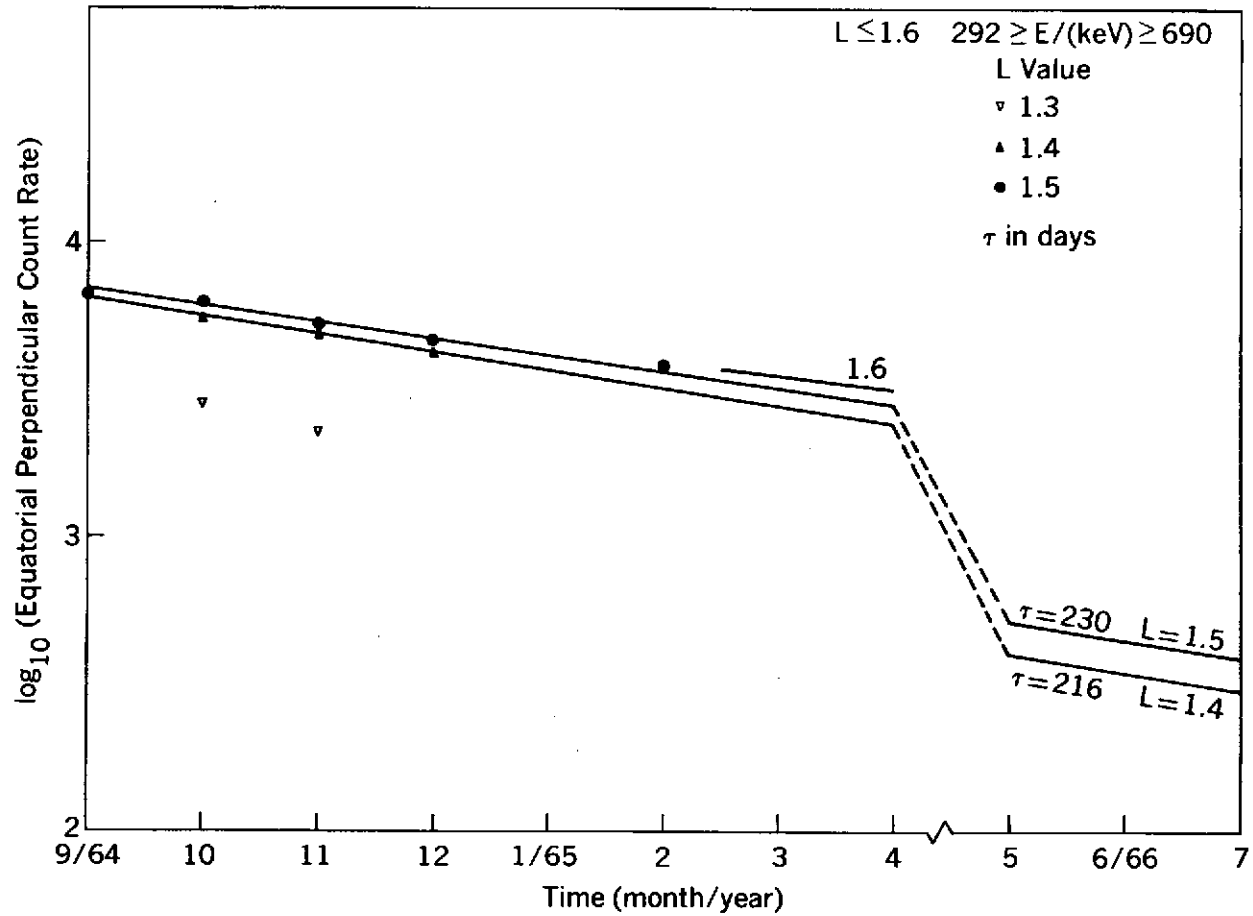


Figure 117. Temporal Variation of Residual Starfish Flux  
Based on OGO 1 Data

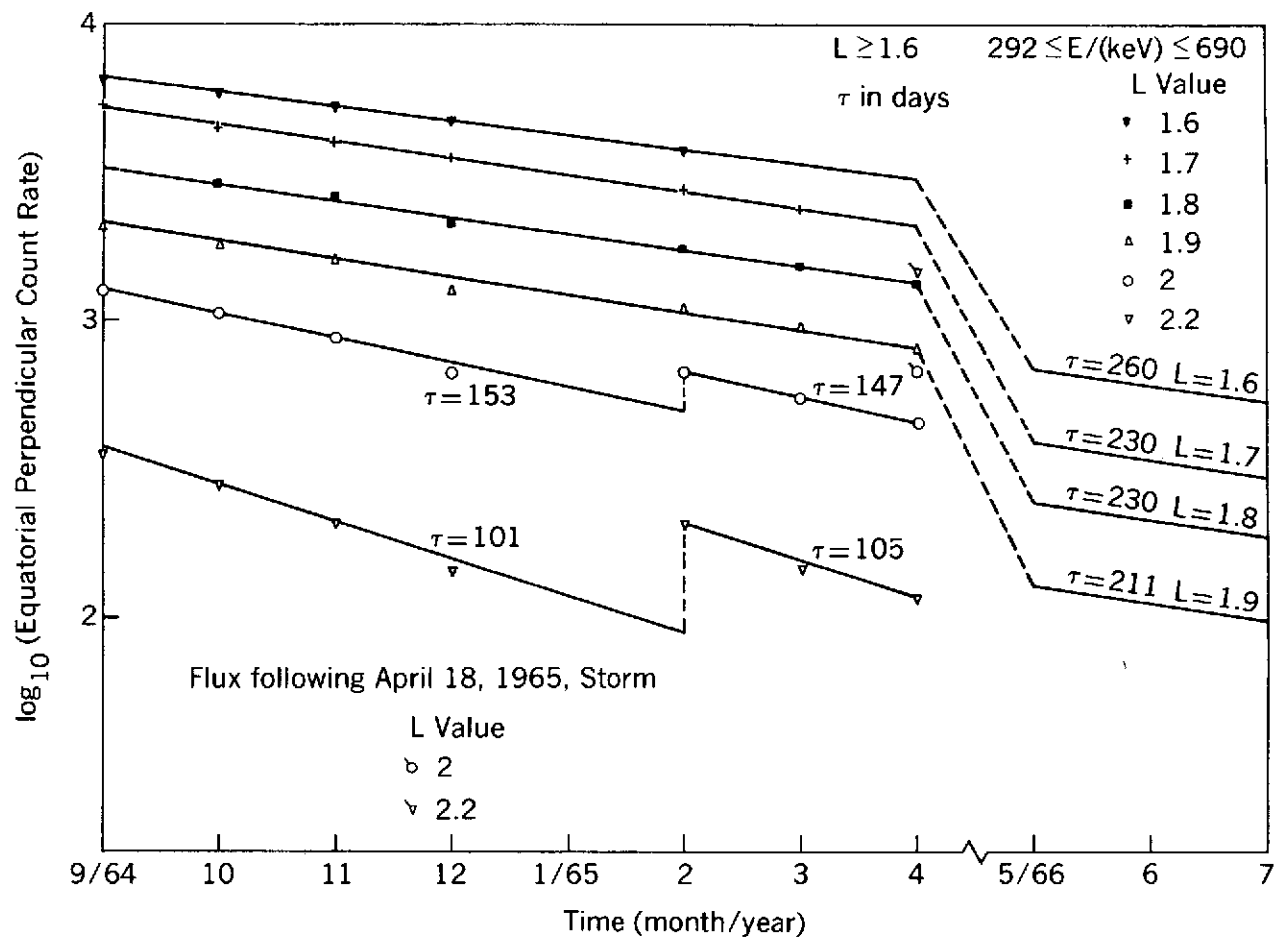
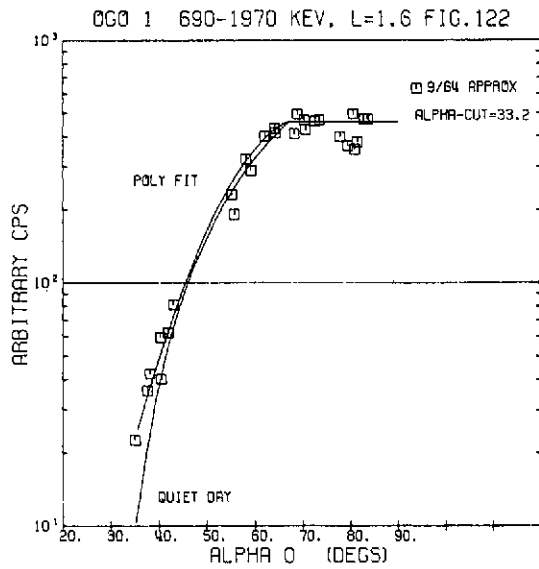
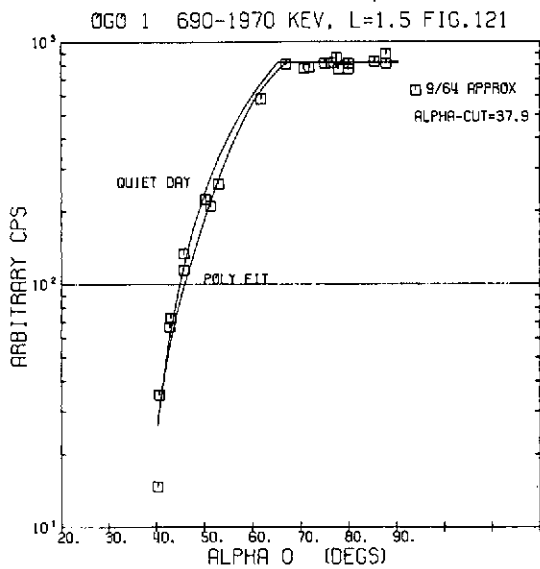
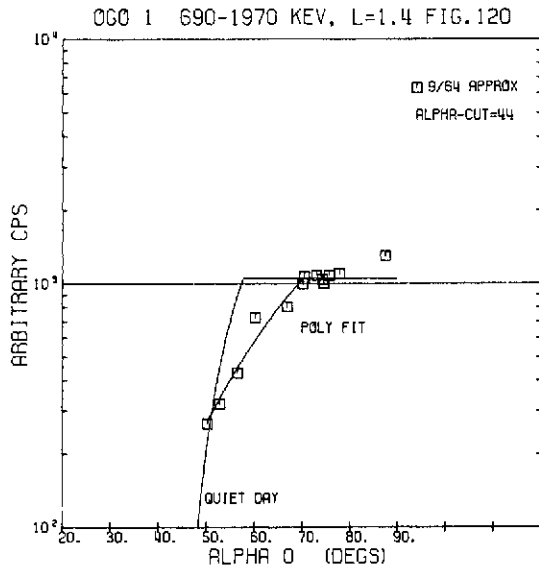
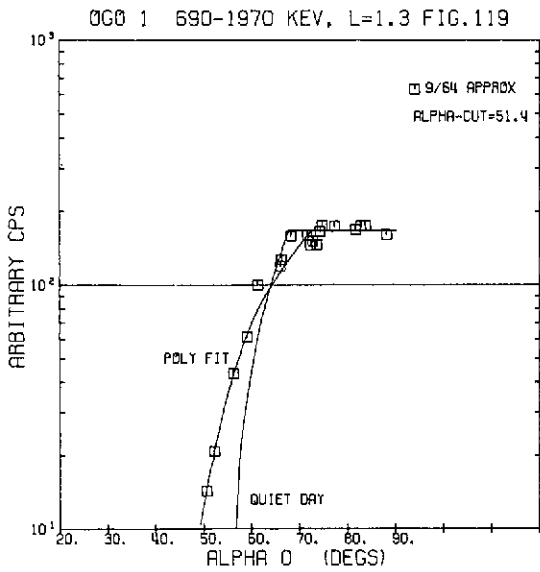
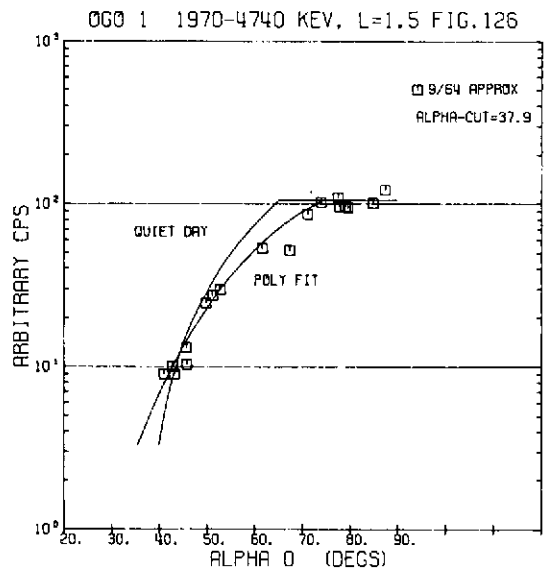
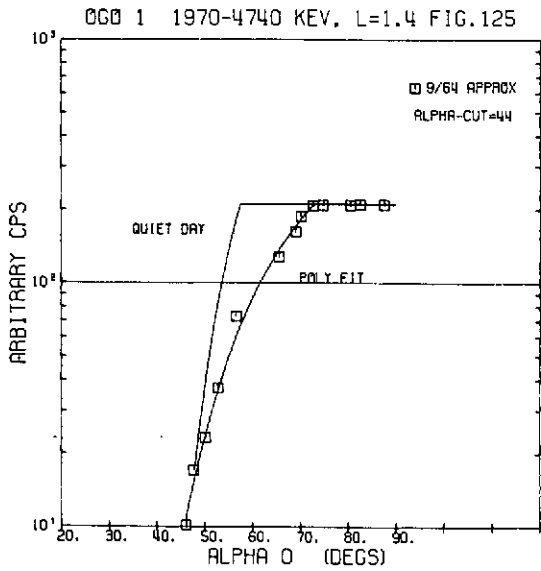
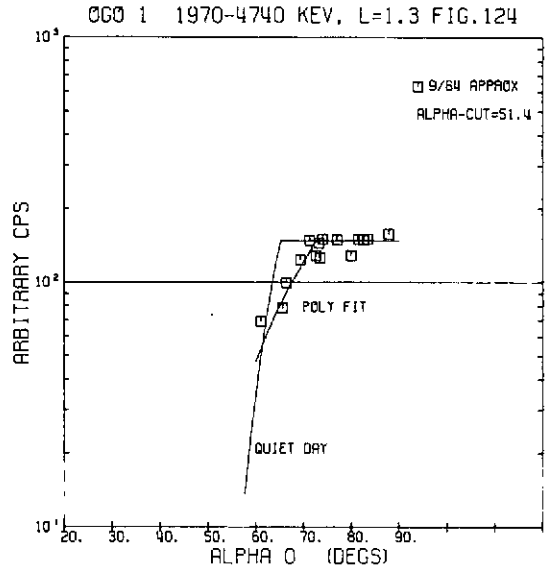
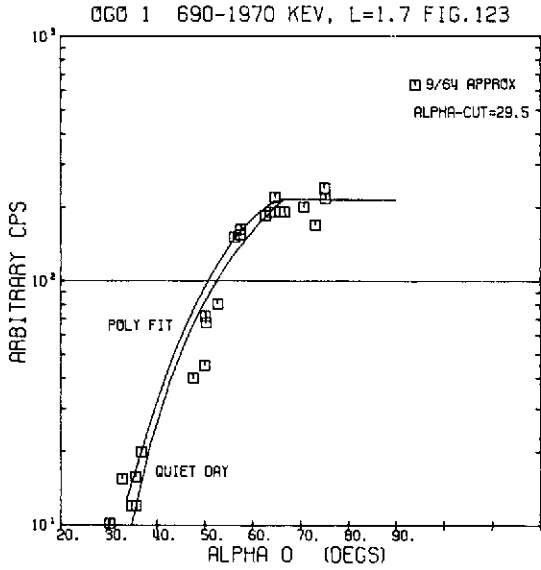


Figure 118. Temporal Variation of Residual Starfish Flux  
Based on OGO 1 Data

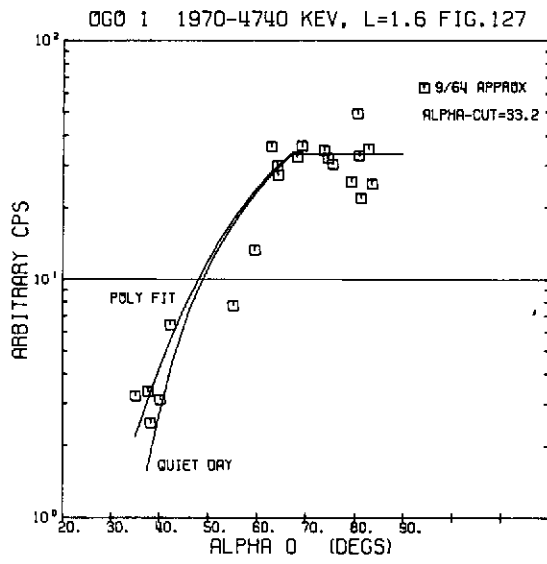
RESIDUAL STARFISH FLUX FIGURES 119 - 122



RESIDUAL STARFISH FLUX FIGURES 123 - 126



RESIDUAL STARFISH FLUX FIGURE 127



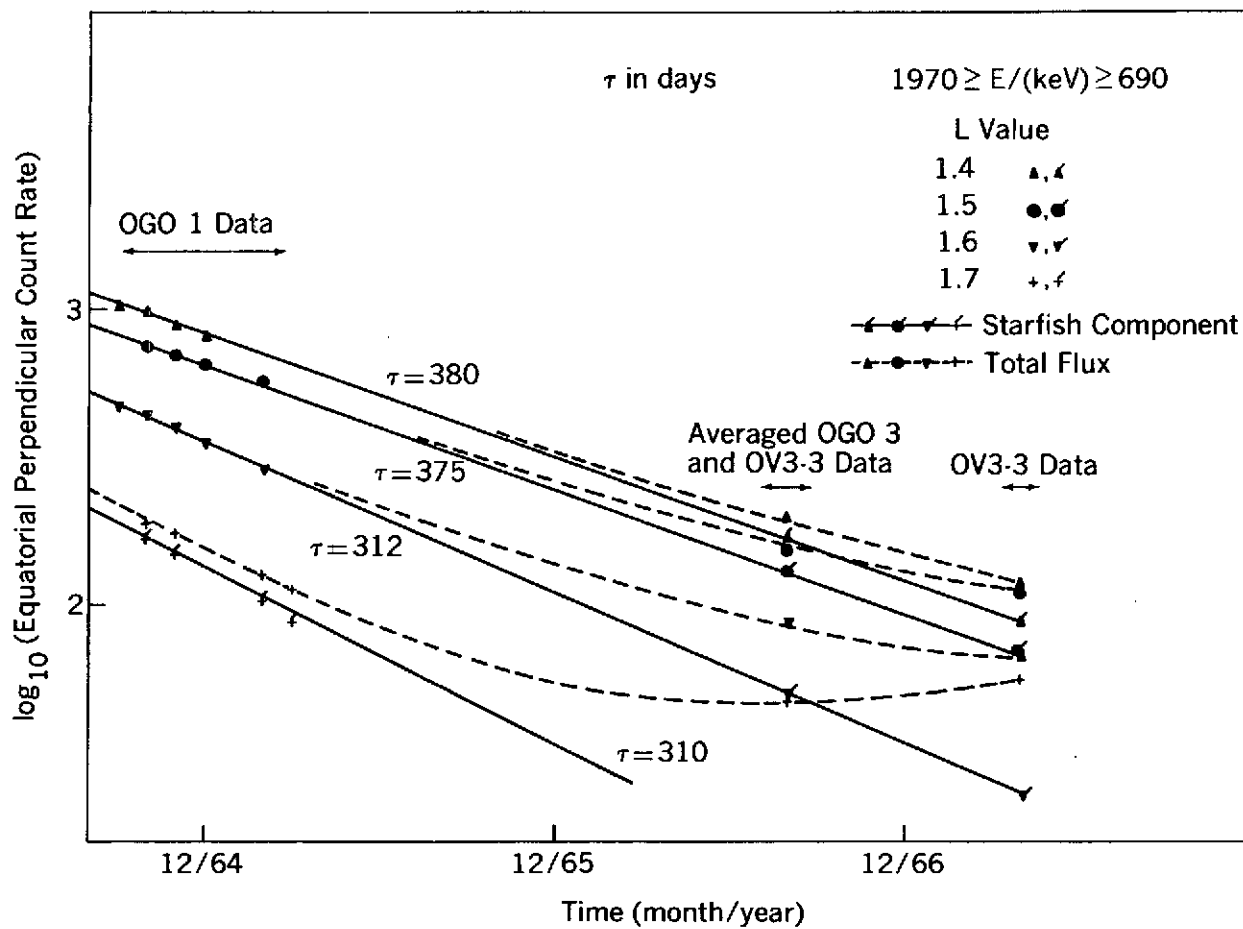


Figure 128. Temporal Variation of High-Energy Residual Starfish Flux

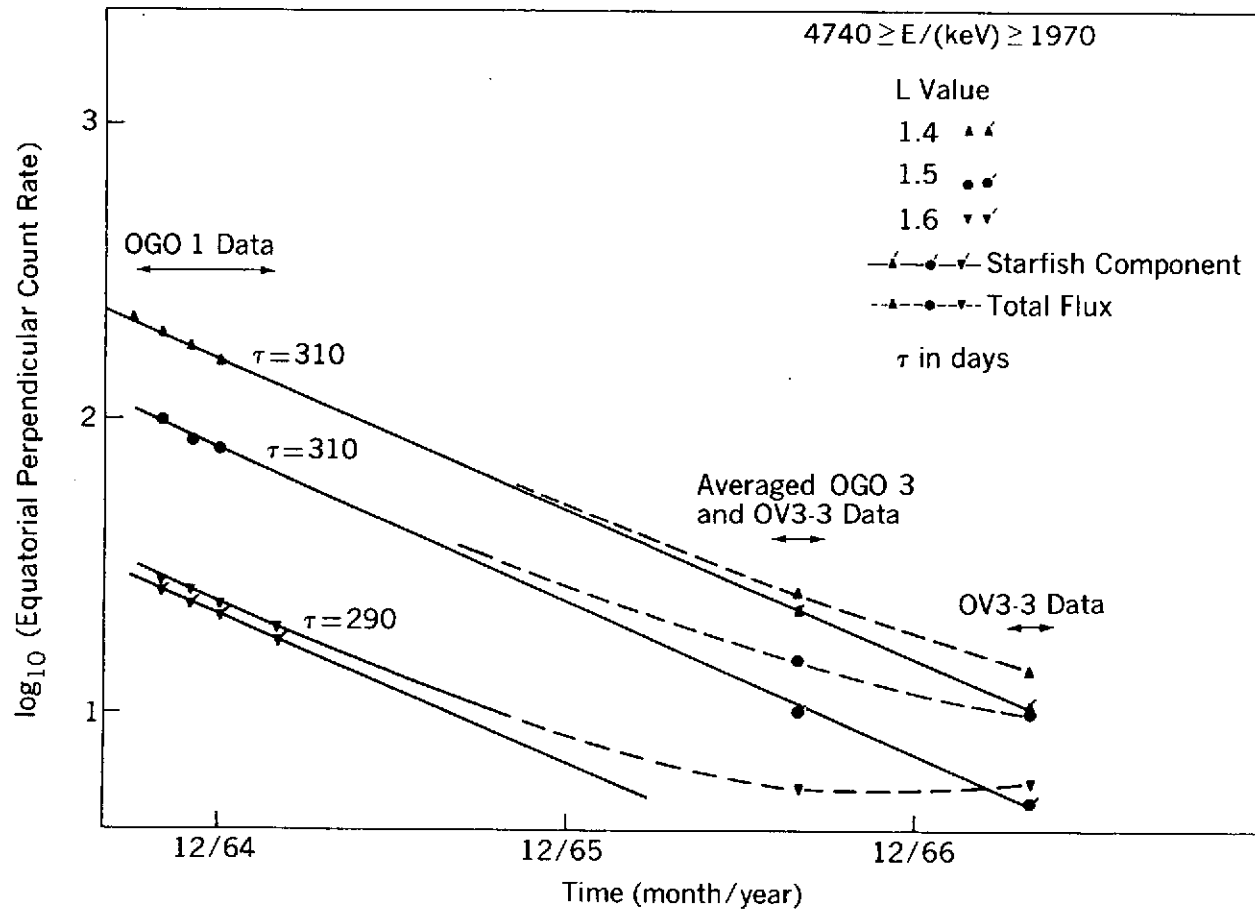


Figure 129. Temporal Variation of High-Energy Residual Starfish Flux

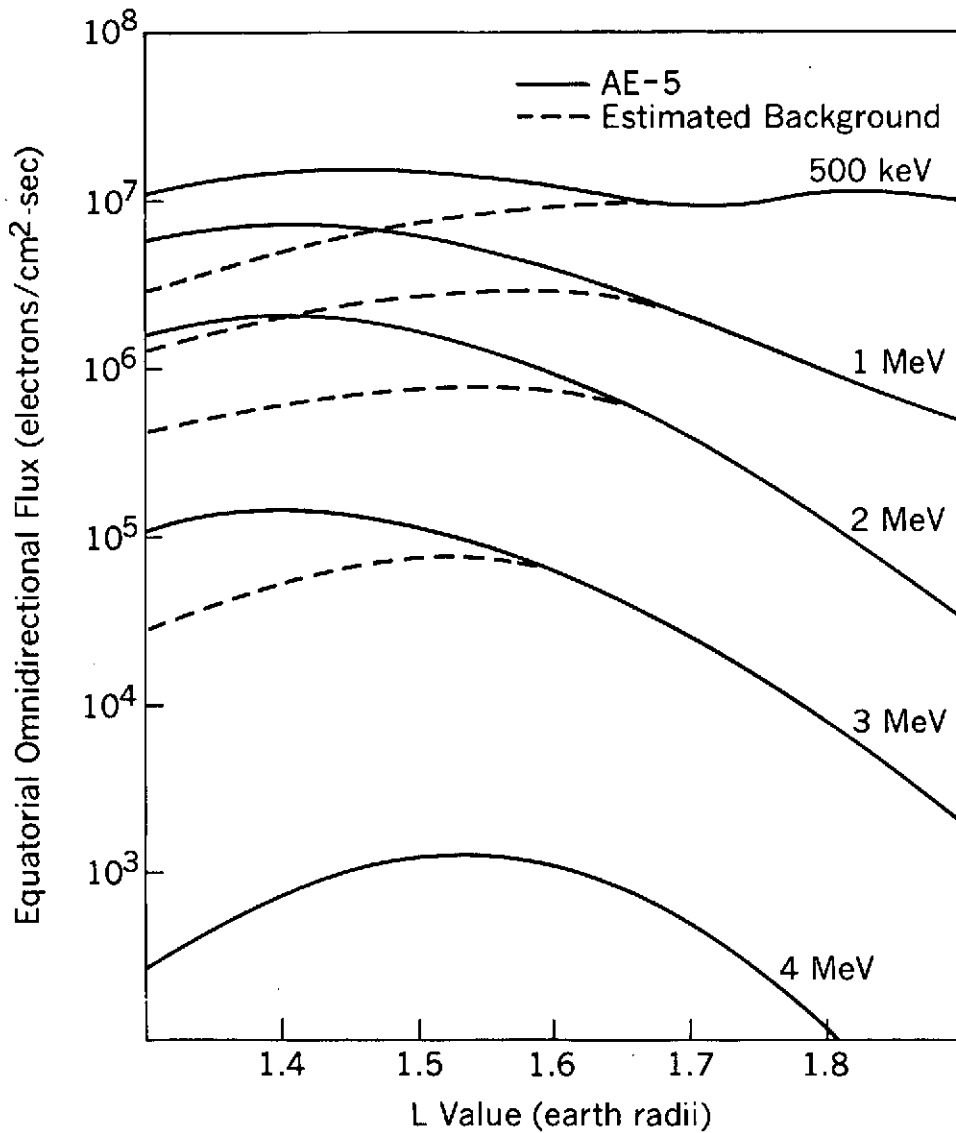


Figure 130. Estimated High-Energy Omnidirectional Background Flux

The AE-5 model radial profiles are shown for a variety of energies (solid lines) for epoch 1967. The broken lines indicate the estimated flux after the Starfish flux component has decayed completely.

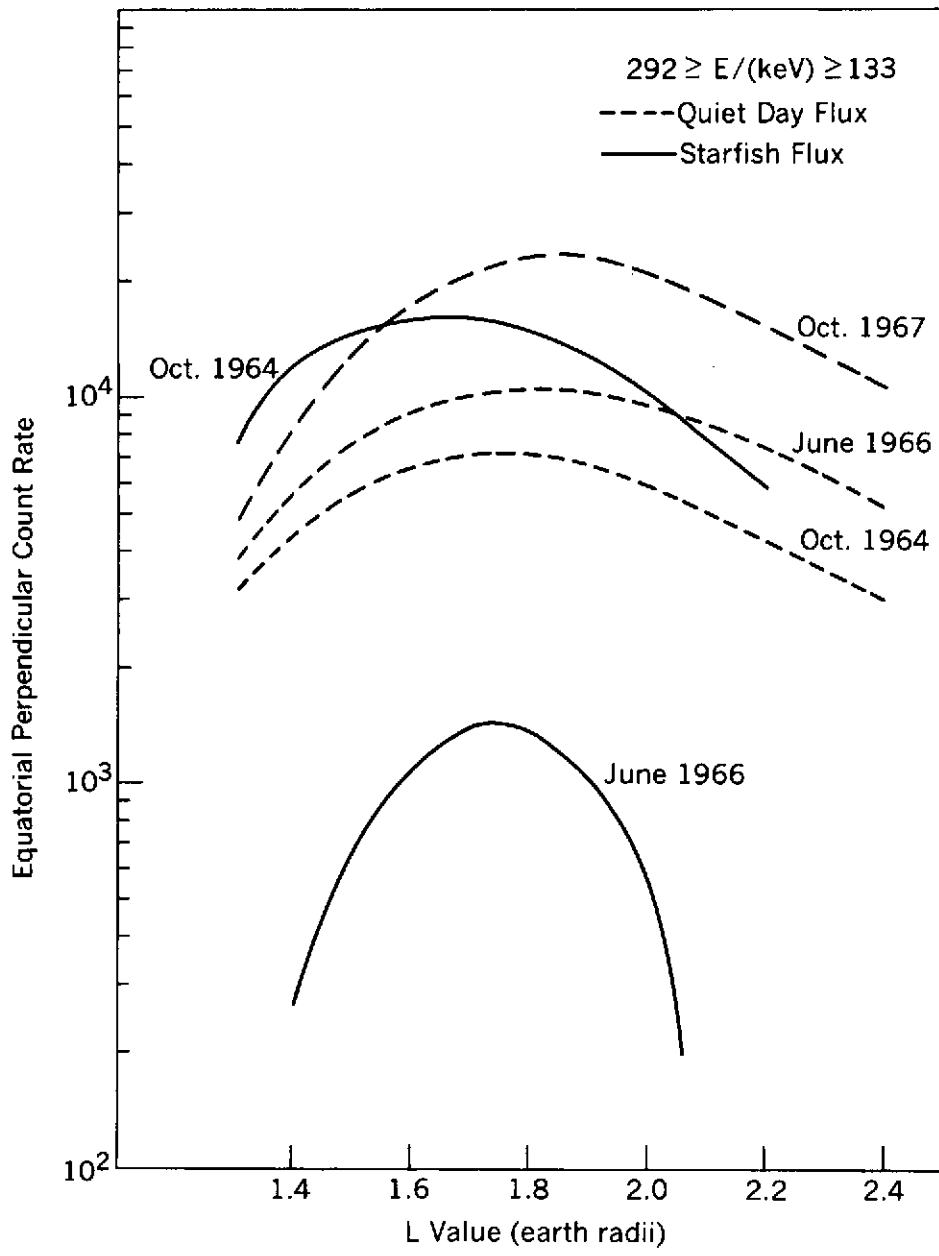


Figure 131. Flux Component Radial Profiles

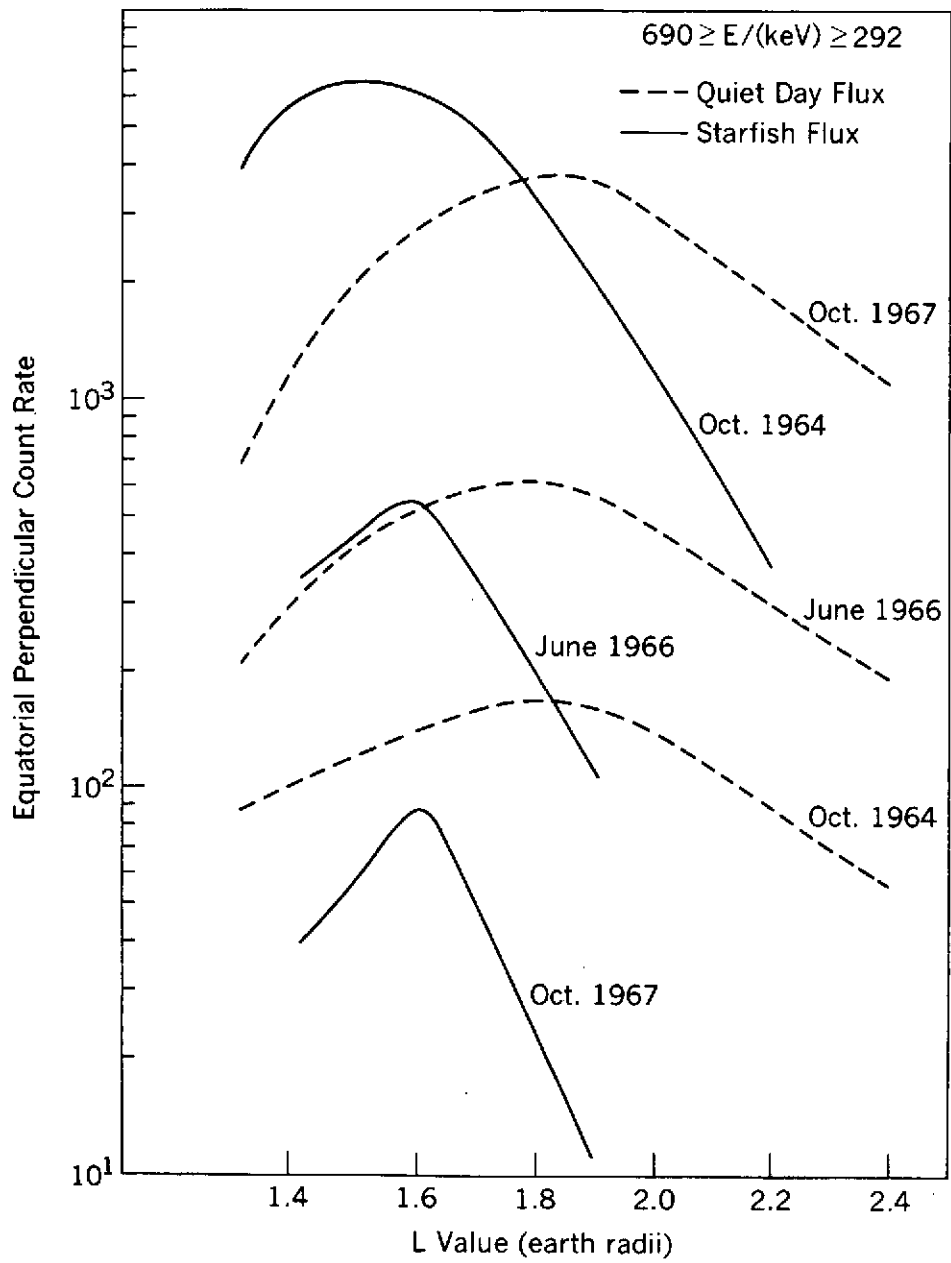


Figure 132. Flux Component Radial Profiles

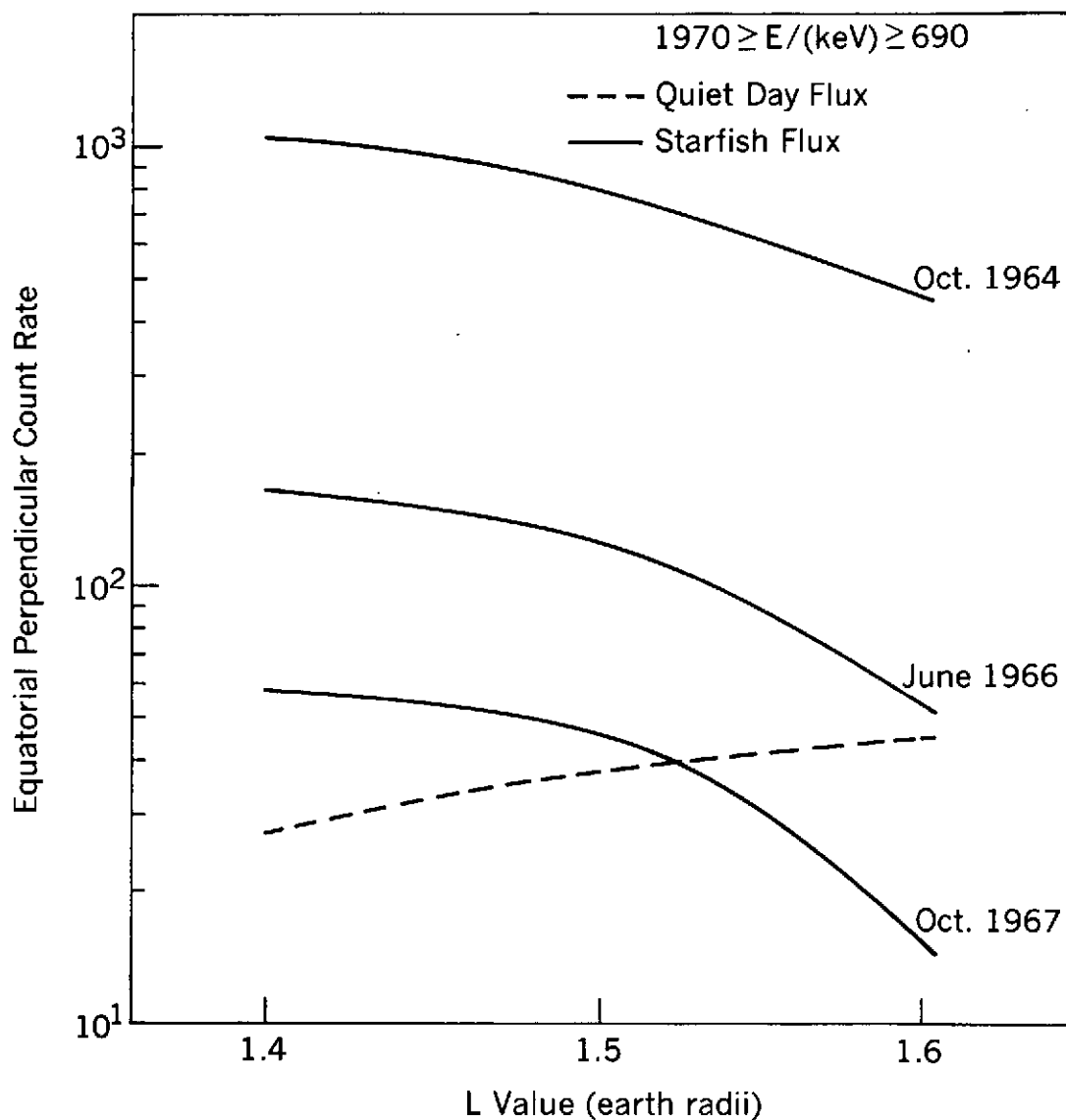


Figure 133. Flux Component Radial Profiles

The Starfish flux and quiet day flux components are compared. The broken line indicates the estimated flux after the Starfish flux component has decayed completely. No time dependence is given for this quiet day flux, and thus it has an arbitrary epoch.

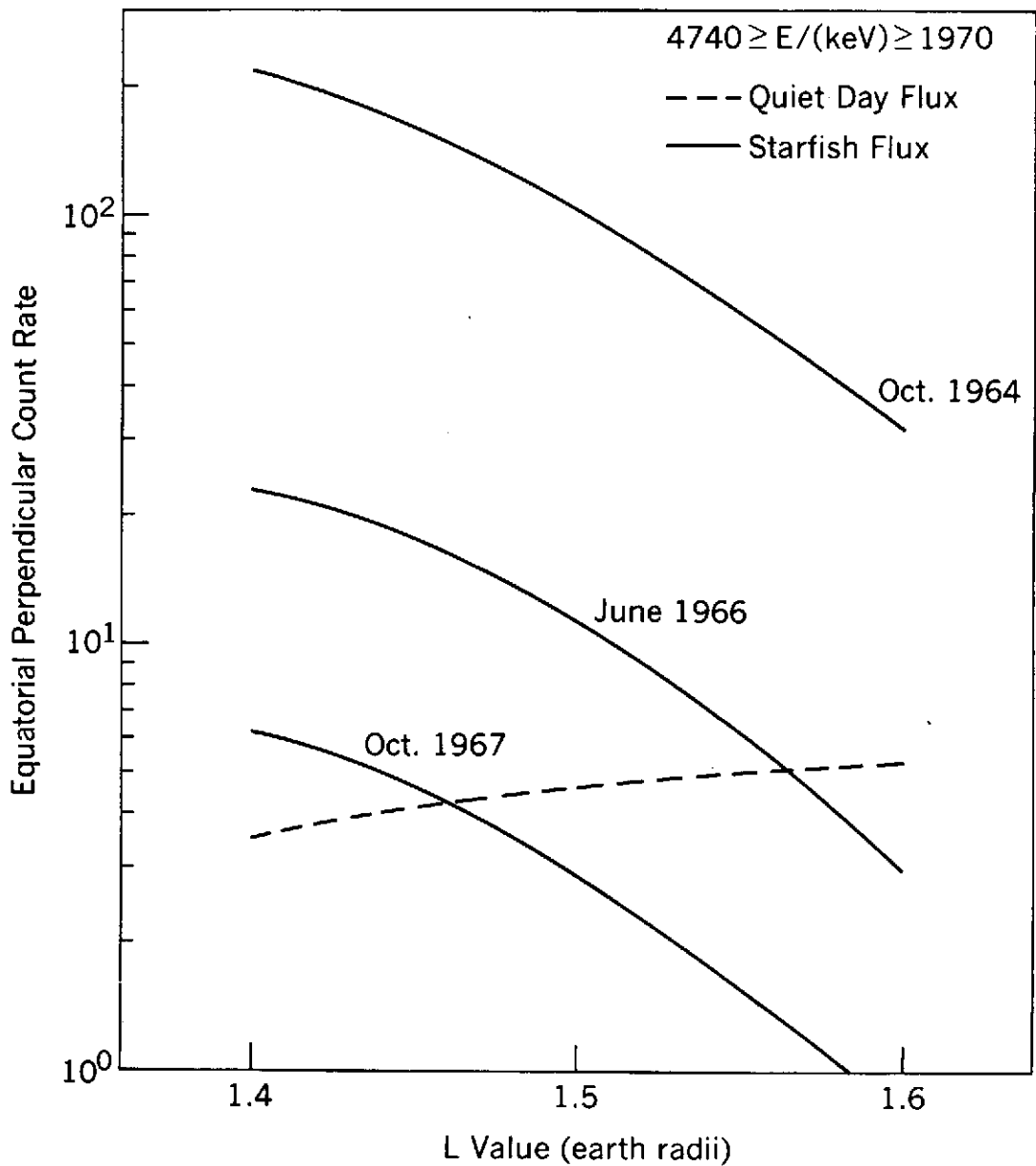


Figure 134. Flux Component Radial Profiles

The Starfish flux and quiet day flux components are compared. The broken line indicates the estimated flux after the Starfish flux component has decayed completely. No time dependence is given for this quiet day flux, and thus it has an arbitrary epoch.

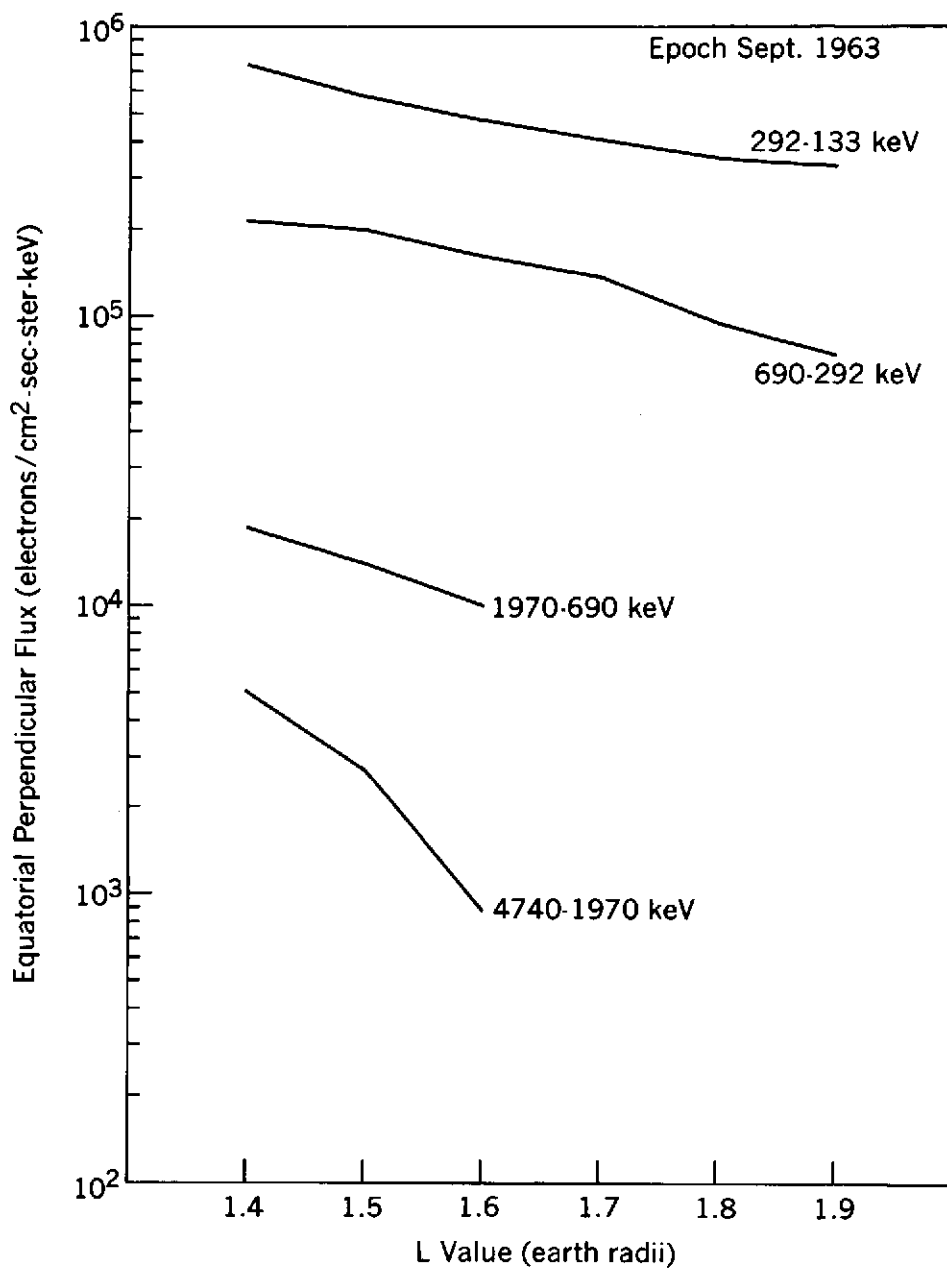


Figure 135. Extrapolated Starfish Radial Profiles

The Starfish model radial profiles for September 1964 are extrapolated to September 1963 to indicate the monotonic radial profile for this epoch.

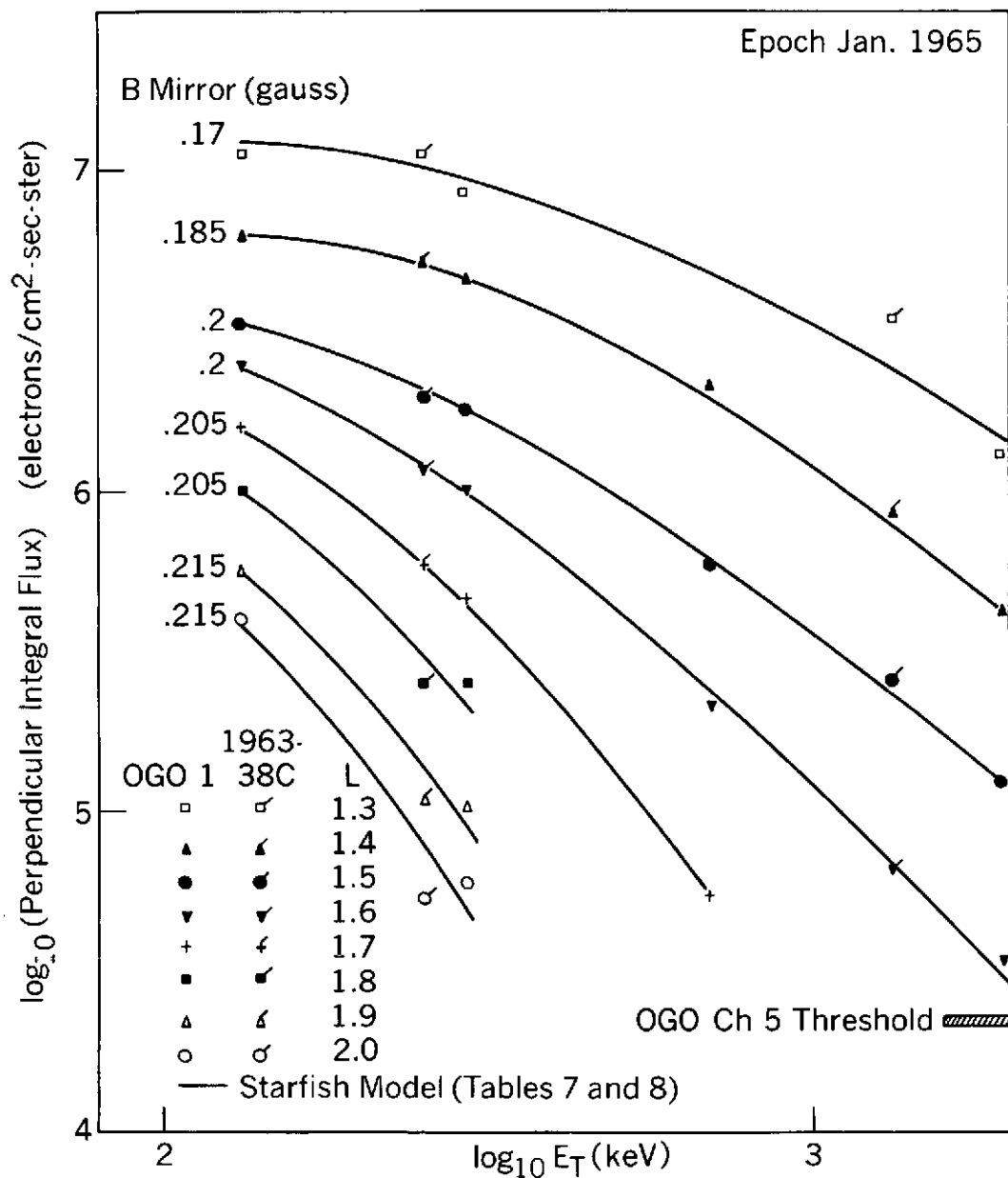


Figure 136. Comparison of OGO 3 and 1963-38C Integral Residual Spectra

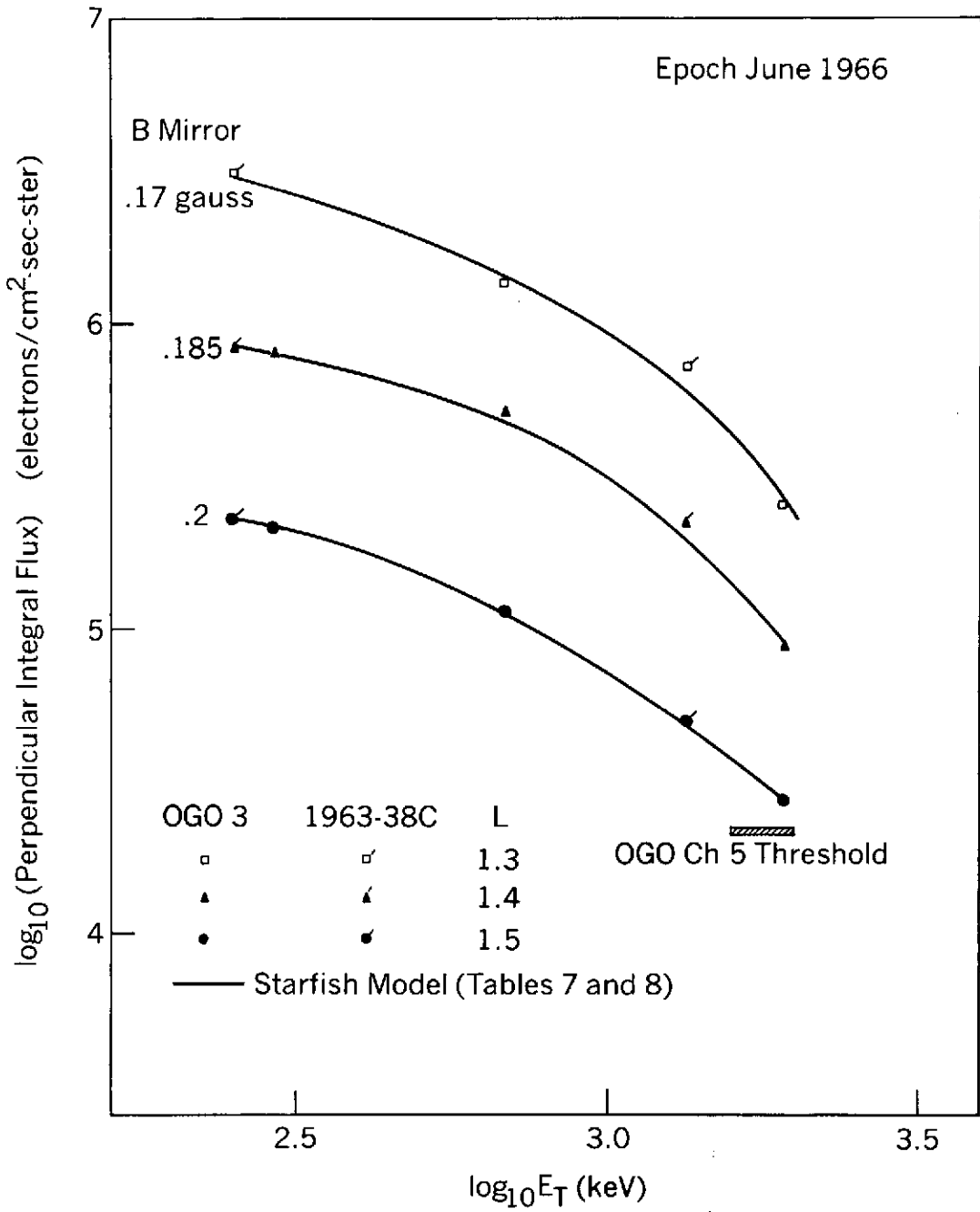


Figure 137. Comparison of OGO 3 and 1963-38C Integral Residual Spectra

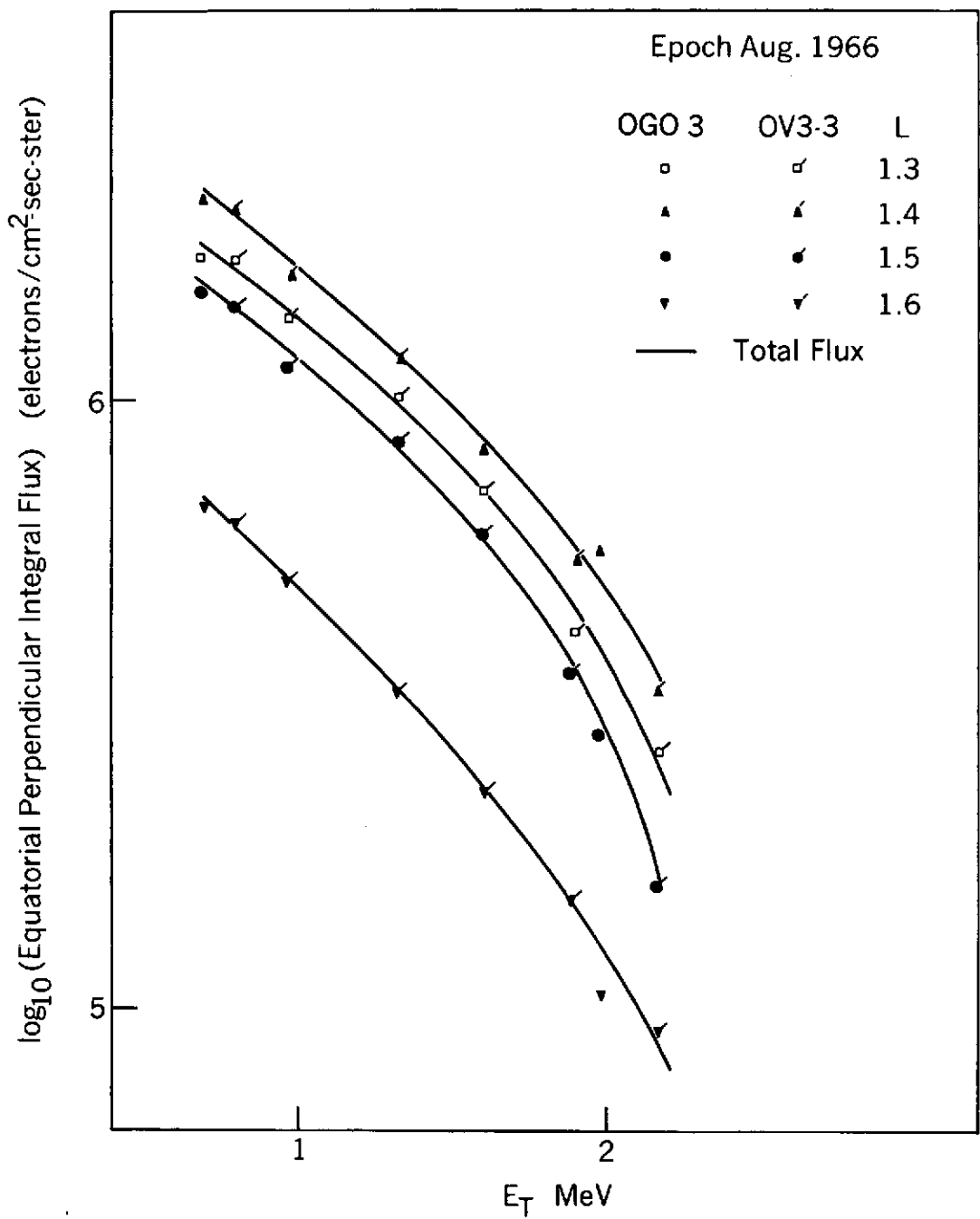


Figure 138. Comparison of OGO 3 and OV3-3 Integral Spectra

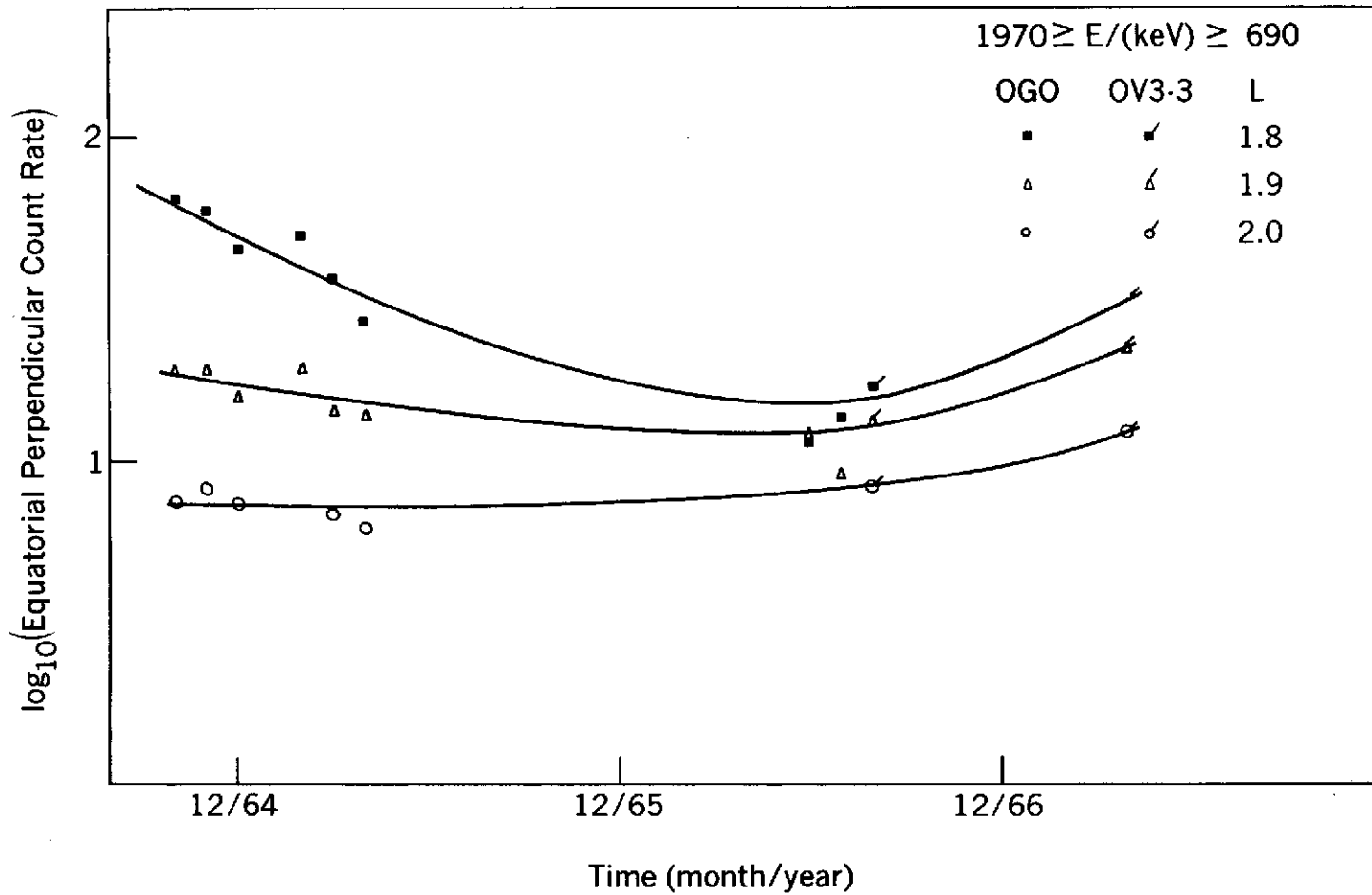


Figure 139. Comparison of OGO 3 and OV3-3 Flux

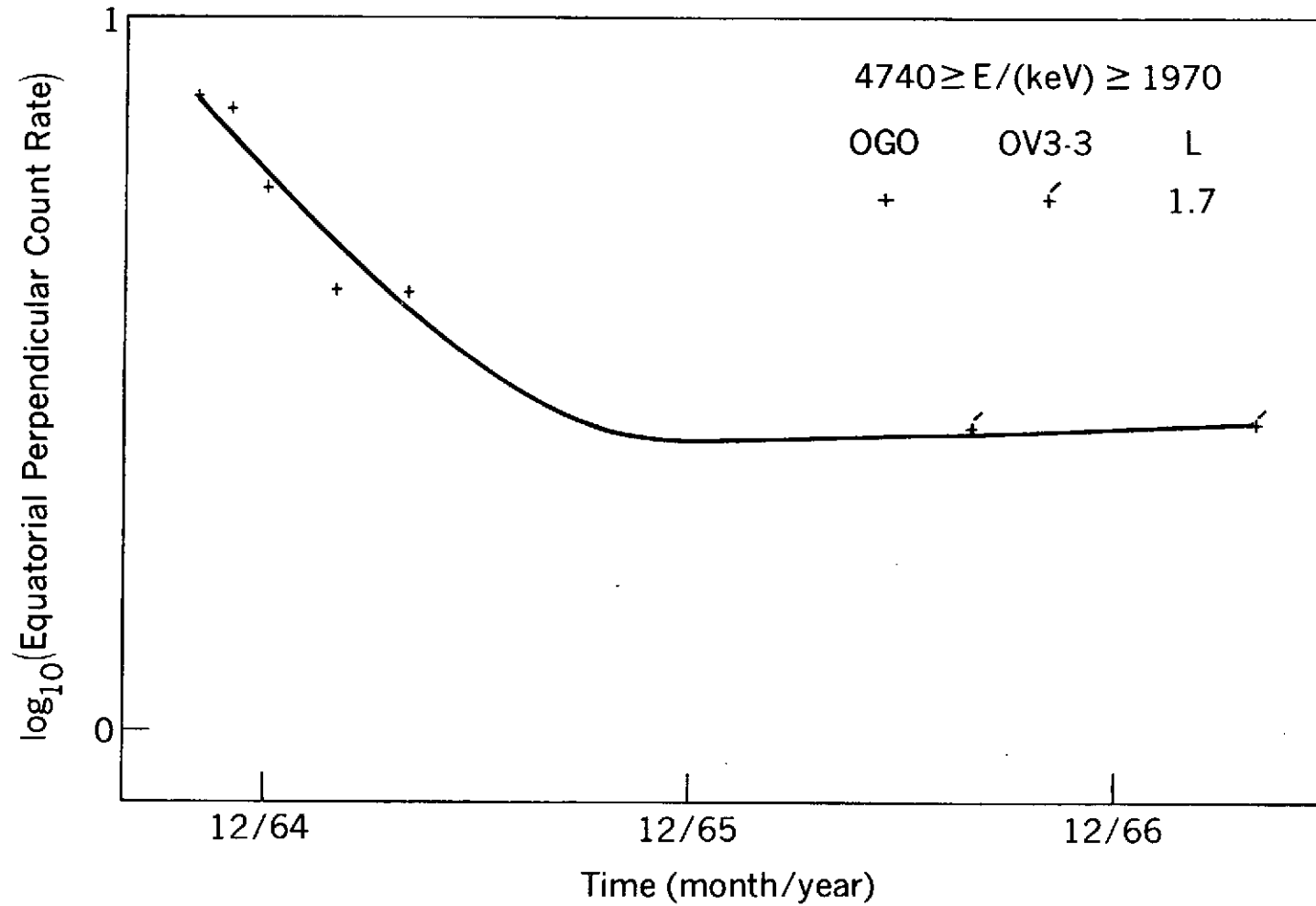


Figure 140. Comparison of OGO 3 and OV3-3 Flux

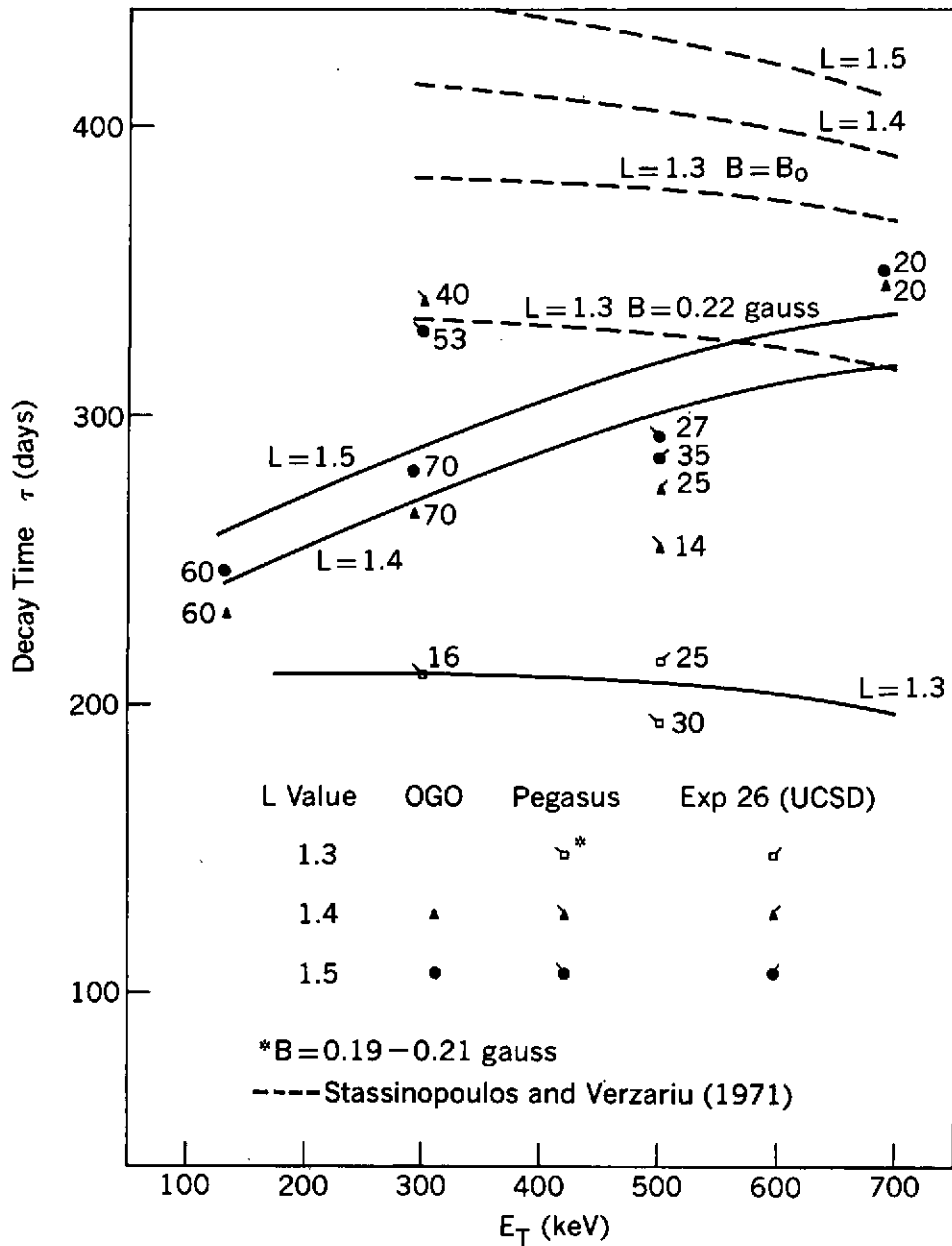
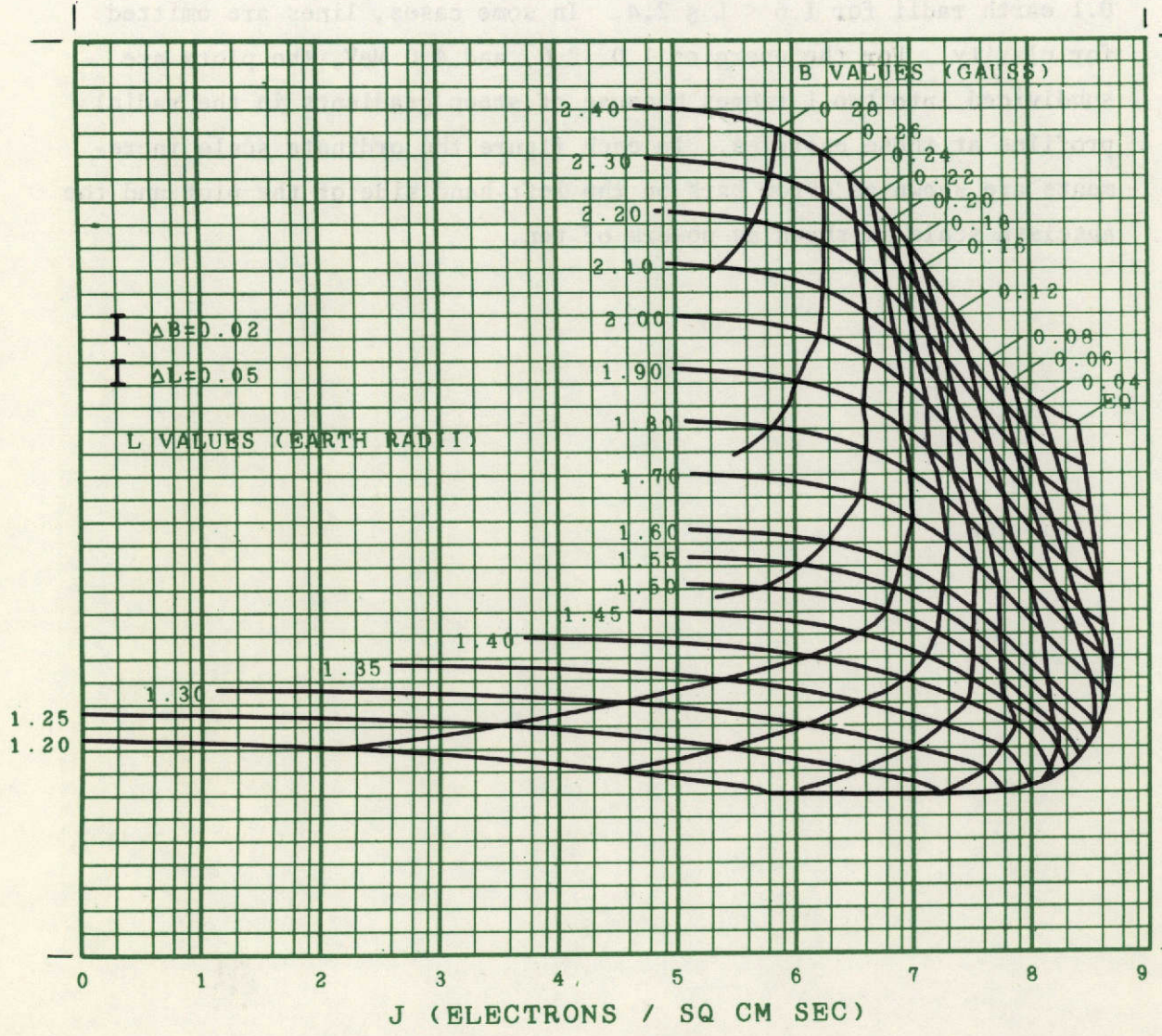


Figure 141. Comparison of OGO, Pegasus, and Explorer 26 Decay Times

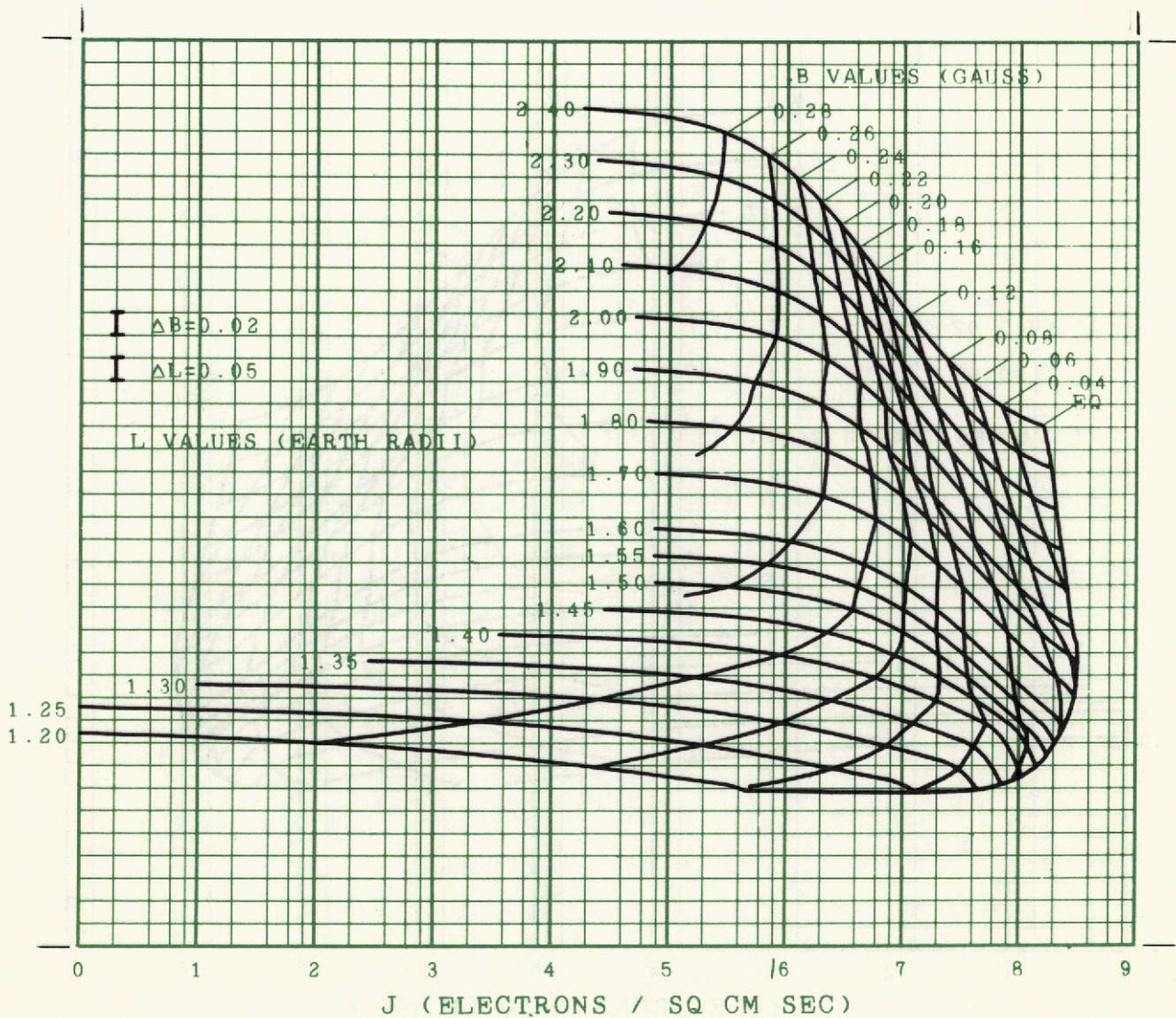
Starfish decay time data from various satellites are compared with the Stassinopoulos and Verzariu model (broken lines). The solid lines indicate the trends suggested by the data. The figures at the side of the data points represent estimates of the errors in days.

Figures 142-148. These computer-generated plots present carpet plots of the AE-5 omnidirectional flux as functions of B and L for threshold energies  $E_T = 0.04, 0.1, 0.25, 0.5, 1.0, 2.0,$  and  $4.0$  MeV. A description of the use of these carpet plots is given in Appendix A. In general, lines of constant B are presented in 0.02-gauss increments from the equator to 0.28 gauss, and lines of constant L are presented in increments of 0.05 earth radii for  $1.2 \leq L \leq 1.6$  and increments of 0.1 earth radii for  $1.6 < L \leq 2.4$ . In some cases, lines are omitted for clarity. For the energies 1.0, 2.0, and 4.0 MeV, the plots are subdivided into two L ranges because of steep gradients in the radial profiles at these energies. In each figure the ordinate scale increments are shown as error bars on the left-hand side of the plot and the abscissa scale is shown as powers of ten.

FIGURE 142  
 AE5 OMNIDIRECTIONAL INTEGRAL FLUX, ET=40 KEV  
 EPOCH OCTOBER 1967



**FIGURE 143**  
**AE5 OMNIDIRECTIONAL INTEGRAL FLUX, ET=100 KEV**  
**EPOCH OCTOBER 1967**



AE5 OMNIDIRECTIONAL INTEGRAL FLUX, ET=250 KEV  
 EPOCH OCTOBER 1967

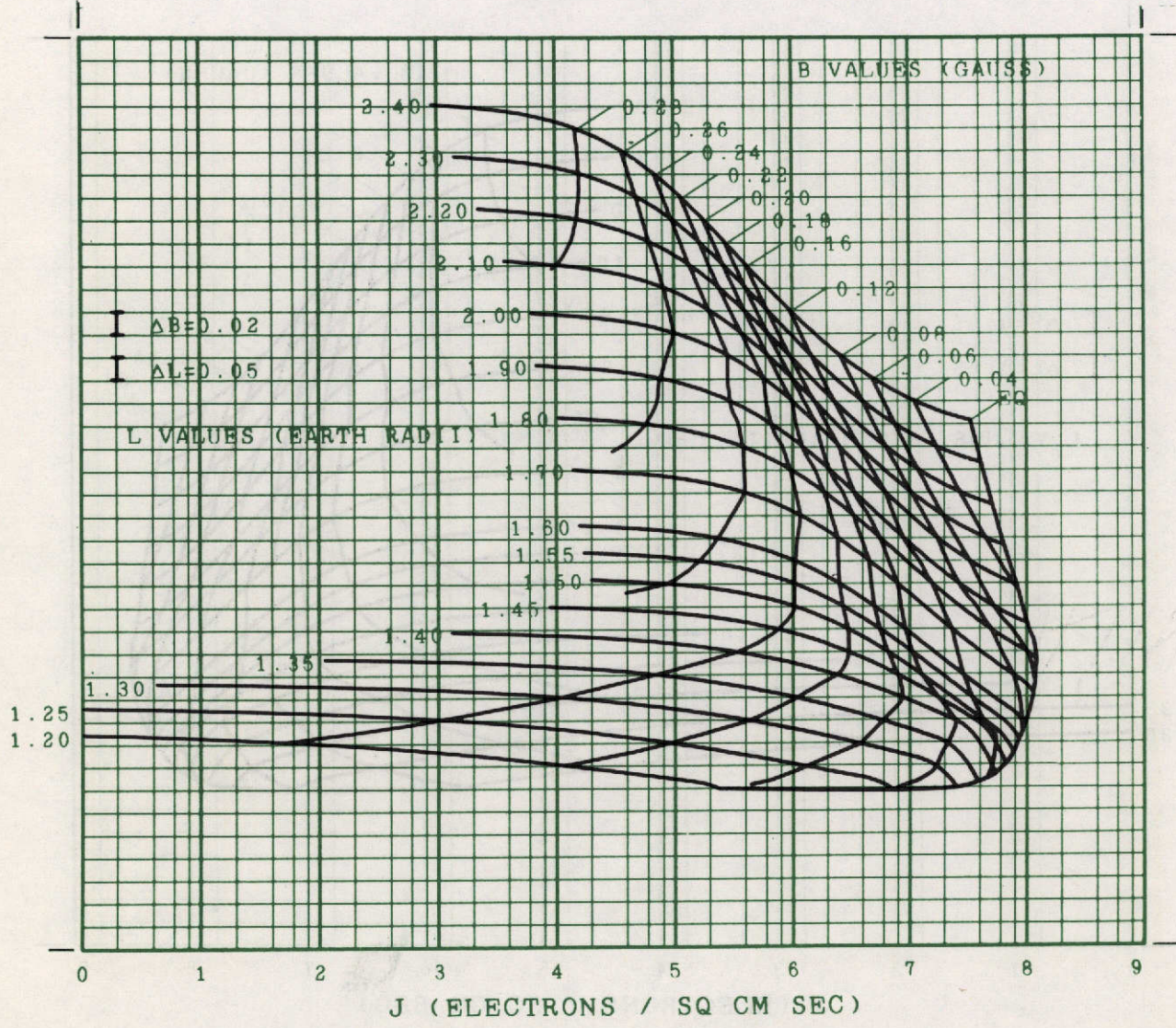


**FIGURE 145**  
**AE5 OMNIDIRECTIONAL INTEGRAL FLUX, ET=500 KEV**  
**EPOCH OCTOBER 1967**

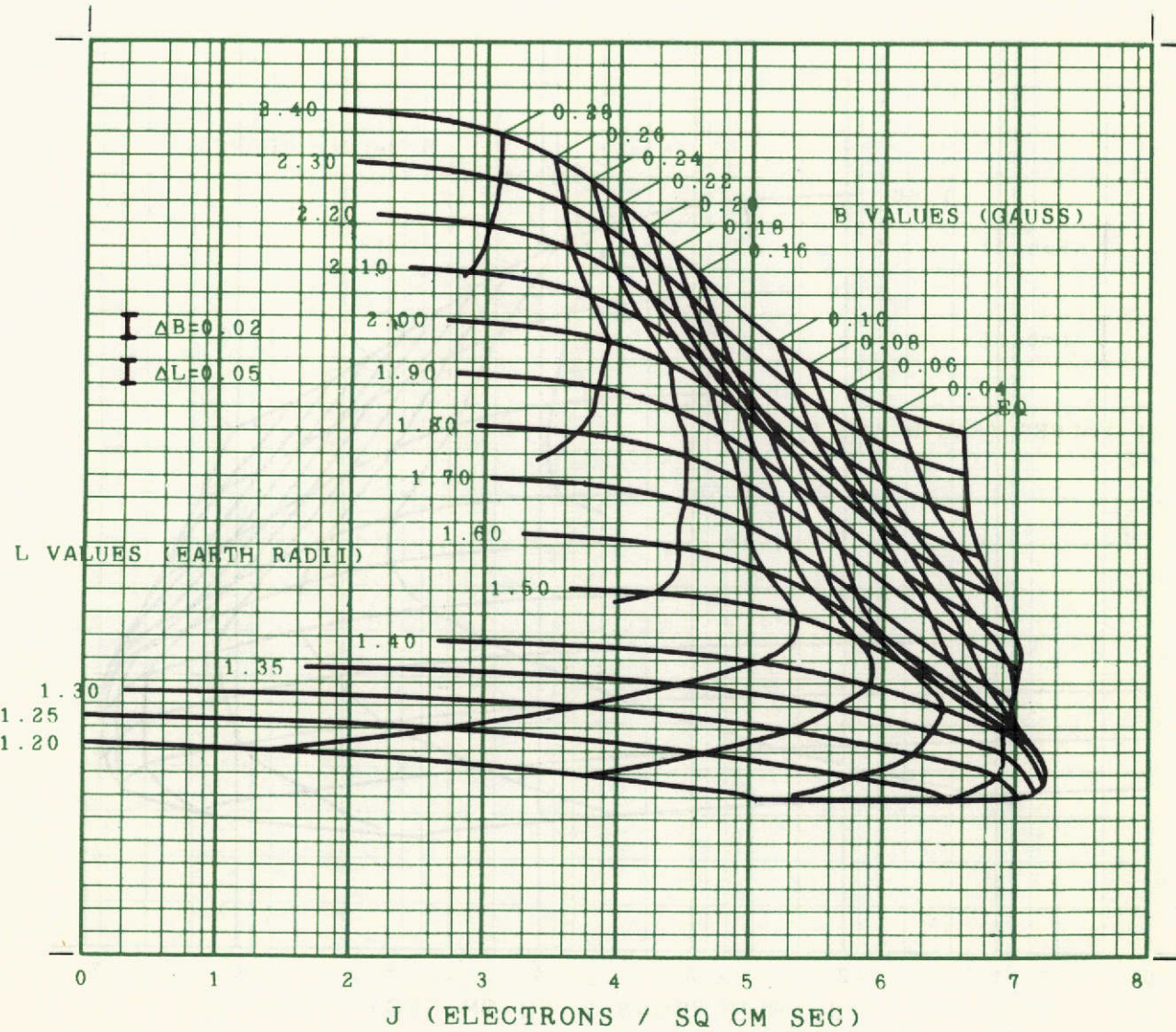


FIGURE 146

AE5 OMNIDIRECTIONAL INTEGRAL FLUX, ET=1 MEV  
EPOCH OCTOBER 1967

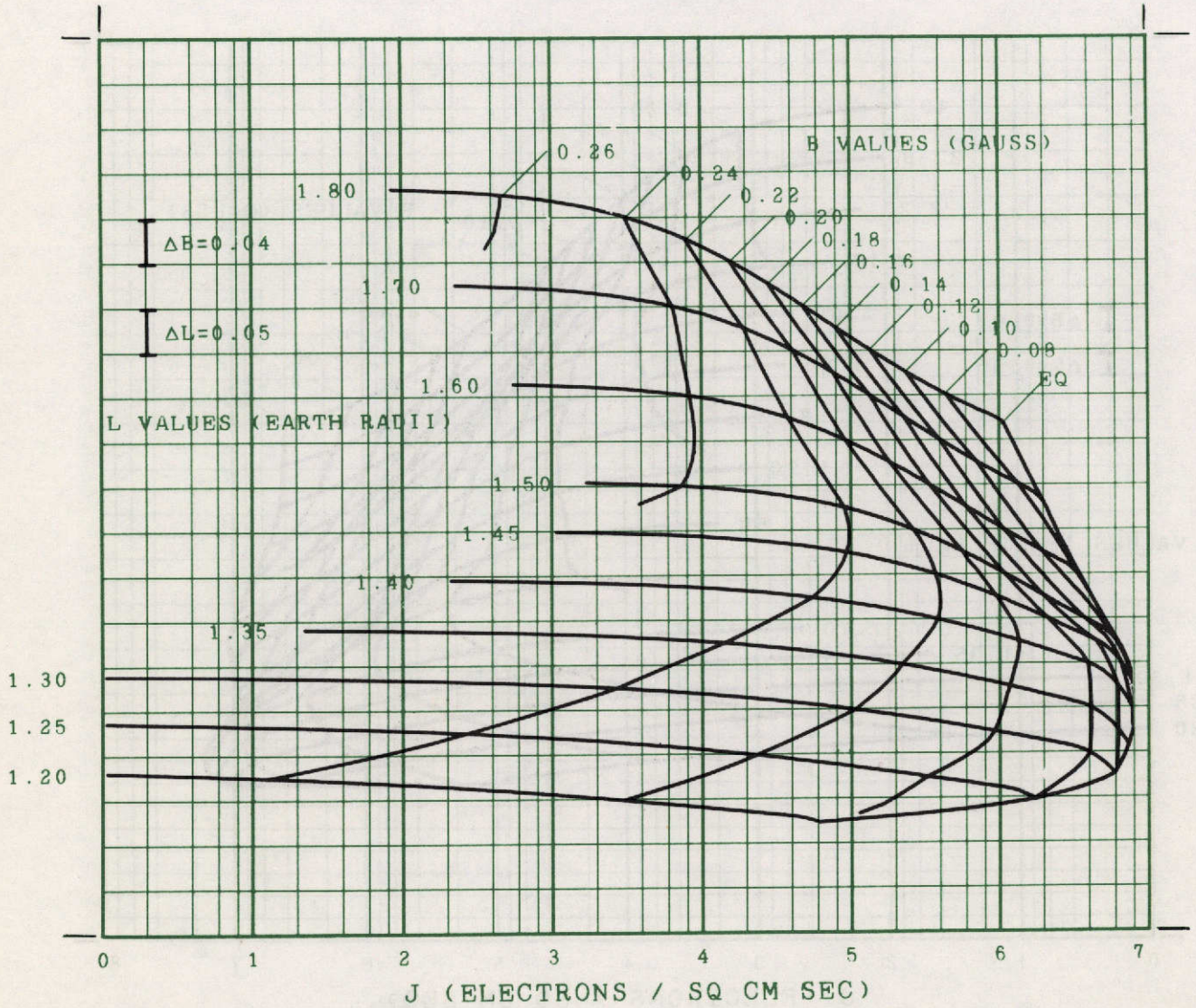


FIGURE 146 CONT  
 AE5 OMNIDIRECTIONAL INTEGRAL FLUX, ET=1 MEV  
 EPOCH OCTOBER 1967

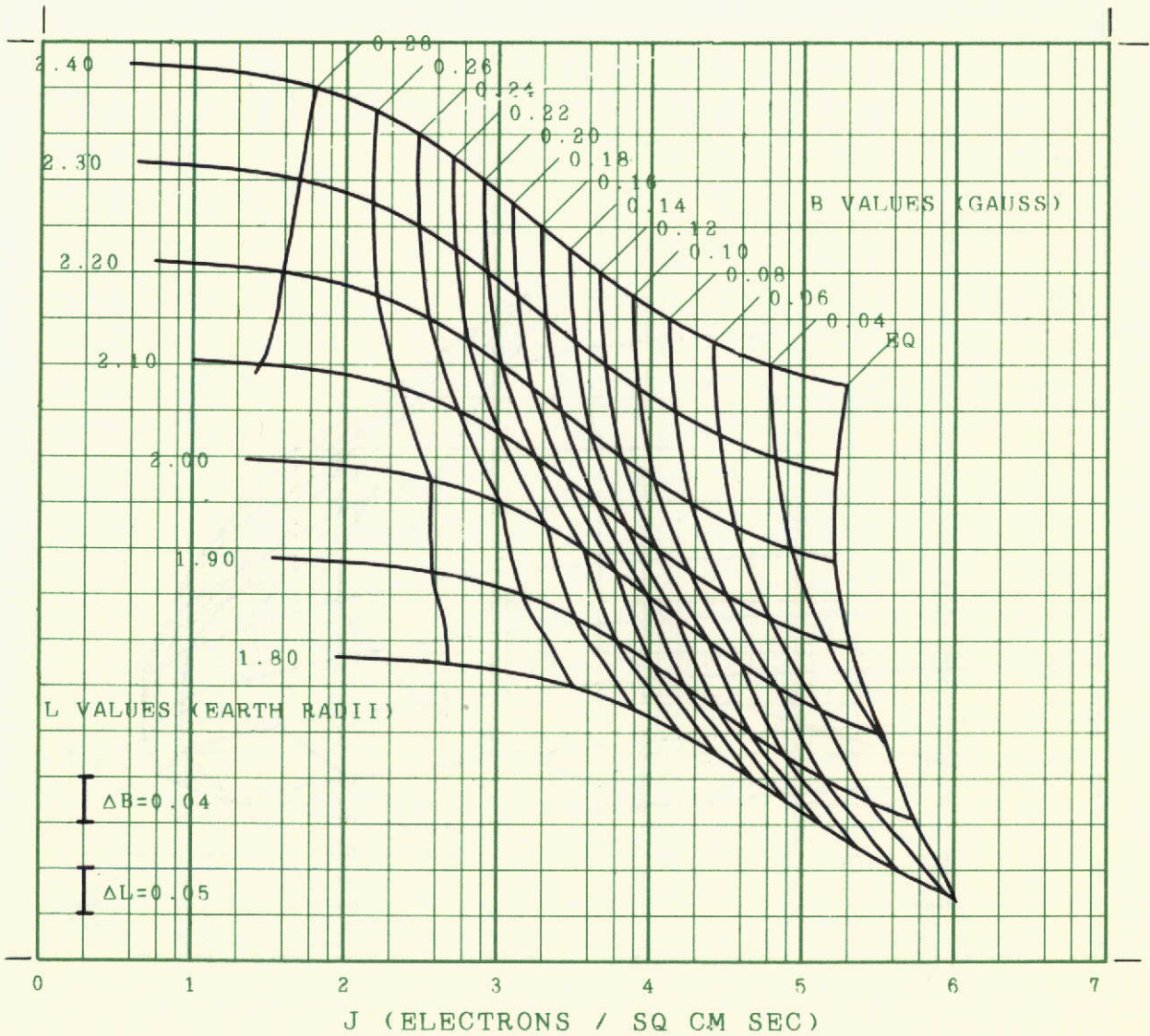
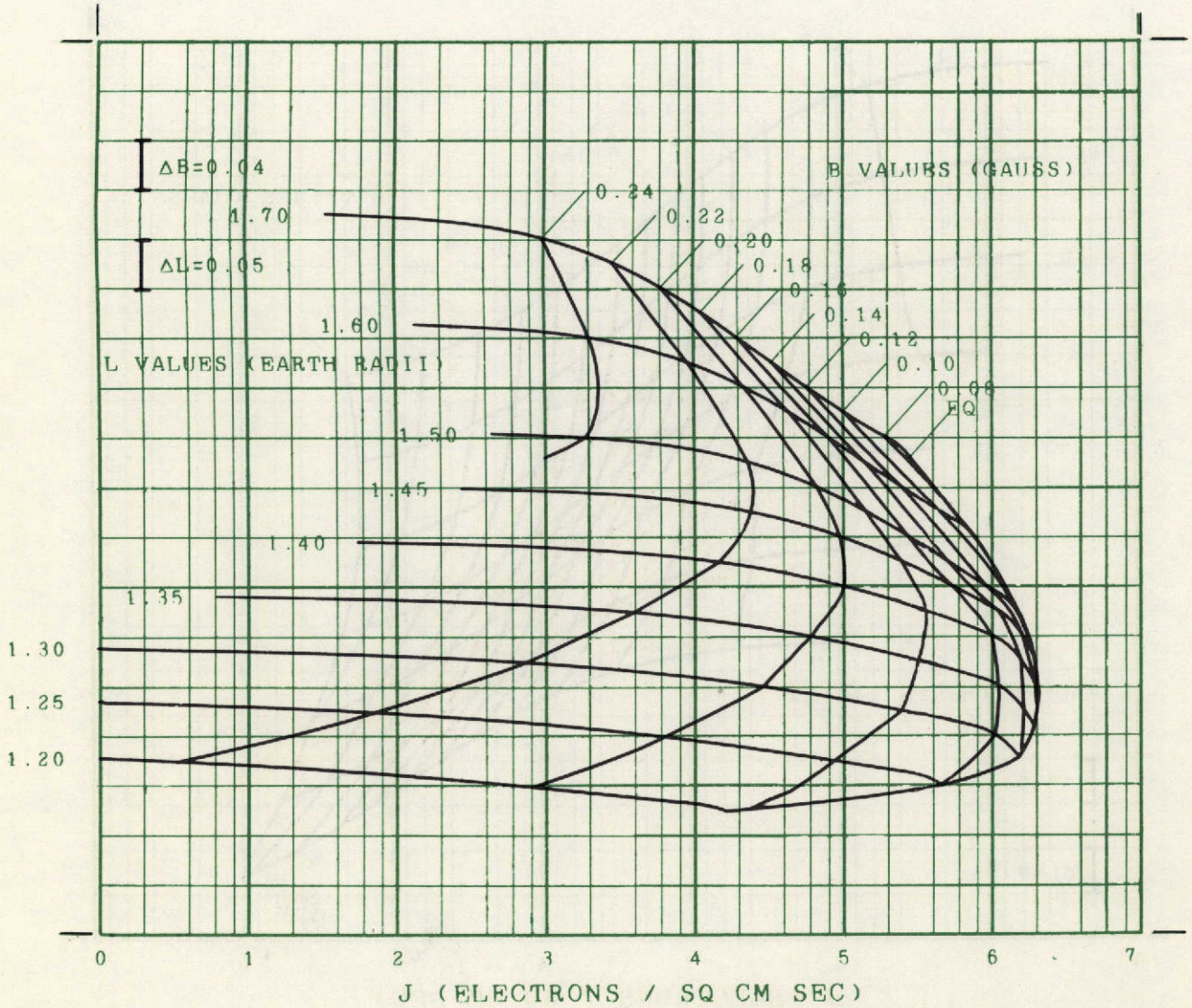
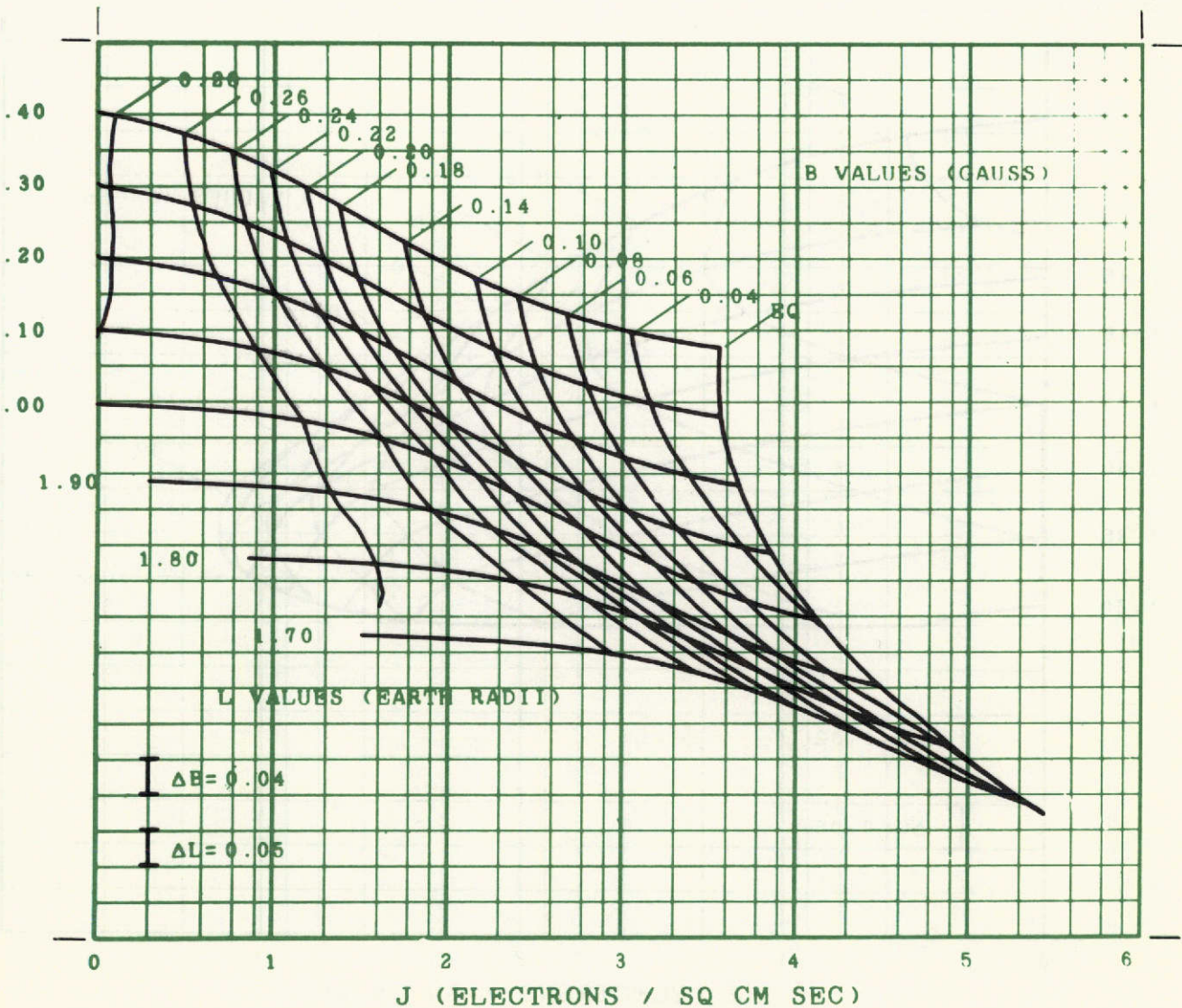


FIGURE 147

AE5 OMNIDIRECTIONAL INTEGRAL FLUX, ET=2 MEV  
EPOCH OCTOBER 1967

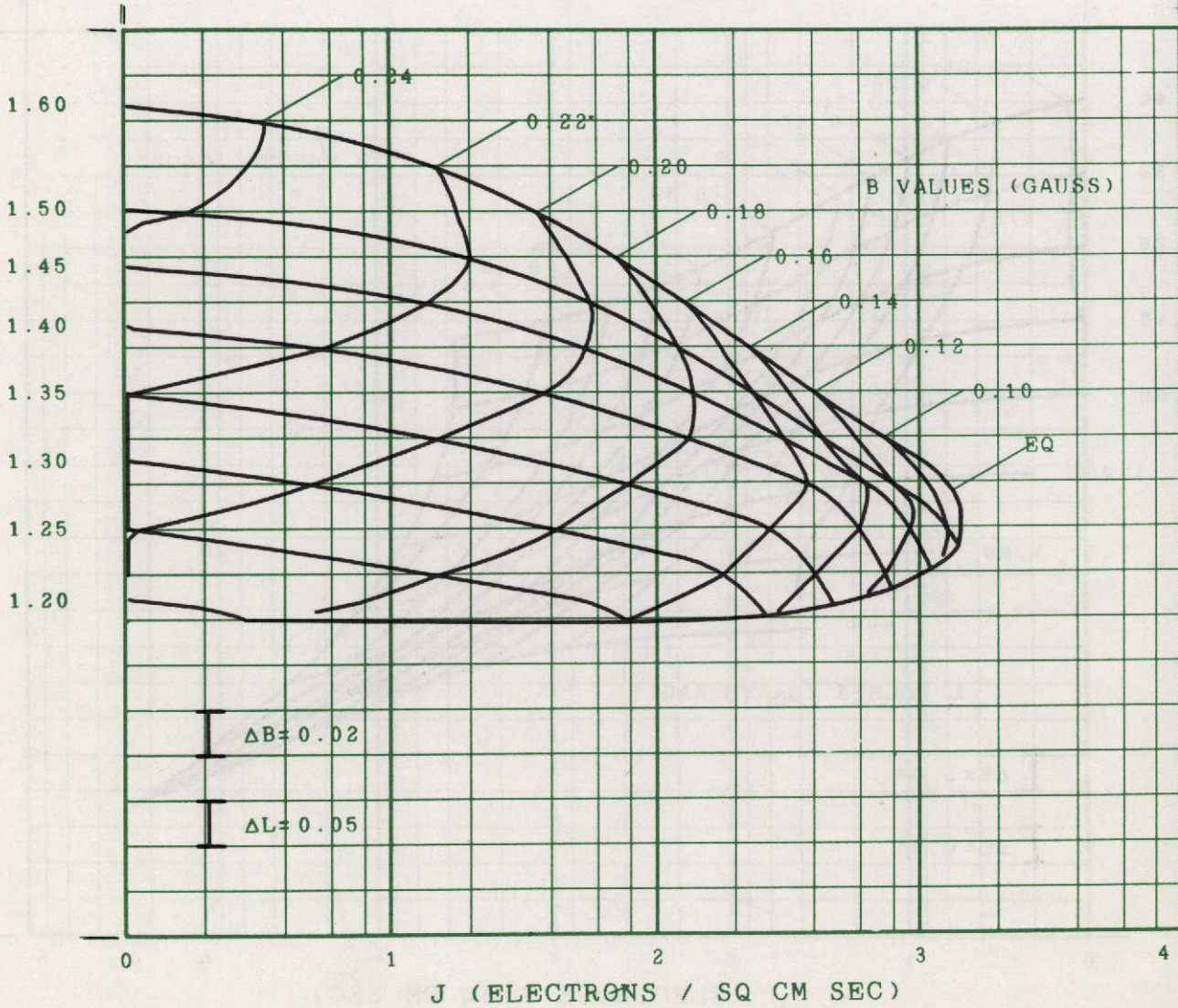


**FIGURE 147 CONT**  
**AE5 OMNIDIRECTIONAL INTEGRAL FLUX, ET=2 MEV**  
**EPOCH OCTOBER 1967**

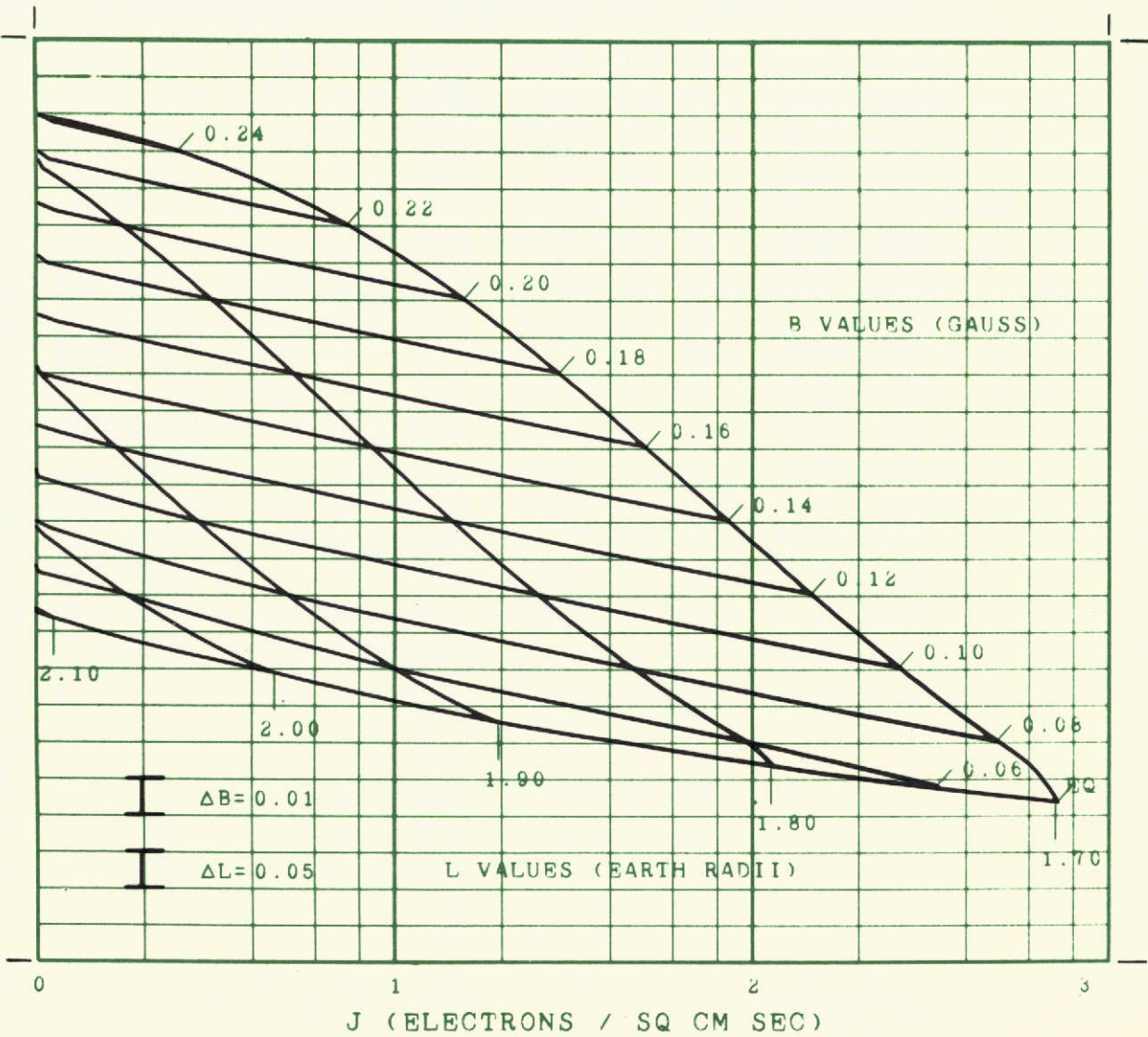


**FIGURE 148**  
 AE5 OMNIDIRECTIONAL INTEGRAL FLUX, ET=4 MEV  
 EPOCH OCTOBER 1967

L VALUES (EARTH RADII)



**FIGURE 148 CONT**  
**AE5 OMNIDIRECTIONAL INTEGRAL FLUX, ET=4 MEV**  
**EPOCH OCTOBER 1967**



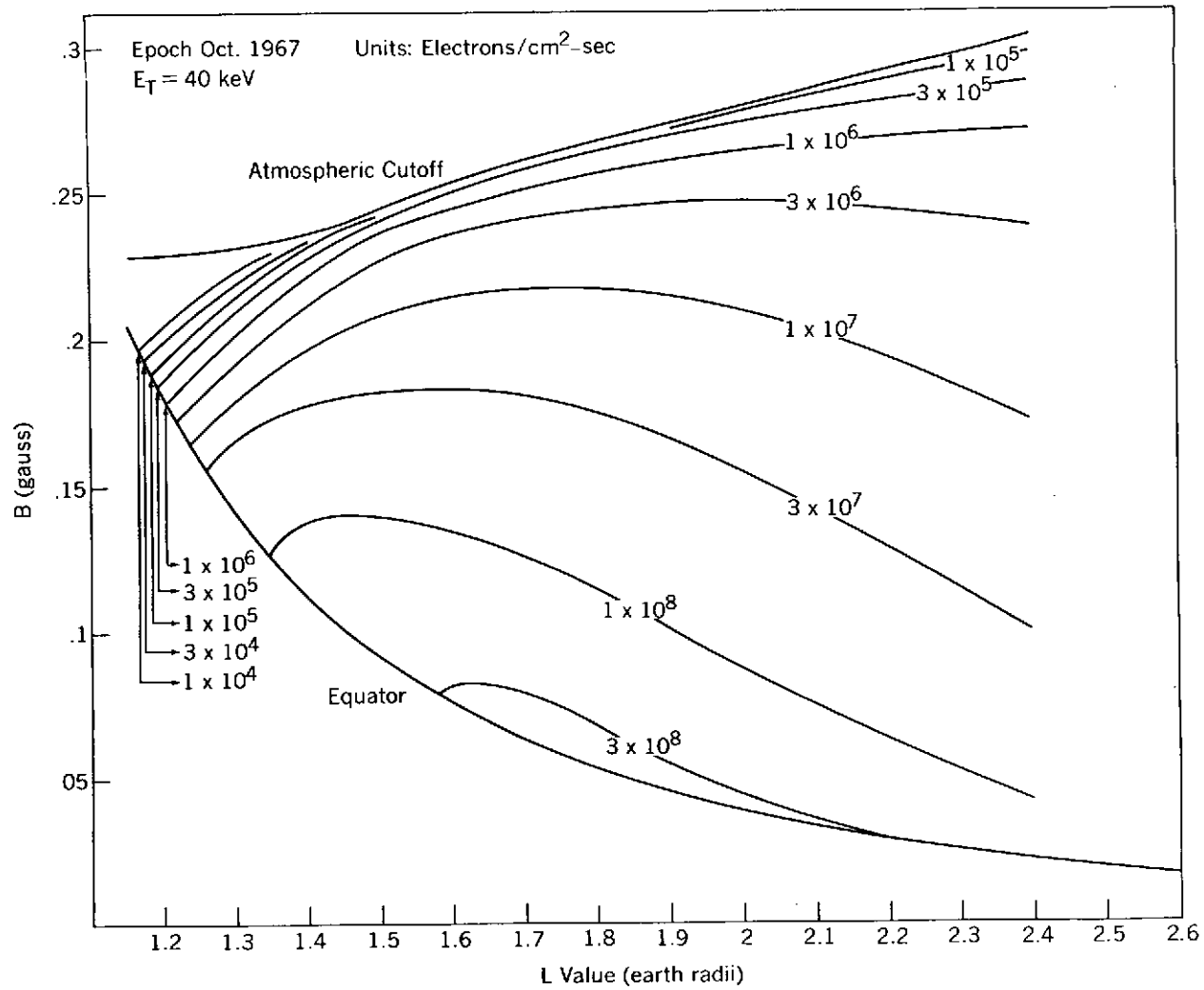


Figure 149. AE-5 B-L Flux Maps

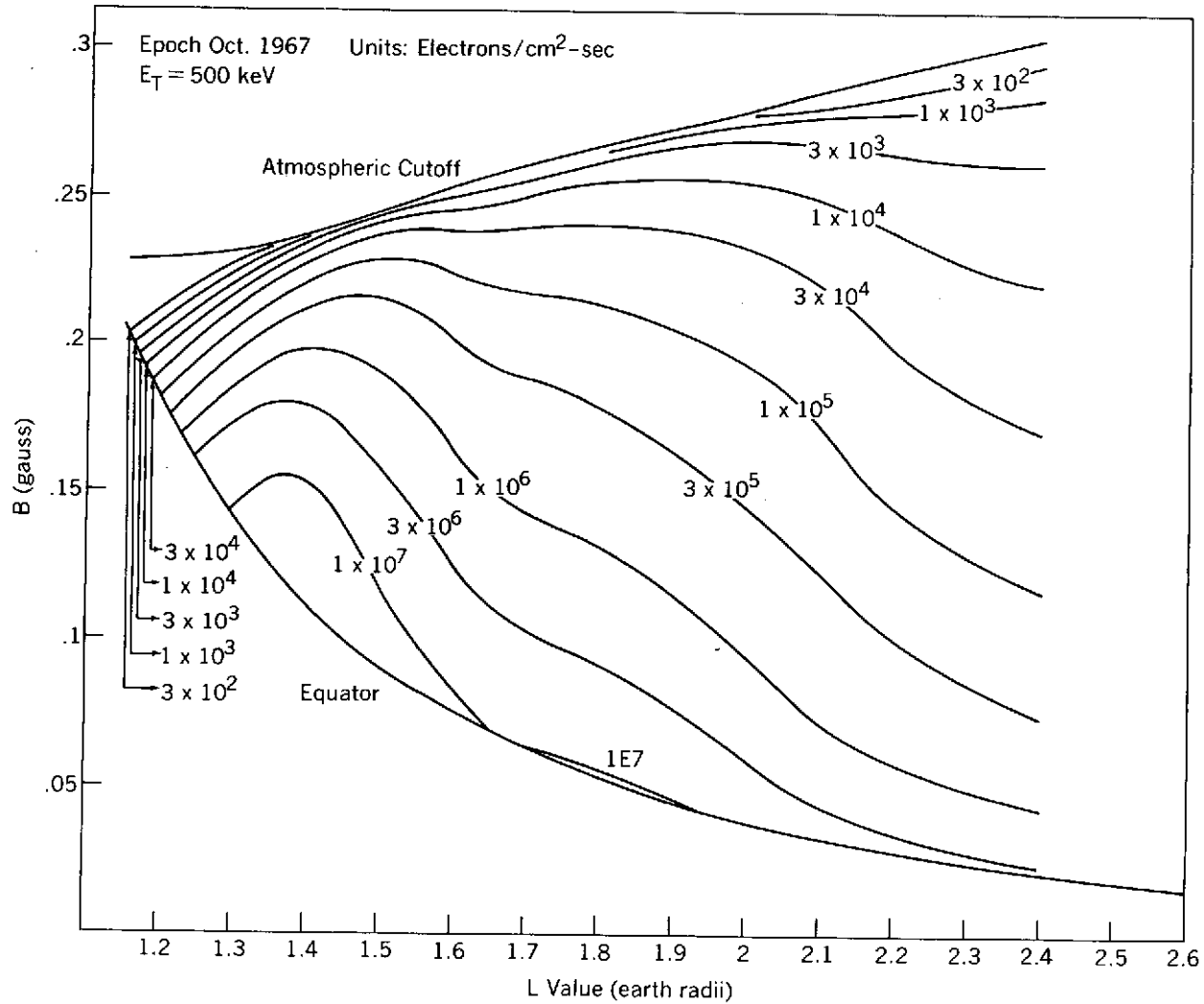


Figure 150. AE-5 B-L Flux Maps

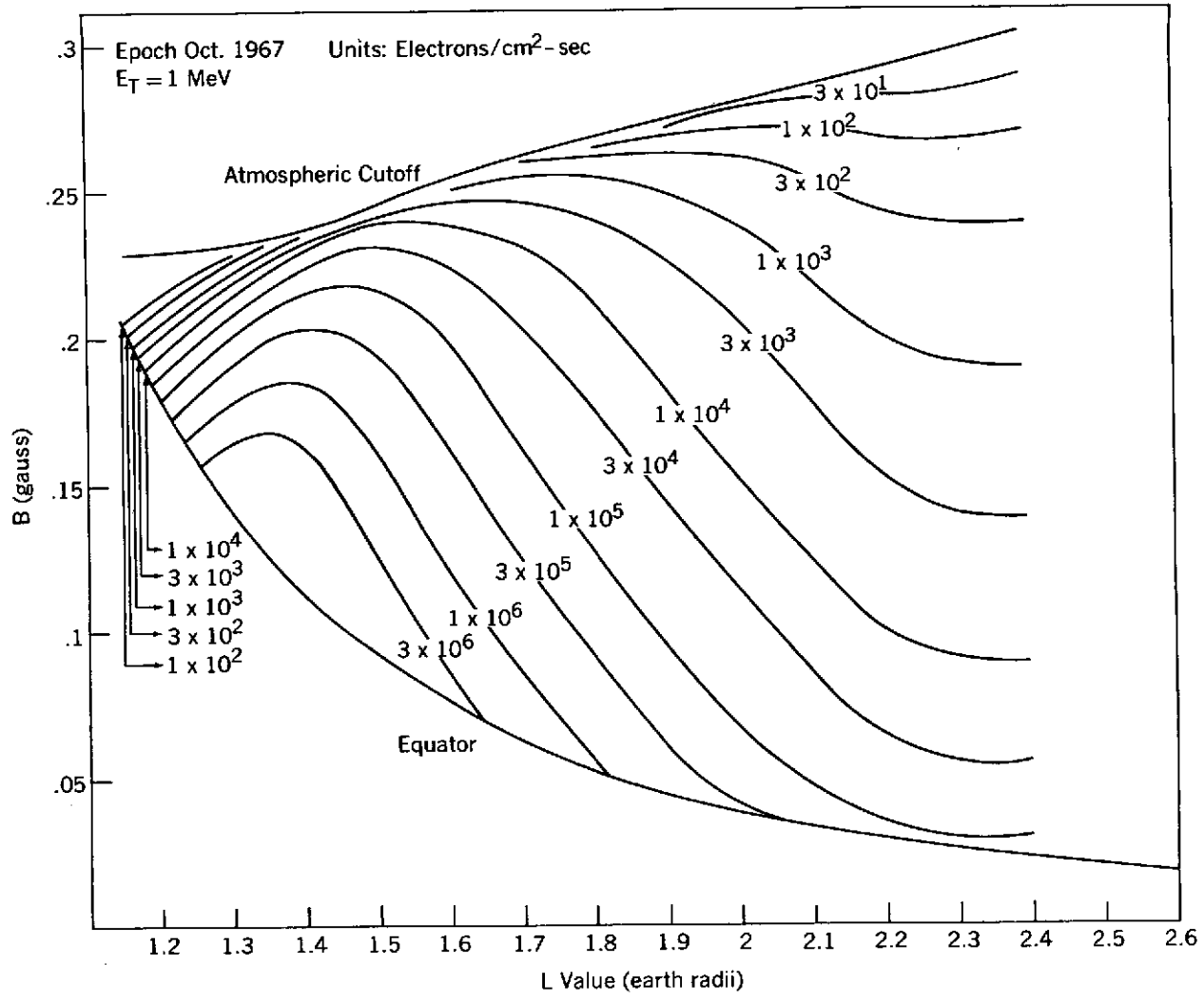


Figure 151. AE-5 B-L Flux Maps

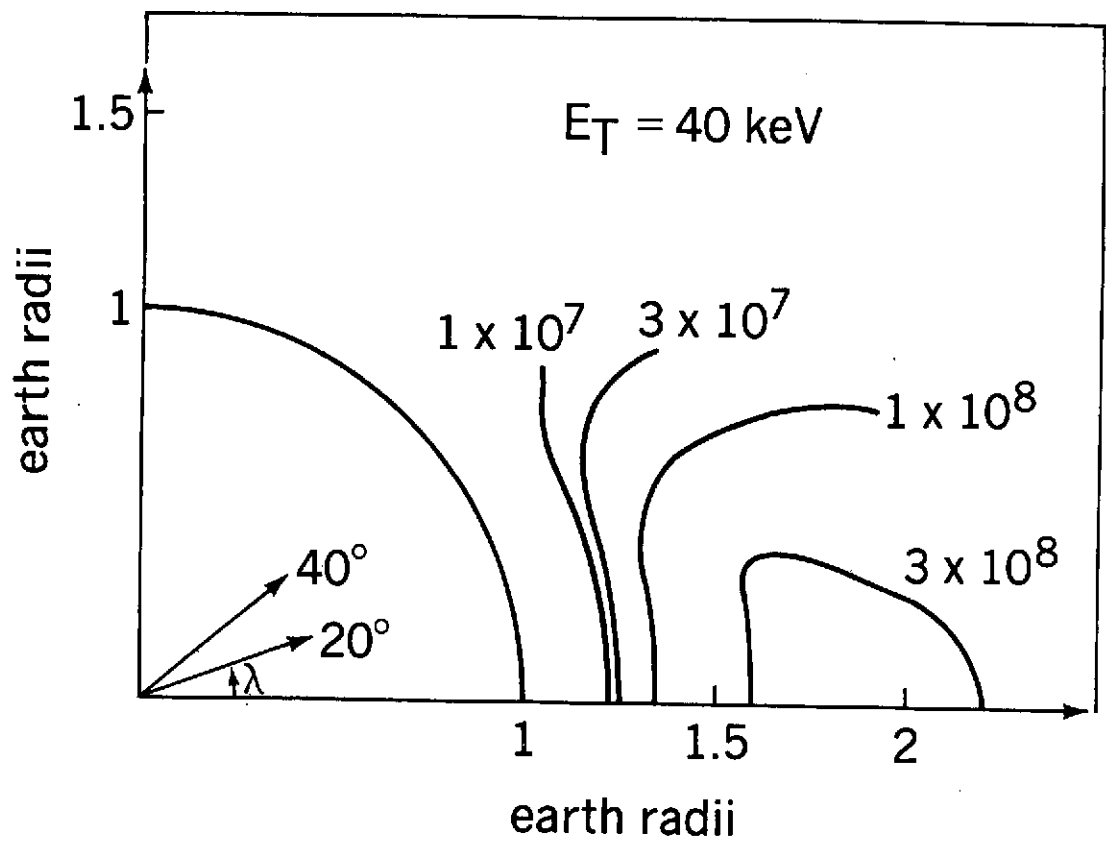


Figure 152. AE-5 R- $\lambda$  Flux Maps

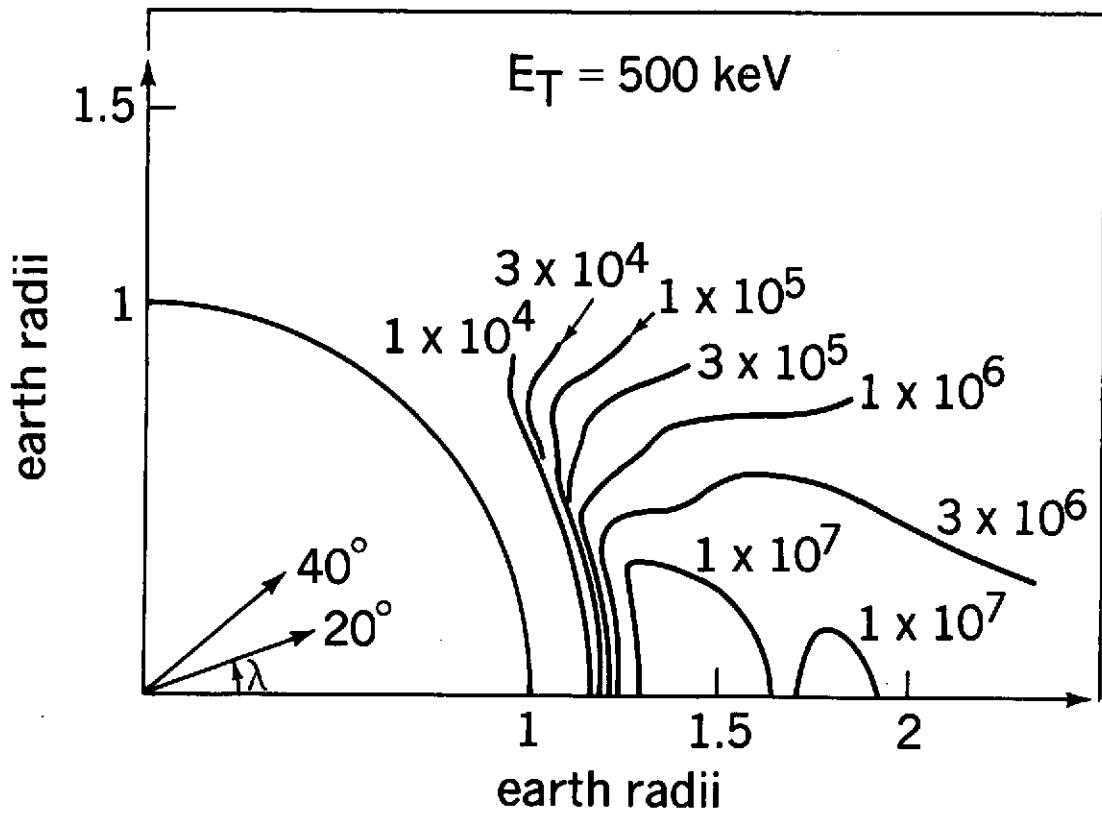


Figure 153. AE-5 R- $\lambda$  Flux Maps

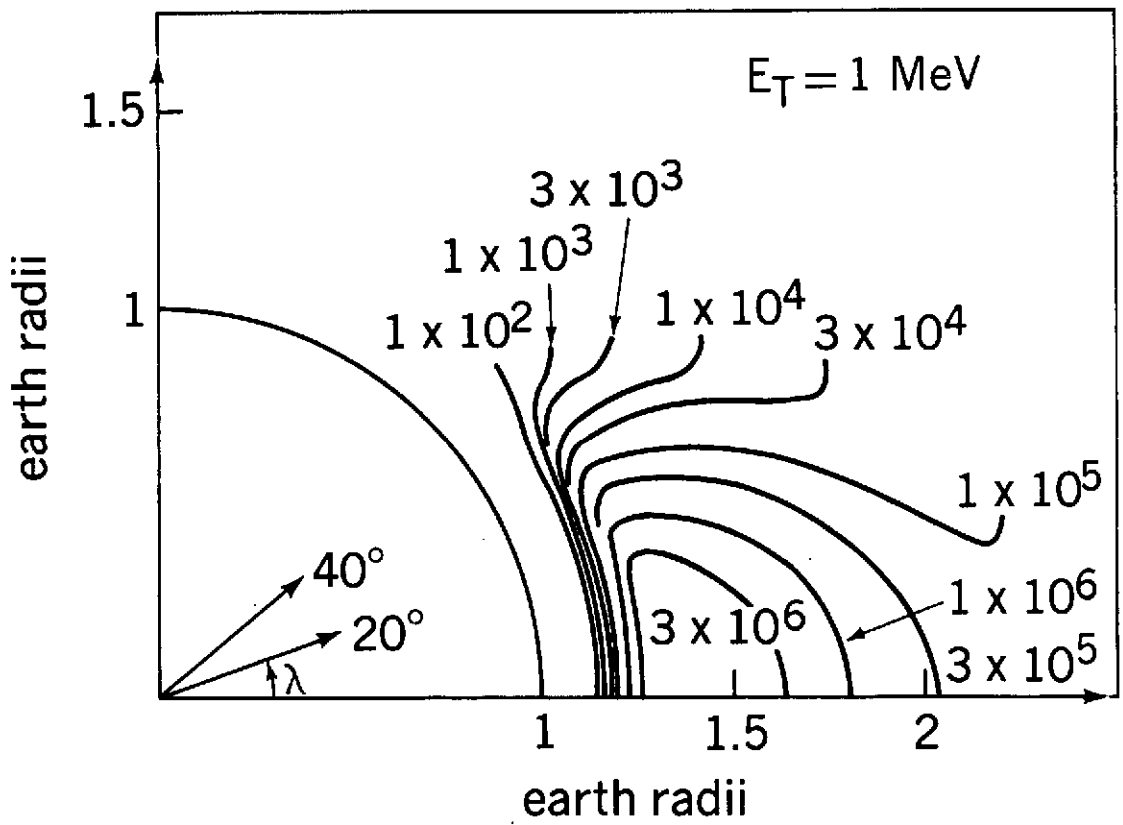
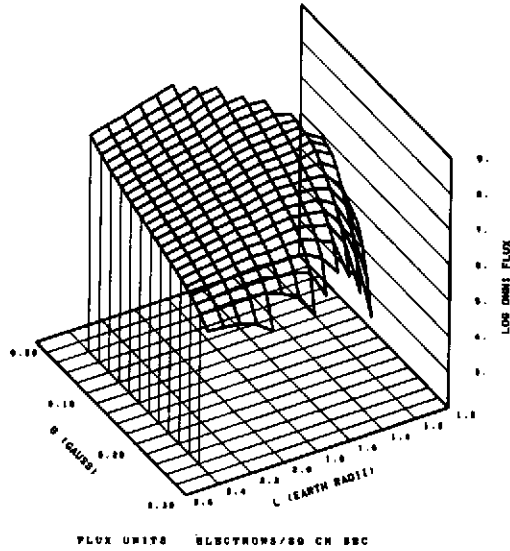
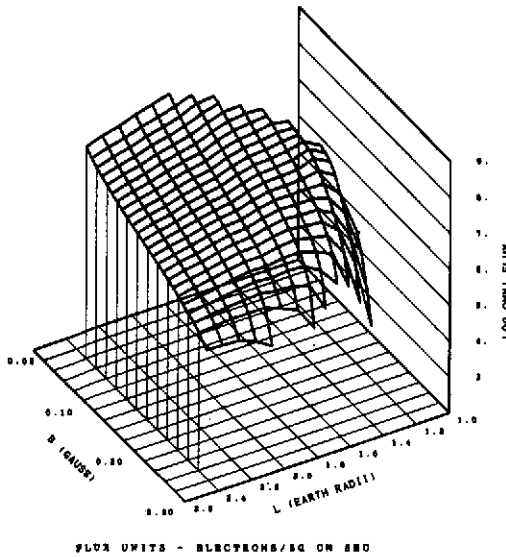


Figure 154. AE-5 R- $\lambda$  Flux Maps

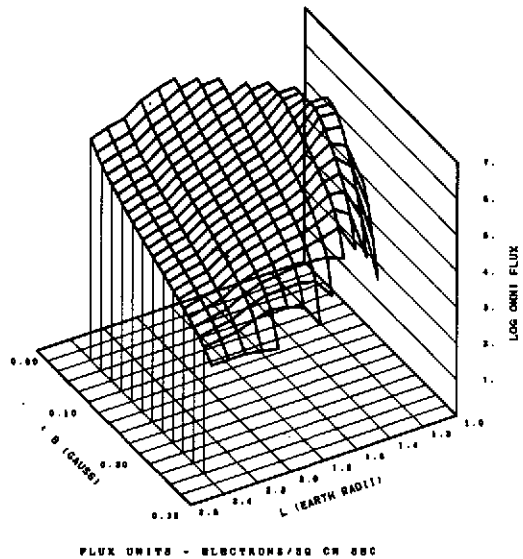
**FIGURE 155**  
**ABS OMNI-DIRECTIONAL INTEGRAL FLUX**  
**GREATER THAN 40 KEV**  
**EPOCH OCTOBER 1967**



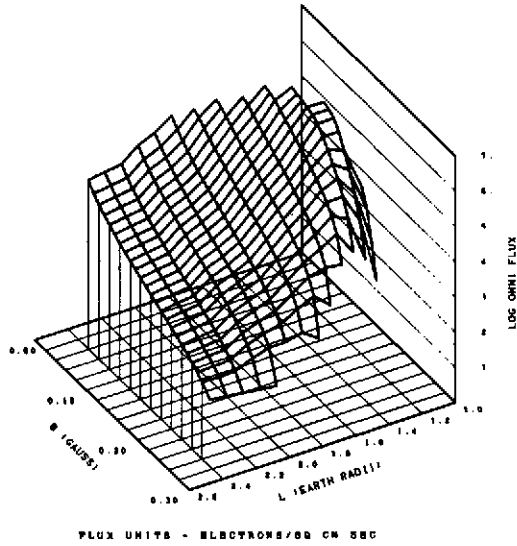
**FIGURE 156**  
**ABS OMNI-DIRECTIONAL INTEGRAL FLUX**  
**GREATER THAN 100 KEV**  
**EPOCH OCTOBER 1967**



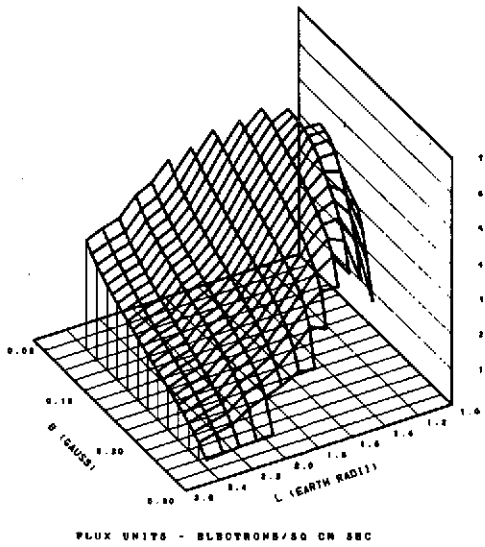
**FIGURE 157**  
**ABS OMNI-DIRECTIONAL INTEGRAL FLUX**  
**GREATER THAN 600 KEV**  
**EPOCH OCTOBER 1967**



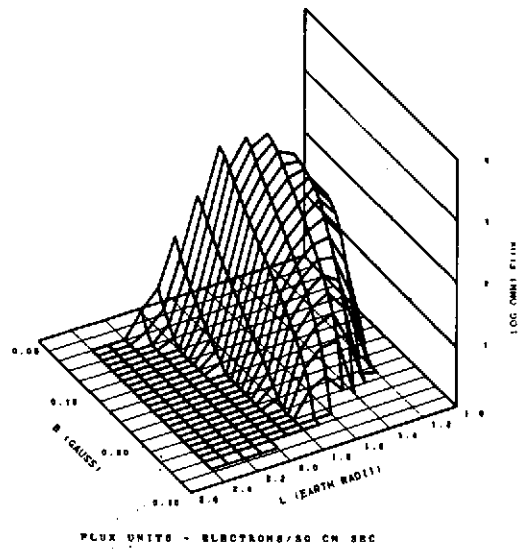
**FIGURE 168**  
 ABS OMNI-DIRECTIONAL INTEGRAL FLUX  
 GREATER THAN 1 MEV  
 EPOCH OCTOBER 1967



**FIGURE 159**  
 ABS OMNI-DIRECTIONAL INTEGRAL FLUX  
 GREATER THAN 2 MEV  
 EPOCH OCTOBER 1967



**FIGURE 180**  
 ABS OMNI-DIRECTIONAL INTEGRAL FLUX  
 GREATER THAN 4 MEV  
 EPOCH OCTOBER 1967



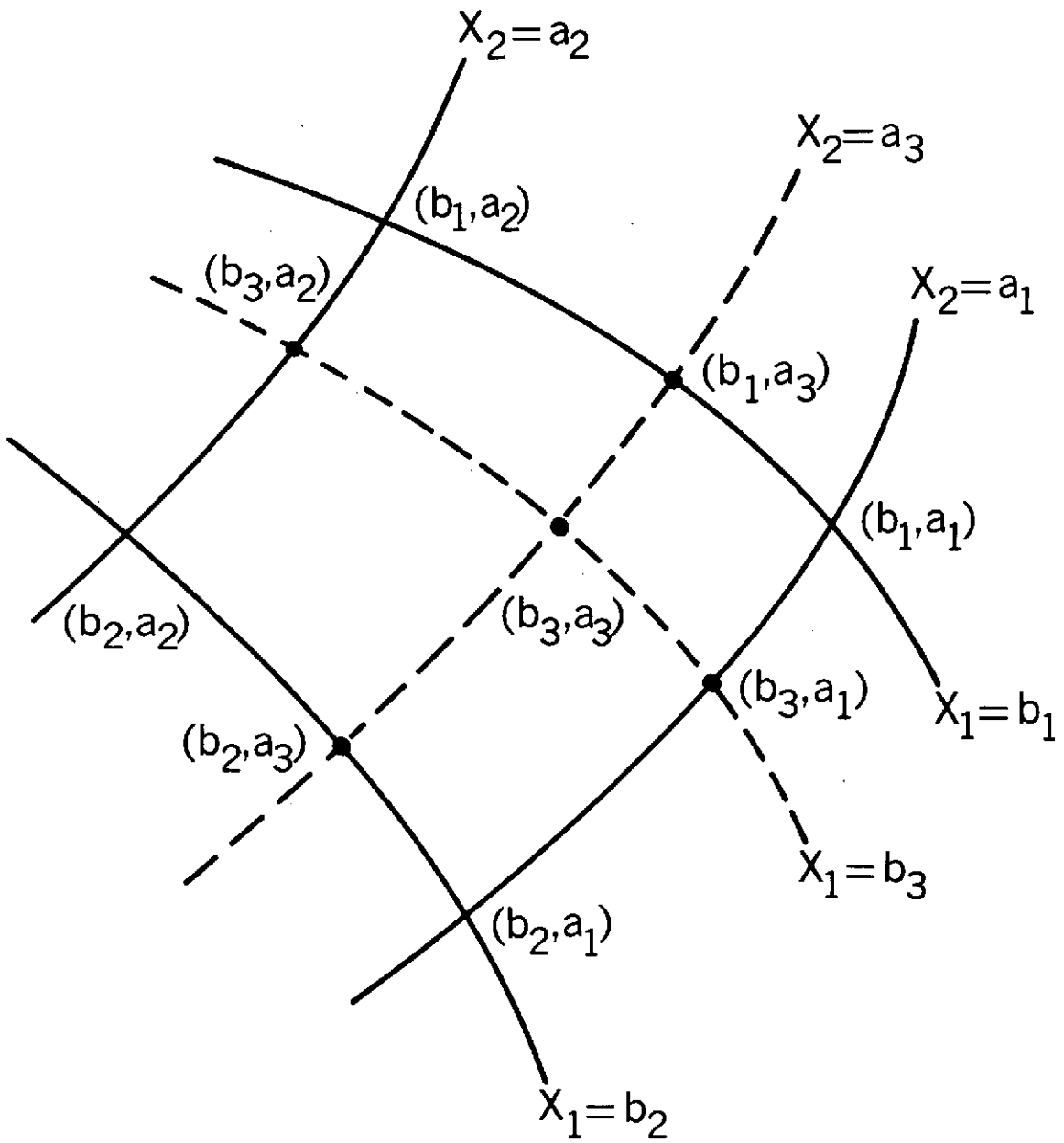


Figure 161. Carpet Plot Interpolation